Population oscillations along the cortico-striatal axis of awake behaving rats

Dissertation

Zur Erlangung der Würde des Doktors der Naturwissenschaften
des Department Biologie der
Fakultät für Mathematik, Informatik und Naturwissenschaften
der Universität Hamburg

vorgelegt von

Constantin von Nicolai
aus Bonn

Hamburg,
2012

Genehmigt vom
Fachbereich Biologie der
Universität Hamburg
auf Antrag von Herrn Professor Dr. A. K. Engel
Weitere Gutachter der Dissertation:
Herr Professor Dr. C. Lohr

Tag der Disputation: 17. Februar 2012

Hamburg, den 02. Februar 2012

Professor Dr. J. Fromm
Vorsitzender des Promotionsausschusses

As in evolution, "what might have been" is not relevant.
—Greg Graffin

Contents

Figures and Tables

List of Figures

List of Tables

Abbreviations

AP	anterior-posterior
AU	arbitrary units
bb/min	beam breaks per minute
BG	basal ganglia
CWT	continuous wavelet transform
D1	dopamine receptor D1
D2	dopamine receptor D2
DA	dopamine
DV	dorsal-ventral
ECoG	electrocorticogram
FFT	Fast Fourier Transform
FSI	fast-spiking interneuron
HVS	high-voltage spindles
LFP	local field potential
M1	primary motor cortex
mad	median absolute deviation
ML	medial-lateral
MSN	medium-spiny neuron
MUA	multi-unit activity
PD	Parkinson's disease
S1	primary somatosensory cortex
sd	standard deviation
sem	standard error of the mean
SNc	substantia nigra, pars compacta

Abstract

The cortico-basal ganglia-thalamocortical system is an integral part of the vertebrate forebrain that is crucially involved in the generation, adaptation, and selection of coordinated patterns of motor and non-motor behavior. It has been suggested that synchronized oscillations of neuronal population activities may be fundamentally important for signal encoding and transmission at the input stage of the basal ganglia, the cortico-striatal axis. This notion is in need of basic experimental support.

We trained Brown Norway rats (*Rattus norvegicus*) to run at different speed levels on a motor driven treadmill. We implanted microelectrodes in sensorimotor cortical and striatal areas of both hemispheres and recorded local field potentials (LFP) and multi-unit activities (MUA) during rest and running. We performed power, phase-coupling, and cross-frequency analyses to determine the spectral characteristics of neuronal signals and their interactions within and between the two structures. Furthermore, we examined in detail the modulation of power and phase-coupling patterns by motor demand.

Our data demonstrate prominent peaks of oscillatory power and the synchronization of cortical and striatal LFPs in low (theta) and high (gamma) frequency ranges during rest and running. MUA only exhibited very weak signs of low-frequency oscillatory synchronization whereas LFP-MUA coherences were statistically significant in the theta range. Most importantly, LFP power and phase-coupling peak frequencies increased between behavioral states. Moreover, peak frequencies but not peak amplitudes scaled linearly with motor demand. In addition, we observed a strong, behaviorally modulated coupling of LFP theta phase and gamma amplitude components as well as a decrease of cross-frequency LFP power correlations between resting and running states. Phase-locking–power correlation interaction analyses revealed a dissociation of the time courses of both coupling measures specifically at low and high running peak frequencies.

The results of the present study underscore that the frequency-specific synchronization of population oscillations may be fundamental for neuronal interactions along the cortico-striatal axis. More specifically, coordinated theta and gamma rhythms may support the functional coupling of both structures at small and large temporal scales according to current behavioral demands. This suggests that similar activity patterns may underlie signal encoding and transmission also at other stages of the cortico-basal ganglia loop.

1 Introduction

1.1 Cerebral cortex-basal ganglia circuitry

1.1.1 General anatomical outline

The basal ganglia (BG) are a group of nerve cell nuclei located in the forebrains of lower and higher vertebrates that are tightly linked to telencephalic, diencephalic, and mesencephalic structures with respect to both their input and output connections (Reiner et al., 1998; Reiner, 2010a; Stephenson-Jones et al., 2011). In most general terms, the basal ganglia "connect the cerebral cortex with neural systems that effect behavior" (Gerfen and Bolam, 2010, page 3). Figure 1.1 displays the central parts constituting this brain system as well as their major connecting axonal projections.[1]

The basal ganglia proper are made up of the striatum, the globus pallidus with its internal (GPi) and external (GPe) parts, the substantia nigra pars reticulata (SNr) and pars compacta (SNc), and the subthalamic nucleus (STN) (Figure 1.1). Brainstem input and output structures left aside, these nuclei form core elements of partially closed anatomical loops originating from and terminating in the cortical mantle (Alexander et al., 1986). In this system, interposed thalamic regions serve as both important processing modules and relay hubs at its final output stage (Haber and Calzavara, 2009). In the following, whenever we talk about the cortico-basal ganglia network, we refer to the circuitry involving cortical, basal ganglia, and associated thalamic structures.

As indicated schematically in Figure 1.1, the striatum is the major input site of the basal ganglia that receives excitatory projections from almost all areas of the cerebral cortex (Alexander et al., 1986; Parent and Hazrati, 1995). Basal ganglia output from the internal part of the globus pallidus and the reticular part of the substantia nigra to the thalamus is inhibitory, while thalamic output to the cortex is again excitatory (Parent and Hazrati, 1995). In marked contrast to basal ganglia input which derives from all cortical lobes, its cortical output projections mainly terminate in frontal regions, i.e., premotor, prefrontal, and orbitofrontal areas (Alexander et al., 1986; but see Middleton

[1] Note that while some of the ensuing descriptions primarily relate to the characteristics of BG anatomy of primates, most underlying principles and details are very similar to those found in other vertebrate species, rodents in particular (Reiner et al., 1998; Gerfen and Bolam, 2010).

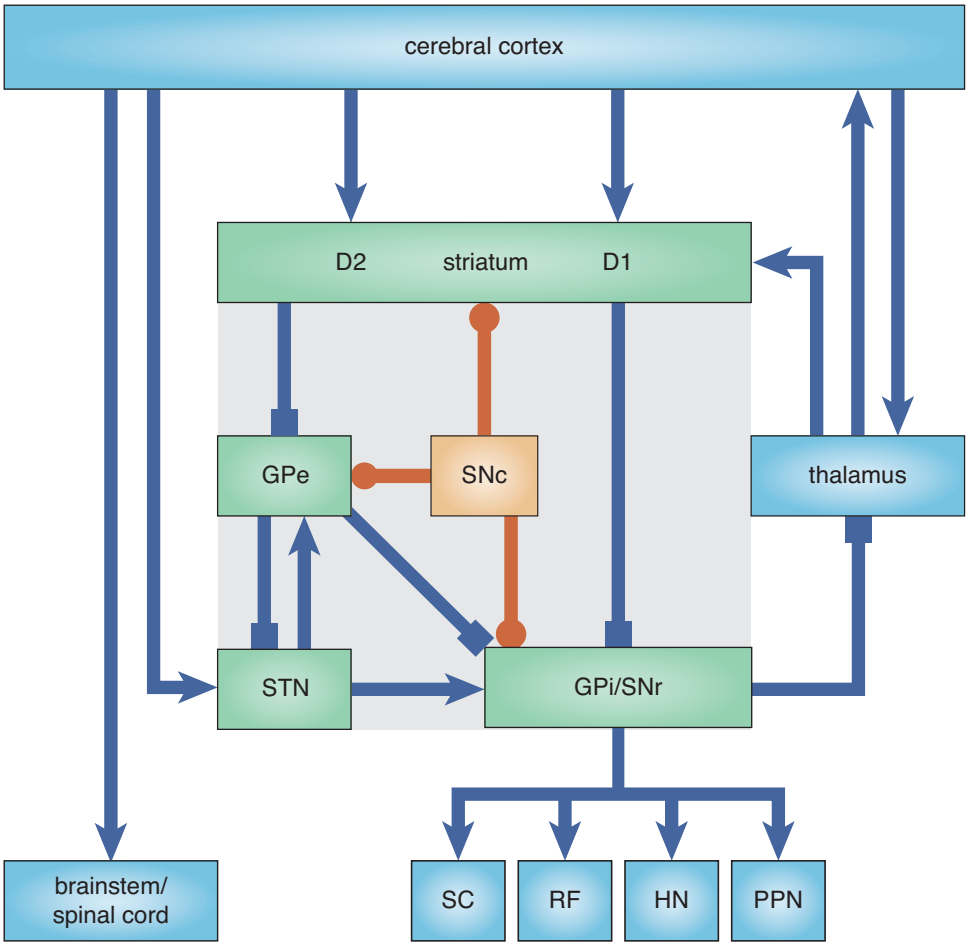

Figure 1.1: General anatomical outline of the cortico-basal ganglia network, including its nuclear constituents (green boxes) as well as the major input- and output structures (blue boxes) as established in the so-called *box-and-arrow model* (see main text). The figure also depicts the distinction between the *direct* and *indirect* pathways of the BG that arise from striatal output neurons preferentially carrying D1 and D2 dopamine receptors, respectively. Signals from the former project directly to basal ganglia output structures, while the latter pathway reaches GPi/SNr indirectly via GPe and STN. The STN also receives direct input from cortical areas via the so-called *hyperdirect* pathway. Furthermore, note the two fundamentally different output pathways of the BG reaching brainstem nuclei on the one hand and thalamic structures on the other. Blue lines ending in arrowheads and squares denote excitatory and inhibitory connections, respectively. The red color of the SNc and the circular endings of its projection lines indicate the neuromodulatory character of dopaminergic neurons. Note that, for reasons of clarity, further structural and connectional details have been omitted. *Abbreviations:* D1/D2: dopamine receptors D1 and D2; GPi/GPe: globus pallidus, internal and external parts; HN: habenular nucleus; PPN: peduncular pontine nucleus; RF: reticular formation; SC: superior colliculus; SNc/SNr: substantia nigra, pars compacta and pars reticulata; STN: subthalamic nucleus. Figure partly inspired by Sharott, 2005 and Alexander et al., 1990.

and Strick, 1996). In this way they form the aforementioned partially closed cortico-basal ganglia-thalamocortical loops (see Section 1.1.2). The cortical output areas of these loops are, amongst other things, involved in the planning and execution of body movement. Other target regions of the BG include, for example, the superior colliculus that is involved in the generation of eye movements, and the pedunculopontine nucleus which plays a role in orienting movements (Gerfen and Bolam, 2010).

Basal ganglia nuclei are anatomically arranged in part serially and partly in parallel, having either excitatory or inhibitory connections, or both (Alexander and Crutcher, 1990a). On its intermediate stages, the BG circuitry has been subdivided into two major pathways, based upon the existence of anatomically distinct projections originating in the striatum (Figure 1.1). The *direct* path consists of the immediate, inhibitory connection of striatal and pallidal/nigral regions, while the *indirect* path reaches the output nuclei via the external part of the GP (Parent and Hazrati 1995; see also Section 1.2.1 below). The exact interplay of both pathways and the impact they exert on basal ganglia output structures has yet to be established. Most generally speaking, as their anatomical makeup suggests, they are assumed to provide a regulatory balance between excitatory and inhibitory signals reaching BG target regions (Gerfen and Bolam, 2010).

The scheme depicted in Figure 1.1 has gained wide popularity as the so-called *Albin-DeLong* or *box-and-arrow* model of basal ganglia functional anatomy. As such, it has been very helpful for the interpretation of some of their key properties in the healthy and the diseased state (Albin et al., 1989; DeLong, 1990; DeLong and Wichmann, 2007). Although important modifications have been put forward in recent years that aim at the model's various explanatory shortcomings and insufficiencies (e.g., Bolam et al., 2000; Bar-Gad and Bergman, 2001), it has continued to provide a unifying outline of the principles governing the functional-anatomical organization of the basal ganglia on which subsequent elaborations could be elegantly build.

1.1.2 Functional anatomy of cortico-basal ganglia loops

As mentioned above (Section 1.1.1), input to the BG derives from virtually all cortical areas. This provides them with a multitude of different types of inputs. That being said, the overall picture of the functional-anatomical organization of basal ganglia circuitry has substantially changed over the last decades.

Overall, according to a peculiar ordering of cortical inputs, the organization of BG circuitry can be conceived of as roughly tripartite (Parent, 1990; Parent and Hazrati, 1995; Joel and Weiner, 2000), with different segments preferentially subserving sensory-motor, associative-cognitive, or limbic-emotional processes (Alexander et al., 1990). Earlier stud-

ies proposed a *funneling* scheme of organization in which the inputs from functionally different cortical domains would be integrated and merged progressively at each subsequent basal ganglia relay point (e.g., Kemp and Powell, 1970). In contrast, more recent reports emphasize the *parallel* nature of information processing along functionally distinct projections that in principle remain segregated throughout the circuit's entire extent, although substantial interactions are supposed to take place between them (Delong et al., 1984; Alexander and Crutcher, 1990a; Bergman et al., 1998; Gerfen and Bolam, 2010; see also Figure 1.3, page 10).

Pioneering studies (e.g., Hoover and Strick, 1993; Middleton and Strick, 1994) have delineated a number of major anatomical tracts conveying activities from different brain systems through the basal ganglia that form the structural substrate of its diverse functional roles (for extensive reviews, see Alexander et al., 1986; Parent and Hazrati, 1995; Wise et al., 1996). In their famous accounts, Alexander and colleagues identified at least five distinct cortico-basal ganglia-thalamocortical loops (sensorimotor, oculomotor, dorsolateral-prefrontal, lateral orbitofrontal, and anterior cingulate) constitutive of the three main segments (Alexander et al., 1986, 1990; Alexander and Crutcher, 1990a). They also speculated about the existence of sub-loops within the larger ones connecting even smaller parts of the structures. In any case, a substantial degree of both convergence and divergence of projections has been proposed to characterize major and minor cortico-basal ganglia loops (Parent and Hazrati, 1993).

The general subdivision of the cortico-basal ganglia-thalamocortical circuitry into different functional domains is now widely accepted in the BG research field. However, several issues such as the degree of separation between the different loops, interactions between them, and the exact way of information processing within and between the participating structures await further elaboration in future studies (Haber et al., 1994; Joel and Weiner, 1994; Mink, 1996; Bergman et al., 1998; Bar-Gad et al., 2003).

1.1.3 Functional role of cortico-basal ganglia systems

For a long time, the basal ganglia and the functional brain systems that they are an integral part of were considered to be concerned primarily with the processing of sensorimotor signals and various aspects of motor control (e.g., Kornhuber, 1971; Marsden, 1984b; Mink, 1996; Brown et al., 1997; Turner and Desmurget, 2010). In clinical terms, the basal ganglia had been shown to be affected in the context of various neurological conditions characterized by severe motor symptoms, such as Parkinson's (PD) and Huntington's disease, different types of dystonia or tremor (Phillips et al., 1993). Results from anatomical and physiological studies had indicated substantial connections with motor

cortical and subcortical areas (Nauta and Mehler, 1966) and their interaction with these systems during behavior as evidenced by findings from single-cell recording experiments in awake animals (DeLong, 1972; Delong et al., 1984; Crutcher and DeLong, 1984a,b; Hikosaka et al., 1989a; West et al., 1990).

However, results from both clinical and experimental studies had also left ample room for the proposition of a more diverse and complex role of basal ganglia systems function and for their implication in other, non-motor aspects of behavior and pathological alterations thereof (Crutcher and DeLong, 1984a,b; Marsden, 1984a; Hikosaka et al., 1989b,c; Bhatia and Marsden, 1994; Brown and Marsden, 1998; Heimer, 2003). Building on the assumption of a roughly tripartite anatomical organization as described in the previous section (1.1.2), at least three major functional domains can be distinguished as well. This suggests basal ganglia systems to take part in the processing of neuronal signals related to sensorimotor, associative-cognitive, and limbic-emotional aspects of behavior as well as a wide variety of combinations between them (Graybiel, 2005; Haber and Calzavara, 2009). Accordingly, various authors have discussed the involvement of basal ganglia circuits and thus the striatum and the cortico-striatal axis (Section 1.2.2) in, amongst other things, movement generation and adaptation (DeLong, 1971; Crutcher and DeLong, 1984b; Romo et al., 1992), external (Brown et al., 1997; Syed et al., 2011) and internal perceptual mechanisms (Buhusi and Meck, 2005), different types of learning (Packard and Knowlton, 2002; Schultz et al., 2003; Yin and Knowlton, 2006; Antzoulatos and Miller, 2011), mechanisms of attention and the control of working memory (Levy et al., 1997; Hikosaka et al., 2000; McNab and Klingberg, 2008) as well as reward processes (Apicella et al., 1991; Robbins and Everitt, 2002; Schultz, 2006). Taken together, these data provide evidence that the BG are, to some degree or another, involved in many different aspects of lower and higher brain functions.

Despite all those findings, the exact contribution of basal ganglia activities to the central nervous systems operations constitutive of these various sorts of behaviors, as much as the kinds of computations carried out in BG circuits on the neuronal signals underlying such network functions, are still far from clear (Mink, 1996; Bar-Gad et al., 2003). The complexity of their anatomical constitution which differs starkly from, e.g., the largely modular organization of neocortical areas (Buzsáki, 2006), as well as the variety of response profiles obtained through recordings of population activities from their constituent nuclei and associated structures suggests a systems-level *integrative* and, at the same time, *selective* role with regard to the processing of a diversity of signals of different origin which is crucial to the generation of complex behaviors (Redgrave et al., 1999; Graybiel, 2005). This rather vague notion gains additional support again from clinical observations of the pattern of symptoms characteristic of disorders of basal ganglia

origin. First, as noted above, symptoms are seldom confined to one functional domain and there is no complete loss of one or several specific capacities such as it is often the case, for example, following stroke. Second, and in relation to that, the way the different behavioral subdomains are afflicted often exhibits a kind of complexity that readily suggests a mixture of systems to be affected by the respective disease (e.g., consider the motor, sensory, and cognitive deficits encountered in patients suffering from Parkinson's disease; Brown and Marsden, 1998; Middleton and Strick, 2000). Investigations into basal ganglia operational mechanisms in the healthy state are comparably equivocal regarding the interpretability of their results. Therefore, the overall role of BG systems in brain function has remained elusive and a matter of intense speculation to date.

1.2 The cortico-striatal axis

1.2.1 Macroscopic and microscopic anatomy of the striatum

The basal ganglia receive the bulk of their input from cortical areas via the striatum, a big structure that spans a considerable portion of the forebrain in both anterior-posterior (AP) and medial-lateral (ML) extents. In primates, the striatum is further subdivided into the caudate nucleus and the putamen by the massive fiber bundles of the internal capsule traversing the structure that carry projection fibers originating in the cortical mantle which is substantially enlarged in higher as compared to lower vertebrates (Rakic, 2009). In the rat, the striatum still consists of only one large nucleus (Gerfen and Bolam 2010; a coronal section through the rat striatum at the level of the so-called *bregma* is depicted in Figure 2.4, page 32). With respect to its neuronal constituents, the striatum is composed of projection cells and interneurons (Parent and Hazrati, 1995), the most important and most extensively studied ones we briefly describe here (Figure 1.2).

There are two major subclasses of projection cells, so-called *medium-spiny neurons* (MSN) that give rise to the inhibitory striatal direct and indirect output pathways (Bolam et al., 2000) described above (Section 1.1.1). They can roughly be distinguished using two main criteria, namely their preferential nuclear targets (Parent et al., 1984; Gerfen and Bolam, 2010) and the type of dopamine (DA) receptors they carry (Gerfen et al., 1990). As indicated in Figure 1.1 (page 2), direct pathway MSNs mainly express D1 receptors, mediating an excitatory influence of dopamine on MSN function. MSNs giving rise to the indirect pathway, in contrast, preferentially carry D2 receptors that mediate an inhibitory modulation of MSN function by the neurotransmitter (Surmeier et al., 2007; Gerfen and Bolam, 2010). These differences result in a net inhibition and disinhibition of striatal output targets via direct and indirect pathways, respectively (Smith et al., 1998).

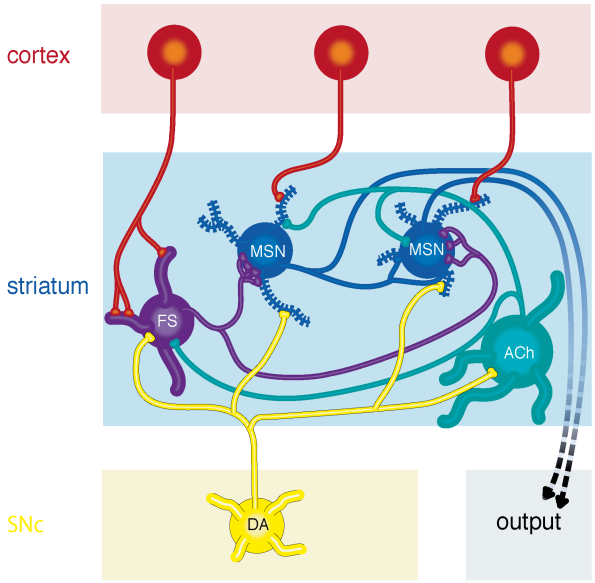

Figure 1.2: The "canonical microcircuit" of the striatum as described by Bolam and colleagues (Bolam et al., 2006, page 166). The figure depicts the main neuronal elements of the structure, the pattern of their local connections as well as their most important external inputs. Blue, medium-spiny projection neurons; green, giant aspiny interneurons; purple, medium-sized aspiny interneurons; red, cortico-striatal projection neurons; yellow, dopaminergic neurons from the substantia nigra pars compacta. Note the differential targeting of structural elements arising from projections connecting the different cellular classes. Cortical input to giant aspiny interneurons has been omitted. *Abbreviations:* ACh, acetylcholine; DA, dopamine; FS, fast-spiking; MSN, medium-spiny neuron. Figure kindly provided by J. P. Bolam, adapted from Bolam et al. (2006) with permission.

The inhibitory output of MSNs is mediated by gamma-aminobutyric acid (GABA) while dopamine is the major external modulatory substance of cortico-striatal inputs before others such as serotonin or histamine (Bolam et al., 2000; Gerfen and Bolam, 2010; Ellender et al., 2011). Because of the specific output activity profiles of successive nuclei along the cortico-basal ganglia loop, the effects of direct and indirect pathway activities are often described as pro-kinetic and anti-kinetic, respectively. This notion has recently received further strong experimental support (Kravitz et al., 2010).

Interneurons of the striatum can be divided into two main groups, the giant aspiny and medium-sized aspiny (also called fast-spiking, FS) interneurons that use acetylcholine and GABA as transmitters, respectively (Tepper and Bolam, 2004). The former, cholinergic interneurons, seem to be a homogenous group, whereas the latter, GABAergic interneurons, can be further classified according to their differential equipment with neuropeptides, amongst other criteria (Kreitzer, 2009). Interneurons exhibit a variety of activity

profiles both spontaneously and in response to external input (Tepper and Bolam, 2004). They are part of the dense intrastriatal cellular network exerting their influences on MSNs through local projections, and their activities are also modulated by dopamine (Figure 1.2; Mallet et al. 2005; Bolam et al. 2006).

In terms of total numbers, projection neurons largely outweigh interneurons, their respective proportions varying between 95 vs. 5% in rodents to 80 vs. 20% in primates (Gerfen, 2004). The very important influence of interneuron activities on striatal function notwithstanding, MSNs can be considered to be the principal integrative cellular elements of the striatum, unifying its diverse inputs and, at the same time, generating striatal output and transmitting it to downstream structures (Smith and Bolam, 1990; Houk and Wise, 1995; Parent and Hazrati, 1995; Gerfen and Bolam, 2010). In terms of their external inputs, they are the target of axons originating from, amongst other structures, the cortex, the thalamus, and the dopaminergic neurons of the substantia nigra pars compacta[2] (Gerfen, 2004). Since in this study we investigate signals along the cortico-striatal axis, this projection is described in more detail in the following section (1.2.2).

1.2.2 Functional anatomy of the cortico-striatal axis

As studies in a variety of vertebrate species have shown, cortical inputs to the striatum arise from virtually all cortical areas. This includes primary and higher order sensory and motor areas, prefrontal and limbic regions, with the extent of the projections differing between functional subsystems and areas (Webster, 1961; Carman et al., 1963; Webster, 1965; Parent and Hazrati, 1995).[3] These connections are excitatory, using glutamate as a neurotransmitter (Bolam et al., 2000). Amongst all cortico-striatal projections, inputs from somatosensory and motor (also combined under the name *sensorimotor* in the following) areas is particularly strongly expressed (Webster, 1961).

Cortical axons from one hemisphere target both ipsi- and contralateral striatal sites (Carman et al., 1965; Künzle, 1975) with an ipsilateral predominance (McGeorge and Faull, 1987). They originate from neurons in both supra- and infragranular layers, primarily from pyramidal cells located in neocortical layers 3 and 5 (Jones et al., 1977; Jones and Wise, 1977; McGeorge and Faull, 1989; Gerfen and Bolam, 2010; Reiner, 2010b). There are cortical, so-called *intratelencephalic* neurons that, apart from forming intracortical connections, establish direct axonal contacts with striatal targets. Members of a second class, so-called *pyramidal tract* neurons, primarily project to other, for exam-

[2] The progressive degeneration of dopaminergic neurons in the SNc underlies the development of Parkinson's disease (Ehringer and Hornykiewicz, 1960; DeLong and Wichmann, 2007)

[3] We focus here on the description of striatal inputs as they arise from neocortical areas, leaving peculiarities of projections from allo- and paleocortical areas aside.

ple brainstem structures and the spinal cord, but provide axon collaterals to the striatum (Reiner et al., 2003; Gerfen, 2004). These neurons also differ with respect to the patterns of axonal arborization in the striatum, their primary localizations in distinct cortical areas, layers and sublayers, their differential targeting of direct and indirect pathway MSNs, and the kind of cortical information they are assumed to transmit to the striatum. Further, they preferentially innervate different striatal subregions, so-called *patch*- and *matrix*-compartments, respectively (Reiner et al., 2010). For an in-depth review of the latter topic that we do not discuss in further detail here see, e.g., Gerfen, 1992.

The way cortico-striatal projections are principally organized has been a matter of intensive research and is still not completely clear. Early accounts suggested a quasi one-to-one projection from a given cortical area to a most adjacent striatal site (Kemp and Powell, 1970). In line with this proposition, the different cortical lobes and their major regions have been found to be indeed connected with distinct parts of the striatum and their projections are both topographically and functionally ordered (Webster, 1961; Flaherty and Graybiel, 1995). On top, the massive striatal projections deriving from somatosensory and motor cortical areas are somatotopically organized (Carman et al., 1963; Flaherty and Graybiel, 1991, 1993; Brown and Sharp, 1995; Nambu, 2011). This means that spatial relations between cortical representations from the same area are maintained at the level of the striatum. However, there is also a substantial degree of overlap between projections from functionally and anatomically related cortical regions (Yeterian and Van Hoesen, 1978; Selemon and Goldman-Rakic, 1985; Flaherty and Graybiel, 1991). A given cortical area targets a longitudinally extended striatal zone by means of substantial divergence of its projecting fibers (Selemon and Goldman-Rakic, 1985; Brown et al., 1998), and functionally related areas send their axons to nearby and even heavily interdigitating sites (Selemon and Goldman-Rakic, 1985; Flaherty and Graybiel, 1993). Also, representations of the same body part deriving from different but functionally related cortical areas overlap in their striatal targets (Brown, 1992).

Figure 1.3 depicts a schematic outline of some of the principles governing the anatomical organization of cortico-striatal as well as striatal output projections reaching downstream targets. As the plot illustrates, inputs arising from different cortical areas and from different sites within one specific area are neither strictly funneled nor do they remain completely segregated at the level of the striatum (Gerfen, 1992). Rather, there is both convergence and divergence in the way cortico-striatal projections are organized. That being said, it is important to note that the number of cortical neurons sending axons downstream is much larger than that of receiving striatal cells. In the rat, this ratio has been estimated to be about 6:1 (Gerfen, 2004) and even 10:1 (Zheng and Wilson, 2002), which is one anatomical indication for an eventual integration of information contained

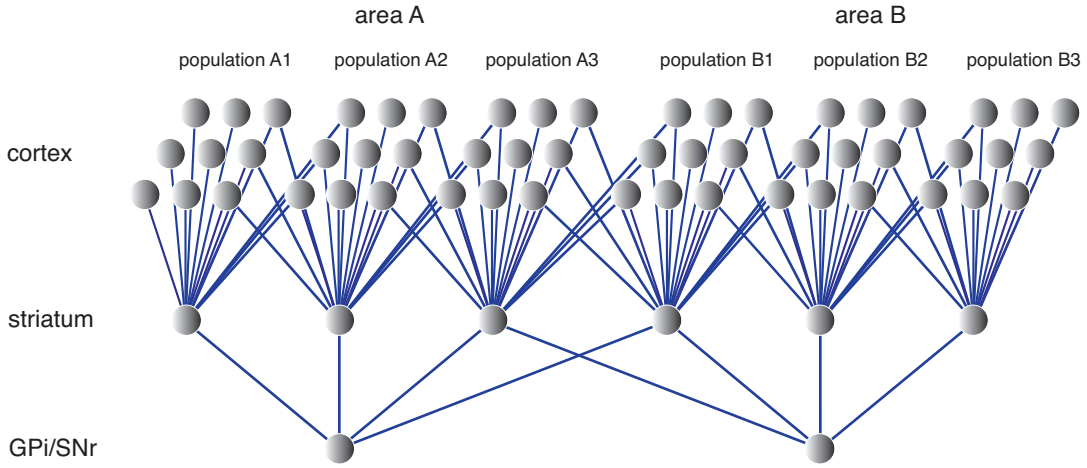

Figure 1.3: Schematic drawing of the organization of cortico-striatal and striatal output projections. Neurons are depicted as filled, grey shaded circles; axonal projections are depicted as blue, straight lines. The plot illustrates both convergence and divergence in the way cortical projections from specific areas and populations reach striatal neurons or neuron groups. It also indicates the massive reduction of neuron numbers on striatal and pallidal/nigral as compared to cortical levels. Striatal projection neurons each receive input from a large number of cortical pyramidal cells, but the degree of similarity of inputs to even adjacent neurons is very limited. For all these reasons, cortico-striatal connections are regionally and topographically specific to some degree but also substantially integrative. These properties reflect the funneling vs. parallel processing schemes mentioned in Section 1.1.2. Note that the figure does depict neither full projection patterns nor true proportions of cell numbers as they are found in organisms. *Abbreviations:* GPi, globus pallidus, pars interna; SNr, substantia nigra, pars reticulata. Figure inspired by Sharott, 2005 and Bergman et al., 1998.

in cortical signals at the striatal level. Another is the way that the terminal fields of cortico-striatal projections are formed which include locally restricted but also massively extended axonal arborizations (Kincaid et al., 1998; Zheng and Wilson, 2002). Further, the cruciform axodendritic pattern of innervation that is typical of cortico-striatal fibers targeting striatal projection neurons and preferentially ending at distal segments of their dendritic trees minimizes the number of contacts made between individual neurons of either structure while it maximizes the number of contacts made between individual MSNs and different cortical cells (Gerfen, 2004). As a consequence of these anatomical properties and the above mentioned disparity in absolute neuron numbers between the two structures, individual and even neighboring MSNs differ substantially with regard to their cortical input patterns (Gerfen, 2004). This finding has important implications for the functional role of the cortico-striatal axis in cortico-basal ganglia networks in general and for the supposed role of the striatum as an integrator of upstream activities

in particular (Wickens and Arbuthnott, 2010). These issue are discussed in more detail in the following section (1.2.3).

1.2.3 Functional role of the cortico-striatal axis

The large body of knowledge that exists on the anatomical organization of the cortico-striatal axis notwithstanding, its exact functional role has remained elusive. The importance of a proper functioning of the regions constituting this pathway for the generation and adaptation of behavioral output patterns is most distinctly illustrated by the severity and diversity of symptoms manifest in patients suffering from Parkinson's disease. In this condition, the loss of dopaminergic input from the substantia nigra pars compacta to the striatum results in profound alterations of neuronal activities along the whole cortico-basal ganglia loop. These alterations give rise to a multitude of pathological changes of various aspects of behavior, including sensory, motor, and cognitive symptoms (Albin et al., 1989). However, the exact cellular and neuronal network mechanisms underlying these changes and symptoms are still insufficiently understood. The same holds true for the exact contribution of neuronal activities within and between basal ganglia structures, the cortico-striatal axis in particular, to behavioral output patterns in the healthy state.

Following a dictum of Buzsáki that "structure defines function"[4], important clues as to the ultimate role of the cortico-striatal axis in behavioral control can again be gained from a close examination of its anatomical and physiological properties. Thus, both the intricate pattern of cortico-striatal projections and the sparse connectivity scheme relating cortico-striatal input with striatal output neurons (Figure 1.3, page 10) as much as the distinct electrophysiological properties of striatal cells (Nisenbaum and Wilson, 1995; Wilson and Kawaguchi, 1996) appear to be major determinants of the way neuronal signals are processed along this anatomical axis and of its final functional role (Houk and Wise, 1995; Wickens and Arbuthnott, 2010). In brief, these properties suggest a context-dependent, part integrative, part segregative role of the striatum with respect to the processing and transmission of cortical signals along the partially closed major and minor loops that are maintained throughout subsequent stages of the cortico-basal ganglia circuitry (Parent and Hazrati, 1993; Mink, 1996; Graybiel, 2005; Wickens and Arbuthnott, 2010; see also Section 1.1). Accordingly, the striatal cellular network in conjunction with its (cortical) input and basal ganglia output stages has been proposed to serve as sort of a filter that selectively gates incoming signals according to current

[4] This is the headline of Cycle 2 in Buzsáki, 2006 (page 29), where he mainly discusses functional properties of cortical circuits as they depend on the details of their anatomical makeup and structural organization. However, Buzsáki points out that this principle holds true for virtually all parts of the brain and their associated functions.

behavioral demands (Redgrave et al., 1999; Murer et al., 2002), extracts salient patterns (Gurney et al., 2001a,b), supports spatially and temporally balanced selection of "competing motor programs" by means of "focused inhibition" (Mink, 1996, page 381ff.; see also Chevalier and Deniau, 1990), or performs dimensionality reduction on its inputs (Bar-Gad and Bergman, 2001; Bar-Gad et al., 2003). Within the boundaries of anatomical specificity as determined by the major and minor cortico-basal ganglia loops, different striatal subregions preferentially subserve the control of different aspects of behavioral output (Schultz et al., 2003; Haber and Calzavara, 2009). Mechanisms of synaptic plasticity and the influences of various neurotransmitter systems from the brainstem, most importantly dopaminergic projections, on striatal network activities are not covered here in detail but are supposed to also play a key role in these functions (Schultz et al., 2000; Reynolds et al., 2001; Kreitzer and Malenka, 2008; Wickens and Arbuthnott, 2010).

The process of pathway or modality specific, spatially and temporally precise integration of cortical signals at the level of the striatum is considerably complex. This is because of both the makeup of the microcircuits that medium-spiny neurons, the main integrative cellular elements of the striatum, are embedded in (Section 1.2.1) and the intricate pattern of inputs deriving from distributed cortical sources (Section 1.2.2), not mentioning additional projections from thalamic and other structures. More specifically, while on the one hand individual MSNs differ substantially with respect to their input patterns, on the other hand they require a large number of synchronized excitatory inputs to reach spiking thresholds (Wilson and Kawaguchi, 1996; Kreitzer and Malenka, 2008). This essentially demands cortico-striatal projection neurons from the same or similar modalities or regions involved in neuronal processes related to particular aspects of a task to exhibit temporal *correlation* of their activities on a very short timescale (Reiner, 2010b). Furthermore, the disparity between absolute neuron numbers in cortex and striatum with a ratio of up to 10:1 (Section 1.2.2) is continued and even still increased in the ratio of neuron numbers in striatum to those in its output targets, i.e., the pallidum and substantia nigra, reaching levels of approximately 29:1 in the rat (Oorschot, 1996). In the resulting scheme of convergent, system-specific pathway projections described above (Sections 1.1.2 and 1.2.2) one would expect that for populations of neurons belonging to functionally related areas or subregions or those with similar response properties to have a functionally relevant impact on cells of the subsequent downstream processing stage their activities would have to be rather precisely coordinated in time.

How could such a precise coordination of input and output activities across members of ensembles of neurons along the cortico-striatal axis be realized on both cellular and network levels? In light of the above we can state that for accurate neuronal communication along this pathway at least two requirements appear to be essential: First, functionally

related neurons at the cortical input stage have to be active almost simultaneously. That is to say, they have to exhibit one or another form of temporal *synchrony* in order to exert a functionally relevant impact on their target cells. Second, groups of neurons at the striatal output stage have to be able to make use of such synchronized inputs in both receiving and sending terms. More precisely, they not only have to preferentially change their activities in reaction to synchronized inputs on an isolated single cell level but again their activities should be modulated in a coordinated and temporally predictable fashion in order for populations of functionally related neurons to form and to collectively influence cells in downstream structures.

Indeed, temporally predictable neuronal communication as subserved by *oscillatory synchronization* of population activities within and between different structures has been suggested to be fundamental to central nervous system function (Buzsáki, 2006). We therefore describe some of the most important general aspects of this notion in the upcoming section (1.3.1). Furthermore, oscillatory synchrony has also been discussed as a potential way of neuronal signaling on various stages of the cortico-basal ganglia circuitry (e.g., Boraud et al., 2005). We briefly review some of the principle findings supporting this proposition in Section 1.3.2 before we name the basic grounds of the more specific idea that oscillatory synchronization of population activities may also be fundamental for neuronal interactions along the cortico-striatal axis (Section 1.3.3).

1.3 Synchrony and oscillations of neuronal activities

1.3.1 General considerations

Questions of how the various elementary and higher-order functions of the brain which are essential for the generation of behavioral output might be implemented on a cellular and a network level have been long-standing issues in the field of systems neuroscience research. In this regard, it is important to note that most if not all central nervous system functions have the activities of not only single cells but populations of neurons as their functional-anatomical basis.[5] Understanding how such assemblies of neurons are formed, i.e., how the activities of individual neurons within and between different areas of the brain are organized and coordinated in both space and time is thus fundamental for elucidating the neuronal mechanisms underlying organized behavior (Singer, 1993).

[5] All of the following considerations are limited in scope to investigations into the workings of *neuronal* elements proper. We are, however, well aware of the likely important but as yet unresolved role that *glial* cellular elements play for integrative central nervous system functions, including neuronal communication on both single cell and possibly network scales. For a review of this topic, see, e.g., Araque et al., 2001 as well as Oorschot, 2010 for information on glia cell types in basal ganglia nuclei.

A vast number of studies carried out during the past decades have suggested a multitude of ways as to how transient interactions between nearby and distant groups of neurons may be implemented in the brain. While the exact mechanisms remain a matter of ongoing debate and investigation, it is becoming increasingly clear that the precise timing of the activities of not only single cells but distinct groups of neurons involves one or another form of temporal *correlation* or *synchrony* of their inputs and outputs on various time scales (Abeles, 1982b; Usrey and Reid, 1999; Salinas and Sejnowski, 2001; Averbeck et al., 2006; Cohen and Kohn, 2011). Despite the fact that the assumption of one of the following two principles does not necessitate acceptance of the other, *synchronization* of population activities in the form of frequency-specific *oscillations* has gained wide interest as a possible mechanism underlying patterns of effective connectivity between nearby and distant neurons fundamental to information exchange in the brain (Salinas and Sejnowski, 2001; Engel et al., 2001; Varela et al., 2001; Wang, 2010).

Evidence for the importance of oscillatory synchronization of neuronal activities in central nervous system function comes from a wide range of studies involving different techniques, species, and virtually all brain regions and functional domains. For example, in sensory areas, they have been linked to the processing of external stimuli (Adrian, 1942; Eckhorn et al., 1988; Gray and Singer, 1989), input scene segmentation (von der Malsburg and Schneider, 1986; Engel et al., 1991), sensory feature binding (Engel et al., 1991; Singer and Gray, 1995; Kreiter and Singer, 1996), and multisensory processing (Kayser and Logothetis, 2009; Panzeri et al., 2010; Hipp et al., 2011). In sensorimotor cortical (Murthy and Fetz, 1992; Pfurtscheller et al., 1993; Sanes and Donoghue, 1993; Murthy and Fetz, 1996a,b; Donoghue et al., 1998; Schoffelen et al., 2005) and various subcortical areas (Welsh et al., 1995; Brown, 2003) they have been assigned an integrative role with regard to the temporal coordination of muscle output and somatosensory (feedback) input (MacKay, 1997; Farmer, 1998). Rhythmic activities in the hippocampus and related regions have been found to be important for spatial navigation, memory encoding and retrieval (Skaggs et al., 1996; Buzsáki, 2002; Fell and Axmacher, 2011). Other cognitive functions such as attention (Fries et al., 2001; Buschman and Miller, 2007; Siegel et al., 2008; Gregoriou et al., 2009), visuo-motor integration (Roelfsema et al., 1997; Womelsdorf et al., 2006; Donner et al., 2007), working memory (Pesaran et al., 2002; Siegel et al., 2009), and decision-making (Pesaran et al., 2008; Donner et al., 2009) also appear to be subserved by oscillatory activities in various frequency bands. Thalamic structures and the cortico-thalamocortical loops which they are embedded in exhibit a wide variety of oscillatory patterns that are closely related to the regulation of the sleep-wake cycle, mechanisms of arousal, and possibly even sensory-motor integration and various cognitive functions (Steriade and Llinás, 1988; Steriade et al., 1993a; Jones, 2009).

On a cellular level, the membrane potential of single neurons exhibits the property to oscillate under certain activation conditions (Buzsáki, 2006). This is due to their specific and differential endowment with a multitude of voltage-gated ion channel types and associated conductances as well as various other morphological and membrane properties and the timed patterning of various input signals including modulatory influences of several neurotransmitters (Wang, 2010). Furthermore, oscillatory membrane potential fluctuations of individual cells tend to synchronize amongst the members of a local group of neurons, in this way subserving the orchestration of population activities needed to communicate with more distant structures (Llinás, 1988). Neurons oscillating in synchrony with their neighboring peers may participate in several ways in such cellular coalitions, for example as oscillators proper (also called *pacemakers*) or *resonators* (Wang, 2010). While the former can exhibit oscillatory activities independently, oscillations in the latter depend on external inputs. In general, the time constants and courses of their activation crucially influence the functional properties of the host network, including optimal input frequencies as well as output spike rates and (correlated) patterns (Llinás, 1988).

Insight into how synchronized oscillations in distinct frequency bands arise in neuronal networks as a result of the interplay of individual cellular elements has been gained from both modeling studies and experimental work (Wang, 2010). Although many open questions remain, it is now widely accepted that a balanced regime of mutual excitation and inhibition between the respective cellular elements is required in order for synchronized oscillations to unfold and stabilize on timescales useful for interactions between neurons (Salinas and Sejnowski, 2000; Hasenstaub et al., 2005; Atallah and Scanziani, 2009; Haider and McCormick, 2009; Wang, 2010). Another important question relates to the ways in which distinct groups of oscillating neurons then come to synchronize their activities in order for such interactions to take place between them which underlie the formation of large-scale networks fundamental to the integrative properties of brain function (Bressler et al., 1993; Engel et al., 2001; Varela et al., 2001). Various models have been proposed (e.g., Traub et al., 1996; Vicente et al., 2008; Wang, 2010) and experimental data have been collected in support of one or another notion, but no common consensus has as yet been reached. Whatever the underlying mechanistic principles, what could be the functional use of a coordination of neuronal activities in the form of oscillatory synchronization? At least two major aspects can be distinguished in this regard which have been the subject of intense research during the last decades.

First, temporal correlation of neuronal activities has been discussed as a mechanism of information coding in contrast or addition to coding in terms of firing rates (von der Malsburg and Schneider, 1986; Eckhorn et al., 1988; Gray et al., 1989; Vaadia et al., 1995; Riehle et al., 1997; Diesmann et al., 1999; Averbeck et al., 2006). Most generally speaking,

in such a scheme neurons with the same or similar activation profiles would exhibit synchronization of their firing in response to, e.g., specific aspects of sensory stimuli or patterns of motor output such as movement of a limb. In extension of this proposition, neurons oscillating in synchrony would constitute a temporally stable population code of the respective variable or mediate the association of sensory (Singer and Gray, 1995) or motor (Graybiel et al., 1994) features into coherent perceptions or actions, respectively. This notion, known as the *binding-by-synchrony* hypothesis, has been hotly debated in recent years and is not of primary concern for the present study (see, e.g., Gerstner et al., 1997; Lamme and Spekreijse, 1998; Gray, 1999; Shadlen and Movshon, 1999; Singer, 1999; Thiele and Stoner, 2003; Chalk et al., 2010; Ray and Maunsell, 2010, for critical evaluations and extensive discussions).

Second, synchronization of neuronal activities has been discussed as a mechanism fundamentally important for signal routing, i.e., propagation of activities between cells, groups of neurons, and brain structures and thus, neuronal communication (Engel et al., 2001; Salinas and Sejnowski, 2001; Varela et al., 2001; Fries, 2005; Kumar et al., 2010). Synchronization, i.e., temporal correlation of action potential firing has been found to enhance the impact or drive of an input population on the activity of a receiving neuron or groups of neurons by influencing their spiking threshold on top and even independently of changes in input rates (Azouz and Gray, 2000; Salinas and Sejnowski, 2001; Azouz and Gray, 2003). Moreover, precise timing of pre- and postsynaptic action potentials has been shown to be important for the modulation of the efficacy of connections between neurons (Markram et al., 1997). This effect is assumed to be enhanced by frequency-specific synchronization of inputs (Jutras and Buffalo, 2010; Wang et al., 2010) and depends on the biophysical capacities of neurons to act as so-called *coincidence detectors*, an idea for which there exists both theoretical as well as experimental support (Abeles, 1982a; Alonso et al., 1996; König et al., 1996; Bruno and Sakmann, 2006). While we do not further discuss the details of the latter process here, it is important to note that signal routing in nervous systems in terms of synchronization is supposed to rely on a precise temporal coordination of the membrane potential fluctuations of the respective sending and receiving neurons and neuronal populations (Salinas and Sejnowski, 2001). Furthermore, effective information transfer and coordination of neuronal activities probably depend on mechanisms which allow for the reliable prediction of periods of excitability of both sending and receiving groups of cells. This requirement can be met by the inherent predictability of the shape and time course of oscillatory cycles (Buzsáki, 2006).

Thus, taking the idea of an important mechanistic role of correlations in nervous system function to a larger, i.e., network scale, oscillatory synchronization of neuronal activities in distinct frequency bands has been proposed to be a particularly effective and also

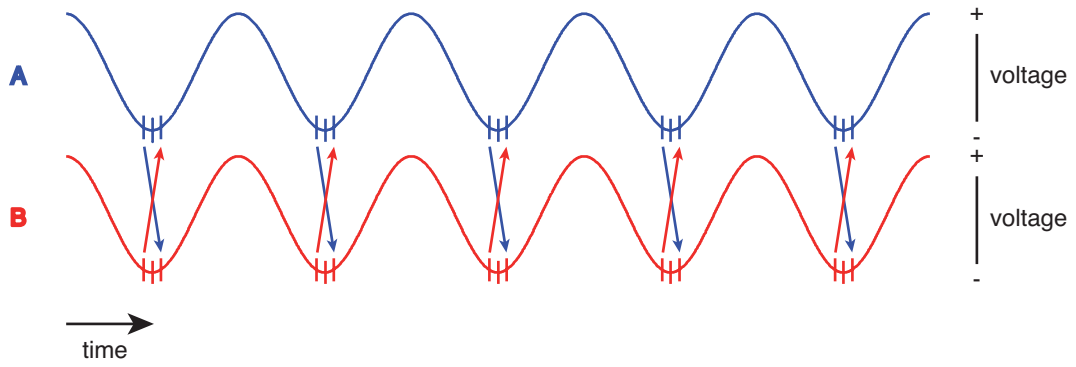

Figure 1.4: Oscillatory synchronization as a means of neuronal communication. The plot shows, first, neuronal activities in two areas A and B which both exhibit rhythmic modulation of their firing patterns. This is indicated by the temporal grouping of spikes (tick marks) around specific phases (throughs) of the population average voltage fluctuations (so-called *local field potentials*) signifying temporal windows of enhanced excitability. Second, activities are synchronized in an oscillatory fashion not only within but also between the two areas. This is indicated by the temporally consistent relationship, so-called *phase coherence*, between local field potential activities of the same frequency from both areas and the temporal alignment of their spike firing times. In this way, spiking activities of distant groups of cells can exert a functionally relevant impact on each other (red and blue arrows), leading to temporally predictable, effective connections between them. This figure was inspired by a very similar one in Fries, 2005.

energetically cheap way to establish temporally stable and robust functional connections between neuronal assemblies (Buzsáki and Draguhn, 2004; Akam and Kullmann, 2010). More precisely, oscillatory activity patterns are assumed to provide temporal windows of enhanced or reduced excitability subserving coordinated timing of action potential firing of distributed groups of cells (Fries, 2005). In such a scheme, rhythmic modulation of input gain and output rate would allow for a precise temporal coordination of signal flow between neurons, thus enhancing their effective connectivity (Womelsdorf et al., 2007).

Figure 1.4 illustrates two fundamental aspects underlying the assumed functional importance of oscillatory synchronization as a means of regulating interactions among the members of and between different populations of nerve cells. This includes (i) the frequency-specific oscillatory synchronization of population activities in distinct groups of neurons, and (ii) synchronization of the activities of different groups of cells in terms of temporal *coherence* of their respective oscillatory patterns. Both aspects are of crucial importance for the motivation of the present study as is outlined below (Section 1.4).

To summarize, frequency-specific input and output patterns of populations of neurons as determined by the resonant properties (also termed "electroresponsiveness" by Llinás, 1988, page 1661) of the respective cells appear to play important roles in both neuronal

signal processing and propagation (Steriade, 2000; Salinas and Sejnowski, 2001). Through the dynamic interplay of groups of neurons oscillating in synchrony, network rhythms can on the one hand selectively drive or inhibit activities in downstream structures and on the other hand serve to control the impact of input signals on the receiving population, much like a spatio-temporally tuned filtering mechanism (Salinas and Sejnowski, 2001; Buzsáki and Draguhn, 2004; Fries, 2005). Classically, much of the work on the roles of oscillations and synchrony in integrative nervous system functions has been carried out in cortical neurons, structures and networks of regions. In recent years, however, there has been growing interest in the functions that these mechanisms could subserve in systems involving subcortical structures, the basal ganglia in particular. We briefly review some important aspects of the current state of knowledge regarding mechanisms and behavioral correlates of oscillatory synchronization in cortico-basal ganglia systems in general (Section 1.3.2) and along the cortico-striatal axis in particular (Section 1.3.3) before we explicitly name the aims and the motivation of the present study (Section 1.4).

1.3.2 Synchrony and oscillations in cortico-basal ganglia systems

Neuronal activity patterns marked by either oscillations, synchrony, or both have been found in different basal ganglia structures in a number of species, in multiple frequency bands, and under a variety of behavioral conditions (Walters and Bergstrom, 2010). Accordingly, they have been suggested to be of fundamental importance for neuronal communication in basal ganglia-related networks in analogy to their hypothesized function in other brain systems and behavioral contexts (Boraud et al., 2005). However, the exact roles of oscillations, synchrony, and their conjunction in terms of synchronized oscillations in networks involving basal ganglia structures have remained elusive as much as the exact conditions and causes of their occurrence (Gatev et al., 2006).

A role for synchronized oscillations in basal ganglia structures in terms of information coding *per se* has been caught into question (Bergman et al., 1998) primarily because a number of studies has shown activities of single neurons to exhibit oscillatory patterns preferentially in the diseased rather than in the healthy state (see, e.g., Bergman et al., 1994; Nini et al., 1995; Raz et al., 1996, 2001; Goldberg et al., 2004). In such a scheme, they are assumed to be disruptive to normal coding patterns relying on a diversification of response profiles which is crucial for the fine-grained coordination of behavioral output patterns (Leblois et al., 2006; Cruz et al., 2009). Oscillatory synchrony of neuronal activities has also been proposed to impair signal transmission within and between basal ganglia structures. This is mainly because entrainment of a large number of otherwise mostly independently active neurons to exaggerate network oscillations (Magill et al.,

2001; Mallet et al., 2008) may reduce functional segregation of different cortico-basal ganglia loops and subloops, thereby disturbing action selection processes (Moran et al., 2008). Accordingly, excess expression of frequency-specific synchronized oscillations is assumed by many authors to play an impairing role in various neurological conditions resulting from damage of basal ganglia structures such as Parkinson's disease or different types of dystonia which are marked by, amongst other symptoms, severe motor disturbances (Levy et al., 2002; Brown, 2003; Hammond et al., 2007; Sharott et al., 2008).

In contrast to the above, however, synchronized oscillations within and between interconnected basal ganglia structures have also been proposed to be important for neuronal pacemaking not only in the diseased but also in the intact organism (Plenz and Kital, 1999; Bevan et al., 2002; but see Humphries et al., 2006). Also, a substantial number of studies has demonstrated close temporal relationships between spiking activities of individual cells and neuronal mass activity fluctuations in terms of local field potential (LFP) oscillations in various frequency bands and in different basal ganglia nuclei (Courtemanche et al., 2003; Berke et al., 2004; Magill et al., 2004b, 2006; Dejean et al., 2007; Berke, 2009; Sharott et al., 2009; van der Meer and Redish, 2009). Accordingly, synchronous population oscillations have been assigned putative roles in orchestrating interactions between different elements of the cortico-basal ganglia circuitry. In this way, they may be fundamental to neuronal communication within this brain system on both local and more global, i.e., inter-structural network scales (Boraud et al., 2005; Lalo et al., 2008). In support of this notion, various experimental studies have revealed the presence of distinct, frequency-specific patterns of oscillatory activities and their synchronization within and between basal ganglia nuclei and associated structures in healthy organisms (Goto and O'Donnell, 2001a,b; Brown et al., 2002; Berke et al., 2004; Magill et al., 2004a; Sharott, 2005; Sharott et al., 2005; Magill et al., 2006). Indeed, rhythmic and synchronized activities in basal ganglia nuclei have been suggested to subserve such diverse aspects of normal behavior as action selection and organization (Courtemanche et al., 2003; Berke et al., 2004), learning and memory (DeCoteau et al., 2007a; Tort et al., 2008), movement execution and adaptation (Masimore et al., 2005; DeCoteau et al., 2007b), reward processing and decision-making (van der Meer et al., 2010).

The above named findings indicate that rhythmic excitability fluctuations may have functions in cortico-basal ganglia circuits similar to those assigned to them with regard to cortical networks proper, like spatially and temporally precise filtering and selective routing of input and output signals (Section 1.3.1). Of crucial importance to the present study, it has been suggested that rhythmic activities in functional-anatomical loops through the basal ganglia in conjunction with temporally precise coordination of cellular activities in their different nuclei are crucially influenced by global forebrain states

as determined primarily by the massive cortical input to these structures (Magill et al., 2000; Gervasoni et al., 2004; Magill et al., 2004a; Sharott et al., 2005, 2009). This notion is of particular relevance in case of the striatum, which represents the major stage of cortical input to the basal ganglia (Section 1.2). In addition, the second largest group of inputs to the striatum derives from thalamic structures which are known to exhibit very tight anatomical and functional connections (Sherman, 2007), expressed in prominent patterns of synchronized oscillations (Steriade, 2000), with virtually all cortical areas (Jones, 2007). These structural and functional features place the striatum in a favorable position to modulate neuronal information flow as subserved by synchronized oscillatory patterns and as originating in its input structures through the large-scale networks of cortico-basal ganglia-thalamocortical loops (Boraud et al., 2005).

1.3.3 Synchrony and oscillations along the cortico-striatal axis

We have pointed above to some of the physiological requirements assumed to underlie well-timed coordination of neural population activities along the cortico-striatal axis (Section 1.2.3). We have stated that neurons at the input stage would have to synchronize their activities to exert a functionally relevant impact on their target cells. Furthermore, we have indicated that striatal MSNs should be capable of making use of such synchronized inputs in both receiving and sending terms. Do striatal projection neurons really exhibit such properties, and how do they depend on brain state and behavior?

At this point, it is important to note that subthreshold membrane potential fluctuations of MSNs have been shown to exhibit robust switches between depolarized and hyperpolarized states (*up-* and *down-states*, respectively) in anesthetized rats (Wilson and Kawaguchi, 1996), similar to those first described in cortico-thalamic neurons (Steriade et al., 1993b). Under such conditions, membrane state transitions of MSNs display periodicity with a frequency of about 1 Hz, and they strongly influence the spiking activity of the respective cells which fire action potentials during the up-state only (Stern et al., 1997). Similar subthreshold membrane potential fluctuations have been been found in cortico-striatal projection neurons as well (Stern et al., 1997) which exhibit tight relationships to slowly fluctuating local field potentials (Mahon et al., 2001; Steriade et al., 2001). The same holds true for populations of ventral striatal neurons and associated field potentials as entrained by inputs from hippocampal areas (Goto and O'Donnell, 2001a). By themselves, subthreshold membrane potential fluctuations of MSNs are strongly dependent on intact, glutamatergic cortical inputs (Plenz and Kitai, 1998; Kasanetz et al., 2006) and they are sensitive to dopaminergic modulation (Murer et al., 2002). Further, they are correlated between single medium-spiny neurons while at the same time their

output firing patterns are not synchronized (Stern et al., 1998). Thus, members of striatal cell assemblies appear to be able to simultaneously exhibit similar global activity states but fine-grained, individualized firing patters (Stern et al., 1998).

Taken together, the above findings suggest that striatal MSNs may in principle be capable of closely coordinating their activities in response to synchronized cortical input (Kasanetz et al., 2002). In this way, processing of upstream information in striatal ensembles along distinct cortico-striatal channels or the large-scale coordination of activities between such channels could be achieved in a temporally and spatially precise manner (Plenz and Aertsen, 1996; Stern et al., 1998; Murer et al., 2002; Kasanetz et al., 2006, 2008). However, while the above described findings point to possible mechanisms subserving interactions between cortical and striatal populations, the very own physiological relevance of up- and down-state transitions along that axis can still be caught into question. Most of the above data have been gathered in anesthetized preparations, and the situation in non-anesthetized organisms is generally more complex and activity patterns there are much more diverse, especially in the awake state (Mahon et al., 2006).

In this regard, frequency-specific oscillatory synchronization of neuronal population activities in connected cortical and basal ganglia regions, among them the striatum, has been proposed to play an important role in the dynamic formation of cell assemblies within these structures as well as for their interaction during natural brain states (Murer et al., 2002; Walters and Bergstrom, 2010). This notion has received some experimental support by a number of studies demonstrating the presence of oscillatory population activities in the striatum of awake animals, their modulation by different aspects of behavior as well as their synchronization across different spatial scales (Courtemanche et al., 2003; Berke et al., 2004; Masimore et al., 2005; DeCoteau et al., 2007a,b; Dejean et al., 2007; Tort et al., 2008; Popescu et al., 2009; van der Meer and Redish, 2009). Furthermore, phase-locking of specific types of striatal neurons to cortical and striatal population oscillations, analogous to findings during anesthetized states (Sharott et al., 2009), has been shown to occur under awake and behaving conditions (Berke et al., 2004; Berke, 2009; van der Meer and Redish, 2009). This indicates that synchronous oscillatory activities are indeed capable of modulating and possibly coordinating spiking activities along cortico-basal ganglia loops and at their striatal input stage. However, evidence for a functionally relevant role of synchronized oscillations for neuronal communication within the striatum and between the striatum and associated regions is still very sparse. Also, the range of behavioral states that influence the properties of these activities, such as preferred frequencies and their modulation by behavioral demands, has remained insufficiently explored. This holds particularly true for the cortico-striatal axis.

1.4 Aims and motivation of the study

To summarize the preceding sections, accurately timed activities of ensembles of cortical neurons are needed to excite striatal neurons above threshold whose activities have themselves to be coordinated in such a way as to exert functionally specific effects on downstream structures. Synchronous population oscillations have been proposed to be an important mechanism mediating these functions along the cortico-striatal axis. However, experimental evidence for this proposition under awake behaving conditions is sparse.

The aim of the present study was thus to investigate the patterns of oscillatory population activities present in sensorimotor cortical and striatal regions in the brains of awake organisms, their synchronization as well as their modulation by gross motor behavioral demands. In this specific constellation, it was motivated by the facts that

(i) the cortico-striatal axis as the major input stage of the cortico-basal ganglia circuitry is supposed to generally have important *integrative* functions in this brain system, a role possibly subserved by synchronous oscillations,

(ii) sensorimotor cortical areas send massive, topographically ordered projections to extended parts of functionally related striatal regions, and

(iii) classically, structures along the cortico-basal ganglia loop have been assigned a primary role in the generation and adaptation of coordinated motor behavior, and the striatum is one of the main sites of affection in Parkinson's disease, a condition marked by severe motor symptoms.

We reasoned that if synchronous population oscillations are indeed functionally relevant for neuronal signaling along the cortico-striatal axis, then distinctly different behavioral states should be reflected in marked changes of frequency-specific synchronous oscillations in a task engaging regions fundamentally important for the execution of normal movements. Furthermore, we speculated that more fine-grained changes of behavioral demand would also be accompanied by parallel modulations of synchronized oscillatory patterns of population activities within and between cortex and striatum.

To explore these issues, we established an animal model of gross motor behavior, i.e., treadmill running, and trained animals to behave reliably in the task on different speed levels. We implanted microelectrodes in sensorimotor cortical and striatal regions of well-behaving subjects for the acquisition of neuronal population activities. We analyzed the data with a focus on *spectral* parameters. We used *power* and *phase-coupling* measures to explore the frequency characteristics and synchronization properties of population activities along the cortico-striatal axis during resting and running states. We examined *interactions* between frequency-specific rhythms and *interrelations* of coupling measures as well as the *scaling* of synchronous oscillations with changing behavioral demand.

2 Methods

2.1 Treadmill apparatus and behavioral environment

The treadmill apparatus used in this study (TSE Systems GmbH; Bad Homburg, Germany) was similar to many of those that have been successfully employed since decades for corresponding behavioral paradigms (e.g., Kimeldorf, 1961; Andrews, 1965; Chapin et al., 1980). We describe here its basic composition and configuration before we turn to more specific modifications made to it and the behavioral environment as prepared for recordings in a later section (2.4.2). Note that large parts of this and the following section (2.2) as well as some minor parts of Section 2.4.2 have been reused and adapted from another manuscript of the author describing in detail the establishment of a treadmill running model in Brown Norway rats (von Nicolai, 2011).

The main part of the treadmill (Figure 2.1) consisted of a rubber belt wrapped around two pulleys whose axes were fixed to an aluminum plate. The belt was stretched tightly between the two pulleys such that it served as a moving ground above the plate on which rodents could sit and walk. This main part was 50×13 cm in size, surrounded by a frame of glass fibre reinforced plastic walls of about 16.5 cm height and covered with a plexiglas top that could be opened and removed for handling of the animals. Another plastic panel was mounted on top of the belt and in the middle between the two sidewalls to split the belt's surface into two lanes for two rats to be run in parallel.

The belt setup was connected to a small, computer-driven motor operated by means of a control software installed on a PC according to user-definable settings. The inclination of the treadmill could also be changed both manually and automatically to range between 0 and 20 degrees with respect to ground level. However, this feature was not used in any of the experiments carried out during the course of this project.

At the back end of the treadmill there was a metal grid attached to the pulley for animals to sit when they had stopped running and had been carried to the back by the moving belt. Originally, this grid had been designed for the application of mild electrical shocks in order to motivate animals to keep running in the task. This shocking device was not used in the present study for several reasons. First, as the results of extensive training sessions on many subjects prior to implantations had shown, the animals used

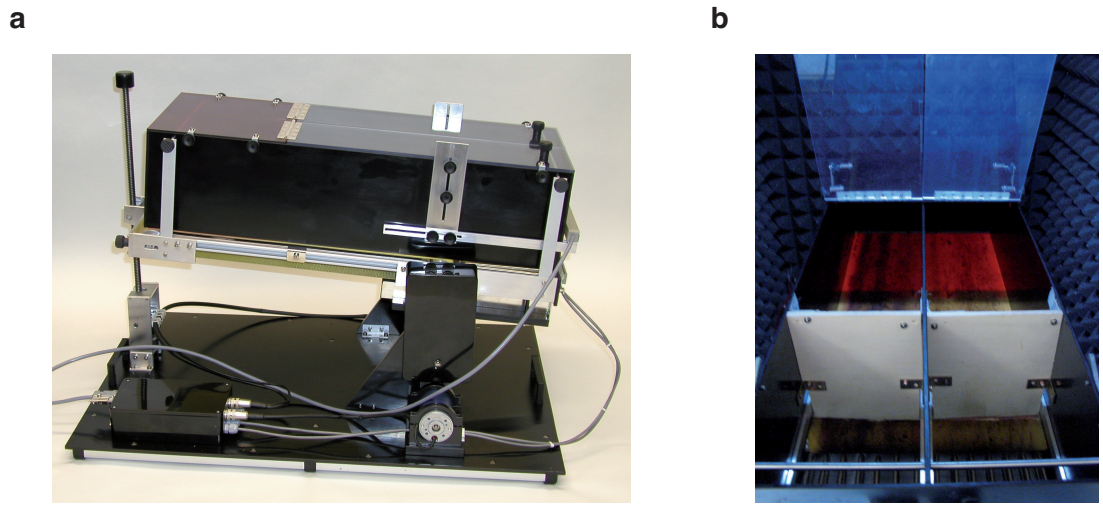

Figure 2.1: (a) Side view photograph image of the treadmill device used in the project as originally distributed by the manufacturer. Image courtesy of TSE Systems GmbH. (b) Rear view photograph image of the treadmill running lanes as seen through the half-open plexiglass top. The picture shows the wooden walls placed right in front of the shocking grids. Also note the darker, red area at the front end of the lanes that served as an additional incentive for the animals to keep running straight.

here could not be motivated to get back to running in response to the shocks but rather gripped onto the grid and stayed there during and after the shocking intervals. Second, for electrophysiological recordings it was highly desirable to largely remove any unnatural kinds of disturbances from the recording environment that could possibly interfere with the experiments. Third, previous studies have shown that the use of a shocking device can be substantially stressful for the subjects (Burgess et al., 1991). Lastly, the gap between the metal grid and the running belt was another source of potential harm for the animals since they could potentially have become entangled with their feet and tails there as also others have explicitly noted (Nakao et al., 1982).

For all these reasons, a different strategy was chosen to keep animals running straight on the track. The treadmill was modified by fixing a wooden wall at the back end of each lane right in front of the shocking grid (Figure 2.1, panel b). Foamed material was attached to their lower ends in order to protect the animals' feet and tails from being scratched at the edges of the walls. We reasoned that animals would experience their hitting of the back wall in case of running errors as a sufficiently aversive event that would motivate them to resume running as quickly as possible. While this turned out to be the case in only a subset of animals, we feel that this approach of trying to keep animals stay on the lanes was by far much better suited to the needs and constraints of the present study and also much less risky and harmful for our subjects.

Behavioral performance on the treadmill was measured in terms of breaks of infrared light beams. These were situated within the front ends of two pairs of thin metal rods attached to the inner walls closely adjacent to the belt's surface at the back end of both lanes. Since the running belt moved from front to back, an animal that would not keep running straight towards the upper end of its lane would be carried to the back and then interrupt the beam. These running errors (beam breaks) were counted for each subject individually by the Process Control Unit that connected the treadmill to a PC.

The treadmill control software that was used to operate the machine also generated a detailed record of the number, time points, and epochs of running errors. In this way, we were able to monitor the behavior at all stages of a given running protocol. These protocols could be designed by the user according to specific needs in terms of trial and epoch lengths, speed levels, and the size of speed changes. The speed range covered by the device was limited to values between 0.07 and 2.00 m/s, and the maximum resolution of behavioral measurements was 5 seconds (i.e., a light beam break could only be elicited once every 5 seconds). This restricted both the accuracy with which the running behavior of the animals could be evaluated and the amount of behavioral control achieved with respect to changes of neuronal activities (see Chapters 3 and 4). For an illustration of the full makeup of trials used for recordings in terms of levels and their basic composition of 5-second epochs, see Figure 2.6 on page 36.

2.2 Animal care and handling

All procedures performed in this study were in accordance with local ethics and Society for Neuroscience (SfN) Guidelines for the Care and Use of Laboratory Animals. Male Brown Norway rats (*Rattus norvegicus*) were acquired at the age of 8–12 weeks (Charles River Laboratories; Sulzfeld, Germany). We housed them either individually or in groups of 2–4 animals in standard cages under a 12 hour light/dark cycle. Water and food were available *ad libitum* and weight development was monitored regularly. In agreement with many previous studies employing treadmill running procedures in rats (see von Nicolai, 2011 for details), animals generally did not experience substantial weight losses during the period of training and recording. Rats were allowed to adapt to the animal facilities for a couple of days before we included them in any of the behavioral experiments. To avoid unnecessary pain, we marked individuals not by perforation of earlobes but using colored, water-resistant labels on their tails.

Every time before a training or recording session, we brought the animals to the laboratory and allowed them to rest again for 2–3 minutes before we took them out of their cages. They were then held quietly in the hands of the experimenter and gently stroked

for a period of 1–2 minutes. We did so to support rapid adaptation of the animals to both the experimental environment and to the experimenter. In this way, rats quickly became used to all procedures and were in general very cooperative and calmly behaving in all experimental settings, usually showing no signs of overt stress or aggression.

The methods and results of extensive behavioral training and pre-operative testing sessions as well as the process of development of criteria used to select runners from non-runners for later implantation with recording devices are described in full detail elsewhere (von Nicolai, 2011). In brief, after we had explored the basic running capacities of Brown Norway rats in the treadmill task and the approximate performance ranges they could support, we developed more sophisticated training schedules that allowed for an evaluation of the running behavior of individual animals as well as their preparation for the more strenuous task conditions during recordings. These schedules included so-called *adptation* and *selection* phases that served, respectively, to first acquaint animals to the running procedures and to then help letting stabilize their performances over a certain amount of time. In this way, we successfully trained a considerable number of rats that we then selected our subjects for electrophysiological experiments from. However, we also note here that animals exhibited a large amount of variability in their performances both across individuals as well as across groups of subjects already during pre-operative training stages (von Nicolai, 2011). This is one reason for why we obtained (behavioral) data of very different quality during recordings (Section 3.1).

2.3 Implants and implantations

2.3.1 Target planning

As mentioned above (Section 1.4), we aimed at investigation of neuronal signals from the sensorimotor part of the cortico-striatal axis. In rats, the corresponding striatal region is located at dorsolateral aspects of the structure, spanning large parts of its anterior-posterior extent (McGeorge and Faull, 1987, 1989). Electrophysiological studies have shown that neuronal responses at these sites can most reliably be evoked by touch as well as passive and active limb movements (West et al., 1990; Carelli and West, 1991).

Cortical input to the sensorimotor striatum mainly derives from primary and secondary sensorimotor areas (McGeorge and Faull, 1987, 1989; Brown et al., 1998). For these reasons, we tried to target cortical areas M1 and S1 (primary motor and primary somatosensory cortex, respectively) with our electrodes, preferentially focusing on those zones within the latter containing functional anatomical representations of forelimbs and hindlimbs (S1FL and S1HL areas, respectively; Hall and Lindholm, 1974). The com-

bination of M1 and S1 regions covers large portions of the rat brain's surface, in both anterior-posterior and medial-lateral directions (Hall and Lindholm, 1974). As their very names suggest, neuronal signals recorded there exhibit a diversity of activity changes in response to sensorimotor engagement of subjects, and movement of body parts can reliably be evoked through electrical stimulation of brain tissue at these sites (Hall and Lindholm, 1974; Donoghue and Wise, 1982; Gioanni and Lamarche, 1985).

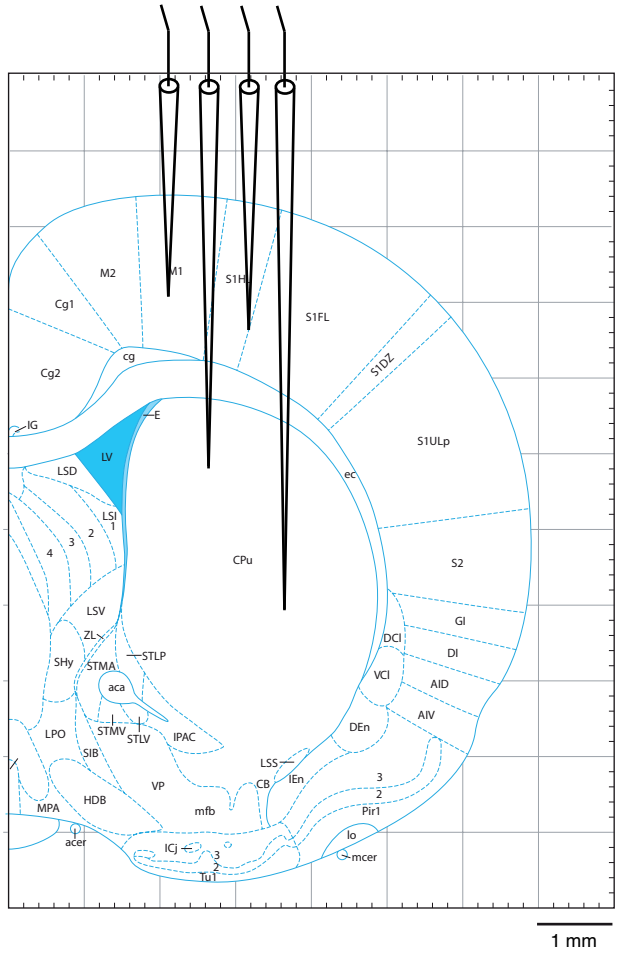

Figure 2.2: Draft of one hemisphere of a coronal histological slice through the rat brain at an AP level of +0.12 mm relative to bregma. Electrode drawings exemplify possible spatial locations of contacts after implantation. Note the huge size of the rat striatum as well as the large mediolateral extent of M1 and S1 areas. The figure is for illustration purposes only; note that electrode sizes are not to scale and that we never implanted any two electrodes fully aligned in either AP or ML planes. *Abbreviations (excerpt)*: CPu, caudate-putamen complex (striatum); M1, primary motor cortex; S1FL, S1HL: primary somatosensory cortex, forelimb and hindlimb areas. Drawing taken and adapted from Paxinos and Watson, 2005, with permission. Original design of this figure by G. Engler.

All anatomical coordinates used in the study and provided in the remainder of this text were taken from the rat brain atlas of Paxinos and Watson (2005). Figure 2.2 shows one hemisphere from a draft of a coronal slice through the rat brain at an anterior-posterior position of +0.36 mm with reference to bregma (for a definition of bregma, see Section 2.3.3 below). It depicts schematic drawings of four electrodes targeting cortical and striatal areas. All cortical areas mentioned above (M1, S1 forelimb and hindlimb areas) and the striatum (caudate-putamen complex, CPu) are readily visible.

We placed three electrodes into both cortical and striatal structures of both hemispheres (i.e., $4 \times 3 = 12$ electrodes in total), with an average two-dimensional distance between them of about 1.0 mm for cortical and 0.5 mm for striatal contacts. Cortical electrodes were aimed at locations situated between +2.8 and −2.5 mm in anterior-posterior and 1.9 to 3.0 mm in medial-lateral directions with reference to bregma. Striatal electrodes were aimed at locations situated between +1.6 and 0 mm in anterior-posterior and 2.7 to 4.0 mm in medial-lateral directions.

Electrodes were individually moveable with watchmaker screwdrivers in the dorsal-ventral (DV) direction, giving us the possibility to vary their positions along that plane after implantation. We moved cortical electrodes to a maximum depth of 3 mm with reference to the brain's surface, and in case of striatal electrodes, we restricted our recordings to positions between 4 mm dorsally and 7 mm ventrally in order to keep to the anatomical boundaries of the two structures.

2.3.2 Implant construction

The implant used for chronic electrophysiological recordings consisted of two main parts. The first was a so-called *microdrive* (Harlan 12 Drive; Neuralynx; Tucson, Arizona, USA), a special holding device which incorporated 12 small drives consisting of plates for attachment and long screws for independent feed of individual electrodes. A connector at its upper end served to link the implant with the so-called *headstage* and a tether cable connecting it to the recording system (for details of the connector, headstage, cable and recording system, see Section 2.4.3 below). Panel b of Figure 2.3 shows a picture of an implant skeleton carrying cap and connector as well as silver wires (see below).

As the second main part we attached a self-designed and specially manufactured cap (Figure 2.3, panels b–d) to the lower end of the implant. It contained a large number of tiny holes arranged and drilled according to the scale of a two-dimensional outline of stereotaxic coordinates of brain structures of interest as provided by templates of an anatomical atlas of the rat brain (Paxinos and Watson, 2005). This allowed for the selective targeting of a wide variety of positions along both anterior-posterior and medial-

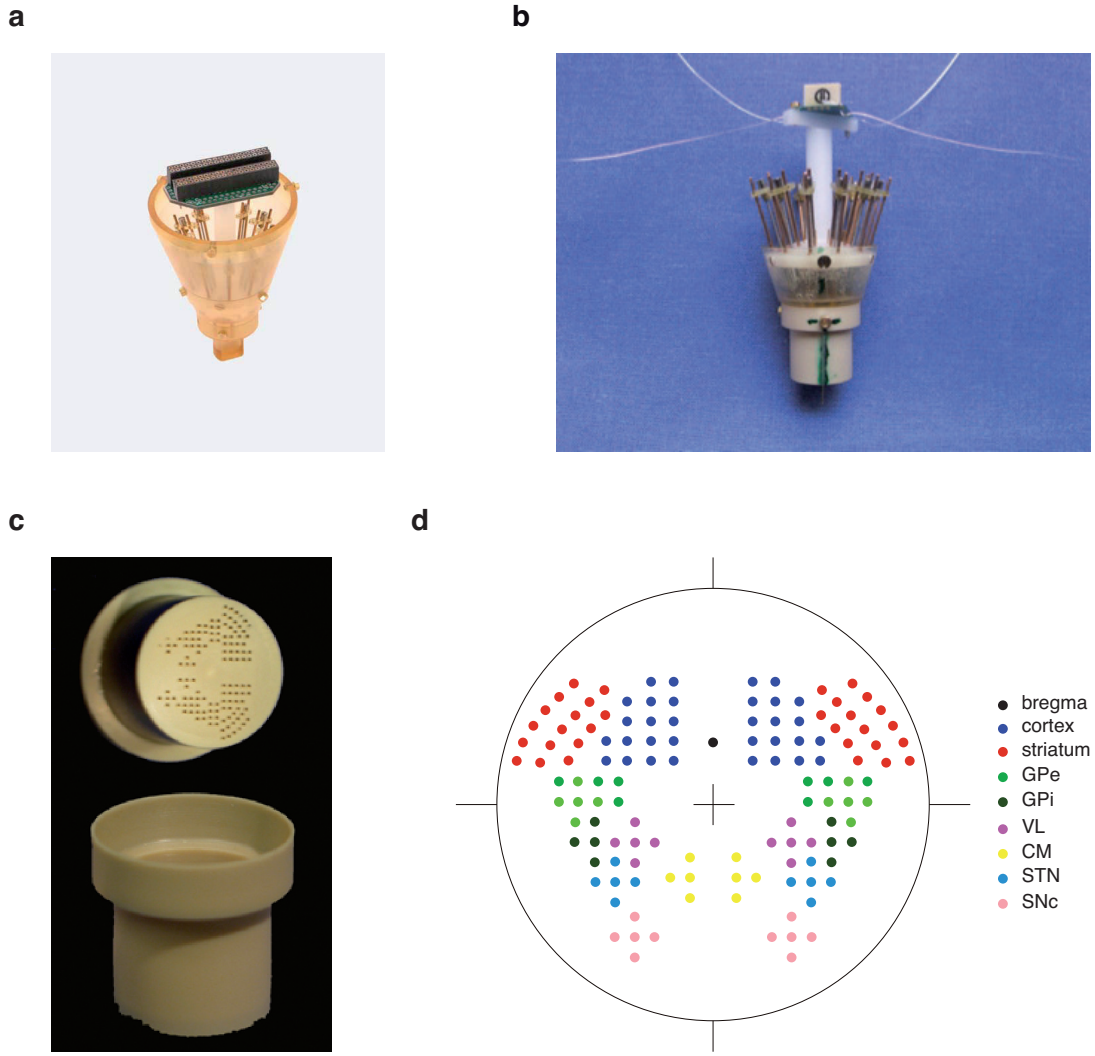

Figure 2.3: Implant used for chronic electrophysiological recordings. (a) Photograph image of the complete original microdrive as distributed by the manufacturer. Image courtesy of Neuralynx. Compare this makeup to the modified one shown in panel b. (b) Front view photograph image of an implant skeleton consisting of the microdrive equipped with a cap for extension of targeting possibilities, and a connector (electrode interface board, see Section 2.4.3) different from that in panel a for use with the appropriate headstage. The small drives consisting of plates and screws are also visible. Four silver wires are attached for connection with ECoG, ground, and reference screws. (c) Bottom and side view photograph images of the cap used for selective targeting of a large number of rat brain structures. (d) Illustration of the pattern of holes situated on the cap's lower side. The black dot above the center crosslines indicates the relative location of bregma. Different colors denote different brain structures. *Abbreviations:* GPe/GPi, globus pallidus, external and internal parts; VL/CM, ventrolateral and centre-median thalamus; STN, subthalamic nucleus, SNc: substantia nigra pars compacta. Original design of the cap by G. Engler, C. K. E. Moll, A. Sharott, C. v. Nicolai.

lateral planes across large brain regions. In contrast, in the original design (Figure 2.3, panel a), targeting of electrodes was limited to a small part of particular brain regions.

The parts of the electrodes (diameter: 75 μm; impedance: 0.8–1.2 MΩ; FHC Inc.; Bowdoin, Maine, USA) located inside the microdrive were led through glass-coated polyimide tubes (Polymicro Technologies, L.L.C.; Phoenix, Arizona, USA), which assured their secure and tight guidance from the bottom of the implant up to the level of the drives. We used gold pins (EIB Large Pins; Neuralynx) to attach the electrodes to the connector's contacts. In addition to the microelectrodes, four silver wires (Science Products GmbH; Hofheim, Germany) were soldered to the connector (Figure 2.3, panel b). We connected them to four stainless-steel screws (Plastics One Inc.; Roanoke, Virginia, USA), placed into burr holes in close vicinity of the dura mater. They served as ground and reference as well as for recording of electrocorticographic (ECoG) signals from above anterior and posterior regions of the brain.

The specific final makeup of the customary microdrive required its complete dismantling and major modifications to its original design. In total, this process of deconstruction and subsequent assembly of a single implant took about 10 to 14 hours on average.

2.3.3 Surgical procedures

We performed the placement of implants under clean conditions and only in animals that showed an overall good health status at the time of operation. Care was taken to avoid any kind of peri-operative stress. We closely monitored the animals' weight on the day before and for three to seven days after surgical procedures.

Animals weighing between 320 and 435 gram were anesthetized initially with a combination of Ketamine (Ketamin Gräub, Dr. E. Gräub AG; Bern, Switzerland; 75 mg/kg bodyweight) and Xylazinhydrochloride (Rompun®, Bayer Vital GmbH; Leverkusen, Germany; 6 mg/kg bodyweight) applied intraperitonally, followed by ventilation with Isoflurane (Isofluran-Baxter, Baxter Deutschland GmbH; Unterschleißheim, Germany) and a mixture of N_2O/O_2 (70/30%). We applied the local anesthetic Lidocain (Xylocain, Astra-Zeneca GmbH; Wedel, Germany) to the operation site on the skull. In order to prevent infections and drying of the eyes, we also locally applied a combination of Bethamethason and Gentamicin (Terracortril®, Dr. Gerhard Mann GmbH; Berlin, Germany) and Dexpanthenol salve (Bepanthen®, Bayer Vital GmbH). Depth of anesthesia was constantly monitored throughout the operation using the so-called *pinch-test*, in which a motor response to a normally painful stimulus applied with a forceps to the animal's paw is regarded as a sign of insufficient anesthetic depth. We kept body

temperature constant with a heating pad and measured it continuously with a rectal thermometer (Fine Science Tools GmbH; Heidelberg, Germany).

Rats were placed into a stereotactic frame (David Kopf Instruments; Tujunga, California, USA) and their heads tightly secured by means of ear bars and a snout holder combined with a ventilation mask. We shove the skin on top of the head and cleaned it with an aseptic agent (Braunoderm®, B. Braun Melsungen AG; Melsungen, Germany). We made a longitudinal cut and removed subcutaneous tissue with a surgical scraper to neatly expose the skull. Colored marks were made on its surface at the positions of anchor screws (Fine Science Tools GmbH), ECoG, ground, and reference screws (Plastics One Inc.; Roanoke, Virginia, USA) using a tissue pen (Securline®, Precision Dynamics Corporation; San Fernando, California, USA).

We calculated the coordinates for placement of the electrodes with reference to the so-called *bregma*, which is defined as the "point of intersection of the sagittal suture with the curve of best fit along the coronal suture" according to Paxinos and Watson, 2005, page VII, in AP and ML planes and marked them with the tissue pen as well. Figure 2.4 depicts the lower surface of the implant (Figure 2.3, page 29) projected onto the drawing of a rat skull, bregma and *lambda* (see figure legend) landmarks as well as all theoretically possible target locations of electrodes and the intended positions of all screws.

We drilled small holes into the skull at the screws' positions and made one large trepanation around the entire target area of the electrodes above each hemisphere. We carefully removed the bone and the dura using forcipes and small hooks and then covered the surface of the brain with sterile silicon oil. Subsequently, the implant was attached to a stereotactic arm and slowly lowered into its final position on the skull's surface where we tightly fixated it by applying dental cement (Paladur®, Heraeus Kulzer GmbH&Co. KG; Wehrheim, Germany) to the bone around it and to the anchor screws. Note that cortical and striatal electrodes had been exposed by 2 and 4 mm, respectively, prior to implantation. This was done in order to directly place electrode tips in their target areas and to ease their feed after the operation. Finally, we closed the opened skin around the implantation site by means of tight surgical sutures and tissue glue (Histoacryl®, Braun Aesculap AG&Co. KG; Tuttlingen, Germany).

As a first postoperative analgetic intervention, we applied a subcutaneous injection of Metamizol-Sodium (Metapyrin®, Medistar Arzneimittel-Vertrieb GmbH; Holzwickede, Germany; 100 mg/kg bodyweight), which we later continued orally via the drinking water when needed (4 mg/ml). Small disturbances in wound healing were treated with Povidon-Iod (Betaisodona®-Solution, Mundipharma GmbH; Limburg (Lahn), Germany). We allowed animals to recover from surgical procedures for at least one week before we started working with them again.

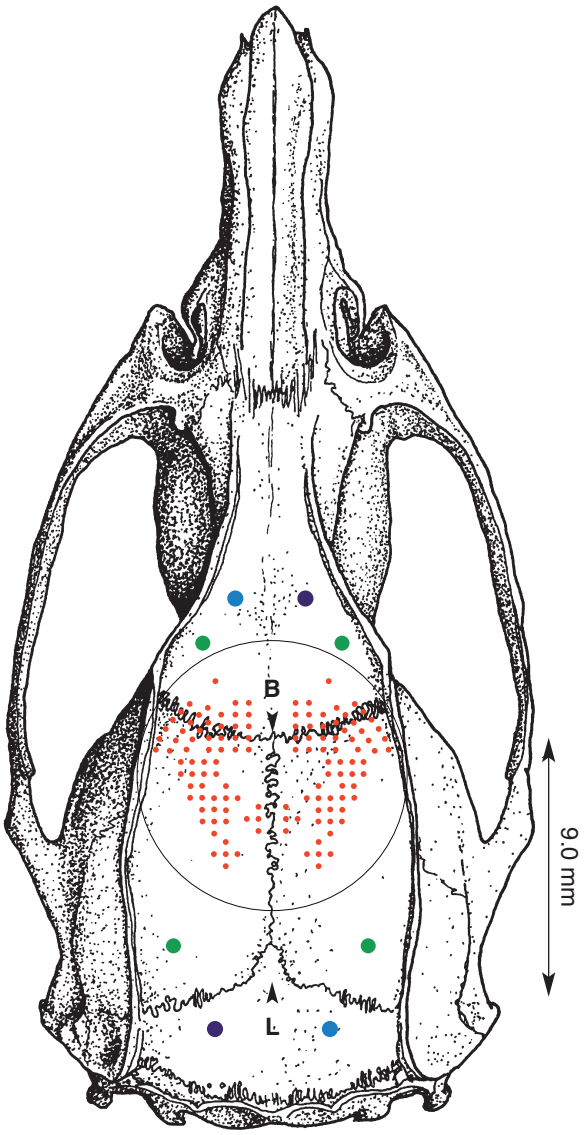

Figure 2.4: Schematic illustration of the implantation site. The lower surface of the cap is projected onto an anatomical drawing of a rat skull. This was the final position of the implant as we fixated it onto the skull's surface after its placement and insertion of the electrodes. The large black circle represents the implant cap's circumference. Red dots denote possible electrode locations with no explicit reference to different structures here (Figure 2.3, page 29); green, blue, and velvet dots mark sites of anchor, ECoG, and ground or reference screws, respectively. Black arrowheads point to the anatomical landmarks bregma and lambda. Lambda is defined as the "midpoint of the curve of best fit along the lambdoid suture" (Paxinos and Watson, 2005, page X). The figure of 9 mm next to the double-arrow denotes the distance between bregma and the so-called *interaural line* (not sketched). *Abbreviations:* B, bregma; L, lambda. The original drawing of the skull, coordinates of anatomical landmarks, and parts of arrows were taken and adapted from Paxinos and Watson, 2005, with permission. Original design of this figure by G. Engler.

2.4 Recording environment and data acquisition

2.4.1 Electrode displacement during rest

The kind of implant used in this study allowed for an alteration of individual electrode positions on a small spatial scale. We changed the dorsal-ventral positions of the electrodes at the beginning of each session in order to sample activities from larger parts of the structures than it would have been possible using fixed, non-moveable electrodes.

To this end, animals were placed in a transparent, cylindrical plexiglas bowl that had an open top and the ground covered with saw dust. We placed the bowl between the legs of a tripod such that the tether cable carrying the headstage that connected the implant with the recording system could be led down from above securely and free from tension. In principle, animals could freely move around and explore the insight of the bowl. However, they quickly adapted to the procedures involved in electrode displacement and spent most of the time sitting inside the bowl quietly at rest. We took care to avoid any additional stress in terms of changing lights or loud noise during handling of the rats.

We moved the electrodes along the dorsoventral axis of the brain by turning the screws of the small drives, with one full turn corresponding to a distance of approximately 156 μm. We mapped the implanted structures in downward and upward directions at least once with each functioning electrode during the entire recording period which lasted between a few weeks up to several months in the different animals. After a change in position, electrodes were left in place at least 10–15 minutes to allow signals to stabilize.

2.4.2 Recording conditions during treadmill running

Following electrode displacement, we transferred the animals from the plexiglas bowl onto the treadmill. In order to protect the recording environment from surrounding noise, we constructed a large box (recording chamber; Figure 2.5) from wooden panels and aluminum bars and lined it with sound-absorbing foam plates on the inside. We attached two light bulbs to the chamber's ceiling that we switched off during recordings to avoid noise contamination of electrophysiological signals. Animals thus had to perform in darkness, but we constantly observed them from the outside via a monitor that we connected to an infrared camera located inside the box right above the running lanes.

Figure 2.5 shows the treadmill apparatus inside the box as we prepared it for recording sessions. We had to make a few major modifications to it to account for the peculiarities of our experimental setting. First, we removed the treadmill's plexiglas top during recordings because with it in place neither would the running lane have accommodated the implanted animal nor had it been possible to connect the electrode interface board

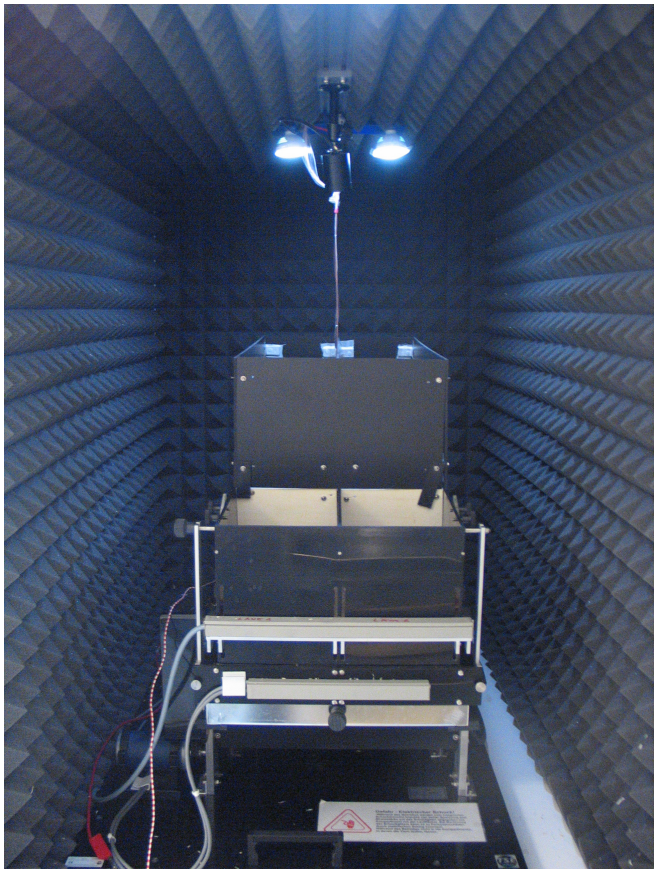

Figure 2.5: The treadmill apparatus inside the recording chamber as we modified it for recording purposes (cf. Figure 2.1, page 24). Note the black frame added to increase the height of the walls as well as the suspension of the tether cable at the mike boom behind the infrared camera that we attached to the ceiling to monitor the animals' behavior.

on the implant with the head stage and the tether cable of the recording system. Second, in order to then prevent animals from escaping the lanes via the low surrounding walls, we enhanced the enclosure by adding a black, four-sided, self-made frame of a height of 16.5 cm to it, yielding a total height of the walls measuring 33 cm from the bottom of the lanes to the top. Third, we attached a special holding device (a so-called *mike boom*) that was rotationally moveable in the DV plane to the ceiling right above the middle of the treadmill. It served to flexibly suspend the cable connecting the implant's connector with the recording system. The tether cable itself was led to the outside through a little hole in the box's ceiling. Those parts of it situated close to the headstage were additionally shielded by wrapping them inside of heat shrink tubings. With these modifications, a secure connection between the implant and the recording system could be established that allowed for relatively stable conditions of data acquisition from the behaving rats.

2.4.3 Data acquisition, online processing, and storage

Acquisition of neural signals was done with an analog 32-channel system (Cheetah 32; Neuralynx; Tucson, Arizona, USA) equipped with an electrode reference panel (ERP-27, Neuralynx) and four differential amplifiers (Lynx-8; Neuralynx). Signals were pre-amplified using a headstage (HS-16; Neuralynx) directly contacting the connector (electrode interface board, EIB-16; Neuralynx) placed on top of the implant (Figure 2.3, page 29) and sent to the recording system via a light-weight tether cable attached to it.

Raw broadband analog signals from all electrodes and ECoG-screws were amplified and filtered twice with separate amplifiers to extract both their low (i.e., LFP and ECoG; sampling rate: 3787 Hz) and high-frequency (i.e., multi-unit activity, MUA; sampling rate: 30303 Hz) components. We amplified the low-frequency components of the signals by factors of 100–2000 and used high- and low-pass filter settings of 1 and 475 Hz, respectively. For the high-frequency components, amplification factors varied between 1000 and 20000, and we used filters settings of 300 (high-pass) and 3000 or 6000 Hz (low-pass), respectively. Analog-to-digital conversion of the signals was performed by the Cheetah-system's A/D-converter. All data were stored on hard disk for offline analysis.

2.5 Behavioral task

Running protocols used for recording sessions were the same as those employed during the Pre-operative stage of the pilot study carried out for establishment of the behavioral model (von Nicolai, 2011) which were in turn closely adapted to those used on preceding training stages. Their design and development over time were subject to several constraints. These included performance ranges and behavioral capacities of the animals under study as well as aspects of data quality and experimental goals. Given a considerable amount of variability between pre- and post-operative performances of individual rats, we had to adapt performance ranges for each subject according to capacities varying during and across recording days, weeks, and months.

Figure 2.6 illustrates the general outline and details of the three behavioral protocols used for recordings. Each recording (also termed *trial* in the following) lasted 7 minutes and included 2 resting periods at the beginning (*pre*) and at the end (*post*) of 60 seconds duration each. We only used data from the first resting period (pre) for comparison with running activities because animals usually did only rest quietly at the front end of the lanes before but not after running. Since the aim was to compare activities during rest with those during running at different levels of motor demand, each protocol included 4 speed levels again of 60 seconds duration each. In addition, an Intro-period of 60 seconds

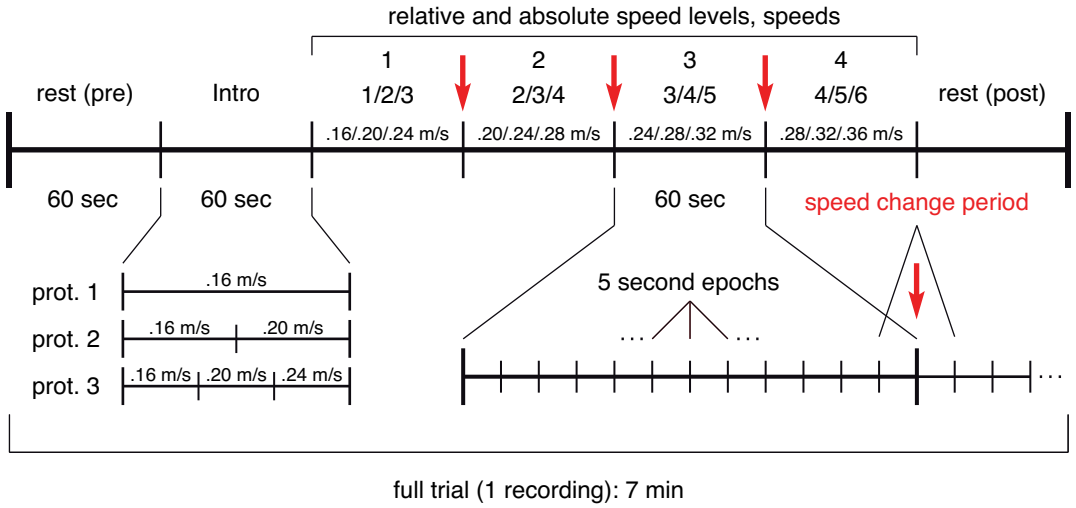

Figure 2.6: Schematic outline of the behavioral task protocol used for recordings. Note the differences between protocols no. 1–3 in terms of details of the Intro-period as well as level composition. The so-called *speed change period* encompassed 2 epochs of 5 seconds length around each speed change event. *Abbreviations:* prot., protocol.

length between resting and the first running levels served to guide the rats progressively to higher running speeds. We had introduced this modification for safety reasons because of particularly unstable initial running patterns in some subjects (Figure 2.6).

Absolute values of speeds ranged between 0.16 and 0.36 m/s, such that the three different protocols had overlapping speed ranges. We chose one of these protocols on an instantaneous basis for a given trial during a given session according to the current behavioral capacities of the respective subject under study. The total number of speed levels was 6, but note that due to differences in level composition of the three running protocols, the first relative speed level could be one of absolute levels no. 1, 2, or 3, and correspondingly different speeds on subsequent levels (Figure 2.6).

The speed of the belt increased abruptly in steps of 0.04 m/s at the moments of transition between successive levels (*speed changes*). In Figure 2.6, speed changes are indicated by red, vertical arrows between relative levels no. 1 and 2, 2 and 3, 3 and 4, respectively. Each speed level was further subdivided into epochs of 5 seconds length, resulting in 12 epochs per speed level. To distinguish epochs electronically, the treadmill control software delivered a TTL-pulse at the transition points of successive epochs. This determined the maximum sampling frequency of behavioral activity allowed by the system since a break of the light beam at the back end of the lanes was counted once every 5 seconds at maximum. It is these epochs that form the smallest units used for analysis of recorded time series data (see Section 2.6.1 below).

2.6 Data preprocessing

2.6.1 Signal quality evaluation

We first cut the entire recording traces of each channel's data (filtered LFPs and multi-unit spike trains, Section 2.4.3) of each trial into epochs of 5 seconds length according to the structure of the behavioral task and as delimited by the epoch triggers emitted by the treadmill device (Section 2.5). We then examined the data for artifacts arising from various sources such as abrupt movements of the animal's head or instability of the recording due to damaged electrodes, moving cables, etc. A given channel had to fulfill three major criteria in order to be judged as valid in terms of pure recording quality, besides more specific conditions such as the estimated spatial location of electrodes with respect to the anatomical boundaries of desired target structures (Section 2.3.1).

First, careful online and offline inspection of raw signal traces was carried out to mark and exclude channels that obviously carried only noise or other unphysiological activities.

Second, we determined the so-called *noise-threshold* (Quiroga et al., 2004; for more details, see Section 2.6.3) of each single channel LFP data epoch and examined wether any rectified (i.e., absolute) signal value would exceed an amplitude of 3–12 times this threshold. Spike data was not evaluated explicitly in this way since the maximum threshold used for spike detection (Section 2.6.3) also served as a means to prevent the inclusion of epochs contaminated by high-amplitude artifacts. An epoch was judged to be valid at a given threshold when there was no amplitude value exceeding it and to be invalid otherwise. For sure, such an automated thresholding operation always implies a trade-off between loosing physiological activity and keeping artifacts. Hence, we computed the

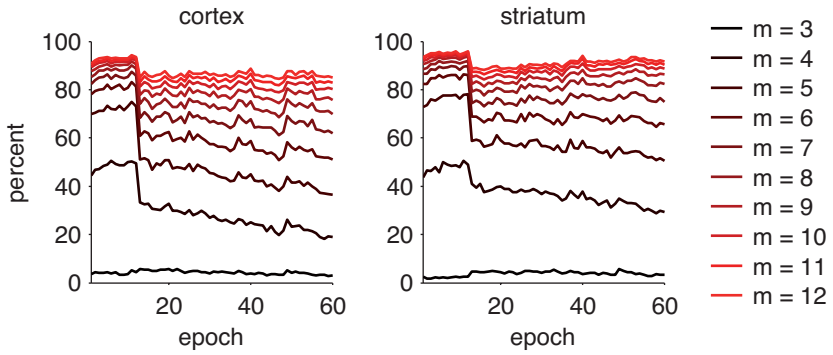

Figure 2.7: Signal quality evaluation by means of amplitude thresholding. The two plots show the percentage of epochs of cortical and striatal LFP data remaining after signal evaluation at 10 different multiples m of the noise threshold. Note the large differences between the first 3–5 thresholds which then decrease towards higher multiples, and the steep decline of percentage residuals after running onset between epochs no. 12 and 13.

percentage of epochs judged as valid at every threshold level separately for each channel from each structure and then pooled the data from all trials and all subjects. The result of this procedure is illustrated in Figure 2.7 demonstrating a threshold value of four times the noise level to be the most appropriate choice for LFP-signals under the above constraints. The plots also indicate a decrease in LFP-signal stability after running onset (epoch no. 13), confirming observations made by visual inspection of raw data traces.

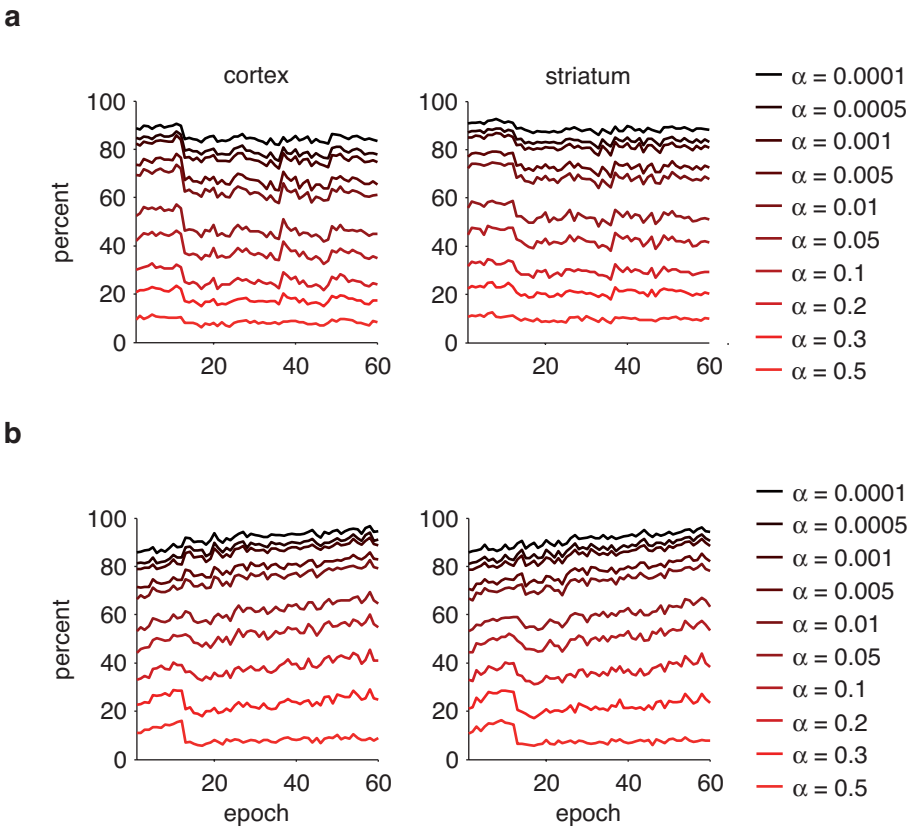

Figure 2.8: Signal stability evaluation by means of variance tests at 10 different α-levels. (a) Local field potentials. (b) Multi-unit activity. Data from cortical and striatal electrodes were pooled across trials and subjects. Note, in all plots, the marked separation of percentage residuals between α-levels of 0.01 and 0.05. In addition, percentages decline and increase steeply between rest and running epochs in (a) and (b), respectively.

Third, we implemented a data stability test based on a judgement of equal variances of root mean square (RMS) values of subsegments of data following an approach described by Moran et al. (2008). In short, each 5-second epoch was cut into 10 parts of 500 ms length, and each of these parts was further subdivided into 10 pieces of 50 ms length each. We determined the root mean square (RMS) values of each 50 ms piece across

data values x in the following manner, yielding 10 different RMS values from each part:

$$RMS = \sqrt{\frac{x_1^2 + x_2^2 + ... + x_n^2}{n}},$$

where n denotes the number of data values. We then used Levene's test to evaluate the null hypothesis of equal variances across data parts, a hypothesis that would have to be rejected in the case of high amplitude artifacts exceeding usual amplitude values (Moran et al., 2008).[1] We computed the test for a number of 10 α-level values between 0.001 and 0.5, and again determined the percentage of data epochs remaining at different thresholds. This revealed an α-level of 0.01 to provide the best trade-off between inclusion and rejection of data segments for both LFP and multi-unit data as is shown in panels a and b of Figure 2.8. As in the case of amplitude thresholding (Figure 2.7), the number of valid epochs declined after running onset. Surprisingly, however, stability of multi-unit signals increased between rest and running.

2.6.2 Preprocessing of Local Field Potentials (LFP)

2.6.2.1 Resampling and digital filtering

Local field potential data were first imported into the MATLAB® environment and down-sampled from a sampling rate of 3787 Hz to a rate of 1000 Hz. Next, we performed two filtering steps on the raw LFPs. Note here that all LFP signal evaluation steps described in the previous section (2.6.1) were performed on filtered data traces.

First, line noise components (50 Hz DC and higher harmonics of 100, 150, 200, and 250 Hz) were removed using a notch filter (fourth-order Butterworth band-stop filter) with a sharp cut-off of $\pm$0.1 Hz around the frequency of interest. Secondly, we applied two fourth-order Butterworth band-pass filters to the notch-filtered data. The first one at 2 Hz (high-pass) was used to remove slow signal drifts caused by movement of the animals. The second one at 256 Hz (low-pass, approximately ½ the Nyquist-frequency of 500 Hz at a sampling rate of 1000 Hz; van Drongelen, 2007) served to reduce the overlap between low- and high-frequency signal components resulting from hardware filter settings (Section 2.4.3). Filtering procedures were performed in both forward and reverse directions on a given data trace to avoid phase distortions of the signal.

Figure 2.9 exemplifies the effects of filtering on the frequency content of LFP-data. In the left plot of panel a, massive line noise components at 50 Hz and higher harmonics

[1] Levene's test is a modified version of Bartlett's multiple-sample test for equal variances. It does not rely on a normal distribution of data values, is less affected by outliers but still robust in case of small sample sizes (Brown and Forsythe, 1974; Lim and Loh, 1996).

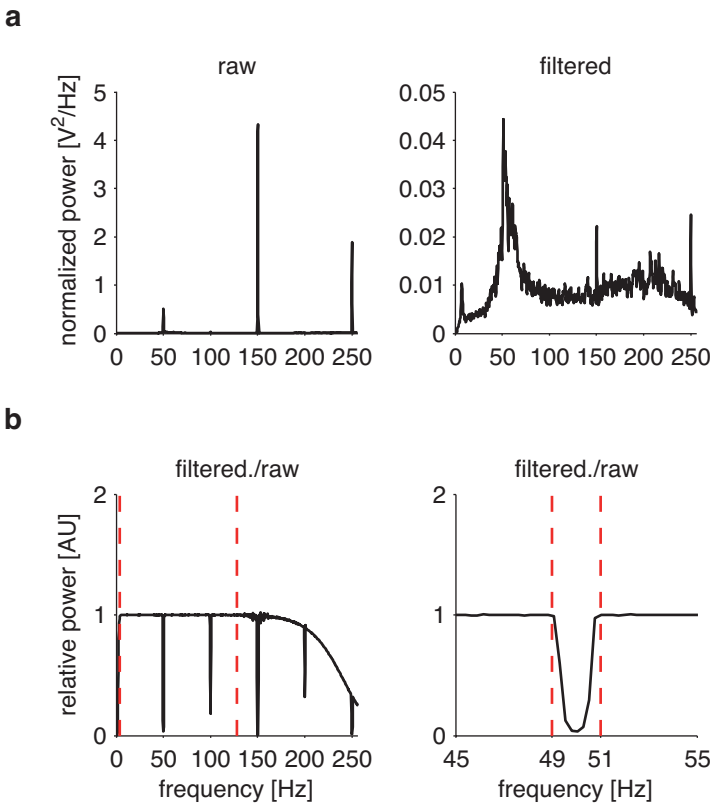

Figure 2.9: Effects of notch-, high-, and low-pass forward-reverse filtering of 60 seconds of raw LFP-data recorded in the striatum of a rat during quiet rest. (a) Power spectra of raw and filtered data, computed using Welch's method (Section 2.7.3.1) and normalized through multiplication with the frequency axis to account for the $1/f^2$ decay of spectral power (Section 3.3.1). (b) Relative power spectra were computed to quantify the effects of filtering in more detail, with values around 1 indicating no change and values below 1 demonstrating a reduction in power of the respective components. Red dashed vertical lines in the left plot are at 4 and 128 Hz. These are the lower and upper limits, respectively, of the frequency range considered for spectral analyses (Section 2.7.3.2).

are readily visible. These components are nicely rejected with band-stop filters, as is illustrated in the right plot of panel a. To quantify the effects of notch-, high-, and low-pass filtering in more detail, we computed the relative power of filtered vs. raw data by dividing the respective spectra. The plots in panel b of Figure 2.9 again demonstrate the strong suppression of undesired frequency components as well as the sharp cut-off of notch filters as illustrated for the case of the 50 Hz component. Further, they show that the band-pass filters introduce considerable slopes below 4 and above 150 Hz in the spectra. Note, however, that the range of frequencies affected by these procedures lies well outside the limits of the frequency range considered later for spectral analyses.

2.6.2.2 Bipolar derivations

A common concern in the analysis of neural voltage measures is a contamination of the signals recorded on one electrode by spillover of activities from adjacent or distant sources through *volume conduction*. It is a serious issue in extracranial recording techniques such as EEG or MEG (e.g., Nolte et al., 2004), but can also be problematic in recordings of intracranial mass activities such as the LFP. In the striatum, one of the two brain structures investigated here, at least some of the LFP-activities recorded there are assumed to be influenced to some degree by volume conduction effects (Berke, 2005).

Several approaches have been proposed to deal with the issue of volume conduction. The one used here is based on the creation of bipolar derivations from two signals recorded monopolarly using a common global reference. It has been applied previously to LFPs recorded from the basal ganglia of rats (Magill et al., 2006; DeCoteau et al., 2007b) and is briefly illustrated in Figure 2.10. The basic idea is that through subtraction of one signal

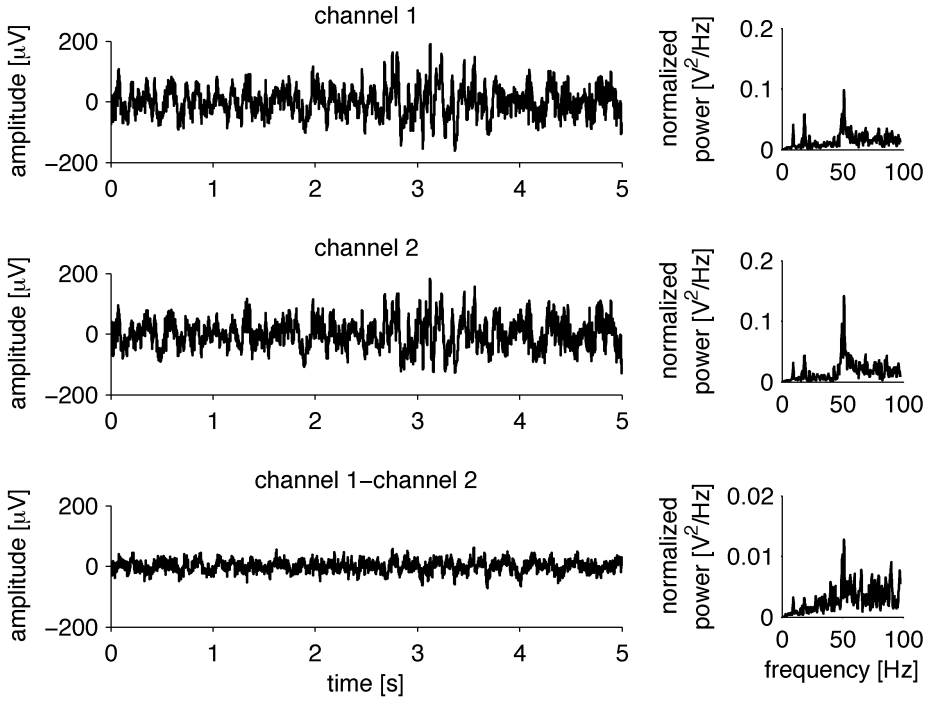

Figure 2.10: Creation of bipolar derivations from field potential recordings. The upper two rows show distinct single-channel traces of LFP-data (left plots) recorded in the rat striatum during quiet rest as well as the corresponding normalized power spectra (right plots) computed using Welch's method (Section 2.7.3.1). The third row shows the difference trace obtained by subtracting the data values of channel 2 from corresponding values of channel 1 and again the resulting power spectrum. Note the considerable reduction in raw signal amplitude and the corresponding decrease in overall power levels.

from another, activities picked up from a common global source that have zero phase lag as it can be expected in the case of volume conduction (Nolte et al., 2004) will cancel. As is obvious from the plots in Figure 2.10, the amplitude of the raw difference trace is markedly reduced. This is also reflected in the massive, roughly 10-fold overall reduction of power in the bipolar spectrum which also exhibits qualitative differences. These two characteristics suggest the elimination of both common global and more specific local signal components exhibiting zero-phase lag between the two electrodes by the derivation process (see Section 4.1.7 for a discussion of consequences).

We created bipolar derivations from monopolar signals recorded on electrodes located in the same structure and the same hemisphere and referenced against a skull screw (Section 2.3.2). This yielded three unique bipolar pairs for each structure-hemisphere combination. Spectral analyses were then carried out on these signals the same way as for monopolar LFPs (Section 2.7).

2.6.3 Preprocessing of Multi-Unit Activities (MUA)

Action potentials emitted by neurons (*spikes*) can be extracted from the high-frequency content of electrophysiological recordings (*spike trains*) by simple application of low and high amplitude thresholds. They represent the minimum and maximum values, respectively, that a voltage signal must and is allowed to cross in order to be distinguished as a spike from ongoing background noise and, at the same time, not to be considered an artifact (Figure 2.11). The determination of a so-called *noise threshold* which is used as a basis for spike detection thresholds is thus a crucial first step in the process of separating single- or multi-units from background activity.

Quiroga and colleagues (Quiroga et al., 2004, page 1668) estimated the noise threshold σ of a band-pass filtered signal x from the median of its normalized absolute values $|x|$:

$$\sigma = median\left(\frac{|x|}{0.6745}\right).$$

The constant of 0.6745 is the absolute value of the standard score[2] of the first and third quartile of the data distribution. It expresses the raw signal values in terms of standard deviations under the assumption of normally distributed data. The motivation for this way of estimating the noise threshold is to avoid a possible bias that can be introduced when a lot of high-amplitude events occur in the data that corrupt threshold estimates based on the mean of raw signal values. Quiroga et al. (2004) used a number of 4σ as the minimum threshold in their paper. Visual inspection of data traces and computation

[2] `http://en.wikipedia.org/wiki/Standard_score`

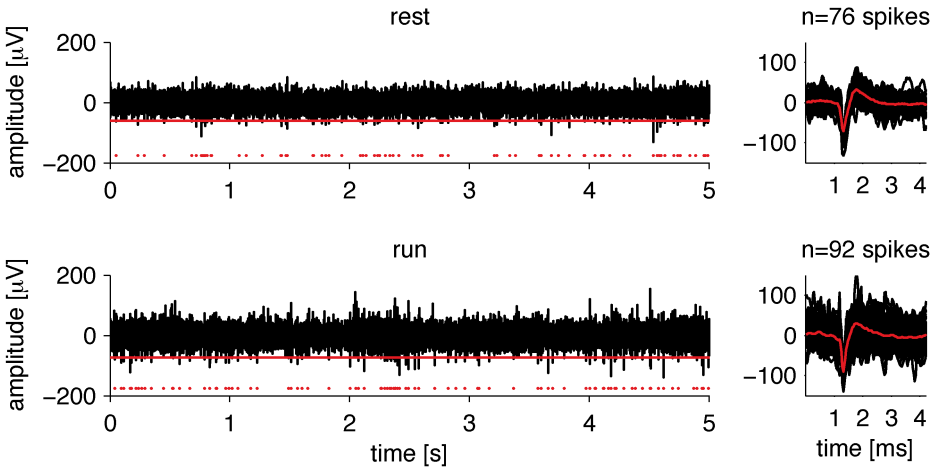

Figure 2.11: Spike detection through amplitude thresholding. The left side of the figure shows two 5-second epochs from spike trains recorded in the striatum of a rat during quiet rest and treadmill running, respectively. The red lines are the lower amplitude thresholds (4σ) applied, and the little red dots beneath denote time points of threshold crossing. The plots to the right of the spike trains are the individual (black) and average (red) waveforms obtained by cutting windows of 128 sample points (corresponding to approximately 4.2 ms of data) out of the raw signal around each spike.

of amplitude distributions revealed this to be a reasonable value for spike detection also for our bandpass-filtered multi-unit data.

After amplitude thresholding, the timestamps of detected events were stored and spiking vectors were created as arrays of zeros filled with ones at the times of spike occurrences. We created down-sampled versions of the high-frequency sampled (Section 2.4.3) spike train signals by adapting the spike times to a sampling rate of 1000 Hz in order to match it to the (re-)sampling rate of the local field potentials. All frequency domain analyses were carried out in the very same way on both types of signals.

2.7 Data analysis

2.7.1 Behavioral analysis

We analyzed the behavioral data from recording sessions in the same way as in the behavioral pilot study (von Nicolai, 2011). Error rates were computed as light beam breaks per minute (bb/min) committed during the 12 × 5-second epochs of each speed level (Section 2.5) and averaged according to the scope of the respective level- or epoch-based analysis step. They are depicted most of the time using the full range of possible values (0–12) to ease comparability of results across animals and running protocols.

2.7.2 Firing rate analysis

We computed firing rates from multi-unit signals by counting the spikes detected by means of amplitude thresholding (Section 2.6.3) within every epoch and then dividing it by the epoch's duration. We adapted both numbers to the size of each epoch's analysis window (3500 points corresponding to 3500 milliseconds of data) as constrained by the demands of time-frequency analyses (Section 2.7.3.2). For level averages, we computed the mean across all valid epochs ($n = 12$ at maximum, see Section 2.7.4) of each level.

2.7.3 Spectral analyses

2.7.3.1 Fourier transform-based frequency analysis

In general, any time domain signal $x(t)$ (or a discrete version $x[n]$ of it) can be transformed into its frequency domain counterpart $X(\omega)$ ($X[k]$) by representing it as the sum of a set of periodic sinusoids of different frequencies (van Drongelen, 2007). Most commonly, this kind of decomposition of a signal is achieved by means of a so-called *Fourier analysis* using either the complex or the real versions of one out of a family of appropriately named functions depending on the signal type (continuous vs. discrete, periodic vs. aperiodic, real vs. complex; for a detailed overview, see Smith, 1997, pages 530-31).

In case of time domain functions that are complex, continuous, and aperiodic, the Fourier Transform $X(\omega)$ of signal $x(t)$ is given by equation (2.1) where ω denotes frequency running from $-\infty$ to $+\infty$, e denotes the exponential function, and j represents the complex number $\sqrt{-1}$:

$$X(\omega) = \frac{1}{2\pi} \int_{-\infty}^{+\infty} x(t) e^{-j\omega t}\, dt. \tag{2.1}$$

In case of discretely sampled signals like those resulting from our measurements of neural activities, the Discrete Fourier Transform $X[k]$ of signal $x[n]$ is computed according to

$$X[k] = \frac{1}{N} \sum_{n=0}^{N-1} x[n] e^{-j2\pi kn/N}, \tag{2.2}$$

where k denotes frequency components evenly spaced between 0 and $N-1$, and N is the length of the time domain signal. Equation (2.2) can be rewritten using Euler's relation,

$$e^{jx} = \cos(x) + j \sin(x).$$

This allows the expression of complex exponentials as the sum of real-valued sinusoids.

In case of the Discrete Fourier Transform, applying Euler's relation yields equation (2.3):

$$X[k] = \frac{1}{N} \sum_{n=0}^{N-1} x[n] \left[\cos(2\pi kn/N) - j \sin(2\pi kn/N)\right]. \tag{2.3}$$

This equation demonstrates the contribution of both cosine and sine wave components to a given frequency domain value. From the real and imaginary parts of these complex numbers the magnitudes (i.e., amplitudes) and phases of the different frequency-specific sinusoids can then be determined (Smith, 1997).

Equations (2.1)–(2.3) all indicate the principle of Fourier analysis which essentially boils down to the *correlation* of a time domain signal with a complex sinusoid, i.e., their multiplication and subsequent integration and summation, respectively, in the continuous and discrete case. Thus, each time domain value contributes to a given frequency domain value, and vice versa in the case of inverse Fourier transforms that we do not consider here. A particularly elegant and computationally inexpensive method to obtain the frequency domain representation of a time domain signal is by means of algorithms implementing the so-called *Fast Fourier Transform* (FFT) which is at the heart of many Fourier-based analysis techniques used today (van Drongelen, 2007). For instance, the FFT forms an essential part of power spectrum estimation techniques such as *Welch's method* that we used for some analyses in the present chapter. For a brilliant introduction to and in-depth discussion of Fourier analysis techniques, see Smith, 1997.

2.7.3.2 Wavelet transform-based time-frequency analysis

Wavelet decomposition of a signal amounts to its analysis in terms of trends and fluctuations, i.e., the computation of weighted averages of and weighted differences between adjacent values. While the former primarily capture overall, slower variations (trends) of the signal, the latter primarily capture its localized, faster variations (fluctuations). The computation of weighted averages and differences, respectively, is achieved through the application of appropriately chosen *scaling signals* and *wavelets* adapted to the characteristics of the respective input signal function to be decomposed (Walker, 2008).

This analytical concept can be extended from the time into the frequency domain and to the decomposition of an input signal into low- and high-frequency components with the former capturing its slower trends (or averages) and the latter capturing its faster fluctuations (or details). In this case, scaling signals and wavelets and their Fourier transforms are employed to act as *low-pass* and *high-* or *band-pass filters*, respectively, on the input signal function and its Fourier transform owing to their different spectral characteristics. A repeated application of appropriately modified scaling signals and

wavelets on different levels of a so-called *multi-resolution analysis* allows for an accurate extraction of the spectral components of an input signal (Walker, 2008).

The Fourier-based approach to frequency analysis as we discussed it in the preceding section (2.7.3.1) and the method of spectral decomposition by means of wavelet analysis are both well suited to detect the frequency characteristics of an input signal. However, when applied in the manner described above, they do not account for the temporal dynamics of non-stationary signals such as those recorded from neural activities. Thus, a *time-frequency analysis* has to be performed to temporally localize the frequency components of such a signal. While different approaches exist for this task, a wavelet-based analysis in terms of a *continuous wavelet transform* (CWT) is a particularly elegant method since it provides the means for a dynamically adapted trade-off between temporal and spectral accuracy (van Drongelen, 2007; Walker, 2008).

The basic idea of CWTs is that through successive translation of frequency-specific *filter kernels* over an input signal, i.e., a repeated correlation of the latter with appropriately designed wavelet functions, a temporally and spectrally precise extraction of its frequency components can be achieved. The CWT can thus intuitively be conceived of as a means to detect specific *features* in a given signal (Smith, 1997). The filter kernels used for this task are derived from a real- or complex-valued mother function also called the *analyzing wavelet*, W, by means of its modification through the application of frequency-specific scale parameters s according to equation (2.4):

$$W_s(t) = \frac{1}{\sqrt{s}} W\left(\frac{t}{s}\right). \tag{2.4}$$

Apart from the basic choice of the particular mother wavelet, crucial factors shaping the time-frequency characteristics of the outcome of a CWT are the settings of its scale, width, and frequency parameters. The *correlations* c of the input signal $x(t)$ with wavelet filter kernels $W_s(t)$ of scale s at intervals τ are given by equation (2.5):

$$c(s,\tau) = \int_{-\infty}^{+\infty} x(t) \frac{1}{\sqrt{s}} W_s(t) \left(\frac{t-\tau}{s}\right) dt. \tag{2.5}$$

In the case of complex-valued wavelet functions, note the correspondence between these kinds of correlations and those in the definitions of the Fourier transforms listed above (Section 2.7.3.1). This indicates the close relationship that exists between the two analytical approaches (van Drongelen, 2007; Walker, 2008).

In the present study, we computed the wavelet transforms of LFP and spiking signals through *convolution* of every epoch's data vector (length: 5 seconds, $n = 5000$ points)

with complex, time- and frequency-dependent kernels (*Morlet wavelets*) w (Figure 2.12):

$$w(t, f) = Ae^{-t^2/2{\sigma_t}^2}e^{i2\pi ft}, \tag{2.6}$$

which essentially yields a *Gabor expansion*[3] (Morlet et al., 1982a) of the signal to be analyzed. This is the CWT approach described by Morlet et al. (1982a,b) for an application to seismic wave data in geophysics which has later been proposed for the analysis of neurophysiological time series data by several authors (e.g., Tallon-Baudry and Bertrand, 1999; Le Van Quyen et al., 2001; Lee, 2002; Li et al., 2007). In equation (2.6), σ_t is the standard deviation of the wavelet function in the time domain, e denotes the exponential function, i denotes the complex number $\sqrt{-1}$, and A is a normalization factor defined as

$$A = \frac{1}{\sqrt{\sigma_t\sqrt{\pi}}}.$$

The normalization factor ensures conservation of energy of the transformed signal, an aspect of general and crucial importance in all kinds of wavelet analyses (Walker, 2008). The wavelet functions w have a Gaussian shape in both the time and frequency domain, with their standard deviations σ_f and σ_t given by

$$\sigma_f = {}^{f}\!/_{q} \text{ and } \sigma_t = \frac{1}{2\pi\sigma_f},$$

respectively, where f denotes the frequency of interest and q is the width of the wavelet. These latter parameters determine both the temporal and spectral resolution of the analysis, as is exemplified in panel b of Figure 2.12.

The first exponential in the wavelet equation (2.6) defines Gaussian-shaped windowing functions that serve to reduce the amount of spectral leakage (Figure 2.12, panel c) resulting from the analysis of signals of finite length (Smith, 1997). The second exponential defines the actual complex sinusoids needed for the detection of frequency components of interest in the signal to be analyzed (see also Section 2.7.3.1). The time points of interest t for which the frequency-specific wavelet functions are defined are calculated as

$$-l\sigma_t \leqslant t \geqslant l\sigma_t$$

in discrete steps of ${}^{1}\!/_{f_s}$. Here, f_s denotes the sampling frequency and l is the absolute length of the wavelet computed in terms of numbers n of standard deviations σ_t of a

[3] A *Gabor expansion* or *Gabor transform* of a signal function is created by computing the Fourier transforms of a sequence of "time localized subsignals" obtained by multiplying the signal with shifted windowing functions of a desired type (Walker, 2008, page 194).

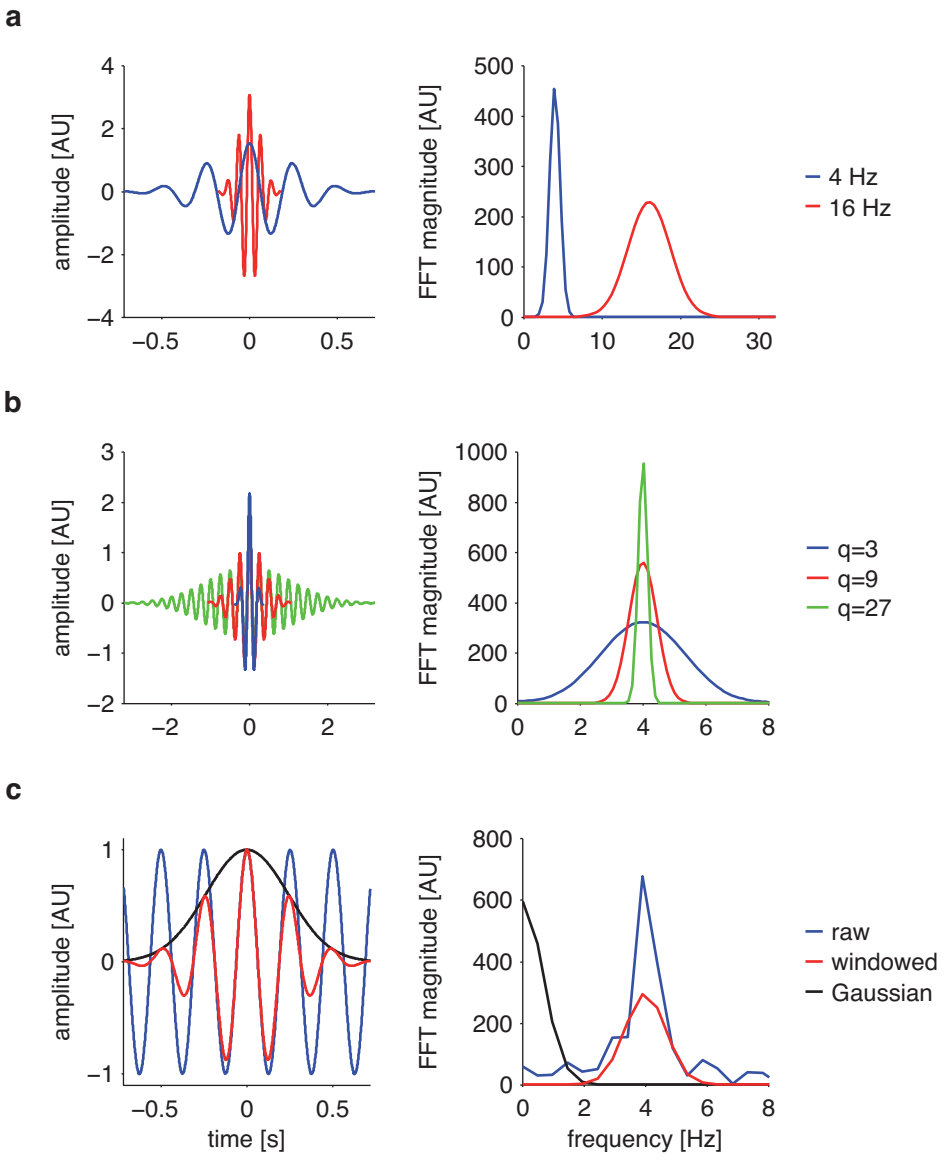

Figure 2.12: Some characteristics of continuous Morlet wavelet transforms. (a) Wavelet functions of different frequencies stretch an equal number of cycles and thus differ in their temporal and spectral widths. (b) Increasing the width q of the wavelets increases the spectral and decreases the temporal resolution (i.e., it decreases σ_f and increases σ_t, respectively; see main text for details). (c) Gaussian shaped windowing functions reduce the amount of spectral leakage into neighboring frequency bands. The raw sinusoid was multiplied by the Gaussian resulting in a dampening of its amplitude at the edges. Note the spectral characteristics of the Gaussian window which is its own Fourier transform (Smith, 1997). For illustration purposes, standard cosine waves were multiplied here with the *magnitudes* of complex Morlet wavelets at the respective frequencies, thus combining their real and imaginary parts. For a very intuitive illustrative coverage of some properties of continuous Morlet wavelet transforms, see Figure 1 in Le Van Quyen and Bragin, 2007.

Gaussian kernel with $n = 3$ in all wavelet-based frequency analyses of the present study:

$$l = n\sigma_t.$$

The time-frequency transformation TFR of the signal $x(t)$ in terms of its convolution with wavelet functions $w(t, f)$ is given by equation (2.7):

$$TFR(t, f) = x(t) * w(t, f), \tag{2.7}$$

where $*$ denotes the convolution operation. To accord with the above definition of frequency analysis by means of continuous wavelet transforms we make use here of the facts that first, multiplication in the frequency domain is equivalent to (complex) convolution in the time domain (van Drongelen, 2007), and second that in the present case of even symmetric analytical Morlet wavelet functions $w(t, f)$ a correlation with the input signal $x(t)$ is exactly equivalent to their convolution (van Drongelen, 2007).

Figure 2.13 depicts the time-resolved and time-averaged power spectra (Section 2.7.3.3) obtained from a time-frequency transformation of LFP data recorded in the rat striatum. The plots illustrate some of the described characteristics regarding the trade-off between temporal and spectral resolution that depends on the choice of parameter settings as well as the variability of temporal and spectral features of the signal that principally calls for its detailed analysis in both the time and frequency domain (Section 4.7).

We computed the frequency components of interest of our analyses on logarithmic scales in terms of *octaves* and in steps of an even number of powers of 2 *voices* (i.e., 1/4 or 1/8 octaves), following propositions made by, e.g., Walker, 2008. We did so to account for the finding of a linear relationship between the natural logarithms of the mean frequencies of band-limited oscillatory neural processes in a scheme where neighboring frequencies exhibit constant ratios (Buzsáki and Draguhn, 2004, page 1926; for the original paper, see Penttonen and Buzsáki, 2003). We limited our analyses to an overall range of frequencies between 4 and 128 Hz (i.e., spanning 5 octaves) and adapted the range and numbers of frequencies of interest to specific analytical motivations. We used wavelet widths $q = 6$ in all analyses since this number is supposed to provide a very good trade-off between time and frequency resolution (Li et al., 2007). Convolution of signals with filter kernels results in a wavelet-width, i.e., in our case frequency-dependent, incomplete coverage of the first and last signal points by the filter kernel (Smith, 1997). We therefore only included transformed values located at the middle 3500 out of 5000 data points (corresponding to 3500 and 5000 ms of data, respectively) in all further analysis steps. This assured an equal number of valid data values at each time-frequency point.

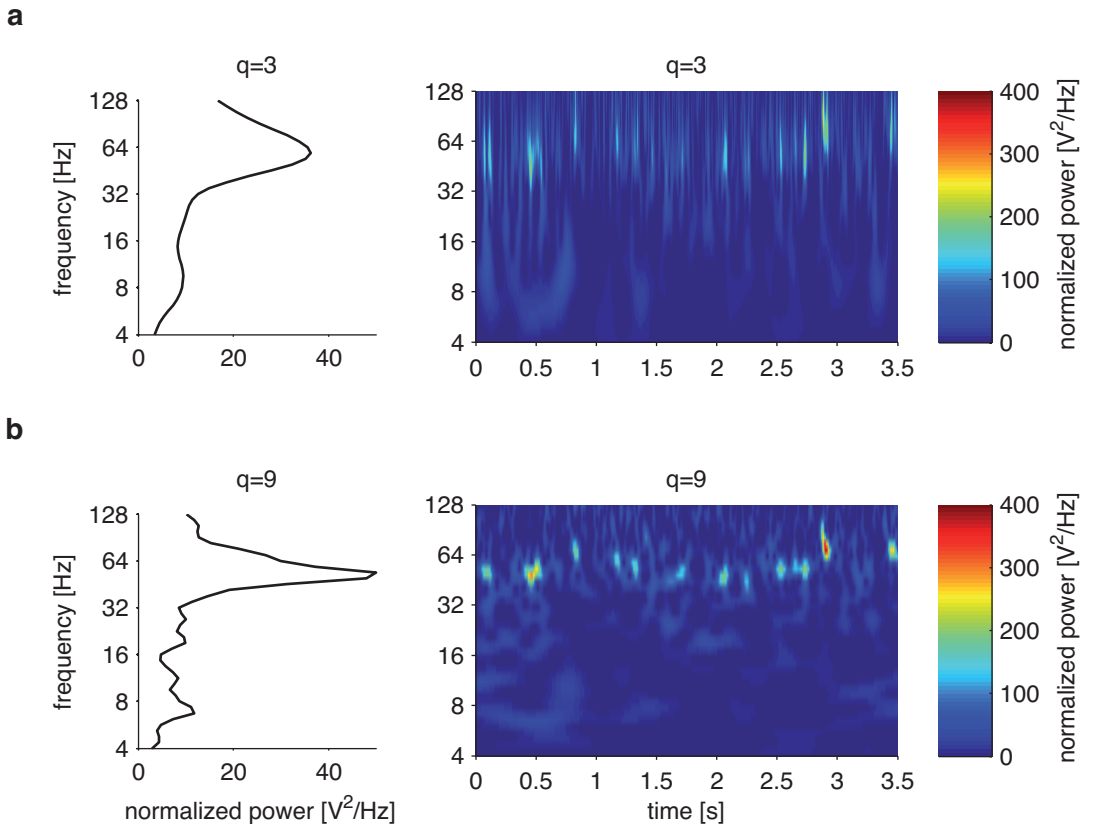

Figure 2.13: Characteristics of time-frequency analyses using continuous Morlet wavelet transforms and the consequences of a change of parameter settings. Panels a and b both show the time-averaged (left) and time-resolved (right) power spectra of LFP data recorded in the rat striatum during rest. The plots illustrate the tradeoff between temporal and spectral accuracy that hinges on the choice of wavelet widths q. Further, note that while the average spectra nicely display the most prominent mean peak frequencies, they fail to reveal the variability of fine-grained temporal and spectral characteristics.

2.7.3.3 Power analysis

A basic and very informative way to characterize a signal in the frequency domain is to describe the distribution of the strengths of its sinusoidal components. Spectral *power* is a measure of the time-average, band-limited energy of frequency components. As such it quantifies the frequency-dependent variance of a stationary signal (M. Siegel, personal communication). The entire power content of a signal in the frequency domain can be defined as its *power spectral density* (PSD). It is obtained through integration of values across the whole *power* or *autospectrum*. The power spectrum describes the distribution of the power of the frequency components of a signal per unit of frequency bandwidth (Smith, 1997; van Drongelen, 2007; McMahon, 2007).

In brief, the *energy* E of a signal $x(t)$ is defined as the integral of its magnitude squared:

$$E = \int_{-\infty}^{+\infty} |x(t)|^2,$$

where || denotes the magnitude, or absolute value of the signal. Accordingly, the energy of a sinusoid of frequency f is the magnitude squared of its Fourier transform X_f:

$$E_f = |X_f|^2.$$

Following the above definition of spectral power, the power P of a signal is equal to its energy E during time period T:

$$P = \frac{E}{T}.$$

The power P of a signal x at frequency f can then be obtained by multiplying the Fourier transform $X(f)$ with its complex conjugate.[4] A corresponding multiplication of all frequency components and normalization by the number of data points N to ensure conservation of energy delivers the power spectrum S_{xx} of signal x:

$$S_{xx} = \frac{XX^*}{N},$$

where * denotes the complex conjugate (van Drongelen, 2007; see Figure 2.14 on page 55 for example Fourier-based power spectra).

In our case of a wavelet transform-based frequency-analysis of time series data (Section 2.7.3.2), the time-varying power of signal $x(t)$ is computed as the squared norm (or magnitude) of the complex time-frequency transformation $TFR(t, f)$ (Siegel et al., 2009):

$$P(f, t) = |TFR(t, f)|^2 . \tag{2.8}$$

To examine the time-average distribution of power values across the frequency spectrum of interest we then computed the mean of the time-varying power estimates of each epoch by averaging across the time dimension ($n = 3500$ points per frequency). In this way, the dependence of power on time vanishes, yielding an expression $P(f)$ which is only dependent on frequency and thus equivalent to the power spectrum. Figure 2.13 on page 50 shows examples of time-varying and time-average power estimates of neuronal signals.

[4] Multiplication of the complex Fourier transformed values $a + jb$ with their complex conjugates $a - jb$ results in an expression $a^2 + b^2$ in rectangular coordinates which is exactly equivalent to the squared magnitude of time-frequency transformed values in circular coordinates included in equation (2.8).

2.7.3.4 Coherency analysis

Spectral power quantifies the strength of individual frequency components contained in individual signals. In contrast, spectral *coherency* is a complex-valued measure of the strength of *phase-coupling* between two signals during time interval T at frequency f.

To be more precise, the complex *cross-spectrum* S_{xy} relates the amplitude and phase characteristics of individual frequency components of different signals $x(t)$ and $y(t)$. It is given by the following relation, where * denotes the complex conjugate:

$$S_{xy} = S_{xx}{}^{*} S_{yy}.$$

From that, the *squared coherence* Cs is obtained by normalizing the squared magnitude of the cross-spectrum by the product of the *autospectra* S_{xx} and S_{yy} of either signal:

$$Cs = \frac{|\langle S_{xy} \rangle|^2}{\langle S_{xx} \rangle \langle S_{yy} \rangle}.$$

Here, the brackets ($\langle\rangle$) denote averaging of individual spectra from several epochs since coherence estimates based on single epochs always have a value of 1 (van Drongelen, 2007; see Figure 2.14 below). As such, the squared coherence only quantifies the strength of phase-coupling without regard to the phase-lag between signals. To differentiate between amplitude and phase components, the cross-spectrum is first normalized by the square root of the product of the autospectra which gives the *coherency* Cy (Nolte et al., 2004):

$$Cy = \frac{\langle S_{xy} \rangle}{\sqrt{\langle S_{xx} \rangle \langle S_{yy} \rangle}}. \tag{2.9}$$

The *coherence* C and *phase* ϕ of the coherency are then computed as the complex magnitude (i.e., the absolute value) and complex argument (i.e., the angle) of this expression:

$$C = |Cy|, \text{ which is equivalent to } C = \sqrt{(real(Cy))^2 + (imag(Cy))^2},$$

and

$$\phi = \arg(Cy), \text{ which is equivalent to } \phi = \arctan\left(\frac{imag(Cy)}{real(Cy)}\right),$$

where *real* and *imag* denote the real and imaginary components (see the polar plot in panel c of Figure 2.14, page 55), respectively, of the complex coherency vector.

In essence, spectral coherence as the *magnitude* of the complex-valued coherency measures the degree of linear predictability of one signal given another based on the frequency characteristics of either signal (Nolte et al., 2004). It is a dimensionless quantity bound

between 0 and 1, with the former indicating no and the latter indicating a perfectly consistent phase relationship. Thus, just as spectral power is a measure of the frequency-dependent variance of one signal (Section 2.7.3.3), coherence quantifies, in the frequency domain, the degree of covariance between two signals normalized by their autovariances.[5]

In addition to the magnitude of coherency, its *imaginary* part Ci can be computed as

$$Ci = imag(Cy).$$

Imaginary coherence is a useful measure in frequency-domain based coupling-analyses of electrophysiological signals since a non-vanishing (i.e., non-zero) imaginary part of coherency is assumed to always reflect true brain interaction. This is in contrast to the magnitude of coherency which also depends on its real part and is thus more prone to be dominated by volume-conduction effects exhibiting zero-phase lag between electrodes (see Section 2.6.2.2 above; for a detailed discussion of this topic, see Nolte et al., 2004). Imaginary coherence is bound between -1 and 1, thus also indicating the *direction* of the phase-coupling between sources whereas coherence proper only indicates its strength.

Panel b of Figure 2.14 (page 55) depicts coherence and imaginary coherence estimates computed from the raw Fourier transform-based cross-, auto-, and resulting coherency spectra of striatal LFP signals. Panel a shows the power spectra of the two signals which both exhibit distinct peaks between 45 and 65 Hz. The coherence spectrum shows a peak at a similar location whereas imaginary coherence values fluctuate closely around zero.

We computed the time-resolved, complex-valued cross-spectra between all signal pairs using the same kind of time-frequency transformation of the time series data of each epoch as explained above (Section 2.7.3.2). Coherence and imaginary coherence estimates of a given epoch were then obtained by normalizing the time-average ($n = 3500$ data points) cross-spectra by the corresponding time-average autospectra ($n = 2 \times 3500$ data points).

2.7.3.5 Phase analysis

For an even more detailed insight into the frequency-dependent temporal relationships between signals, *phase-locking values* (PLV) and *phase angles* (φ) can be determined. They quantify the average strength and angle, respectively, of their phase-coupling after appropriate normalization of the *individual* cross-spectral vectors to account for differences in instantaneous power between the two partners.[6]

[5] This is the reason why spectral power and coherence are equivalent to the Fourier transforms of the time-domain based auto- and cross-correlation functions, respectively (McMahon, 2007).

[6] The normalization in the coherency equation (2.9), in contrast, is performed by dividing the *average* cross-spectrum by the product of the *average* power spectra.

More precisely, the complex values of cross-spectra are related in terms of their cartesian and polar coordinates according to

$$a + jb = M(\cos\theta + j\sin\theta).$$

Furthermore, using Euler's relation (Section 2.7.3.3) this expression can be written as

$$a + jb = Me^{j\theta}.$$

Here, a and b represent the real and imaginary parts of complex numbers in cartesian coordinates, and M and θ represent their magnitudes and phases in polar coordinates; e is the exponential function (for a brilliant exposition of these relations, see Smith, 1997). Dividing both sides of this equation by M achieves a normalization of the cross-spectral vectors to a magnitude of 1 (see Figure 2.14).[7] This prepares them for averaging across individual cross-spectra to yield the so-called *normalized phase-vector* PhV according to

$$PhV = \langle e^{j\theta} \rangle,$$

where the brackets ($\langle\rangle$) denote averaging and j represents the complex number $\sqrt{-1}$. Phase-locking and phase angle values of a given epoch are then computed as the complex magnitude and complex argument of the PhV, respectively (Lachaux et al., 1999):

$$PLV = |PhV| \text{ and } \varphi = arg(PhV).$$

The left plot of panel c of Figure 2.14 depicts phase-locking and phase angle values computed from the raw Fourier transform-based cross-spectra of striatal LFP-signals. Note the similarity between phase-locking and coherence values in panel b. The right plot of panel c shows all the endpoints of individual phase vectors computed from individual epochs of the data segment as well as their average magnitude and phase angle. Note the extremely high phase-locking value and small phase angle at that frequency.

For each epoch, we computed phase-locking values as averages across the individually normalized, complex values of time-resolved cross-spectra ($n = 3500$) obtained from time-frequency transformed data (Section 2.7.3.2). Phase angles at each frequency ($n = 3500 \times 41$ values) were sorted into histograms of 61 evenly spaced bins of a size of 6° (~ 0.1047 rad/s) stretching from $-\pi$ to $+\pi$ rad/s with the middle bin centered on 0°.

[7] This holds true since the real and imaginary parts of the cross-spectral values can be expressed as $a = M(\cos\theta)$ and $b = M(\sin\theta)$, and after division by M their sums are always equal to 1 according to the Pythagorean trigonometrical identity: $\cos^2\theta + \sin^2\theta = 1$ (Sterling, 2005).

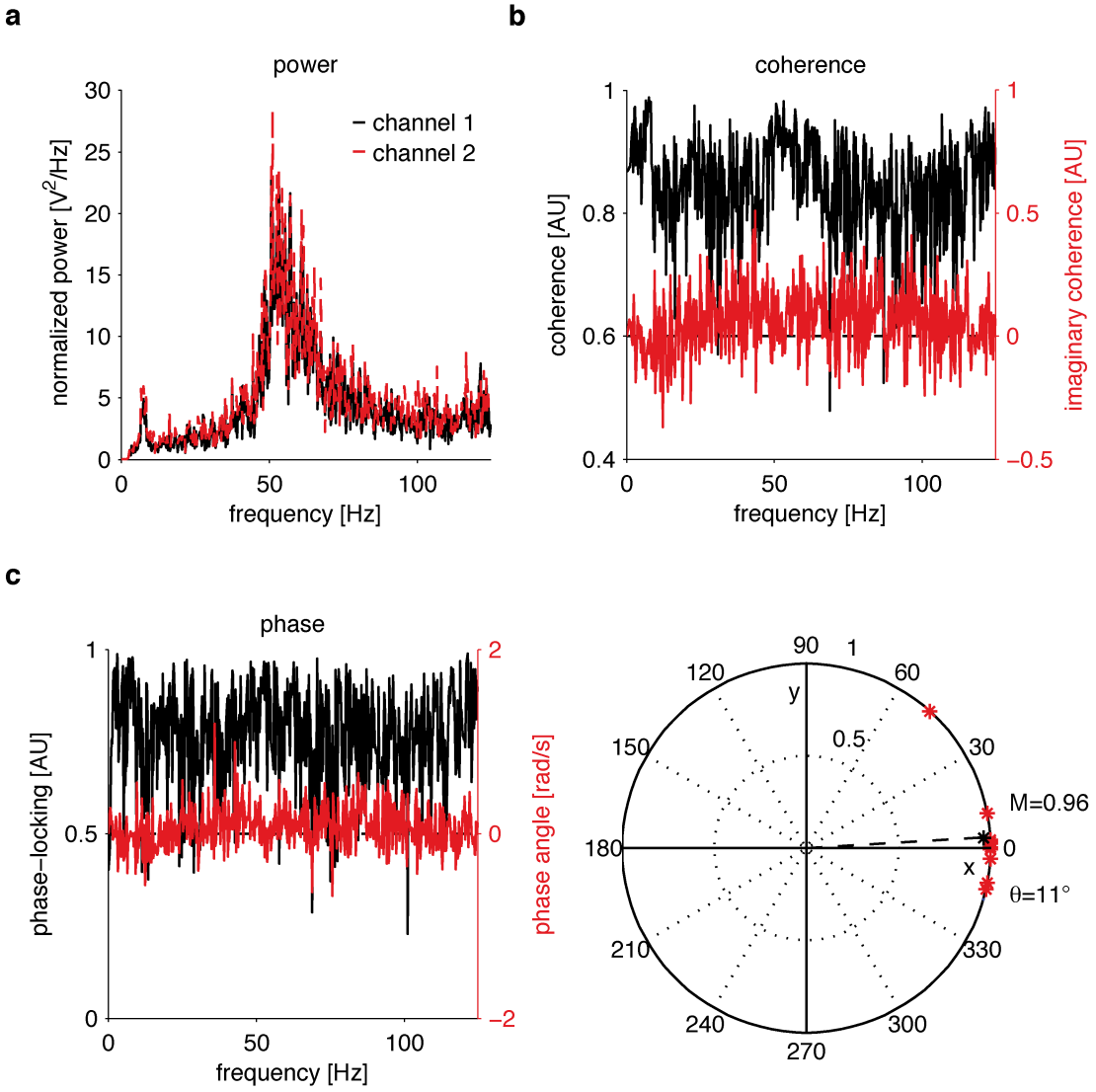

Figure 2.14: Power, coherency, and phase-related spectral estimates as computed from striatal LFP data recorded on two electrodes in a resting rat. (a) Frequency-normalized power spectra. (b) Coherence and imaginary coherence spectra. (c) Phase-locking and phase angle spectra. (d) Magnitudes of individual (red stars) and average (black star and dashed line) phase vectors at a single frequency of about 53 Hz are depicted in a polar plot. X- and y-axes in (d) represent real and imaginary components, respectively, of the complex coherency vectors in *rectangular* coordinates. We computed all spectra directly from the raw FFTs (Section 2.7.3.1) of the signal epochs ($2 \times 10 \times 6$ seconds) without additional windowing of the data vectors, which partly explains their peaky appearance. Note the different units of left and right y-axes in (b) and the left plot in (c) as well as the fact that all individual phase vectors in the polar plot have magnitudes of 1. Black dashed horizontal lines in (b) and the left plot of (c) indicate zero imaginary coherence and zero phase angle values, respectively. *Abbreviations:* M, θ: magnitude and angle of the average phase vector. The polar plot in panel c was inspired by van Drongelen, 2007.

2.7.3.6 Phase-amplitude analysis

We computed the magnitude and phase of the complex *phase-amplitude coupling* values calculated between different frequency components of LFP signals. This measure provides an estimate of the temporal consistency of the relationship between phase and amplitude components of oscillatory processes (Figure 2.15). As such, it can be used to detect cross-frequency interactions in signals such as modulations of the amplitude of a high- by the phase of a low-frequency component (Jensen and Colgin, 2007; Tort et al., 2010).

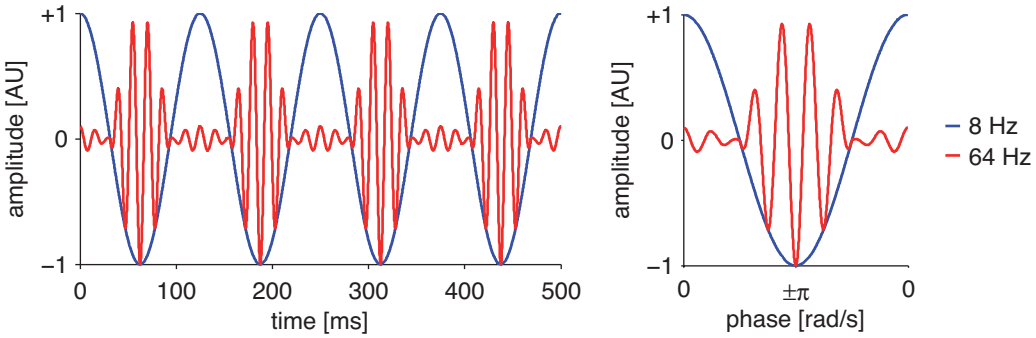

Figure 2.15: Illustration of the principle idea of phase-amplitude coupling analyses. The left plot shows the amplitude of a high-frequency oscillation to waxe and wane in a fixed relation to particular phases of a low-frequency oscillation. The right plot quantifies this relation more explicitly displaying the average high-frequency amplitude as a function of the low-frequency phase, which indicates modulation of the former by the latter.

We followed here an approach used by Canolty et al. (2006) and Siegel et al. (2009) whereby the time-average magnitude M and phase ϕ of the coupling of two frequency components across N time points t are defined as the complex norm ($||$) and argument (arg), respectively, of the point-wise correlation of their phases θ and amplitudes A:

$$M = \left| \frac{1}{N} \sum_{t=1}^{N} A(t) e^{i\theta(t)} \right|,$$

$$\phi = arg \left(\frac{1}{N} \sum_{t=1}^{N} A(t) e^{i\theta(t)} \right).$$

We computed the coupling between phases and amplitudes of all frequency components of each data epoch ($n = 3500 \times 41$ time-frequency points), yielding matrices of size 41×41. We normalized the raw time-frequency transformed values by the mean amplitude in each frequency bin prior to analyses to account for physiological differences in signal strength.

2.7.3.7 Power correlation analysis

We computed correlation matrices between all pairs ($n = 41 \times 41$) of frequencies of time-resolved power spectra ($n = 3500$) of each epoch of LFP data to examine cross-frequency interactions and same-frequency amplitude coupling patterns between temporal fluctuations of frequency-specific local population activities possibly distinct from those captured by phase-amplitude and phase-coupling analyses, respectively. This yielded correlation coefficients (i) between power values across both electrodes and frequencies, and (ii) between power values at the same frequencies across electrodes (cases *cross-electrode, cross-frequency*, and *cross-electrode, same-frequency*, respectively; see Section 3.7 below).

For correlation analyses, we made use of a method devised by Masimore et al. (2004) for the detection of fundamental frequencies in time-varying power estimates of neuronal signals. In this scheme, the *correlation* c of power estimates P at frequencies i and j across a number of N data (i.e., time) points of a given signal epoch is given by

$$c_{i,j} = \frac{\sum_{t=1}^{N}(\langle P(i)\rangle - P_t(i))(\langle P(j)\rangle - P_t(j))}{(N-1)\sigma_i\sigma_j}, \tag{2.10}$$

where $\langle P(i)\rangle$, $\langle P(j)\rangle$ are the time-average power estimates at frequencies i and j, $P_t(i)$, $P_t(j)$ are the power estimates at frequencies i and j at time point t, and σ_i, σ_j are the standard deviations of power estimates at frequencies i and j. This yields values between -1 and 1 indicating perfectly anti-correlated and correlated power fluctuations, respectively, and values of 0 indicating no correlation between frequency-specific processes. In order to approximate normal distributions of data values before taking the mean across epochs for level averages, we applied Fisher's z-transformation[8] and its inverse given by

$$z = \frac{1}{2}\log\left(\frac{1+r}{1-r}\right) \text{ and } r = \frac{e^{2z}-1}{e^{2z}+1},$$

respectively, to correlation coefficients r of each epoch where e is the exponential function.

Figure 2.16 illustrates the motivation for the computation and the outcome of power correlations using example data from a single epoch of striatal LFP data. As panel a shows, power in different frequency bands waxes and wanes over time and also appears to covary temporarily between lower and upper spectral regions. This is also obvious in the band pass-filtered raw data pieces shown in the left plots of panel b which demonstrate the amplitudes of slow and fast rhythmic activities to increase and decrease in unison. Power correlation matrices as depicted in the right plots of panel b provide a quantitative handle on the temporal consistency of the relationships between different frequency components.

[8] `http://en.wikipedia.org/wiki/Fisher_transformation`

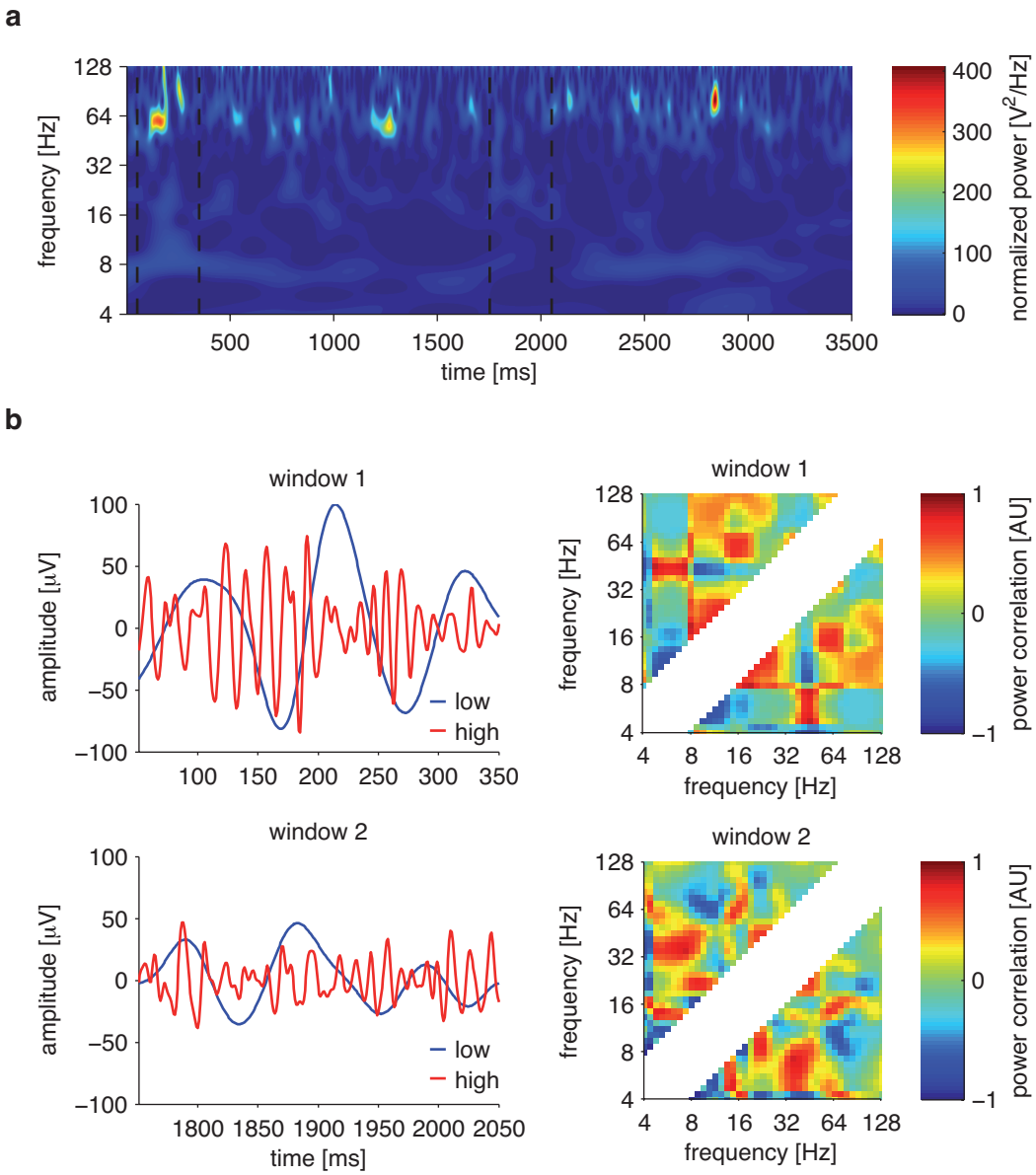

Figure 2.16: Power correlation analysis. (a) High-resolution (interpolated in steps of 1/128 voices) time-frequency spectrum of LFP power on a striatal electrode in a rat during rest. Power in different frequency bands waxes and wanes over time. Black dashed vertical lines delimit two time windows used for analyses in panel b. (b) *Left plots:* Zoom into two time windows of the raw data epoch underlying the spectrum in (a) displaying LFP data band-pass filtered between 4–16 (low, blue) and 32–128 Hz (high, red). Note the oscillatory shape of LFP fluctuations in low and high frequency bands as well as the different sizes and ratios of amplitudes in upper and lower plots. *Right plots:* Color-coded matrices depicting correlations between power values at 41×41 frequencies within the corresponding time windows to the left. For conceptual reasons and illustration purposes, values up to one octave off the main diagonal were whitened.

2.7.3.8 Phase-locking–power intercorrelation analysis

We examined the temporal relationships between frequency-specific fluctuations of phase-locking and power correlation estimates of LFPs by correlating the respective measures within each epoch. Since both parameters are defined only across multiple samples (Sections 2.7.3.4 and 2.7.3.7), we performed sliding window analyses on the time-frequency transformed data ($n = 3500 \times 41$ points) of each epoch. We first calculated phase-locking and power correlation values within windows of 500 ms length and in steps of 50 ms (corresponding to 500 and 50 sampling points, respectively). We then computed correlation coefficients between the respective estimates ($n = 61$ values for each) using the formula in equation (2.10) above (Section 2.7.3.7).

2.7.4 Statistical specifications

As outlined above (Section 2.3), our recording setup included 12 microelectrodes inserted into both hemispheres of the rat brain, with electrodes located in cortex and striatum of either side. We recorded data from $n = 10$ animals that each contributed a highly variable number of trials, yielding 622 recordings (i.e., trials) in total (Table 2.1). One trial of the behavioral task encompassed 1 resting and 4 running levels lasting 1 minute and thus consisting of 12 epochs of 5 seconds length each (Section 2.5).

After preselection of data as described in Section 2.6.1 we were left with a variable number of valid epochs from different animals, electrodes, and recordings from different sessions and thus from partly differing electrode *positions*. Unfortunately, we were not able to accurately verify the coordinates of the latter. We hence decided to pool the parameter averages (behavioral data, firing rates, spectral measures) obtained for individual or pairs of electrodes from resting and running levels of each trial first across trials within individual subjects and then across subjects to yield grand average estimates.

Furthermore, we defined threshold criteria with regards to the minimum number of epochs needed to contribute to a valid level average of an individual recording ($n = 3$) and the number of trials needed to contribute to across-trial averages of individual electrodes or electrodes pairs ($n = 3$). Recordings and electrodes or electrode pairs not fulfilling these criteria were excluded from further analysis. We did so in order to account for the highly variable number of valid epochs and trials each subject contributed to the data pool and in order to guarantee a minimum level of robustness and comparability between data averages obtained for different trials, electrodes, and electrode pairs.

We computed across-epoch and across-level averages as the mean of the respective sample under the assumption of consistent recording conditions during the course of individual trials. In contrast, averages across trials before the final analysis step were

Subject ID	Recordings
a6	115
a7	1
a8	10
a11	100
a12	39
a14	85
a15	37
a16	15
a17	199
a18	21
$n = 10$	$n = 622$

Table 2.1: List of animals implanted and used for recordings under treadmill running, and the number of recordings (i.e., trials) obtained from each individual. The subjects are referred to by means of a unique ID. Note that the mere number of recordings performed may not be representative of the amount of valid data remaining from the respective subject after preselection by means of signal evaluation and data average thresholding.

computed as the median of the respective sample to reduce the possible influence of outliers. Grand averages across all trials from all subjects were again computed as the mean and are shown with one standard error in both positive and negative directions, thereby providing an estimate of the precision of the respective average (Motulsky, 1995).

We expressed the change between rest and running phase-coupling magnitudes (Section 3.6) by taking the mean across median difference z-scores zsc computed for each trial of each electrode pair:

$$zsc = \frac{x_{run} - \langle x_{rest} \rangle}{\frac{\sigma_{rest}}{\sqrt{N}}}.$$

Here, x_{run} denotes the phase-coupling strength during an average single-trial running level, $\langle x_{rest} \rangle$ and σ_{rest} are the mean and standard deviation, respectively, of the phase-coupling strength across all resting levels of an individual electrode pair, and N denotes the number of samples. Z-scores were computed to display both the statistical strength and the sign of the coupling difference between behavioral conditions.

We relied on nonparametric statistical tests (Wilcoxon rank-sum and sign-rank tests) to ensure against possible violations of the assumption of normally distributed data. Bar plots that depict comparisons of different samples of measured values show the final average as the median with one unit of median absolute deviation.[9] The latter provides

[9] `http://en.wikipedia.org/wiki/Median_absolute_deviation`

an estimate of the median scatter of data values around the median of the sample. The reason for this is that the ensuing statistical tests are based on ranks of values and hence rely on the median rather than the mean as a measure of the average of the data scatter.

We computed regression coefficients (Spearman's ρ) to test for a significant linear scaling of multi-unit firing rates and spectral peak parameters (peak magnitudes and peak frequencies) with running speed. Throughout the study, we generally assumed a significance level of $\alpha = 0.01$ for all test statistical procedures. In all computations necessitating multiple tests and not involving permutation statistics (see below), Bonferroni-correction was used to adjust α-levels to the number n of tests (Motulsky, 1995), according to

$$\alpha = \frac{0.01}{n}.$$

We tested the statistical significance of spectral estimates by means of comparisons of measured values with those obtained from alternative distributions (Figure 2.17). For raw values of bivariate parameters (coherency, phase, power correlation, phase-amplitude coupling estimates), alternative distributions were obtained by circularly shifting the values of the complex time-frequency transformation matrices (3500 time points×41 frequencies; Section 2.7.3.2) of one of the two partners by step size s, where s could be any number randomly drawn from the set of integers $I = \{1, 2, ..., 3500\}$. Since all of the above parameters in essence quantify the consistency of amplitude or phase relationships between paired signals, destroying the original temporal relationship while preserving their individual temporal structures should yield magnitudes of coupling estimates that are, on average, only as large or even smaller than those obtained from the original data. To save computation time, we calculated one estimate of the parameter of interest from both real and time-shifted data of each epoch. We then averaged shifted and real values in exactly the same way to obtain level, trial, and electrode pair averages.

For relative estimates (i.e., ratio and difference spectra) of both univariate (i.e., power) and bivariate spectral parameters (see above), we compared the original data with those obtained through averaging of alternative partitions created by randomly permuting the level memberships of data epochs. This approach was based on the assumption that if there was no difference between the distributions of spectral values during both major behavioral states (rest and running), ratio and difference values calculated from rest and running spectra obtained through averaging of correctly labeled epochs should not be significantly different from those obtained through averaging of randomized epochs. To account for different amounts of valid rest and running epochs present in each trial ($n = 12$ and $n = 48$, respectively, at maximum), we stratified their respective numbers to equal half the number of valid epochs of a given level and a given trial. For each level, we

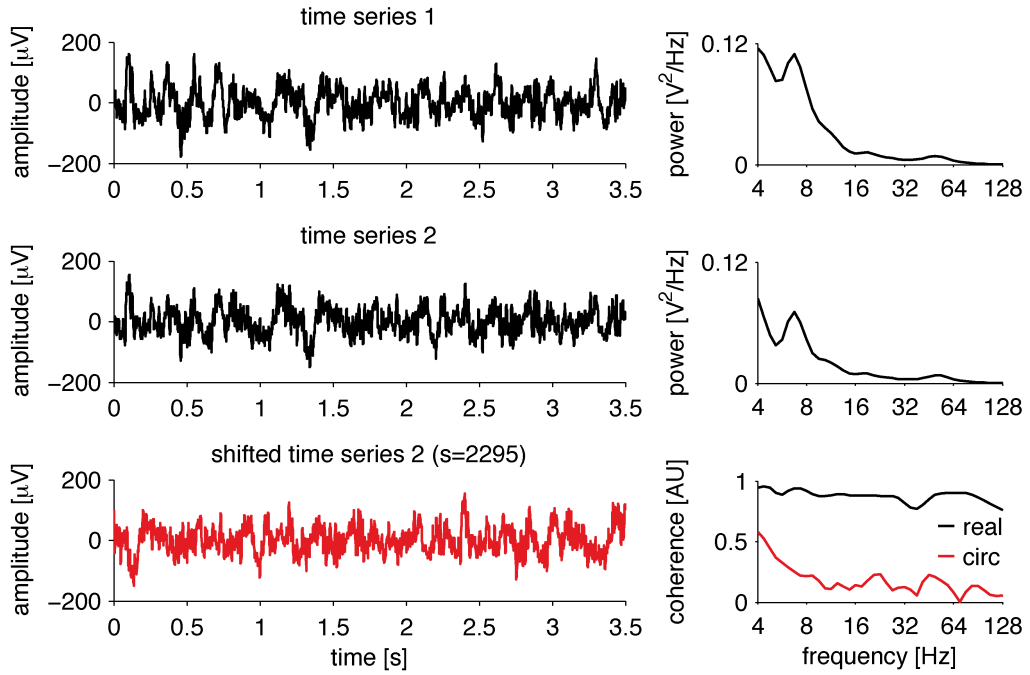

Figure 2.17: Illustration of the principle idea behind time series shift-based statistics. The upper two left and right plots display different raw striatal LFP time series from a resting rat and the corresponding power spectra, respectively. The lower left plot shows the second time series circularly shifted by a step size s of 2295 points (see main text). The lower right plot demonstrates the effect of the temporal shift on the phase-coupling strength. While coherence is high between the two LFP signals which exhibit very similar frequency content and comparable temporal structure, the consistent phase relationship is largely destroyed after rotation of the second time series. Note that the power spectrum of the shifted time series is exactly the same as for the measured values, which is why we do not depict it here. We statistically compared the resulting grand average real and shift-based bivariate estimates by means of nonparametric tests in each frequency bin.

calculated $n = 10$ alternative partitions from rest and running epochs and then obtained average alternative distributions by taking their mean. This was done to increase the reliability of estimates based on highly limited numbers of epochs ($n = 12$ at maximum for each level). Averaging across levels, trials, and electrodes or electrode pairs was then again performed in exactly the same way for both real and permuted relative spectra. For modified versions of permutation based statistics in case of some parameters (e.g., cross-hemispheric LFP phase-coupling), see the respective results section (Chapter 3).

We tested the statistical significance of the spectral parameters of interest through non-parametric, paired comparisons (Wilcoxon sign-rank test) of real and shifted or permuted averages obtained for each electrode or electrode pair individually at each frequency, frequency pair (in case of power correlation and phase-amplitude coupling estimates), or

frequency-phase bin pair (in case of phase histograms) of interest. These comparisons are tests of the null hypothesis of no difference between the medians of grand average distributions of spectral values obtained from real and time-shifted or permuted data, respectively. We again assumed a general significance level of $\alpha = 0.01$ for individual tests taking shifting and permutation procedures to function as implicit controls of the false discovery rate and thus to account for the problem of multiple comparisons to be performed on large numbers of spectral values ($n = 41$ for one- and $n = 41 \times 41$ or $n = 61 \times 41$ for two-dimensional estimates, respectively). For a general introduction into permutation statistics, see Ernst, 2004. For applications of related methods in systems neuroscience research, see Maris and Oostenveld, 2007 and Maris et al., 2007.

2.8 Computational implementation

This document was written and typeset using LaTeX with TeXShop (version 2.43). Figures were modified or created using Adobe® Illustrator® CS5.

We used the MATLAB® programming environment for all steps of data analysis in this study. A large number of custom-made scripts and functions was written for that purpose. In addition, we used parts of functions implemented in the Fieldtrip[10] (Oostenveld et al., 2011) and Wave_clus[11] (Quiroga et al., 2004) toolboxes for frequency analysis and spike amplitude thresholding steps, respectively. Data were processed either locally on Apple Macintosh® computers and PCs or were distributed on a Linux-cluster to save computation time.

[10] `http://fieldtrip.fcdonders.nl/start`
[11] `http://www.vis.caltech.edu/~rodri/Wave_clus/Wave_clus_home.htm`

3 Results

3.1 Behavior

Behavioral data epochs corresponded to those used for signal analysis (Section 2.5). We assessed treadmill running performance during recordings with a focus on two major aspects: first, average error rates on the different speed levels, of both individual subjects and across animals. Second, error rates during individual epochs, particularly those immediately prior to and following speed changes between levels.

Panel a of Figure 3.1 depicts the mean error rates of individual subjects on each speed level. The large variability of performances as well as the patterns of level scores differing between animals are readily visible, with a marked overall decrease in average performances between earlier (a6) and later (a18) subjects. Note that, as is indicated also in Table 2.1 (Section 2.7.4, page 59), different animals contributed highly variable numbers of trials to the data pool. Also, not every animal accomplished each protocol.

Panel b of Figure 3.1 summarizes the performances of individual rats on different speed levels of different protocols that overlapped in their speed ranges. We observed the very same performance trends as in the behavioral pilot study (von Nicolai, 2011) considering an overall decline of error rates with increasing running speed both within and across protocols. However, this effect was not as distinct as it generally was prior to implantation (von Nicolai, 2011), particularly during protocol no. 3.

As is shown in panel c of Figure 3.1, the overall trend of performance increase with running speed is also reflected in the detailed grand averages computed for individual epochs of the different protocols. Further, these plots demonstrate that performances fluctuated moderately between subsequent epochs of each protocol. Most remarkably, error rates were almost always increased during post- as compared to pre-speed change epochs. However, pairwise comparisons of all pre- and post-speed change epochs at a very conservative, Bonferroni-corrected α-level of 0.001 ($\alpha = 0.01$ corrected for $n = 9$ comparisons) showed that none of these differences was statistically significant (paired, two-sided Wilcoxon sign-rank tests for pre- vs. post-speed change epochs no. 1, 2, and 3 of protocols no. 1, 2, and 3: $p = 0.218, 0.437, 0.005$, $n = 214$ trials; $p = 0.405, 0.096, 0.216$, $n = 161$ trials; and $p = 0.423, 1.000, 0.071$, $n = 247$ trials, respectively).

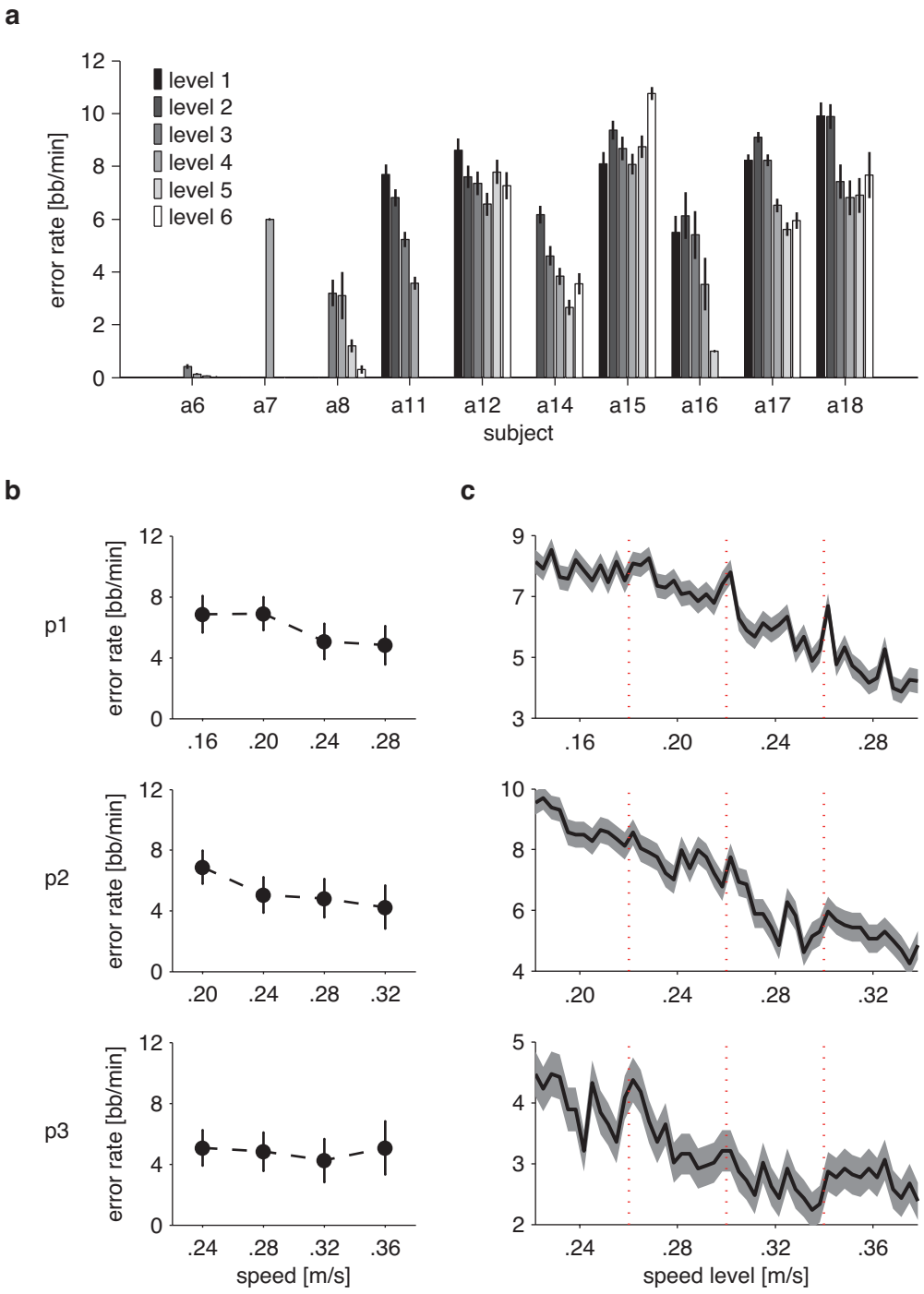

Figure 3.1: Behavioral performance during recordings. (a) Average error rates of individual subjects on different speed levels (mean±sem). (b) Grand across-subject average error rates on different speed levels of three protocols (mean±sd). (c) Grand across-trial average error rates during all epochs ($n = 12$), levels and protocols. Red dotted lines mark transition points between levels. *Abbreviations:* p1, p2, p3: protocols no. 1, 2, 3.

3.2 Firing rates

We computed average firing rates from spike trains recorded in cortex and striatum in order to quantify the effects of behavioral state on overall levels of multi-unit activities in both structures. We first calculated firing rates of individual epochs, averaged these values across epochs of each level and each trial and then across trials of each electrode. Finally, we pooled the data across electrodes from all subjects to obtain the grand average.

Panel a of Figure 3.2 depicts the mean firing rates of cortical and striatal multi-units during rest and on all running levels (left plot) as well as the statistical comparison of median rest vs. average running level activities (right plot). Grand average firing rates increased markedly between the two behavioral states. These changes were statistically significant in both structures (two-sided Wilcoxon rank-sum test; $p < 0.005$, Bonferroni-corrected for $n = 2$ comparisons; $n = 48$ cortical and $n = 48$ striatal electrodes).

The left plot of panel a further indicates a steady increase of grand average firing rates in cortex with increasing running speed. In striatum, firing rates remained relatively stable across all running levels and even decreased slightly on average from the first to the last level. We statistically quantified these findings by means of linear regression analyses on the data from both structures. As the plots in panel b of Figure 3.2 show, firing rates exhibited a trend for a linear increase with running speed in cortex ($r = 0.215$, $p = 0.024$) although this trend was not quite statistically significant. In contrast, striatal firing rates did not scale linearly with running speed ($r = 0.093$, $p = 0.374$).

While the above results suggest a modulation of firing rates not only by behavioral state but also, at least in cortex, by running speed, they have to be interpreted with some caution. We did indeed observe a marked increase of unit activities between both behavioral states in virtually every subject investigated and hence, the grand average results are very robust. However, as the large error bars in the plots of panel b indicate, the variability of firing rates and their development with running speed were pretty substantial between subjects. Also, the discrepancy between mean and median rates shown in left and rights plots, respectively, of panel a further indicates the presence of some outliers in the data pool. Nevertheless, in 4–5 out of 8 animals that contributed valid data, we observed an increase of cortical and striatal firing rates with increasing running speed. Firing rate modulations in striatum were generally less pronounced and more variable than those in cortex. For a more detailed discussion of overall multi-unit data quality and the constraints on its interpretability, see Section 4.1.5.

In summary, these results provide evidence for a robust change of spiking activity in cortex and striatum with overall behavioral state. Further, they also indicate a modulation at least of cortical but less likely of striatal firing rates by motor demand.

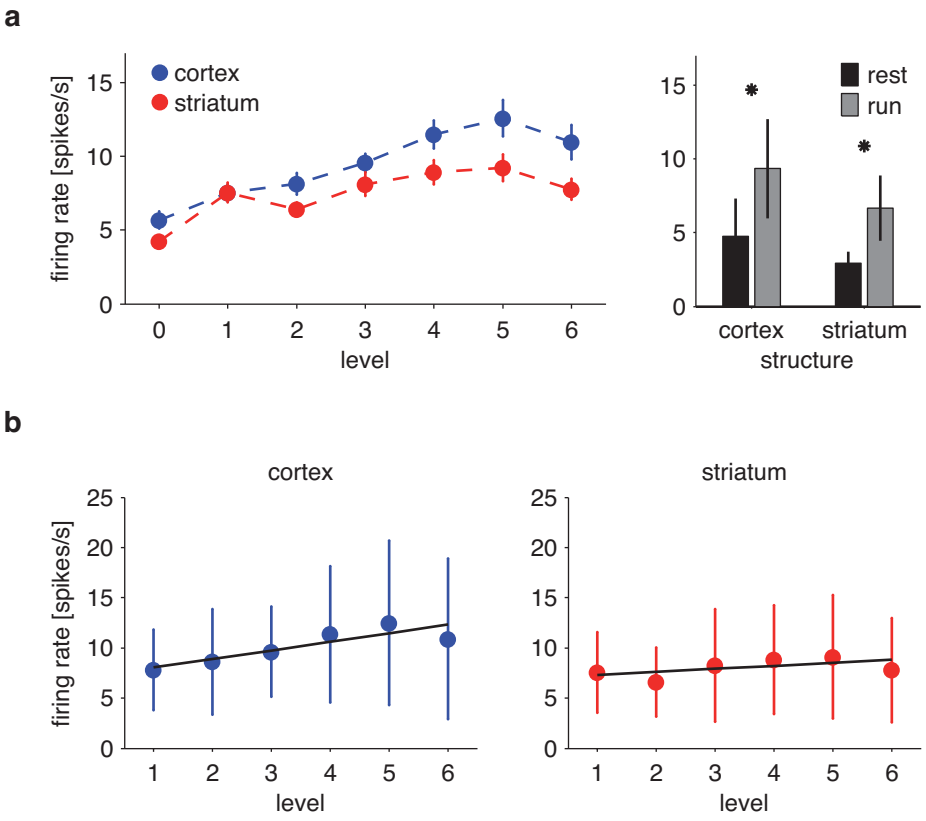

Figure 3.2: Multi-unit firing rates. (a) Left: Firing rates in cortex and striatum during rest and on all running levels (mean±sem). Right: Comparison of rest and average running level activities (median±mad). Black stars (*) above differently shaded bars denote significance. (b) Linear regression analyses on the development of firing rates in cortex and striatum during running at increasing speeds (mean±sd).

3.3 Power

We examined the frequency-specific characteristics of local neuronal population activities during both behavioral states by calculating raw and percentage power spectra from the signals recorded on each electrode. Power was computed from time-frequency transformed data of every single epoch of both monopolar and bipolar LFPs as well as MUAs. Spectra were averaged across valid epochs of each level to obtain estimates of the mean power during rest and all running levels of a given trial. For a basic comparison of resting with running activities, we computed power spectra at 41 frequencies between 4 and 128 Hz and averaged across running levels ignoring differences in running speed. For examinations of specific power characteristics, spectra were computed at more frequencies within smaller ranges and data from different running levels were retained (Section 3.9).

3.3.1 Power: Local Field Potentials

3.3.1.1 Raw LFP power

LFP power spectra were normalized prior to level-based statistical analyses through multiplication of power with the square of frequency values to account for the approximately $1/f^2$ decay of spectral power (Miller et al., 2009; Siegel et al., 2009).[1] Note, however, that the qualitative findings described in this section are not artifacts of the normalization procedure *per se* which is performed at this point for illustration purposes only. We obtained the same qualitative results when computing purely raw spectra.

Grand average raw, normalized power spectra of monopolar LFPs as shown in panel a of Figure 3.3 display three prominent features. First, power increases considerably between rest and running, with absolute values being largely comparable between structures during both behavioral states. Second, all spectra exhibit two localized peaks, one of them situated in lower and the other one situated in higher frequency ranges. Third, both low- and high-frequency peaks shift from below to around 8 and 64 Hz, respectively, between resting and running states.

We explicitly quantified the change in spectral power between behavioral conditions by computing the relative power taking resting as a baseline for running activities. For each trial, we divided the power values at each frequency of the level-average running spectrum by the corresponding values of the resting spectrum. We then performed statistical tests of the null hypothesis of no difference between resting and running power separately for the data in each frequency bin by comparing the respective values pooled across all electrodes against those of alternative distributions obtained through random assignment of epoch labels (Section 2.7.4). Panel b of Figure 3.3 shows the grand average relative power spectra of cortical and striatal monopolar LFPs. A strong increase of power is obvious across almost the entire spectrum in both structures which is largest in terms of magnitude and variability in lower regions where also distinct peaks below and above 8 Hz can be observed. The increase of raw power is smaller in intermediate regions reaching its lowest values around the resting high peak-frequency. After that, power increases again and reaches a plateau beyond the running high peak-frequency (cf. panel a of Figure 3.3). These changes of spectral power are statistically significant in both structures and across the whole frequency range investigated (paired, two-sided Wilcoxon sign-rank tests, $p < 0.01$; $n = 24$ and $n = 30$ cortical and striatal electrodes, respectively).

Panel c of Figure 3.3 depicts the grand average power spectra computed from bipolar derivations of cortical and striatal LFPs (Section 2.6.2.2). As in the case of monopolar

[1] Note that power is still given in units of V^2/Hz but referred to as 'normalized power' where appropriate.

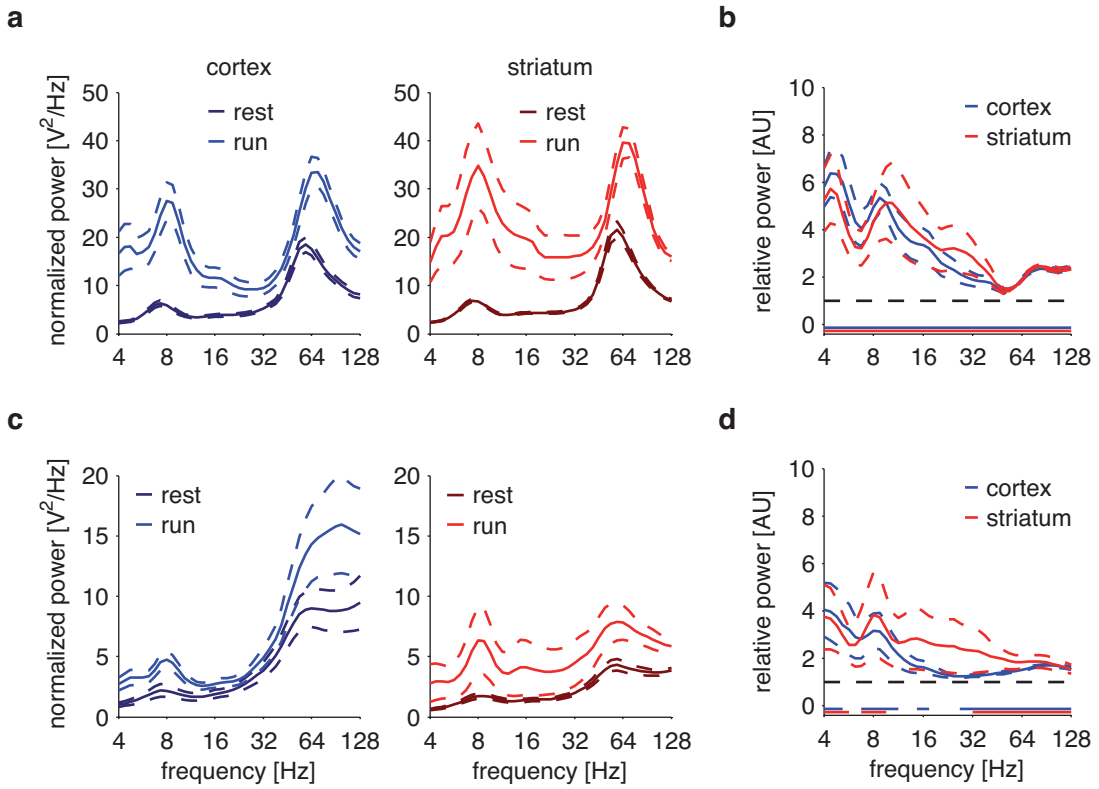

Figure 3.3: Grand average raw LFP power. (a) Monopolar LFPs: raw, normalized power. (b) Monopolar LFPs: relative, normalized power. (c) Bipolar LFPs: raw, normalized power. (d) Bipolar LFPs: relative, normalized power. Results are given as mean±sem. Black dashed lines in panels b and d indicate no change. Colored bottom lines denote significance.

LFPs, bipolar spectra all exhibit a bimodal distribution of power between lower and higher frequency ranges. Second, power mostly increases between resting and running states and most prominently so at lower frequencies. Third, a small, positive shift of low peak frequencies can be observed in both cortex and striatum between behavioral states. However, absolute power values in both structures are smaller in the bipolar as compared to the monopolar spectra, and power changes between rest and running are also markedly reduced. In addition, power is more broadly distributed in the high frequency range. As a result, either no or far less prominent high-frequency peaks are present in bipolar spectra as compared to monopolar ones, with no obvious shifts of peak frequencies between resting and running states. Also, in most of the spectra from single subjects peak frequencies were found to be different from their monopolar counterparts and they were more diverse in terms of exact location, overall shape, and magnitude of

shift. We note here, however, that we did indeed also observe high-frequency peaks and associated shifts in some within-subject average power spectra from both structures.

Panel d of Figure 3.3 depicts the grand average relative power spectra of bipolar LFPs. Overall, they exhibit similar qualitative characteristics as their monopolar counterparts. Note, however, the smaller absolute values of bipolar as compared to monopolar relative LFP power in both structures and the larger variability in mid-frequency regions of striatal spectra. Still, power changes in both low and high peak-frequency ranges as defined based on monopolar raw spectra were found to be statistically significant in the bipolar case as well (paired, two-sided Wilcoxon sign-rank tests, $p < 0.01$; $n = 12$ and $n = 22$ cortical and striatal bipolar electrodes, respectively).

3.3.1.2 Percentage LFP power

In view of the marked, spectrum-wide increase of raw power between rest and running we aimed to determine the relative contributions of power components from different frequency ranges to the total amount of power in the whole spectrum during both behavioral states. To this end, we divided each individual power value of the frequency-normalized spectra of each level by the sum of all values of the respective spectrum. This is a common approach in spectral analysis of neuronal signals and yields a representation of power in each frequency bin expressed as percentage of total power in the whole spectrum.

Figure 3.4 depicts the grand averages of percentage power of monopolar (panel a) and bipolar (panel c) cortical and striatal LFPs. Some of the major findings described in the previous section (3.3.1.1) are present here as well, including a bimodal distribution of fractions of power between upper and lower parts of the spectra as well as a shift of peak frequencies between rest and running in both low and high frequency ranges. Remarkably, percentage power values in the different parts of the spectra are practically equal between the two structures during rest. Note, however, that the fraction of high-frequency power during running is larger in striatum as compared to cortex.

Changes of percentage power between behavioral states are again quantified explicitly in relative power spectra shown in panels b (monopolar LFPs) and d (bipolar LFPs) of Figure 3.3.1.2. Fractions of monopolar power increase between rest and running almost exclusively in the lowest frequency range between 4 and 16 Hz while they are diminished from above that point up to about 64 Hz and largely unaltered from there up to the end of the spectra, as is also confirmed by the results of corresponding statistical tests (paired, two-sided Wilcoxon sign-rank tests, $p < 0.01$; $n = 24$ and $n = 30$ cortical and striatal electrodes, respectively). In contrast, percentage bipolar power values change in a statistically significant fashion only in terms of a decrease between 16 and 32 Hz in

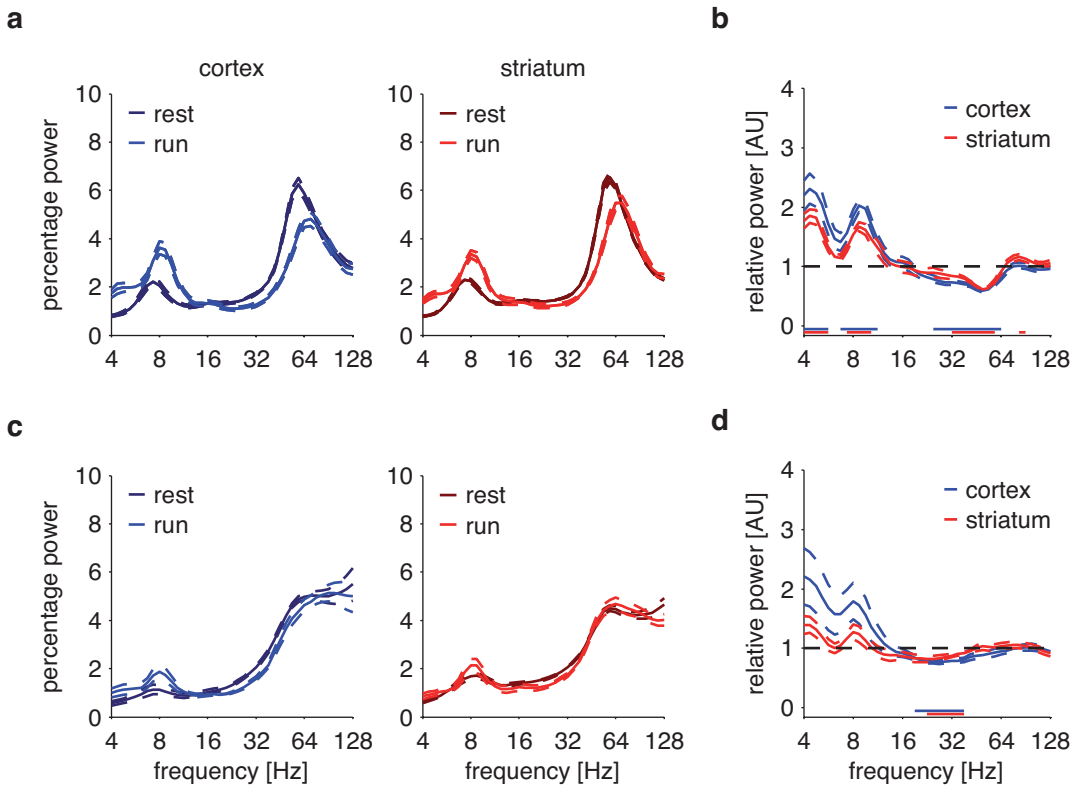

Figure 3.4: Grand average percentage LFP power. (a) Monopolar LFPs: raw, percentage normalized power. (b) Monopolar LFPs: relative, percentage normalized power. (c) Bipolar LFPs: raw, percentage normalized power. (d) Bipolar LFPs: relative, percentage normalized power. Results are given as mean±sem. Black dashed lines in panels b and d indicate no change. Colored bottom lines denote significance.

both cortex and striatum (paired, two-sided Wilcoxon sign-rank tests, $p < 0.01$; $n = 12$ and $n = 22$ cortical and striatal bipolar electrodes, respectively).

We obtained valid monopolar LFP data from both structures and both behavioral states in 7 out of 10 animals initially implanted and valid data from the striatum of another subject. Grand average results presented here and above (Section 3.3.1.1) were highly consistent across animals. In the case of raw LFP power, with the exception of 2 cortical and 3 striatal within-subject averages all spectra unambiguously exhibited all three of the above described characteristics. In the others, low-frequency peaks and their shifts were variable or hardly present at all. In contrast, high-frequency peaks were much more robust and could be observed in all cortical and all striatal spectra during rest as well as in all striatal and all but one cortical spectrum during running, which holds also true for their shifts. In the case of percentage power spectra, within- or between-trial

fluctuations of power are more readily leveled out through normalization, rendering some qualitative findings even more distinct in certain subjects.

3.3.2 Power: Multi-Unit Activities (MUA)

3.3.2.1 Raw MUA power

We computed power spectra of multi-unit activities following the creation of spiking vectors from thresholded signals (Section 2.6.3) in the same way as described for LFPs. Panel a of Figure 3.5 shows the grand average raw cortical and striatal MUA power spectra from both behavioral states. Absolute power values here are much lower than in

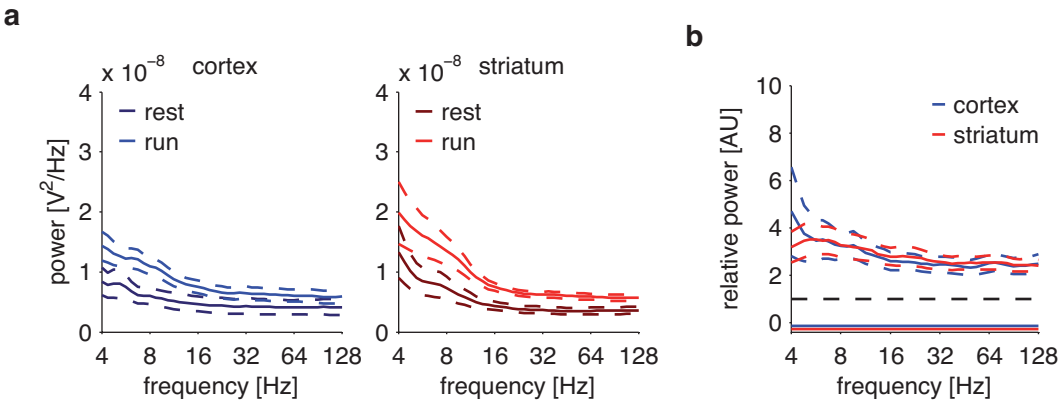

Figure 3.5: Grand average raw MUA power. (a) Raw power. (b) Relative power. Results are given as mean±sem. Black dashed lines in panel b indicate no change. Colored bottom lines denote significance.

the case of LFPs which results from the fact that the underlying signals are composed solely of zeros and ones, with a massive bias towards the former. As in the case of LFPs, most MUA power is basically concentrated in lower regions of the spectra not normalized by frequency, and it first decays with increasing frequency and then flattens out from a point around 16 Hz. In glaring contrast to the LFP results, however, there are hardly any characteristic peaks in cortical and striatal power spectra, besides very small bumps below and around 8 Hz in both structures and in running spectra in particular. Owing partly to their evanescent character, no clear shift of peak frequencies can be observed in this range between behavioral states. Note that we obtained the same results when we multiplied the raw power with the square of the frequency values as we did in case of LFPs (Sections 3.3.1.1–3.3.1.2), which is why we do not show normalized spectra here.

As the raw spectra in panel a and the relative spectra shown in panel b of Figure 3.5 demonstrate, MUA power increases between rest and running in a statistically significant

fashion across the whole spectrum in both structures (paired, two-sided Wilcoxon sign-rank tests, $p < 0.01$; $n = 20$ and $n = 31$ cortical and striatal electrodes, respectively). Moreover, cortical and striatal spectra exhibit almost identical distributions of relative power values, although the latter are of a more bump-like shape in low spectral regions. In general, raw and percentage MUA power results as described in the next section (3.3.2.2) were more variable within and between individual subjects than their LFP counterparts. As stated above (Section 3.2) and repeatedly below, this was another reason why we did not consider any MUA data for more detailed spectral analyses.

3.3.2.2 Percentage MUA power

We computed percentage MUA power spectra in the same way as described above for LFPs (Section 3.3.1.2). The results depicted in panel a of Figure 3.6 demonstrate that qualitatively, percentage power values in both states are distributed in a fashion largely similar to their raw counterparts. However, note that the bumps located below and around 8 Hz described above are more clearly visible in percentage as compared to raw MUA power plots (cf. Figure 3.5, page 72), most probably due to normalization effects.

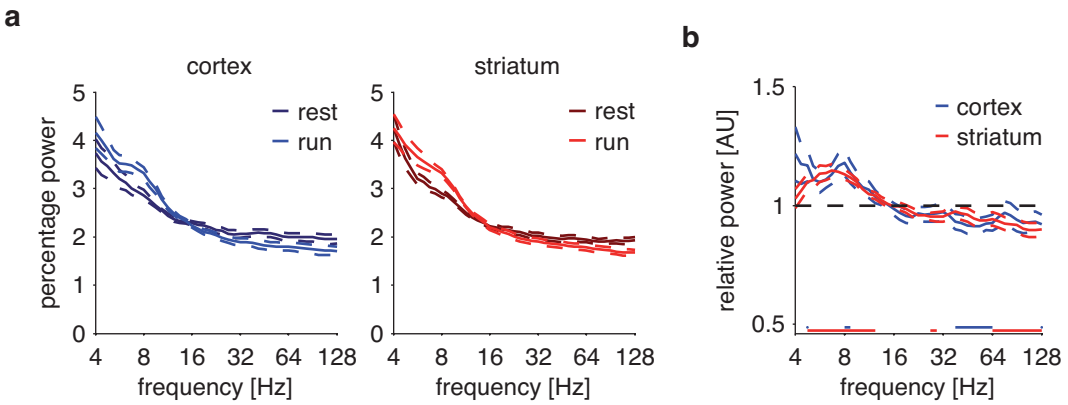

Figure 3.6: Grand average percentage MUA power. (a) Percentage power. (b) Relative, percentage power. Results are given as mean±sem. Black dashed lines in panel b indicate no change. Colored bottom lines denote significance.

Similar to the case of LFPs (Section 3.3.1.2), percentage MUA power values increase from 4 up to about 16 Hz only where they fall below resting levels and remain decreased until the upper ends of the spectra. As panel b of Figure 3.6 demonstrates, percentage MUA power changes are statistically significant within limited parts of the spectra only, most consistently so in striatal low and high frequency ranges (paired, two-sided Wilcoxon sign-rank tests, $p < 0.01$; $n = 20$ and $n = 31$ cortical and striatal electrodes, respectively).

3.4 Coherency

We examined frequency-specific interactions between local neuronal population activities in terms of their phase-coupling first by means of coherency estimates calculated between pairs of electrodes during single epochs of individual trials. Coherency spectra were obtained separately for both only LFPs and only MUAs as well as for combinations of the two signal types. One or both of their real-valued derivatives, i.e., *ordinary* coherence (coherency magnitude, also simply termed *coherence* in the following) and *imaginary* coherence values, were then computed from the complex coherency estimates depending on the kind of signal (LFP, MUA) or signal combination (LFP-MUA) under investigation.

We considered three types of *structure pairings*, i.e., cortico-cortical, cortico-striatal, and striato-striatal electrode pairs for statistical analyses, yielding estimates of coherencies both within and between the respective structures. As for power estimates, average coherency spectra of individual levels were obtained by taking the mean across the respective valid epochs. We averaged the data from all running levels again for a grand comparison of resting and running activities as presented in this section. They were later considered individually for an examination of running speed-related coherency effects (Section 3.9). Significance tests of raw coherence values were performed by comparing measured with time shift-based spectra. Coherence differences were evaluated by comparing measured estimates pooled across electrode pairs against alternative distributions obtained through random assignment of epoch or hemisphere labels (Section 2.7.4).

3.4.1 Coherency: Local Field Potentials (LFP)

3.4.1.1 Ordinary LFP coherence

Panel a of Figure 3.7 depicts grand average ordinary coherence spectra of monopolar LFPs. Spectral characteristics are very similar among all structure pairings and between behavioral states. First, coherence values are generally rather high and statistically significant (paired, two-sided Wilcoxon sign-rank tests, $p < 0.01$; $n = 33$, $n = 107$, and $n = 57$ cortico-cortical, cortico-striatal, and striato-striatal electrode pairs, respectively). However, they are considerably larger in absolute terms in lower as compared to higher frequency ranges. Second, they mostly either increase or remain unchanged between rest and running. Third, during both behavioral states, all spectra exhibit a roughly bimodal distribution of coherence values with local minima between two prominent peaks. Fourth, in all structure pairings these peaks shift from below to around 8 and 64 Hz, respectively, between rest and running. Thus, ordinary monopolar LFP coherence results qualitatively match some of the major characteristics of corresponding power estimates.

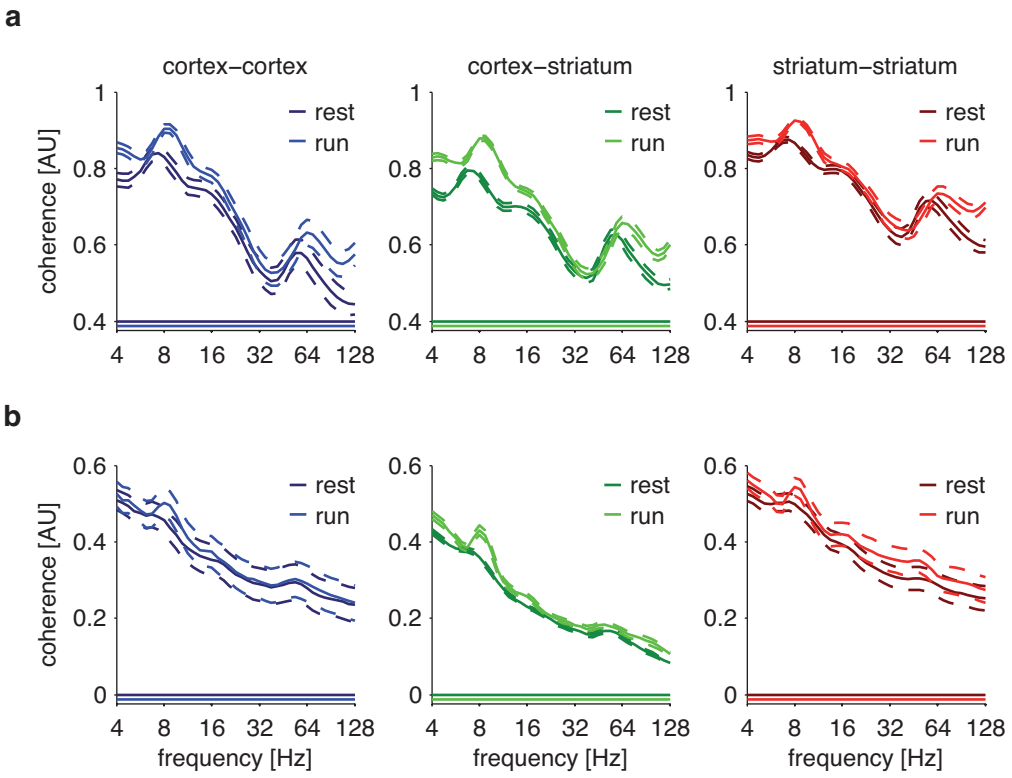

Figure 3.7: Grand average ordinary LFP coherence. (a) Monopolar LFPs. (b) Bipolar LFPs. Results are given as mean±sem. Colored bottom lines denote significance.

We quantified the change in coherence between behavioral conditions by computing the difference between resting and average running level spectra of each trial. We then performed statistical tests of the null hypothesis of no difference between behavioral states as described above. The spectra shown in panel a of Figure 3.8 show an almost exclusive increase of coherence between rest and running. Note, in particular, the narrow peak of significant coherence increase centered above the running low peak-frequency of 8 Hz and the localized decrease of cortico-striatal and striato-striatal coherence around the point of the resting high peak-frequency. Furthermore, coherence increases strongly from below the running high peak-frequency of 64 and up until 128 Hz. Another low coherence difference peak is located slightly above 4 Hz in all structure pairings.

We obtained valid monopolar LFP coherency data from 7 out of 10 subjects implanted, and from 5, 6, and 6 subjects from cortico-cortical, cortico-striatal, and striato-striatal structure pairings, respectively. We observed a bimodal distribution of values and a shift of high peak frequencies in all their ordinary coherence spectra. Those spectra with distinct low-frequency peaks also exhibited typical shifts between behavioral states. Coherence differences varied to some degree but showed consistent trends across subjects.

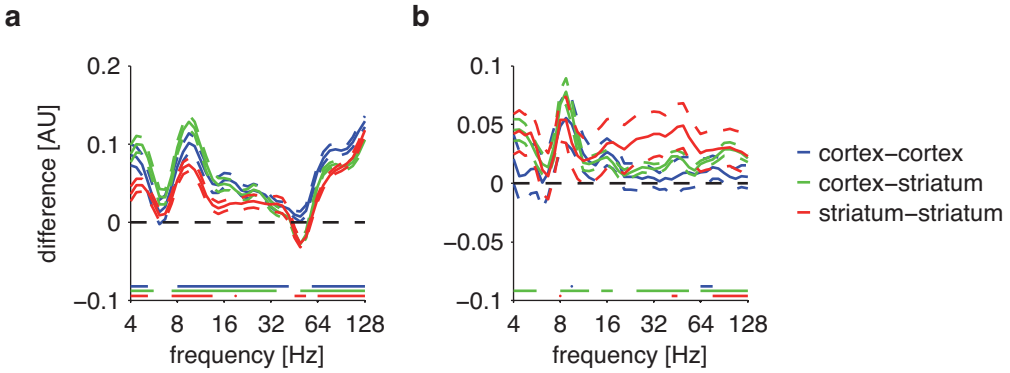

Figure 3.8: Grand average ordinary LFP coherence difference. (a) Monopolar LFPs. (b) Bipolar LFPs. Results are given as mean±sem. Black dashed lines indicate no change. Colored bottom lines denote significance.

We extended the above examination of bipolar power spectra (Section 3.3.1) to corresponding coherency estimates computed between the same bipolar derivations of LFP signals. A maximum of three bipolar electrodes per structure and hemisphere could be used to form pairs for analyses. Grand average ordinary coherence spectra of bipolar LFPs are shown in panel b of Figure 3.7. As for the strengths of bipolar power estimates (cf. Figure 3.3, page 69), coherence values are only about half their monopolar counterparts (cf. Figure 3.7, panel a). Still, they are statistically significant across almost the entire spectrum in all structure pairings (paired, two-sided Wilcoxon sign-rank tests, $p < 0.01$; $n = 28$, $n = 99$, and $n = 53$ cortico-cortical, cortico-striatal, and striato-striatal bipolar electrode pairs, respectively). Remarkably, bipolar coherences of within-structure cortico-cortical and striato-striatal pairings appear to be even more similar between behavioral conditions than monopolar ones. Further, while bipolar coherences are clearly stronger again in the lower as compared to the higher regions of the spectra, distributions of values are not as distinctly bimodal as in monopolar cases. In line with this, resting high-frequency maxima as observed in the latter are only present as faint and broadly based bumps or elevations arising below to above 64 Hz rather than as sharp and truly localized peaks centered at that frequency. In contrast, low-frequency coherence maxima and corresponding peak shifts as observed in monopolar LFPs are preserved in all and are most distinct in cortico-striatal bipolar electrode pairs.

We quantified bipolar coherence changes between rest and running by means of difference spectra as shown in panel b of Figure 3.8. Note the statistically significant increase of coherence between cortico-striatal bipolar electrodes across large parts of the spectrum. Further, all spectra exhibit well-localized low difference peaks. These changes are again significant mainly between cortico-striatal bipolar electrodes.

3.4.1.2 Imaginary LFP coherence

We extracted the imaginary parts of coherency estimates in order to quantify the strength of frequency-specific coupling of LFP signals at non-zero phase. The plots in panel a of Figure 3.9 reveal striking differences between grand average imaginary coherence spectra of within- vs. between-structure pairings of monopolar LFPs. The former are essentially flat with values fluctuating closely around zero. In contrast, the latter exhibit both considerably larger absolute values across almost the entire frequency range and distinct, well-localized low-frequency peaks that shift between behavioral states. Moreover, these peaks are situated at the same points on the frequency axis as in ordinary monopolar coherence spectra (cf. Figure 3.7, page 75). Most strikingly, imaginary coherence values are positive and statistically significant between cortico-striatal pairings at frequencies below 32 Hz but increasingly negative and again significant at frequencies above 32 Hz, indicating different temporal dynamics of the underlying processes (paired, two-sided Wilcoxon sign-rank tests, $p < 0.01$; $n = 33$, $n = 107$, and $n = 57$ cortico-cortical, cortico-striatal, and striato-striatal electrode pairs, respectively).

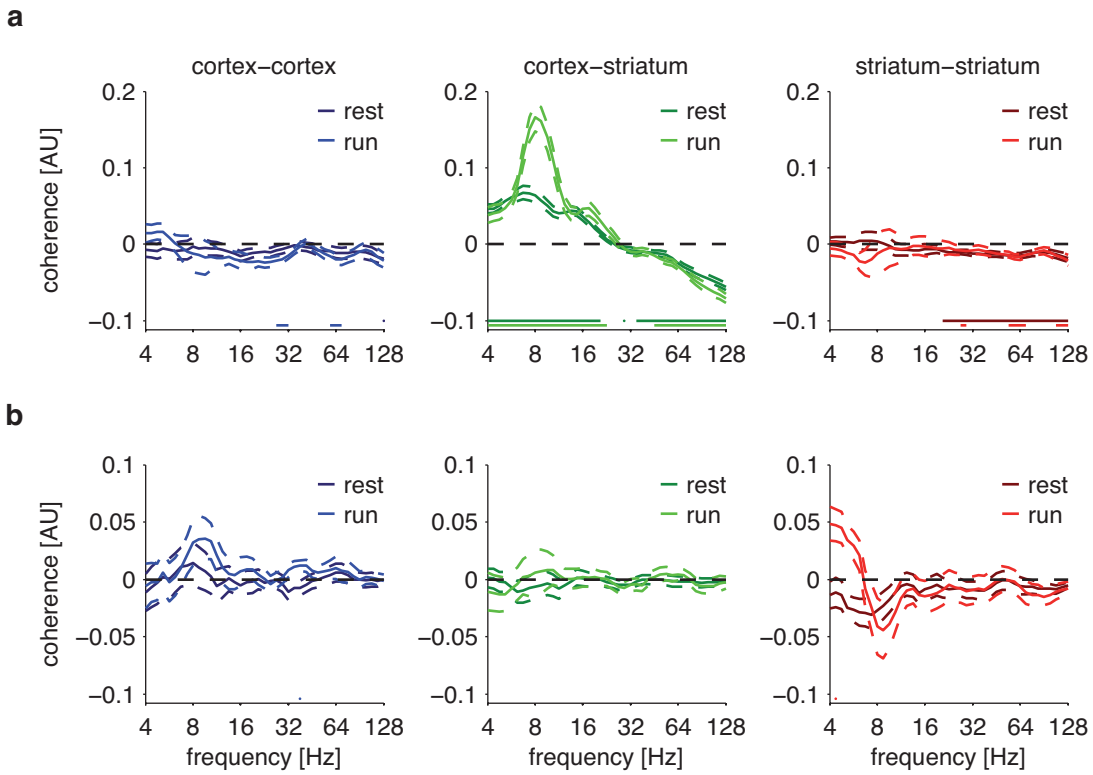

Figure 3.9: Grand average imaginary LFP coherence. (a) Monopolar LFPs. (b) Bipolar LFPs. Results are given as mean±sem. Colored bottom lines denote significance.

As panel a of Figure 3.10 shows, imaginary coherence difference spectra of within-structure monopolar LFP pairings exhibit non-significant values very close to zero across almost the entire frequency range. In contrast, the cortico-striatal spectrum exhibits sharp peaks centered on 8 Hz, a little bump centered on 16 Hz, and a small but nonetheless significant, broad-band decrease of imaginary coherence between 64 and 128 Hz.

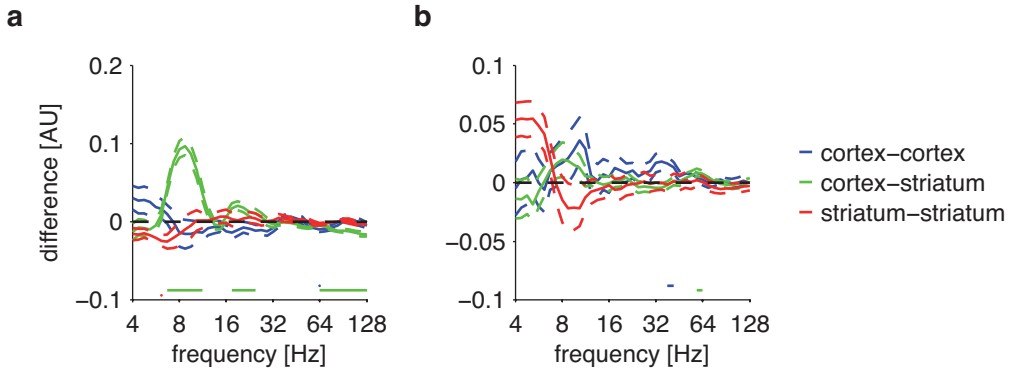

Figure 3.10: Grand average imaginary LFP coherence difference. (a) Monopolar LFPs. (b) Bipolar LFPs. Results are given as mean±sem. Black dashed lines indicate no change. Colored bottom lines denote significance.

Panel b of Figure 3.9 depicts the grand average imaginary coherence spectra of bipolar LFP signals. Apart from very few and small non-zero modulations in within-structure pairings, imaginary coherence values are mostly close to zero and non-significant. As panel b of Figure 3.10 demonstrates, imaginary coherence between bipolar LFPs hardly changes in a consistent manner between rest and running. Note, however, the small but significant increase in coherence between cortico-striatal bipolar electrodes slightly above 64 Hz (paired, two-sided Wilcoxon sign-rank tests, $p < 0.01$; $n = 28$, $n = 99$, and $n = 53$ cortico-cortical, cortico-striatal, and striato-striatal bipolar electrode pairs, respectively).

3.4.2 Coherency: Multi-Unit Activities (MUA)

Figure 3.11 depicts grand average MUA coherence spectra. Values are statistically significant and largely similar in all structure pairings (paired, two-sided Wilcoxon sign-rank tests, $p < 0.01$; $n = 21$, $n = 85$, and $n = 60$ cortico-cortical, cortico-striatal, and striato-striatal electrode pairs, respectively). They are highest during both behavioral states in lower spectral regions with a consistent decay towards higher frequencies. Coherences are lower than those of monopolar LFPs (cf. Figure 3.7, page 75), and there are no localized resting and no high-frequency peaks during running. Still, note the small but distinct and confined bumps of coherence increase centered on 8 Hz in all running spectra.

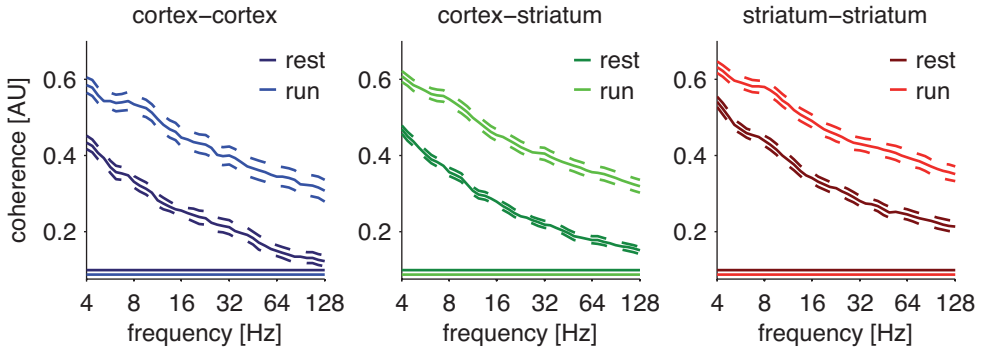

Figure 3.11: Grand average MUA coherence. Results are given as mean±sem. Colored bottom lines denote significance.

Figure 3.12 depicts the change of ordinary MUA coherences between rest and running. Coherences rise markedly and in a statistically significant manner in all structure pairings. Also, note the faint bimodal distribution of changes mainly in within-structure pairings.

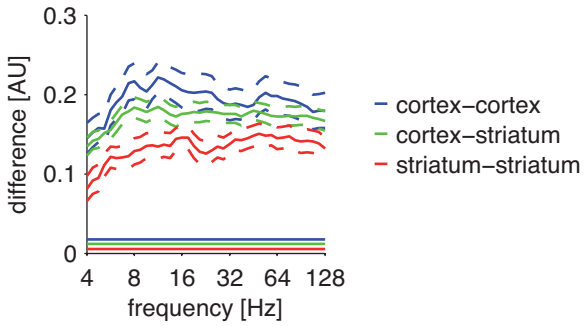

Figure 3.12: Grand average MUA coherence difference. Results are given as mean±sem. Colored bottom lines denote significance.

Overall, MUA coherences of individual subjects agreed well with grand average results. However, we stress that MUA coherences were still generally more variable with regard to certain features than monopolar LFP coherence results. For instance, while we found a substantial increase of coherences between behavioral states in all subjects with enough valid data, low-frequency running peaks could only be observed in a subset of animals.

3.4.3 Spike-Field (LFP-MUA) coherency

As a third measure of intra- and inter-area coupling we computed coherences between LFPs and MUA (LFP-MUA or *spike-field coherence* (SFC)) to investigate frequency-specific relationships between the two signal types. For within-structure pairings, we

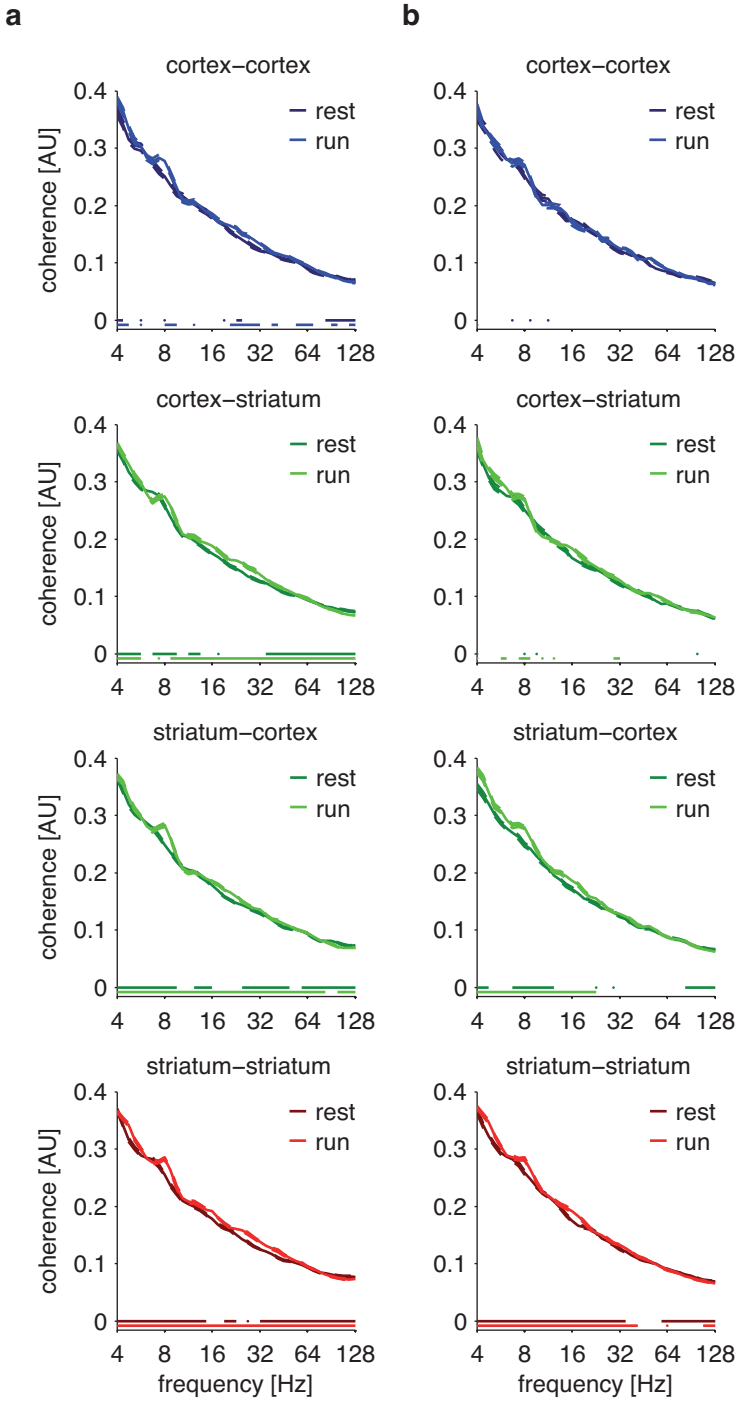

Figure 3.13: Grand average LFP-MUA coherence. (a) Monopolar LFP-MUA coherence. (b) Bipolar LFP-MUA coherence. Results are given as mean±sem. Colored bottom lines denote significance. For interpretation of figure titles, note that in all cases LFPs always figured as the first partner in a coherence pair.

excluded combinations of spikes and fields recorded on the same electrode to prevent artificial coherence effects due to spillover of spiking activities into LFP traces (Bar-Gad and Bergman, 2001; Siegel et al., 2009). For between-structure pairings, we separately combined cortical LFPs with striatal MUA and vice versa to account for coherence differences due to the different physiological origins of the two signal types (Mitzdorf, 1985).

Figure 3.13 shows grand average spike-field coherence results involving monopolar (panel a) and bipolar (panel b) LFPs. Absolute values are lower as in the case of LFP-LFP and MUA-MUA coherences (cf. Figures 3.7 and 3.11 on pages 75 and 79, respectively). Further, spike-field coupling is very similar in terms of strength and distribution of values in all structure-signal type pairings. With the exception of cortico-cortical pairings, LFP-MUA coherences are significant across wide parts of both lower and higher spectral regions. However, spectra do not exhibit distinct high-frequency peaks. In contrast, small low-frequency bumps can be discerned in some spectra during rest. During running, all LFP-MUA coherence spectra exhibit small but distinct peaks centered on 8 Hz. Note that these peaks are significant in pairings of monopolar striatal LFPs and cortical MUA but not between monopolar cortical LFPs and striatal MUA (paired, two-sided Wilcoxon sign-rank tests, $p < 0.01$; $n = 36$, $n = 79$, $n = 80$, and $n = 118$ cortico-cortical, cortico-striatal, striato-cortical, and striato-striatal monopolar LFP-MUA pairs, respectively). In general, bipolar LFP-MUA coherences are significant less often than their monopolar counterparts (paired, two-sided Wilcoxon sign-rank tests, $p < 0.01$; $n = 22$, $n = 33$, $n = 68$, and $n = 98$ cortico-cortical, cortico-striatal, striato-cortical, and striato-striatal bipolar LFP-MUA pairs, respectively).

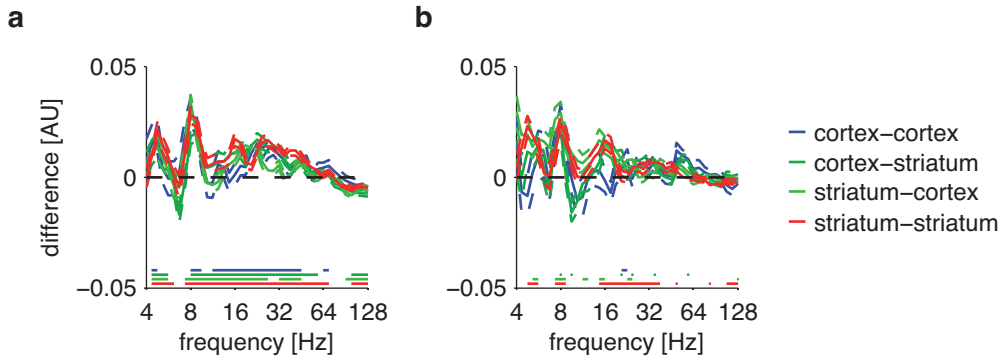

Figure 3.14: Grand average LFP-MUA coherence difference. (a) Monopolar LFP-MUA pairs. (b) Bipolar LFP-MUA pairs. Results are given as mean±sem. Black dashed lines indicate no change. Colored bottom lines denote significance.

We quantified the change in spike-field coherences between behavioral conditions by means of difference spectra as shown in panels a and b of Figure 3.14. Both monopolar

(panel a) and bipolar (panel b) LFP-MUA difference spectra exhibit prominent peaks of significant coherence increase around 8 Hz. A second low-frequency peak of coherence change is centered slightly above 4 Hz in all structure-signal type pairings. Also, spike-field coherence increases consistently between 16 and 32–64 Hz in monopolar LFP-MUA pairings, and it decreases significantly from below up to 128 Hz. Changes of bipolar LFP-MUA coherences are generally less consistent and significant mostly between striato-cortical and striato-striatal electrode pairs.

LFP-MUA coherence results were rather robust across subjects with respect to some of the features described. In particular, low-frequency running peaks could be observed in most animals. Coherence difference results were much more variable between animals.

3.5 Phase

3.5.1 LFP phase-locking

As noted above (Section 2.7.3.4), coherency measures basically quantify the temporal consistency of the frequency-specific coupling of two signals. However, they do not explicitly differentiate between phase and amplitude components of these relationships (Section 2.7.3.5). Given the strong and qualitatively similar characteristics of both LFP power and coherence spectra, we computed phase-locking values of each epoch to determine the degree of phase-locking between electrodes after normalization of the complex cross-spectral vectors to unit length. We computed test statistics the same way as for coherencies (Section 2.7.3.4) and as described in general above (Section 2.7.4).

Panel a of Figure 3.15 shows grand average phase-locking spectra of monopolar LFPs. Note the striking similarity between these plots and those of monopolar LFP coherences in Figure 3.7 (page 75) which nicely illustrates the close analytical relationship between the respective parameters. However, absolute phase-locking values are smaller than coherence values throughout almost the entire spectrum in each pairing with this feature sparing the low-frequency running peaks to a large extent. Nevertheless, phase-locking values are statistically significant throughout the entire extent of all spectra (paired, two-sided Wilcoxon sign-rank tests, $p < 0.01$; $n = 33$, $n = 107$, and $n = 57$ cortico-cortical, cortico-striatal, and striato-striatal electrode pairs, respectively).

We divided average ordinary coherence by corresponding phase-locking estimates of each electrode pair to directly compare the relative strengths of the two phase-coupling measures. We computed test statistics of the null hypothesis of no difference between coherence and phase-locking values through comparisons of real estimates with alternative distributions obtained as averages of $n = 1000$ random partitions created from both

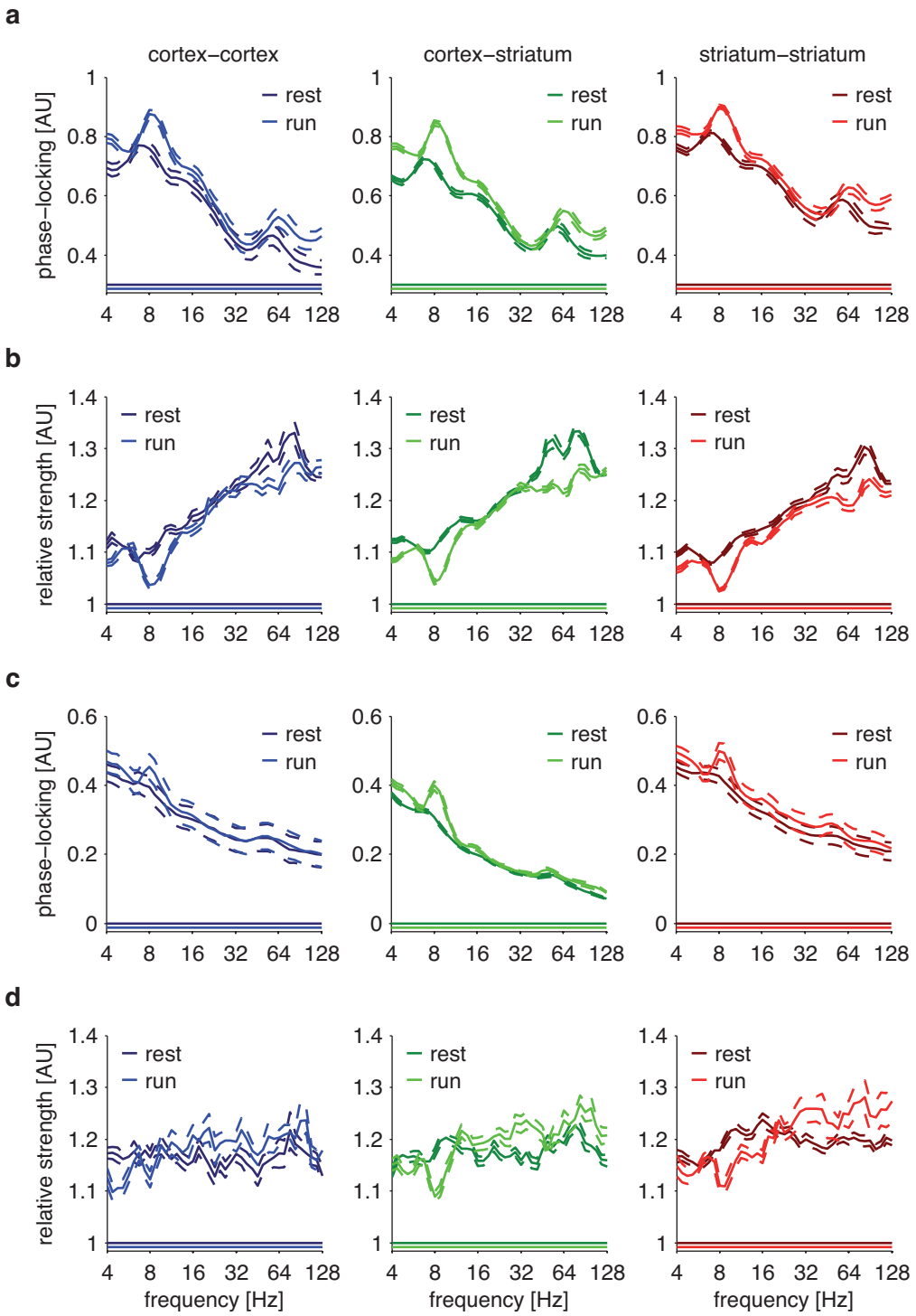

Figure 3.15: Grand average LFP phase-locking and relative coherence–phase-locking strength. (a) Monopolar LFPs: phase-locking. (b) Monopolar LFPs: coherence–phase-locking ratio. (c) Bipolar LFPs: phase-locking. (d) Bipolar LFPs: coherence–phase-locking ratio. Results are given as mean±sem. Colored bottom lines indicate significance.

measures. The plots in panel b of Figure 3.15 demonstrate a strong inverse relationship between frequency and relative strength of coherence in terms of phase-locking values of monopolar LFPs. Furthermore, low-frequency valleys occupy virtually the same points on the frequency axis as low-frequency phase-locking and coherence peaks. In contrast, high-frequency relative peaks are located at a point above the running monopolar phase-locking and coherence peaks at 64 Hz. Another local peak between 32 and 64 Hz can be observed in cortico-striatal resting spectra.

Panel c of Figure 3.15 depicts grand average phase-locking spectra of bipolar LFPs. Note again their qualitative similarity to corresponding coherence spectra (cf. Figure 3.7, page 75). As panel d of Figure 3.15 shows, ratios between bipolar coherence and phase-locking values are comparable on average to those of monopolar LFPs and statistically significant throughout all spectra (paired, two-sided Wilcoxon sign-rank tests, $p < 0.01$; $n = 28$, $n = 99$, and $n = 53$ cortico-cortical, cortico-striatal, and striato-striatal bipolar electrode pairs, respectively). The spectra also exhibit frequency-specific structure with a marked dip around 8 Hz where ratios are again close to one in cortico-striatal and striato-striatal pairings. However, ratios do not show a strong inverse scaling with frequency.

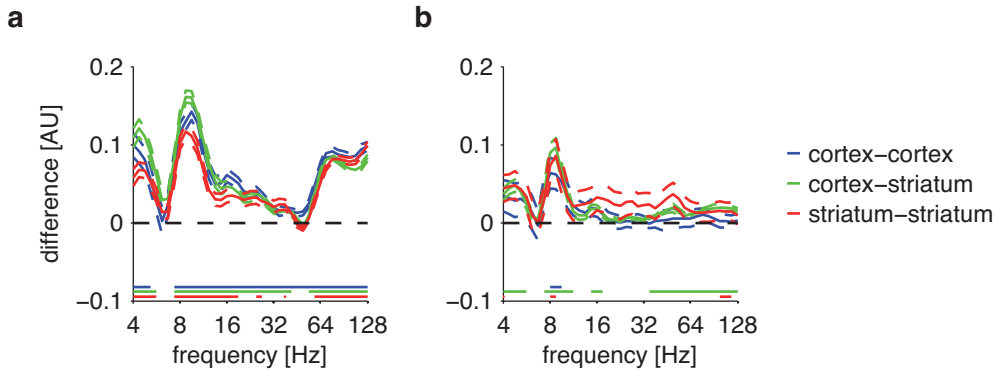

Figure 3.16: Grand average LFP phase-locking difference. (a) Monopolar LFPs. (b) Bipolar LFPs. Results are given as mean±sem. Black dashed lines indicate no change. Colored bottom lines denote significance.

We quantified changes in phase-locking between rest and running by computing difference spectra analogous to those of coherency estimates (Section 3.4). As shown in panels a and b of Figure 3.16, phase-locking differences are very similar to coherence differences (cf. Figure 3.8, page 76). However, note the larger absolute values and the more distinct shape of both monopolar and bipolar difference spectra. Bipolar phase-locking values increase significantly in all structure pairings specifically around 8 Hz. Phase-locking is also significantly increased in a broad band above 32 Hz between cortico-striatal pairs.

3.5.2 LFP phase angles

As outlined in Sections 2.7.3.4–2.7.3.5, coherency and phase-locking measures quantify the *magnitude* of signal coupling in the frequency domain. However, they do not reveal the *angles*, i.e., the temporal lags, between activities recorded on different electrodes. We aimed to determine the distribution of angles of each epoch to examine the phases of coupling at each frequency of interest of the cross-spectral measures. To this end, angles were sorted into histograms centered on 0° containing 61 equally spaced phase bins.

Panel a of Figure 3.17 depicts grand average monopolar LFP phase angle histograms. The plots demonstrate a marked concentration of phases around 0° in both low and high spectral regions during both behavioral states at the respective cross-spectral peak frequencies as revealed by coherence and phase-locking analyses (cf. Figures 3.7 and 3.15 on pages 75 and 83, respectively). Overall, phase distributions are more tightly constrained in lower than in higher spectral regions but still significant at almost every frequency–phase-bin pair (paired, two-sided Wilcoxon sign-rank tests, $p < 0.01$; $n = 33$, $n = 107$, and $n = 56$ cortico-cortical, cortico-striatal, and striato-striatal electrode pairs, respectively). Remarkably, while phase distribution maxima are located at exactly zero virtually everywhere in all histograms of within-structure pairings, there are substantially more non-zero bins of maxima in histograms of cortico-striatal pairings. Most strikingly, bins of phase maxima in low and high frequency ranges exhibit opposite signs, indicating different temporal relationships between the respective signal components.

Panel b of Figure 3.17 shows grand average phase angle histograms of bipolar LFPs. Phase angle distributions are less structured and non-significant more often than their monopolar counterparts (paired, two-sided Wilcoxon sign-rank tests, $p < 0.01$; $n = 28$, $n = 99$, and $n = 53$ cortico-cortical, cortico-striatal, and striato-striatal bipolar electrode pairs, respectively). Interestingly, bins of significant bipolar LFP phase distribution are grouped in two bands centered roughly around $+\frac{\pi}{2}$ and $-\frac{\pi}{2}$ rad/s (corresponding to 90° and -90°, respectively). Also, phase distribution maxima are non-zero more often in bipolar than in monopolar histograms.

3.5.3 Cross-hemispheric LFP phase-coupling

Given the characteristic structure of monopolar LFP coherence and phase-locking spectra, we made use of the signals recorded simultaneously in both hemispheres of our subjects by comparing the strength of phase-coupling between electrodes located on the same with those located on different hemispheres. For each trial with at least one valid ipsilateral and contralateral electrode pair we first computed within- and across-hemisphere coherence and phase-locking values and then subtracted contralateral from

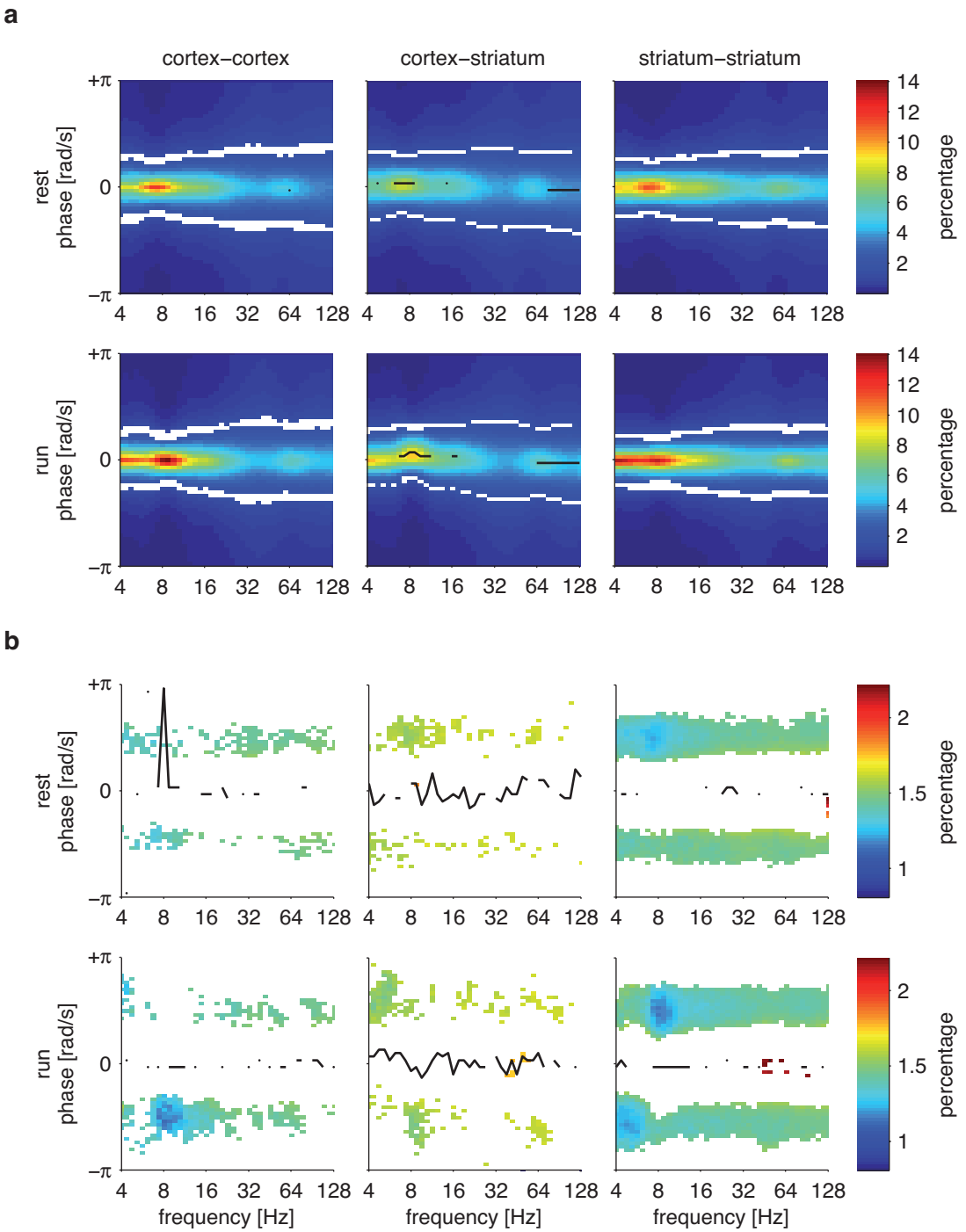

Figure 3.17: Grand average LFP phase angles. (a) Monopolar LFPs. (b) Bipolar LFPs. Black line segments denote non-zero maxima at each frequency. Phase bins are of size 6°, corresponding to approximately 0.1047 rad/s in polar coordinates. Test statistics computed using time-shifted estimates quantify the significance of phase concentration within each bin at each frequency. Bins of non-significant phase concentration are whitened.

ipsilateral spectra. In addition, we created alternative distributions of the original data of each trial by computing the mean across $n = 10$ partitions obtained through random assignment of hemisphere labels. We then pooled the original and permuted data across all trials to compute grand average results and to perform test statistical comparisons of the null hypothesis of no difference between ipsilateral and contralateral values.

The plots in panel a of Figure 3.18 demonstrate a spectrum-wide difference between ipsilateral and contralateral coherences in all structure pairings with the former being larger than the latter. This effect exhibits a strong frequency-dependence. More specifically, while ipsi- vs. contralateral differences are almost zero around 8 Hz, they increase markedly between 8 and 32 Hz and remain elevated up until 128 Hz. Difference spectra also exhibit localized peaks above 32 and 64 Hz which are more pronounced in cortico-cortical and striato-striatal than in cortico-striatal pairings. Cross-hemispheric difference spectra from both behavioral states are qualitatively very similar, and difference values are significant throughout almost their entire extents. However, absolute difference values are mostly larger in within- as compared to between-structure pairings.

Panel b of Figure 3.18 depicts ipsi- vs. contralateral phase-locking difference spectra of monopolar LFPs. Note the striking similarity to coherence spectra in panel a. Again, difference values are significant almost everywhere in lower and higher spectral regions and during both behavioral states (paired, two-sided Wilcoxon sign-rank tests, $p < 0.01$; $n = 87$, $n = 258$, and $n = 260$ trials with ipsi- and contralateral cortico-cortical, cortico-striatal, and striato-striatal electrode pairs, respectively).

The similarity of coherence and phase-locking difference spectra indicates that the hemispheric bias of coherence between structures is indeed due to a larger phase-coupling proper between ipsilateral as compared to contralateral electrode pairs. We substantiated this assumption by computing the difference between cross-hemispheric coherence and phase-locking difference spectra of each trial. We tested the significance of grand average values through comparison of measured differences with those obtained from the means of $n = 1000$ random partitions created from coherence and phase-locking cross-hemispheric difference values of each structure pairing and each level.

The results in panel c of Figure 3.18 demonstrate that differences in lower spectral regions are mainly negative between cortico-cortical and striato-striatal pairings whereas they are virtually zero between cortico-striatal electrode pairs, indicating a stronger hemispheric bias for phase-locking values between the former. However, note the non-significant difference in all structure pairings at the running low peak-frequency of 8 Hz seen in monopolar LFP coherence and phase-locking spectra. In contrast, cortico-striatal spectra exhibit two positive difference peaks centered around 32 Hz and between 64 and 128 Hz during both rest and running, indicating a stronger hemispheric bias for coherence

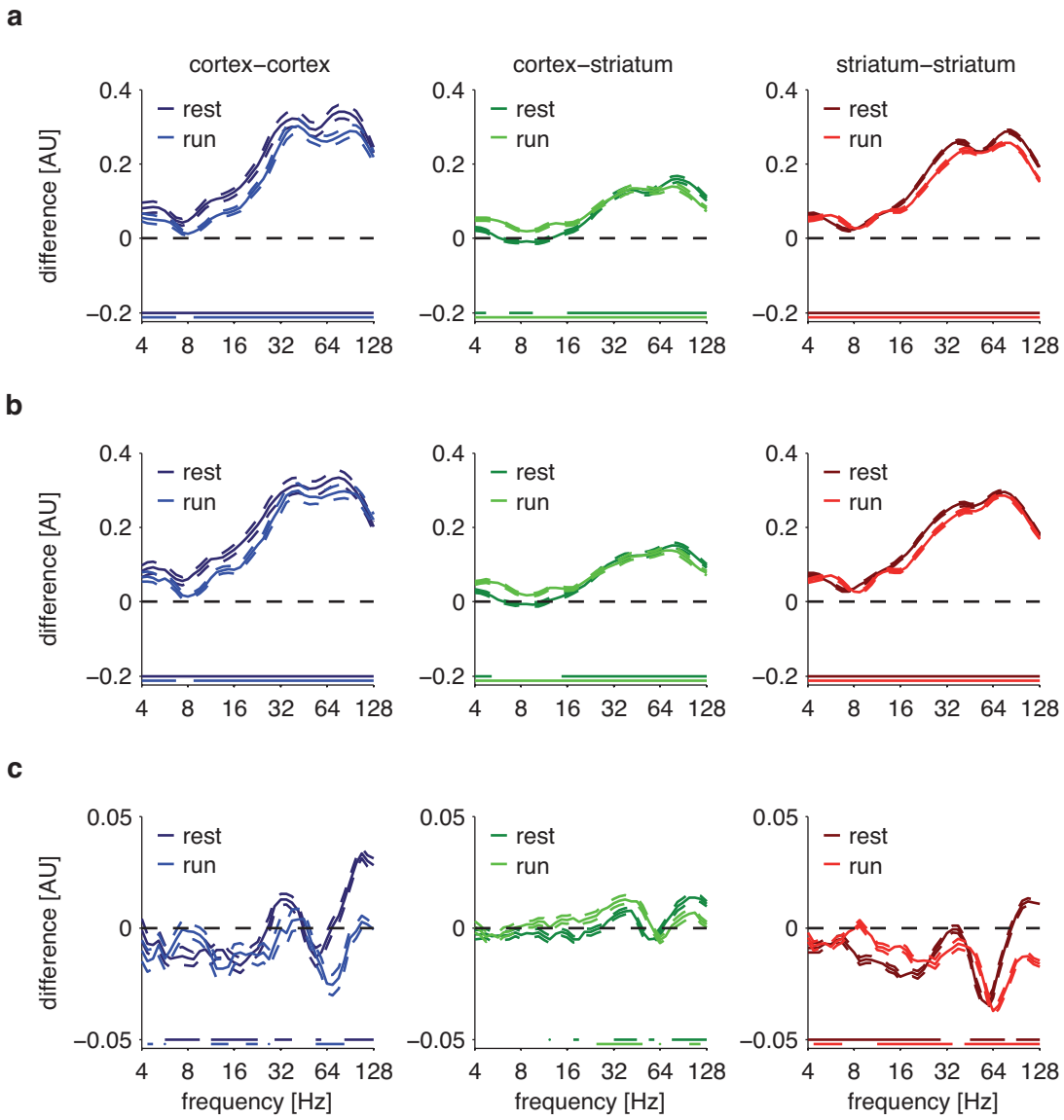

Figure 3.18: Grand average cross-hemispheric LFP phase-coupling. (a) Coherence. (b) Phase-locking. (c) Coherence–phase-locking difference. Panels a and b depict differences between ipsilateral and contralateral values. Panel c displays differences between ipsi- vs. contralateral coherence and phase-locking estimates. Results are given as mean±sem. Black dashed lines indicate no difference. Colored bottom lines denote significance.

values at these frequencies. Cortico-cortical and striato-striatal spectra display both and only the second one of these peaks, respectively, during rest. Remarkably, all three structure pairings exhibit two significant, negative difference peaks centered below and around 64 Hz during rest and running, respectively. This indicates a stronger hemispheric

bias of phase-locking as compared to coherence values exactly at the high peak frequencies of both behavioral states (cf. Figures 3.7 and 3.15 on pages 75 and 83, respectively).

3.6 Phase-amplitude coupling

We computed the magnitudes and phases of coupling between phase and amplitude components of monopolar LFPs to examine the consistency of their relationship possibly indicating a modulation of high- by low-frequency rhythms (Section 2.7.3.6). We basically used here the very same structure pairings employed above for phase-coupling estimates. Note, however, that in the present analysis involving two distinct signal components, this included a bidirectional, non-symmetrical pairing of cortical and striatal electrodes as well as a doubling of electrode pairs for both within-structure pairings. For conceptual reasons, we only display the results of phase-coupling analyses between lower phase and higher amplitude components separated by at least one octave of spectral distance.

Figure 3.19 depicts grand average phase-amplitude coupling magnitudes of monopolar LFPs. All matrices display prominent peaks at pairs of lower phase and higher amplitude frequencies. During rest, couplings are strongest between phase components of around 4 up to below 8 Hz and amplitude components localized above 64 Hz and broadly distributed between 64 and 128 Hz. During running, phase-amplitude interactions increase in overall strength and couplings become more distinctly localized in terms of prominent, broadly based peaks and extended bands centered on phase frequencies of up to 8 Hz and covering amplitude frequencies from below 64 up to 128 Hz. However, these peaks are clearly offset from phase frequencies around 4 Hz. Interestingly, pairs of center frequencies of phase-amplitude coupling maxima do not exactly coincide with low and high peak frequencies of power and phase-coupling (coherence and phase-locking) estimates (cf. Figures 3.3, 3.7, and 3.15 on pages 69, 75, and 83, respectively). This holds particularly true for amplitude frequencies during rest and phase frequencies during running.

In addition to these major effects, phase-amplitude coupling values are also significantly modulated in a localized fashion between phase frequency components of 8–16 Hz and amplitude frequency components of again 64–128 Hz. Somewhat weaker but still significant interactions between phase frequencies of 4–8 and amplitude frequencies of 16–32 Hz are present in all but cortico-cortical electrode pairs during running, with striato-striatal pairs displaying similar characteristics during rest. Overall, phase-amplitude couplings are most significant between striato-striatal followed by striato-cortical electrode pairs, and the least significant between cortico-cortical pairs (paired, two-sided Wilcoxon sign-rank tests, $p < 0.01$; $n = 66$, $n = 107$, $n = 107$, and $n = 114$ cortico-cortical, cortico-striatal, striato-cortical, and striato-striatal electrode pairs, respectively).

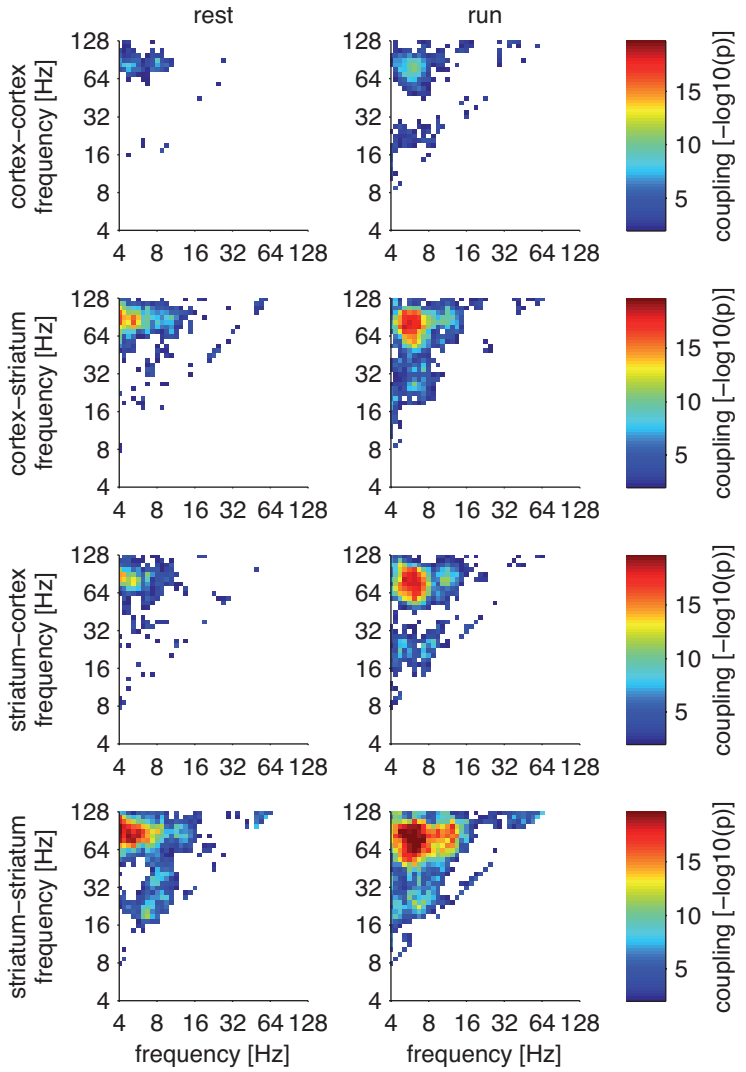

Figure 3.19: Grand average phase-amplitude coupling magnitudes of monopolar LFPs. Phase and amplitude frequencies are displayed on x- and y-axes, respectively. Results are given as the negative common logarithm of test-statistical $p-$values. Non-significant values and coupling estimates involving amplitude frequencies < 8 Hz and phase frequencies > 64 Hz were blanked and whitened.

We extracted the angles of the complex phase-amplitude coupling terms computed for each epoch and averaged the respective values as explained in Section 2.7.3.5. We plotted the resulting grand average data after masking to only display phases at frequency pairs exhibiting significant coupling strengths (cf. Figure 3.19). The plots in Figure 3.20 show that average phases of significant coupling tend to markedly cluster around values between $+\frac{\pi}{2}$ to $+\pi$ rad/s, with a bias towards the latter particularly during running. As

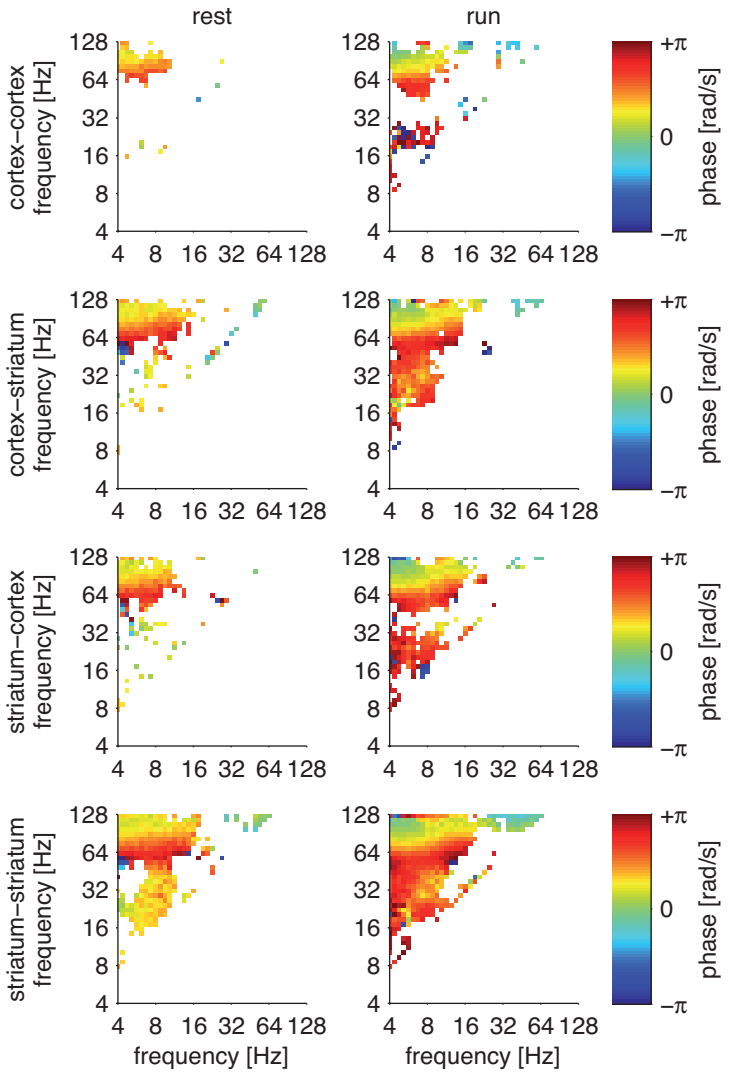

Figure 3.20: Grand average phase-amplitude coupling phases of monopolar LFPs. Phase and amplitude frequencies are displayed on x- and y-axes, respectively. Results are given as mean. Phases of frequency pairs exhibiting non-significant coupling strengths (cf. Figure 3.19) and coupling estimates involving amplitude frequencies < 8 Hz and phase frequencies > 64 Hz were blanked and whitened.

Figure 2.15 on page 56 demonstrates, these phase values at low-phase–high-amplitude frequency pairs correspond to the trough regions of extracellularly recorded LFPs, providing a physiological link between low- and high-frequency fluctuations.

We quantified the changes between rest and running phase-amplitude couplings by means of difference matrices as shown in Figure 3.21. They demonstrate a well-delineated, massive increase in phase-amplitude coupling between phase frequency components be-

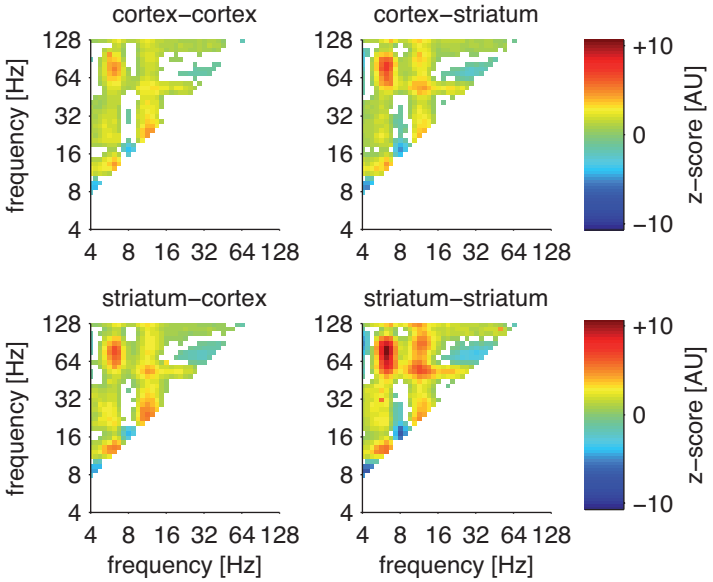

Figure 3.21: Grand average phase-amplitude coupling magnitude differences of monopolar LFPs. Phase and amplitude frequencies are displayed on x- and y-axes, respectively. Results are given as grand average within-trial z-scores (Section 2.7.4). Non-significant values and coupling estimates involving amplitude frequencies < 8 Hz and phase frequencies > 64 Hz were blanked and whitened.

low 8 and amplitude frequency components from below 64 up to 128 Hz. This effect is again strongest in striato-striatal and weakest in cortico-cortical structure pairings. Remarkably, the significant increase of coupling between phase and amplitude frequencies of 8–16 and 64–128 Hz is divided into two well-separated, peak-shaped components with amplitude frequencies centered below and above 64 Hz, respectively. In addition, note the significant increase between phase and amplitude components of approximately doubled frequency. Furthermore, coupling decreases significantly between phase and amplitude frequencies of 4 and 8, 8 and 16 as well as around 32 and 64 Hz, respectively.

3.7 Power correlation

We computed correlations between monopolar LFP power values of different frequencies as explained in Section 2.7.3.7. We again employed the exact same structure pairings as for phase-coupling analyses (Sections 3.4 and 3.5). We only considered values at least one octave off the main diagonal of correlation matrices for statistical analyses of cross-electrode, cross-frequency estimates to avoid spurious findings resulting from statistical dependence of power values at neighboring frequencies. We treated cross-channel, same-frequency estimates separately for both conceptual reasons and illustration purposes.

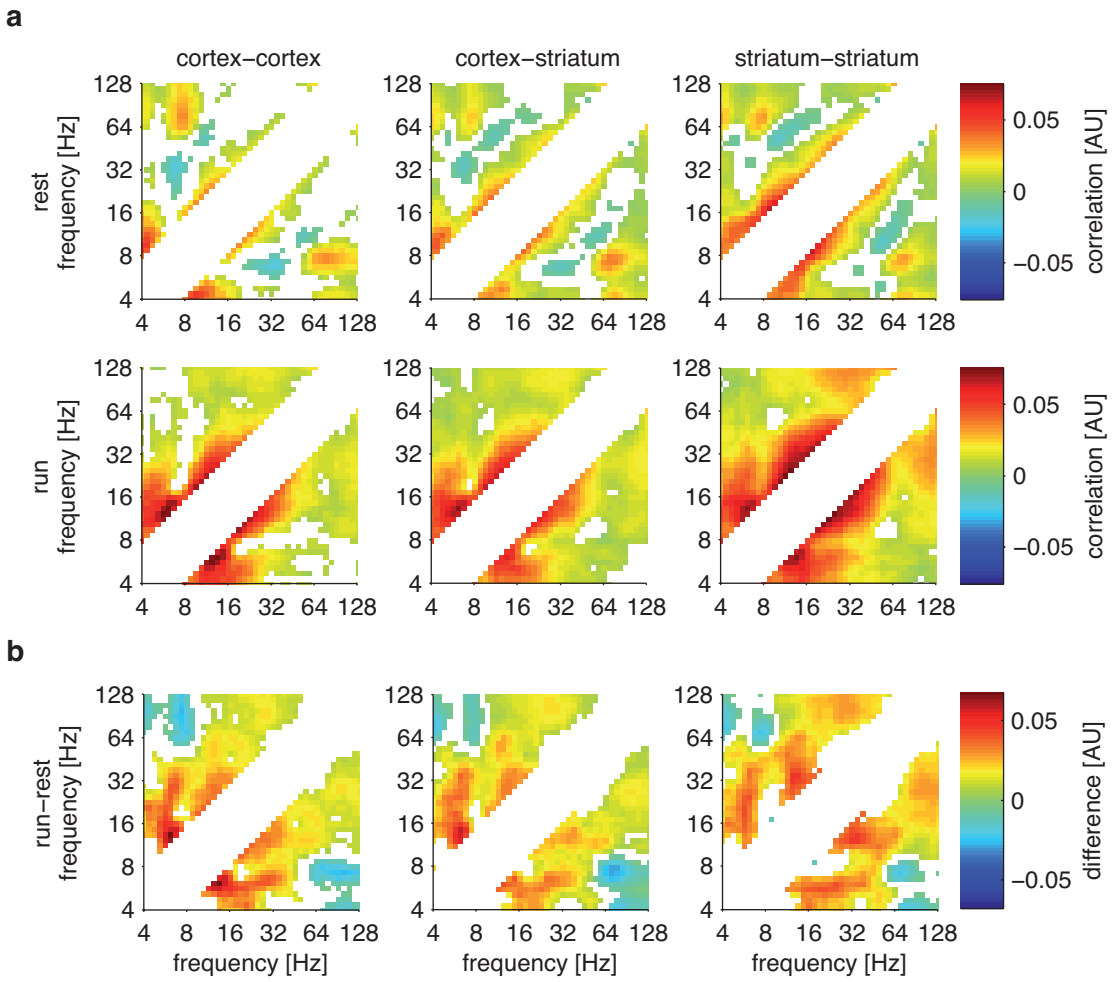

Figure 3.22: Grand average cross-electrode, cross-frequency monopolar LFP power correlations. (a) Raw power correlations. (b) Power correlation differences. For interpretation of figure titles, note that in all cases the first and second structures referred to in a pair map onto frequency components along x- and y-axes, respectively. Non-significant correlations and values up to one octave off the main diagonal were blanked and whitened.

Panel a of Figure 3.22 depicts grand average cross-electrode, cross-frequency power correlations of all structure pairings. Both resting (upper plots) and running (lower plots) matrices exhibit several prominent features. First, resting power values at many spots and along extended bands between 4 and 32 Hz are significantly correlated with values of approximately double their own frequency between 8 and 64 Hz in all structure pairings. This feature becomes even more pronounced during running. Second, however, during the latter state significant correlations between lower frequency components are more broadly dispersed also off double-frequency diagonals. This effect is particularly

distinct in a spectral region stretching from below 16 and up to below 64 Hz and most strongly expressed between striato-striatal electrode pairs. Third, during running power values within a broad region around 32 Hz become significantly correlated with values above 64 and up to 128 Hz. Fourthly, resting but not running matrices exhibit strong, distinctly localized peaks and bands of significant values between frequencies centered slightly below 8 and around to above 64 up to 128 Hz. Significant correlations are most broadly distributed between cortico-cortical and most narrowly focused between striato-striatal electrode pairs, respectively. Notably, they are stronger between striatal low- and cortical high-frequency components than vice versa. Further, highly similar correlation characteristics are present between frequencies around 4 and between 64 and 128 Hz.

Panel b of Figure 3.22 explicitly quantifies the changes of power correlations between rest and running. Correlations between frequency components slightly below 8 and from below 16 to above 32 Hz increase strongly across an extended band. A second band of strong correlation increase is located at frequency pairs between 8 to and above 16 and up to almost 64 Hz, with more peak-like modulations present in between-structure as compared to within-structure pairings. All matrices also display the significant increase of correlation between frequency components of 32 and those below to around 128 Hz which is most prominent and widespread in striato-striatal pairings. Most strikingly, correlations between low- and high-frequency components of 4 and 8 and between 64 and 128 Hz decrease in a statistically significant manner between behavioral states in all structure pairings (paired, two-sided Wilcoxon sign-rank tests, $p < 0.01$; $n = 33$, $n = 107$, $n = 57$ cortico-cortical, cortico-striatal and striato-striatal electrode pairs, respectively).

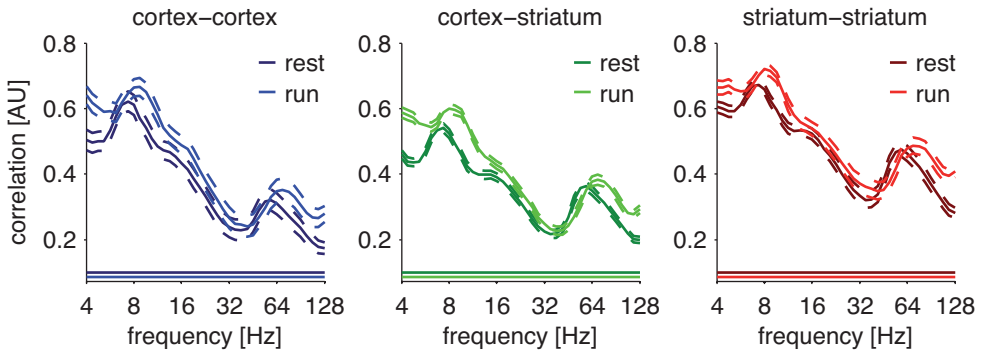

Figure 3.23: Grand average cross-electrode, same-frequency monopolar LFP power correlations. Results are given as mean±sem. Colored bottom lines denote significance.

Figure 3.23 depicts grand average cross-channel, same-frequency power correlations as extracted from the main diagonal of cross-channel, cross-frequency correlation matrices. Note the striking qualitative similarity between power correlation spectra on the one

hand and LFP coherence and phase-locking spectra shown in Figures 3.7 (page 75) and 3.15 (page 83), respectively, on the other. Power correlation values are statistically significant across the entire spectrum in all structure pairings. They are largest between striato-striatal and similar between cortico-cortical and cortico-striatal electrode pairs but consistently smaller than their phase-coupling counterparts (Section 3.8).

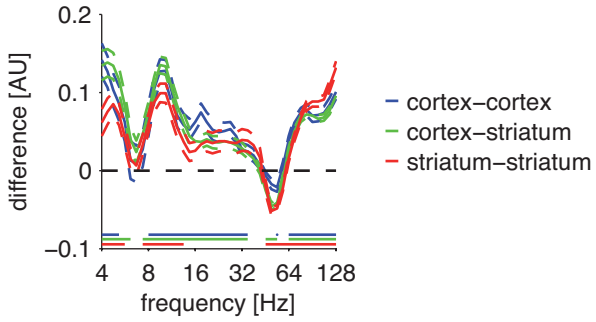

Figure 3.24: Grand average cross-electrode, same-frequency monopolar LFP power correlation differences. Results are given as mean±sem. Black dashed lines indicate no change. Colored bottom lines denote significance.

Difference spectra shown in Figure 3.24 quantify the changes between resting and running cross-channel, same-frequency power correlations. Note again their striking similarity to corresponding coherence and phase-locking difference plots (cf. Figures 3.8 and 3.16 on pages 76 and 84, respectively). In particular, power correlations change significantly in a localized fashion around 4 and 8 as well as below and above 64 Hz.

3.8 Phase-locking–power interrelation

Given the strong qualitative similarity between phase-coupling and cross-electrode, same-frequency power correlation estimates, we directly related both measures of neuronal interaction to quantify their overall and more fine-grained mutual temporal dependencies.

We first compared relative strengths by dividing phase-locking by cross-channel, same-frequency power correlation spectra. We performed test statistical comparisons of the null hypothesis of no difference between measures the same way as for coherence–phase-locking ratios (Section 3.5.1). As Figure 3.25 shows, phase-locking is consistently stronger in all structure pairings. This effect is largest in cortico-cortical and smallest in striato-striatal pairings. Remarkably, relative spectra exhibit a prominent peak centered on 32 Hz and a rising flank of values up to 128 Hz. Phase-locking–power correlation ratios are smallest in low spectral regions and around resting and running high peak frequencies.

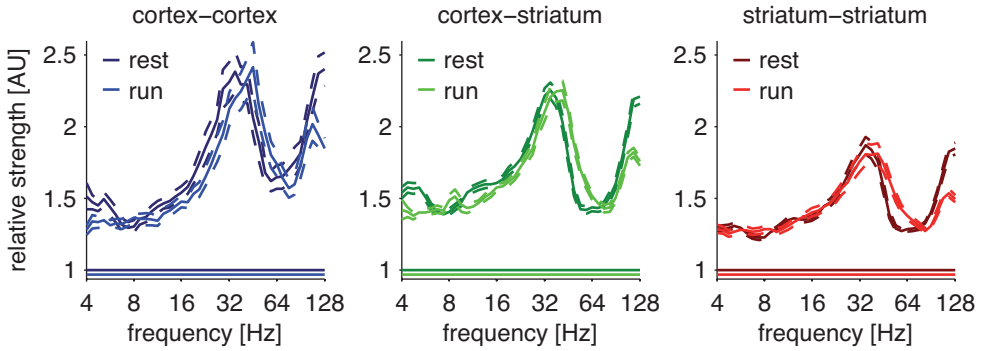

Figure 3.25: Grand average phase-locking–power correlation ratios of monopolar LFPs. Results are given as mean±sem. Colored bottom lines denote significance.

Figure 3.26 depicts phase-locking–power correlation ratio changes between behavioral states. The bias of stronger phase-locking values increases significantly around the resting high phase-coupling peak-frequency below 64 Hz in all structure pairings but decreases between 64 and up to 128 Hz. Most strikingly, with the exception of a significant change in striato-striatal pairings, there are no alterations of phase-locking–power correlation ratios at the running high peak-frequency of 64 Hz. In lower spectral regions, the bias also tends to decrease but does not change significantly around the low running peak-frequency of 8 Hz (paired, two-sided Wilcoxon sign-rank tests, $p < 0.01$; $n = 33$, $n = 107$, and $n = 57$ cortico-cortical, cortico-striatal, and striato-striatal electrode pairs, respectively).

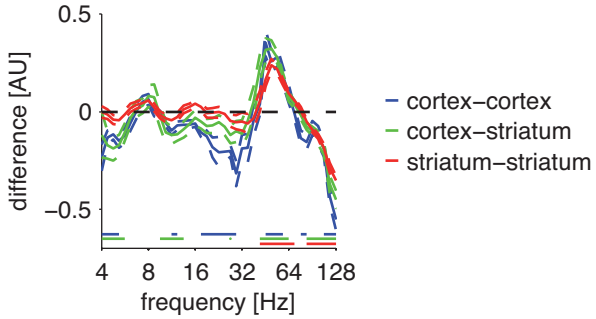

Figure 3.26: Grand average phase-locking–power correlation ratio differences of monopolar LFPs. Results are given as mean±sem. Black dashed lines indicate no change. Colored bottom lines denote significance.

The above phase-locking–power correlation ratios only quantify the relative, time-average strength of both interaction measures but do not reveal the detailed temporal dynamics of their relationship. We therefore determined the interrelation of both coupling measures on a small time scale by calculating correlations between phase-locking and

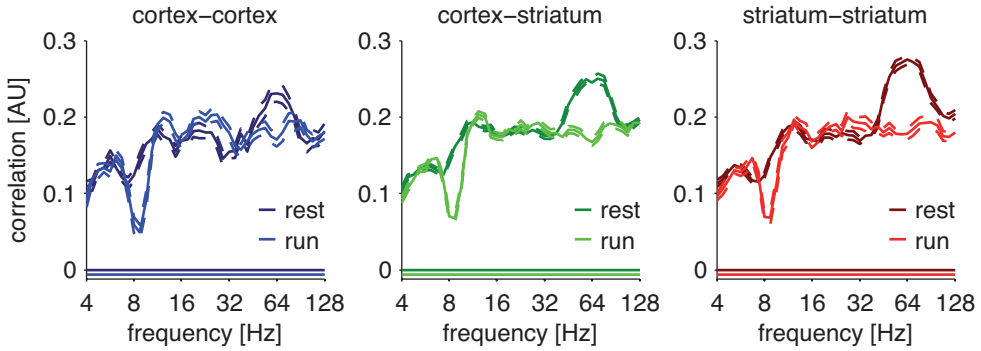

Figure 3.27: Grand average raw phase-locking–power intercorrelations. Results are given as mean±sem. Colored bottom lines denote significance.

power correlation values as described in Section 2.7.3.8. We computed test statistics by comparing measured coefficients with those obtained through correlation of randomized partitions of phase-locking and power correlation values created for each individual epoch.

Phase-locking–power intercorrelation spectra shown in Figure 3.27 reveal spectrum-wide significant correlations between both coupling measures. In general, correlations are stronger in higher than in lower spectral regions. Furthermore, prominent, broadly based resting peaks are centered on 64 Hz and smaller resting valleys are centered below 8 Hz in all structure pairings. Remarkably, correlations change substantially between behavioral conditions, with resting high-frequency peaks vanishing and resting low-frequency valleys deepening and their bottoms shifting towards center frequencies of 8 Hz. These changes are explicitly quantified in phase-locking–power intercorrelation difference spectra shown in Figure 3.28. They reveal significant decreases of correlations centered exactly on 8 Hz in the low and on 64 Hz in the high frequency range but hardly any significant changes of intercorrelations in other spectral regions of all structure pairings.

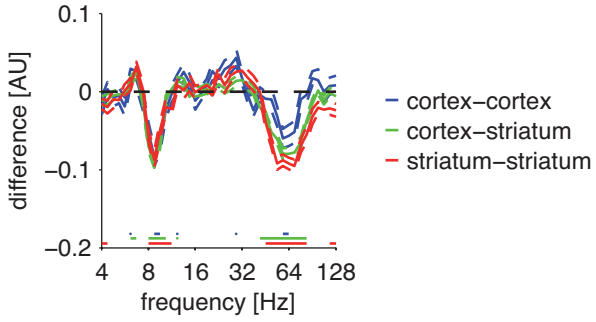

Figure 3.28: Grand average phase-locking–power intercorrelation differences. Results are given as mean±sem. Black dashed lines indicate no change. Colored bottom lines denote significance.

3.9 Peak-frequency changes

Monopolar LFP power, coherence, and phase-locking spectra exhibit prominent low and high frequency peaks indicating true oscillatory processes present in the underlying signals. These peaks shift markedly in an upward direction between resting and running states. Further, the spectra also indicate increases of power and phase-coupling strengths within narrowly delimited bands centered around these low and high peak frequencies. We thus sought to (i) assess the statistical significance of both power and phase-coupling increases as well as associated peak-frequency shifts between the two major behavioral states, and (ii) find out wether these changes would also scale in a linear fashion with corresponding linear changes of running speed on the different levels. We chose phase-locking instead of coherence estimates for peak-frequency analyses of phase-coupling measures in order to clearly distinguish between changes resulting from amplitude and phase-locking effects proper, respectively (see Sections 2.7.3.5, 3.4, and 3.5 above).

We computed power and phase-locking values in steps of 32 instead of 8 voices within low and high frequency bands stretching from 5.66–11.31 and 45.25–90.51 Hz, respectively, and spanning one octave of spectral bandwidth each. We then interpolated the resulting spectra in 128 logarithmic steps using cubic splines. For peak-frequency analyses we were interested in specific changes within very limited frequency bands. We thus computed, for each structure and both resting and running states, the first derivative of the respective grand average power and phase-locking spectra as well as their peak-frequency. We then determined the points of maximum positive and negative slope of the spectral peak within the limits defined above. We chose the final frequency bounds used for peak localizations to be the minimum lower and maximum upper frequencies calculated across both structures or structure pairings and behavioral states.

To differentiate between changes of average power or phase-locking strengths and changes of peak frequencies proper we calculated mean power and phase-locking values within the bounds determined. We localized peak frequencies by computing maximum power and phase-locking values and extracted the corresponding frequency values. To asses the significance of peak-frequency changes between rest and average running levels, we pooled data from all trials with valid data available from both states. To analyze the relationship between average power or phase-locking values as well as associated peak frequencies and movement speed of the animals, we performed linear regression analyses on the data of each level pooled across trials from all subjects with running speed as the predictor. We restricted regression analyses to those structures or structure pairings marked by a significant overall positive shift of peak frequencies between rest and running and to trials and levels marked by a shift in peak-frequency > 0.

3.9.1 Power peaks

Figure 3.29 shows statistical comparisons of average power values (panel a) and average peak frequencies (panel c) of low, frequency-normalized LFP power spectra. Limits used for peak detection were 6.37 and 9.67 Hz. Power increased and peak frequencies shifted significantly towards higher values between behavioral states in both structures (paired, two-sided Wilcoxon sign-rank tests, $p < 0.005$ at α-levels of 0.01 Bonferroni-corrected for $n = 2$ comparisons; $n = 24$ and $n = 30$ cortical and striatal electrodes, respectively).

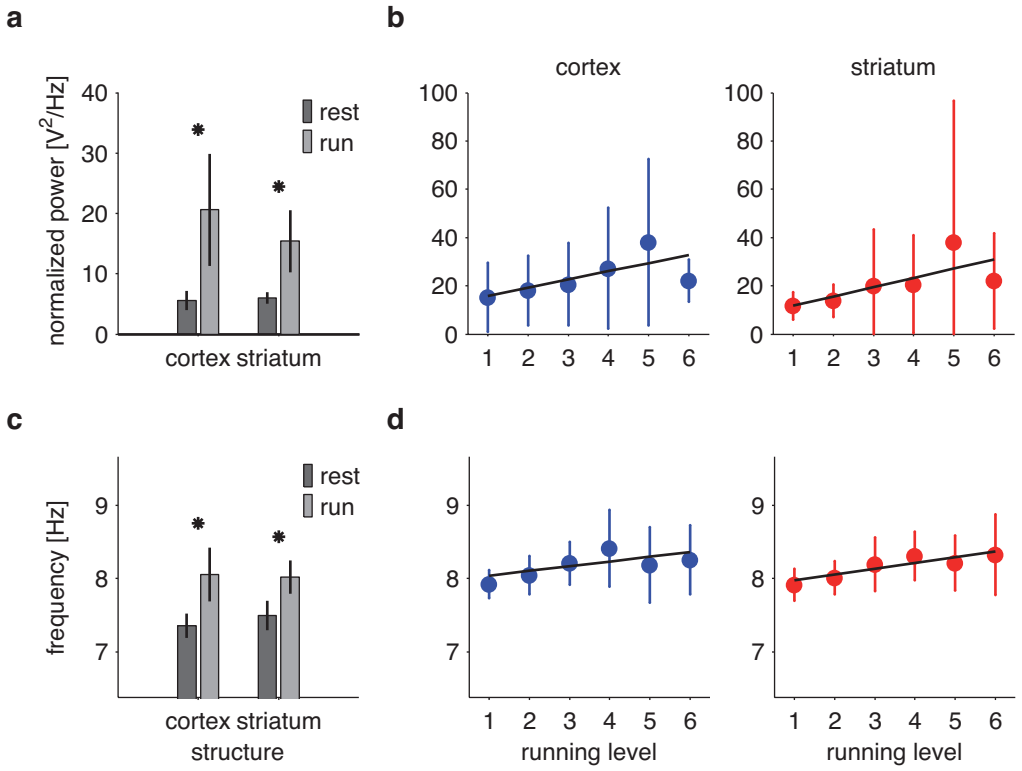

Figure 3.29: Low peak-frequency changes of monopolar LFP power. (a) Mean rest and average running level power. (b) Mean running level power. (c) Rest and average running level peak frequencies. (d) Running level peak frequencies. Results are given as median±mad (a, c) and mean±sd (b, d). Asterisks (*) denote significance.

An average of 58 and 56% of cortical and striatal electrodes exhibited positive shifts of low peak frequencies between rest and running levels. Panels b and d of Figure 3.29 depict average power and peak-frequency values from all running levels ($n = 10, 13, 20, 23, 17, 11$ cortical and $n = 16, 18, 28, 27, 21, 16$ striatal electrodes for levels 1–6, respectively). Power in both structures increased with regression values of $r = 0.22$ for cortex and $r = 0.20$ for striatum. However, these changes were not statistically significant. Peak

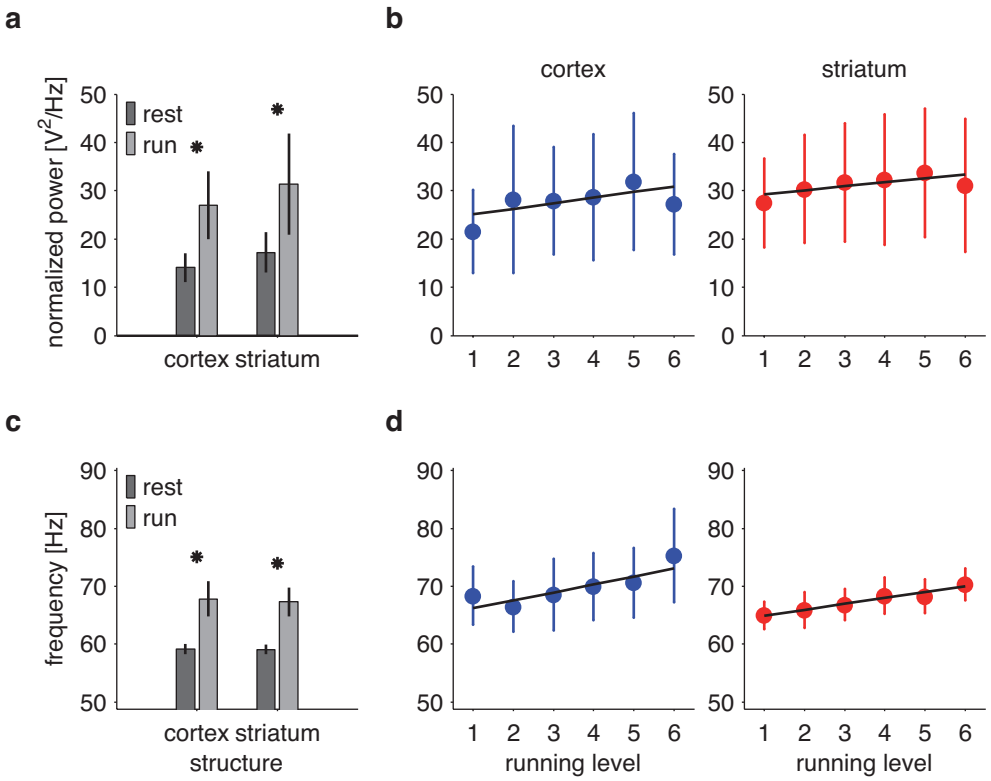

Figure 3.30: High peak-frequency changes of monopolar LFP power. (a) Mean rest and average running level power. (b) Rest and average running level peak frequencies. (c) Mean running level power. (d) Running level peak frequencies. Results are given as median±mad (a, c) and mean±sd (b, d). Asterisks (*) denote significance.

frequencies also increased with behavioral demand and scaled significantly ($p < 0.005$) in a linear fashion with running speed in striatum ($r = 0.32$) but not in cortex ($r = 0.22$).

Panels a and c of Figure 3.30 show rest and average running level power and peak frequencies from high, frequency-normalized LFP power spectra. Limits used for peak detection were 48.82 and 90.51 Hz (note that we clipped frequency axes in Figures 3.29, 3.30, 3.31, and 3.32 at the respective values). Average power and peak-frequency estimates increased in a statistically significant manner between behavioral states ($p < 0.005$).

An average of 67% of both cortical and striatal electrodes exhibited positive shifts of high peak frequencies between rest and running levels. High peak-frequency power (Figure 3.30, panel b) varied greatly and did not increase linearly with running speed ($r = 0.14$ for cortical and $r = 0.10$ for striatal electrodes). In contrast, both cortical ($r = 0.33$) and striatal ($r = 0.48$) peak frequencies (Figure 3.30, panel d) scaled linearly in a statistically significant manner with behavioral demand ($p < 0.005$; $n = 11, 15, 22, 24, 16, 11$ cortical and $n = 16, 20, 28, 29, 19, 16$ striatal electrodes for levels 1–6, respectively).

3.9.2 Phase-locking peaks

Figure 3.31 depicts mean phase-locking values (panels a and c) and associated peak frequencies (panels b and d) of monopolar LFPs during rest and average running levels in low (a, b) and high (c, d) frequency ranges. Spectral limits used for peak detection were 5.94 and 11.31 Hz for the low and 46.50 and 90.51 Hz for the high frequency band, respectively. As the plots show, both phase-locking values and peak frequencies increase between rest and running. In particular, peak frequencies of all structure pairings shift markedly from around 7 to values of about 8 Hz in the low and from below 60 to values around 65 Hz in the high frequency range. Changes of average phase-locking values are less pronounced and more variable. Still, all phase-locking and peak-frequency changes were statistically significant (paired, two-sided Wilcoxon sign-rank tests, $p < 0.0033$ at α-levels of 0.01 Bonferroni-corrected for $n = 3$ comparisons; $n = 33$, $n = 107$, and $n = 57$ cortico-cortical, cortico-striatal, and striato-striatal electrode pairs, respectively).

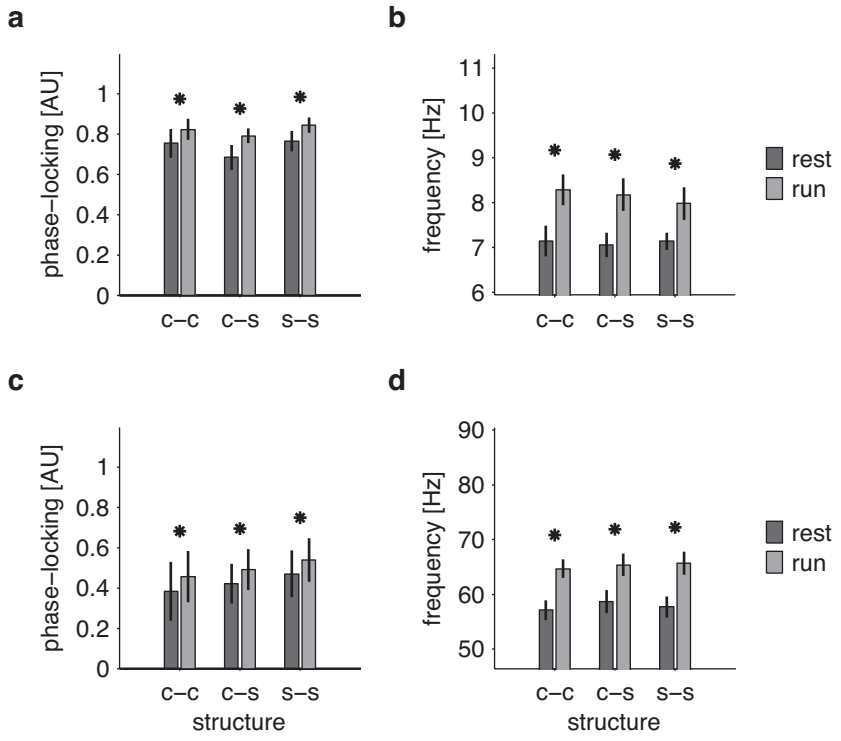

Figure 3.31: Level-average peak-frequency changes of monopolar LFP phase-locking values. (a) Mean phase-locking: Low frequency range. (b) Peak frequencies: Low frequency range. (c) Mean phase-locking: High frequency range. (b) Peak frequencies: High frequency range. Results are given as median±mad. Asterisks (*) denote significance. *Abbreviations*: c-c, cortex-cortex; c-s, cortex-striatum; s-s, striatum-striatum.

We again analyzed the relationship between changes of phase-locking values and associated peak frequencies and running speed of the animals. An average number of 78, 84, and 86% of cortico-cortical, cortico-striatal, and striato-striatal electrode pairs exhibited positive shifts of low phase-locking peak frequencies between rest and running levels. Phase-locking values within the low frequency band (Figure 3.32, panel a) varied substantially and scaled linearly in a statistically significant manner ($p < 0.0033$) with running speed between cortex and striatum only ($r = 0.22$, $r = 0.50$, and $r = 0.08$ for cortico-cortical, cortico-striatal, and striato-striatal electrode pairs, respectively). Remarkably, cortico-striatal phase-locking values did not increase but decreased with behavioral demand ($n = 1, 1, 10, 10, 7, 9$ cortico-cortical, $n = 10, 10, 45, 45, 33, 32$ cortico-striatal, and $n = 15, 18, 33, 33, 18, 15$ striato-striatal pairs for levels 1–6, respectively).

In striking contrast, low phase-locking peak frequencies (Figure 3.32, panel b) increased markedly and scaled linearly with running speed in all structure pairings ($r = 0.86$, $r = 0.79$, and $r = 0.75$ for cortico-cortical, cortico-striatal, and striato-striatal electrode pairs, respectively). All these changes were statistically highly significant ($p < 0.0033$). Note here the extremely small standard deviations on all levels of all structure pairings.

Similar to average low frequency phase-locking values, average high frequency phase-locking values varied substantially on each running level of each structure pairing (Figure 3.32, panel c). They did not scale at all with running speed in within-structure pairings ($r = 0.01$ for cortico-cortical and $r = 0.02$ for striato-striatal electrode pairs). However, average phase-locking values again decreased in a statistically significant linear fashion between cortex and striatum with increasing behavioral demand ($r = 0.29$, $p < 0.0033$; $n = 1, 1, 8, 9, 8, 8$ cortico-cortical, $n = 11, 11, 40, 42, 31, 32$ cortico-striatal, and $n = 15, 16, 33, 33, 18, 15$ striato-striatal pairs for levels 1–6, respectively).

High phase-locking peak frequencies as shown in panel d of Figure 3.32 were again much more consistent across electrode pairs. Accordingly, they exhibited a highly significant linear scaling with running speed in all structure pairings ($r = 0.71$, $r = 0.58$, and $r = 0.67$ for cortico-cortical, cortico-striatal, and striato-striatal electrode pairs, respectively; $p < 0.0033$). Note here the larger scatter of average peak-frequency values across running levels in cortico-cortical as compared to the other structure pairings, but also again the consistently small standard deviations on all levels of all pairings.

We repeated the above analyses using monopolar LFP coherences to compare peak-frequency changes in both phase-coupling measures (data not shown). Level-average changes of mean coherence values and associated peak frequencies were significant in all structure pairings and in both frequency ranges. Level-resolved mean coherence and peak-frequency estimates in low and high frequency ranges also exhibited exactly the same characteristics and similar $r-$ and $p-$values as corresponding phase-locking results.

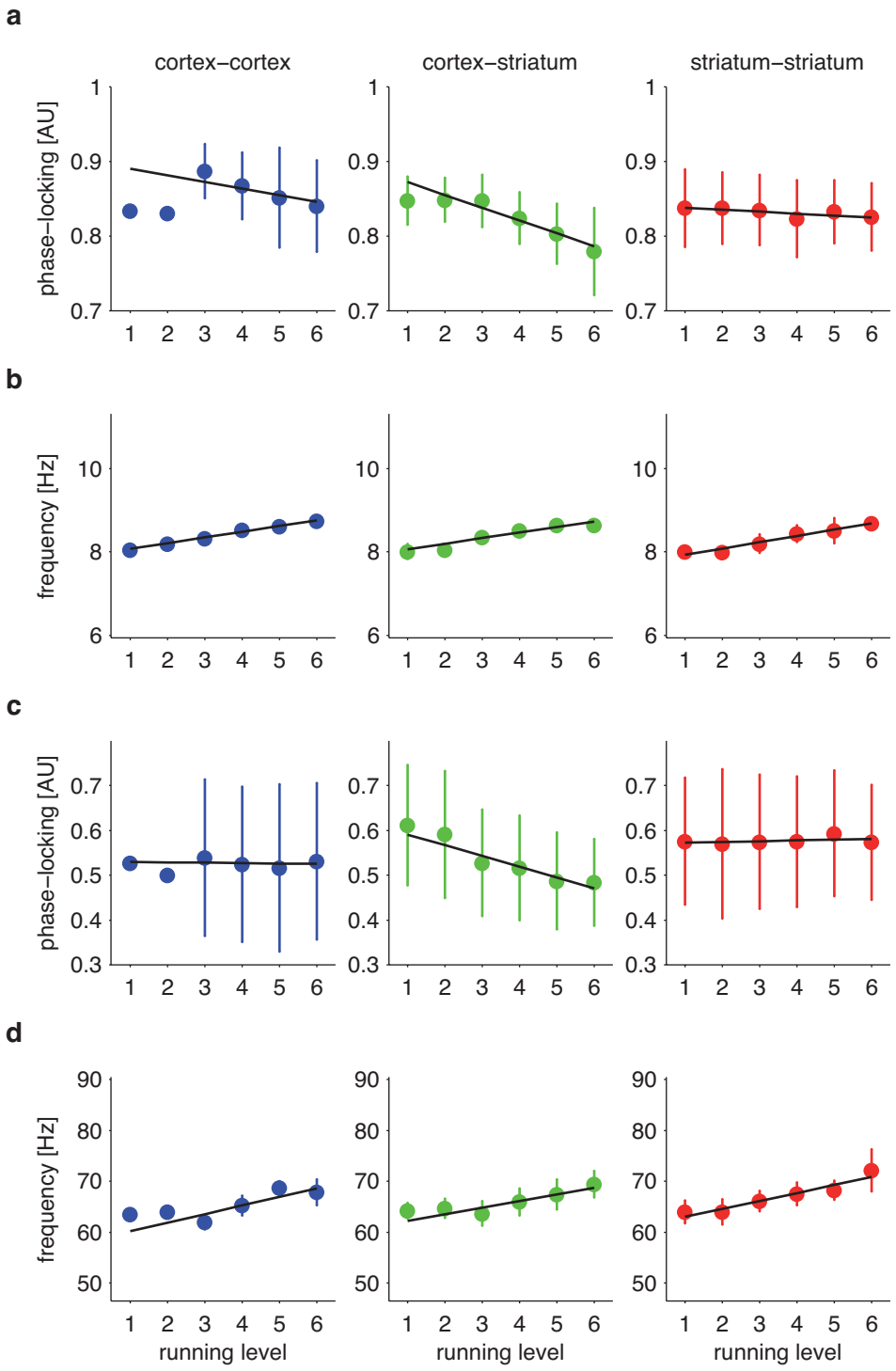

Figure 3.32: Level-resolved peak-frequency changes of monopolar LFP phase-locking values. (a) Mean phase-locking: Low frequency range. (b) Peak frequencies: Low frequency range. (c) Mean phase-locking: High frequency range. (b) Peak frequencies: High frequency range. Results are given as mean±sd.

4 Discussion

We had set out to study the spectral characteristics of population activities in structures along the cortico-striatal axis. Our results revealed prominent low- and high-frequency oscillatory patterns in cortex and striatum during resting and running states. Oscillations were synchronized within and between both structures and exhibited characteristic alterations of peak frequencies in relation to changes in motor demand, indicating their behavioral relevance. We also found distinct cross-frequency interactions between low- and high-frequency spectral components as well as intricate relationships between phase-coupling and power correlation measures that changed markedly with behavioral state.

In the following, we first discuss a couple of methodological issues (Section 4.1) that are important for the outcome of the present study and make suggestions for improvement of future experiments. Second, we provide a detailed evaluation of the results and compare them with those of other studies (Sections 4.2–4.6). Third, we interpret and discuss our findings with regard to their functional implications on a systems-level (Section 4.7) before we close the chapter by naming directions of possible future research endeavors (Section 4.8). Note that for reasons given below (Sections 4.1.5 and 4.1.7), we will mainly focus on the results of monopolar LFP analyses.

4.1 Methodological considerations

4.1.1 Behavioral model

We trained Brown Norway rats to reliably perform in a substantially demanding motor task designed to allow for a stable parallel recording of extracellular neuronal signals from their brains. As the results of a prior behavioral pilot study had shown (von Nicolai, 2011), this proved to be a considerable challenge. First, basic treadmill running capacities of individual Brown Norway rats vary considerably and in a largely unpredictable manner, which makes it difficult to quickly separate runners from non-runners. Second, since only about 25% of animals initially trained exhibit good and reliable performance capacities, this demands testing large samples before selection of the final experimental subjects. Third, for reasons discussed extensively by von Nicolai (2011), treadmill run-

ning according to a task design and in a behavioral environment such as ours can be potentially hazardous to the health of subjects which further limits the freedom to vary training parameter settings. Fourth, even in case of well-trained animals, our experience showed that pre- and post-operative behavioral capacities were not always well correlated and also varied considerably during days, weeks, and months following implantations. For all these reasons, treadmill training of Brown Norway rats for neuronal recordings under behaviorally demanding conditions is both time consuming and the outcome not easy to predict. Thus, we cannot unequivocally recommend the use of this animal model for studies of brain activities under awake behaving conditions. For an in-depth discussion of questions regarding optimal treadmill training parameters and general treadmill running capacities of Brown Norway rats, see von Nicolai, 2011.

Despite these limitations, we obtained a substantial amount of valid data from a decent number of subjects during both rest and locomotion on 6 different speed levels ranging from walking to high speed running. Behavioral results showed that subjects were in principle able to sufficiently perform in the task under recording conditions. They also exhibited some of the main features known from pre-operative training sessions (von Nicolai, 2011), such as large inter-subject variability of error rates and a strong trend towards an improvement of performance with increasing running speed. Challenges in terms of abrupt speed changes between levels only modestly increased error rates during subsequent epochs, indicating that animals were generally well capable of adapting behaviorally to sudden increases of motor demand. Still, many subjects exhibited considerably worse performance capacities after as compared to before implantations. In addition, behavioral results show that while a few animals ran very well and consistently both within as well as across trials and recording sessions, others performed close to the upper bound of error rates allowed by the setup, leaving only few trials with enough behaviorally valid epochs for level-based analysis of neuronal signals.

The makeup of implants and the very nature of the recording conditions also often constrained the amount of data useable for analysis. That is to say, obtaining artifact-free neuronal signals from awake animals running at high speeds over extended time periods and not just walking or trotting was by itself experimentally challenging because whole-body movement and its disruption during error periods are substantial sources of mechanical instability. This is certainly one reason why similar studies involving truly comparable task conditions are quasi absent from the literature (for examples of neurophysiological experiments employing treadmill running as a behavioral model, see Chapin and Woodward, 1982a,b; Chang et al., 2003, 2006; Shi et al., 2004, 2006). Variations in implantation outcome such as electrode state and placement or tissue affection further enhanced the vulnerability of recordings to external perturbations (see also Section 4.1.5).

4.1.2 Recording setup

In addition to difficulties associated with the behavioral model used, peculiarities of the recording environment also constrained the conditions of data acquisition. In particular, a smooth transfer of implanted animals connected to the recording system via headstage and tether cable onto the treadmill apparatus inside its box (Section 2.4.2) turned out to be of crucial importance for both safety of animals and materials as well as for the stability of some signal types. For example, we unfortunately lost almost all of the single-unit signals just detected during rest while transferring the rats from the plexiglas bowl onto the treadmill (Section 2.4.1). While this may also have been due to insufficient implant and implantation qualities, we consider the design of a recording environment better adapted to the peculiarities of the treadmill running model to be one necessary step to improve the outcome of data collection. One possible solution in this regard would be to combine the treadmill with a directly attached compartment to be used for electrode displacement during rest, such that animals could easily and even voluntarily move to the actual task environment. This would overcome the constraints imposed by the narrowly enclosed running lanes surrounded by high walls which are, on the one hand, needed to restrict the movement path of subjects but which prevent, on the other hand, electrode displacement during rest to be performed with animals on the treadmill.

4.1.3 Implantation issues

We used a self-modified microdrive equipped with 12 individually moveable microelectrodes to record neuronal signals from cortical and subcortical structures of both hemispheres of the rodent brain. We are not aware of any other study using a directly comparable approach for neuronal data acquisition under awake behaving conditions. However, the unique makeup of the implant also brought about particular technical challenges.

First, the current design of the cap attached to the bottom of the microdrive (Figure 2.3, page 29) only allowed for an approximate placement of the implant due to its size and stereotaxic manageability. Thus, targeting of specific, particularly small structures may be difficult although we do not consider this very problematic in the present case (see Section 4.1.4 below). More importantly, however, the cap's size and makeup resulted in an incomplete closure of the area between the skull's surface and the implant right around the large bilateral craniotomies. While we carefully tried to restrict the spread of dental cement used to fix the implant to the skull and to the anchor screws (Section 2.3.3), we cannot fully exclude occasional affections of neither electrodes nor brain tissue. A modification of the cap's design or a different way of its attachment to the skull may potentially better protect the implantation site and better ensure movability of electrodes.

Second, guidance of electrodes from the bottom of the implant to the top of the microdrive by means of polyimide tubes was complicated by the need to considerably bend them to allow for a targeting of specific holes inside the cap (Figure 2.3, panels c and d, page 29). We were surprised by the basically smooth movability of electrodes both before and after implantation. Nevertheless, in some cases electrodes got stuck somewhere on their way down from the top to the bottom of the implant impeding any further displacement. A mutual adaptation of the microdrive's and the cap's designs or even a switch from individually moveable to chronically fixed electrodes may be better apt to take full advantage of the cap's outline originally intended to allow for massively parallel, full-loop recordings from the basal ganglia and associated structures.

Third, the overall size of the implant was both potentially annoying for the animals as well as demanding for the experimenter with regard to their handling in the recording environment (Section 2.4.2). In general, animals appeared to very well tolerate the implant and quickly adapted to it. In most cases, wound healing was undisturbed and no outer affections of the implantation site were visible. However, note that while we obtained stable recordings from some subjects over the course of up to three months, others lost their implants after only about four to six weeks (see also Section 4.1.4 below). Post-mortem examination of bone structures showed that this was most probably the result of macerations around anchor screws and below areas covered by dental cement. Use of other materials for screws or smaller implantation sites, themselves necessitating the use of smaller implants, may be possible solutions to these problems.

Fourth, despite careful construction of implants and their thoughtful placement, we experienced a non-negligible loss of electrodes due to bending not only outside but also inside the brain. The use of electrodes larger in diameter than 75 μm may allow for better endurance when combined with an implant such as ours. For a more general discussion of methodological issues regarding ensemble and field potential recordings from awake behaving animals, rats in particular, see, e.g., Buzsáki et al., 1989; Kralik et al., 2001; Jog et al., 2002; Buzsáki, 2004.

4.1.4 Electrode positions

As mentioned above (Section 4.1.3), exact guidance of electrodes into target structures was complicated by peculiarities of the implant's design. Unfortunately, we did not obtain histological samples sufficient to ascertain recording positions post-mortem by means of electrolytic tissue lesions. This was due to both failures of perfusions and the fact that many subjects lost their implants prior to the end of experimental sessions.

However, we took great care on pre-operative planning stages, during surgeries, and during recordings to ensure correct placement of electrodes. First, coordinates were chosen such as to be comfortably accessible by means of large but circumscribed craniotomies. Second, we always advanced cortical and striatal electrodes by about 2 and 4 mm, respectively, prior to implantation to ease a direct hit of target structures by implantation alone. Third, we restricted our recordings to DV positions of up to 3 mm depth in case of cortical and between 4 and 7 mm depth in case of striatal electrodes (Section 2.3.1). Finally, as is shown in Figure 2.2 (page 2.2), the striatum is a huge structure covering large parts of the rat's forebrain. Our cortical electrodes were also aimed at regions covering extended areas of the brain's surface in both AP and ML planes. We are thus very confident that our electrodes were indeed correctly placed.

4.1.5 Data quality

As stated in Section 4.1.1, recording enough data of sufficient quality for signal analysis under treadmill running conditions was a substantial challenge. Because of behavioral and implantation issues, we recorded LFPs and MUA from 8 out of 10 rats successfully implanted. However, the quality of that data varied considerably both within and between subjects, necessitating a careful evaluation of signals prior to analysis.

We applied several methods ranging from on- and offline visual inspection of raw traces to automatic amplitude thresholding and variance tests (Section 2.6.1). We then excluded channels and epochs of trials failing to fulfill any one of those criteria from further analysis. Importantly, note that data selection took place *prior* to signal analysis and was thus not biased by specific later outcomes. Furthermore, we emphasize that to our knowledge the host of signal evaluation methods used here by far exceeds the average number of such steps carried out in other studies involving neuronal recordings from awake behaving animals. We are thus confident that the results reported are not substantially distorted by recording artifacts in the strict sense of the word (for a discussion of LFP data quality with regard to volume conduction issues, see Section 4.1.6).

Our trust in overall quality of LFP data notwithstanding, we point out that we interpret the quality of multi-unit activities in terms of signal strengths with considerable caution. As exemplified in Figure 2.11 on page 43, inspection of a large number of raw spike trains showed that signal-to-noise ratios were very low in many cases. This may well explain the quasi absence of MUA power peaks and the only small peaks in spike-field as compared to LFP coherence spectra. In addition, the variability of MUA analysis results across subjects was substantially larger than that of corresponding LFPs.

Certainly, none of these findings do by themselves unambiguously speak against good quality of MUA data. Accordingly, we did indeed find spiking signals to exhibit substantial modulations between behavioral states. Again, however, we stress that possibly due to impedance limitations signal-to-noise ratios of high-frequency components appeared to be much smaller than those of field recordings, imposing limitations on their validity and necessitating caution in their interpretation. We will therefore focus on the discussion of (monopolar) LFP data in upcoming sections, treating MUA results with diffidence.

4.1.6 Volume conduction

Field potential recordings are generally susceptible to artificial contaminations resulting from electrical activity generated by a single source being picked up by multiple, spatially separate sensors. Power and phase-coupling analyses of monopolar LFPs indicated strong, frequency-specific activities and highly similar coupling characteristics within and between structures. How sure can we be that these effects were due to strictly localized activities and proper phase-locking between them rather than volume conduction effects?

First, despite their similarity, cortical and striatal power as well as ordinary coherence and phase-locking spectra of within- and between-structure pairings did exhibit quantitative differences, arguing against an exclusive origin from one common source. Second, imaginary coherence spectra and phase angle histograms of cortico-striatal electrode pairs were qualitatively and quantitatively clearly distinct from those of cortico-cortical and striato-striatal pairs. They exhibited distinct structure and indicated frequency-specific, non-zero phase-coupling between the two regions. These findings are incompatible with the instantaneous effects of volume conduction. Third, coherence and phase-locking values displayed substantial, frequency-specific, cross-hemispheric biases which we would not expect in case of a global, artificial spread of activities. Fourth, despite a low signal-to-noise ratio (Section 4.1.5), multi-units and LFPs from the same and different structures were significantly coherent across wide spectral regions. Since MUA are assumed not to be susceptible to volume conduction, such signs of local interactions argue strongly against a purely artificial origin of LFPs. Finally, bipolar LFP power and phase-coupling spectra retained substantial amounts of power and exhibited significant coherence and phase-locking values in both low and high frequency ranges, respectively. Thus, even after cancellation of common source signal components by means of bipolar derivations localized activities underlay to a considerable degree the effects originally observed.

Taken together, we are confident that monopolar LFP effects were not primarily caused by volume conduction. Nevertheless, we also stress that a reference electrode placed inside the brain at an electrically largely neutral spot such as white matter regions

may further enhance signal quality and stability. Directly performing bipolar recordings instead of offline derivation of signals would be another option, although this may also negatively affect the outcome of data collection as is discussed in the next section (4.1.7).

4.1.7 Bipolar derivations

We created bipolar derivations from monopolar LFPs to reduce the influence of common source effects on local activities. Low-frequency running power and phase-coupling peaks were largely robust to differentiation. Bipolar spike-field coherence spectra also retained many of their characteristics, although couplings were less often significant.

However, bipolar derivation procedures also substantially altered qualitative and quantitative characteristics of power, coherence, and phase estimates, most prominently so in higher frequency regions. Most strikingly, phase angle measures between bipolar LFPs revealed a substantial alteration of distributions, with values being much less specifically concentrated than in the monopolar case (Figure 3.17, page 86). At this point, note that the plots shown in Figure 3.17 depict distributions thresholded for phase angle concentrations deviating significantly from those obtained from phase-coupling measures between time-shifted LFPs. Inspection of non-thresholded frequency-phase histograms revealed that bipolar LFP phase angle concentrations were actually *lowest* in terms of absolute values in significant bins and that phase angles were much more broadly distributed and statistically more close to random distributions in other regions of the histograms. This was particularly the case for phase angle measures between cortical and striatal electrodes where distributions were largely flat across the spectrum. Related observations were made when comparing imaginary monopolar and bipolar coherence spectra (Figure 3.9, page 77). There, the characteristic spectral structure of non-zero phase coupling between cortical and striatal signals is lost following signal derivation.

We do not generally deny the potential usefulness of bipolar derivations in canceling of artificial common source effects. Still, given the above findings and comparing them with those of monopolar LFPs, we argue that these procedures may not only have improved but also partly distorted the quality of our data. This is because first, monopolar LFP power and phase coupling spectra exhibited distinct structure, including characteristic cross-hemispheric biases, significant differences between coherence and phase-locking values and frequency-specific temporal lags between cortical and striatal activities that are by themselves indicative of a non-artificial origin of the underlying signals (Section 4.1.6).

Second, the near-zero phase coupling particularly between within-structure pairings does not by itself prove volume contamination of LFPs. In fact, popular theories of intra- and inter-areal neuronal communication that are based on mechanisms of coherent

oscillations as major operational principles explicitly allow for near-zero phase coupling of population activities (Fries, 2005; see also Figure 1.4 on page 17) which has also been observed in earlier studies of functional interactions between different cortical areas during behavior (e.g., Frien et al., 1994; Roelfsema et al., 1997).

Third, studies into the spectral characteristics of basal ganglia structure population activities have not only revealed prominent, frequency-specific oscillations in *monopolar* LFP signals of anesthetized as well as awake animals but also distinct relationships between those oscillations and the firing patterns of single cells (e.g., Berke et al., 2004; Berke, 2009; Sharott et al., 2009; van der Meer and Redish, 2009). Unfortunately, we are not able to provide equivalent evidence of such relationships in our data. However, using recording techniques similar to the ones employed in those studies we have no *a priori* reason to suppose that our signals would not have exhibited similar features.

Fourth, with the exception of a few examples (Magill et al., 2006; DeCoteau et al., 2007b), bipolar derivations of monopolarly recorded LFP signals are hardly ever employed in the analysis of spectral characteristics of basal ganglia activities. In case of the striatum, caution is indeed much warranted since its non-laminar constitution promotes a wide spread of electrical fields for mere structural reasons. Thus, subtraction of signals recorded at different spots not too far spatially separated can be readily expected to lead to a cancellation of local signal components having similar amplitude and phase characteristics.[1] Indeed, the study by Magill et al. (2006) found power and coherence spectra of striatal and pallidal LFP signals to only exhibit prominent low-frequency (∼8 Hz) but no high-frequency peaks, in partial agreement with our results. In the study by DeCoteau and colleagues (DeCoteau et al., 2007b), prominent striatal theta activities as seen in monopolar LFPs survived bipolar derivation procedures with similar consequences as in our case, namely a reduction in absolute power and coherence strengths.

Finally, reflection of the method used for bipolar derivation indicates that the signal components mostly affected by it are those having near-identical instantaneous amplitudes and phases but by no means must be completely of common origin. At the same time, as discussed above, these may also be the ones most important for appropriately timed communication between neuronal ensembles. Thus, we do interpret the outcomes of bipolar LFP analyses with considerable caution and do not take them as indisputable evidence for an artificial origin of monopolar LFP results. This is why we will mainly discuss the latter in upcoming sections.

[1] Similar arguments may also hold for laminar structures such as the cortex. Note also that the physical reasons for an intracerebral spread of electrical fields are not identical to those affecting extracranial recordings of neuronal mass activities like EEG or MEG-signals such as disturbances deriving from bone and skin tissue (Nolte et al., 2004).

4.1.8 Signal analysis

We pooled data from rest and running epochs to obtain averages of the respective behavioral levels. At this point, how sure can we be that these epochs only contained signals recorded during proper rest and actual running? With regard to resting conditions, we note that although some animals sometimes moved around a bit or showed sniffing and grooming behavior before and even during the 60 seconds before the start of a trial, they mostly indeed sat quietly at the back end of the running lane. This state was clearly distinct from that during locomotion, and we expect signal characteristics during occasional minor movement episodes prior to running to have mostly averaged out due to the much larger number of true resting epochs. In case of running epochs, we think that our way of separating movement episodes from those of supposed movement errors (i.e., in the worst case, an animal resting on the moving belt) by means of epochs as delimited by the treadmill software (Section 2.1) was sufficient to obtain real running data.

This is because first, in the one animal (a6; Table 2.1, page 60) that we obtained the best (LFP) data from, behavior was close to perfect with the animal running at the front end of the lanes almost all over the time (Section 3.1). We thus obtained long, continuous records lasting up to the full number of 48 5-second running epochs undisturbed by movement errors. These data exhibit all of the most prominent grand average characteristics and they are clearly distinct from resting results which, in addition, also were best in this animal which behaved most calmly in comparison to all its peers.

Second, a simple calculation shows that even a single 5-second epoch judged as behaviorally valid because no light beam break occurred is incompatible with a rat resting instead of running on the belt. That is, given the lowest speed of belt movement of 0.16 m/s (corresponding to 16 cm/s) and a length of the running lane of 50 cm, an entire epoch of rest on the belt would have directly resulted in an error. To reply to the objection that animals may have only moved briefly in short bouts when approaching the back ends and then returned to rest again, we state that we hardly ever observed such behavioral patterns. We do acknowledge the possibility of an even more restricted sampling of behavioral epochs by means of exclusion of also those actually valid epochs in immediate vicinity to invalid ones. Note, however, that our approach may have at maximum only worked against us and that we would expect even more distinct differences between resting and running activities when analyzing the data in this way.

4.1.9 LFP origins

For reasons given in Section 4.1.5, we will mainly focus on the discussion of LFP results as a measure of population activities in the following. Thus, what are the anatomical

and physiological underpinnings of local field potentials? According to Mitzdorf, "[...] Field potentials, although easy to record, are difficult to interpret. They are indirect and ambiguous reflections of the underlying neuronal activities. Action potentials, on the other hand, are clearly identified as the unique output signals of single units." (Mitzdorf, 1985, page 38). To put things more straightforward, LFPs are generated by inward and outward current flows across neuronal membranes resulting in current sinks and sources as viewed from extracellular space (Mitzdorf, 1985). As such, they can be taken to reflect the average electrical activity of a large number of cells. The spatio-temporal average of excitatory and inhibitory postsynaptic potentials (EPSPs and IPSPs, respectively) of a population of cells likely makes up the largest part of the LFP, which is why they are generally assumed to mostly represent the input to an assembly (Freeman, 1975; Mitzdorf, 1985; Logothetis et al., 2001; Buzsáki, 2006). However, the effects of spontaneous subthreshold membrane potential oscillations and unit activities such as spike afterhyperpolarizations do also contribute to the LFP (Moran and Bar-Gad, 2010).

There has been an ongoing debate as to the spatial range over which neuronal sources contribute to the LFP measured at one location. Theoretical considerations and estimates based on experimental measurements indicate an extent of a few hundred micrometers up to several millimeters in cortical areas (Mitzdorf, 1985; Engel et al., 1990; Logothetis et al., 2001; Katzner et al., 2009). A very recent study using careful parallel recordings of evoked electrical and optical signals in cat visual cortex estimated that more than 95% of the LFP signal reflecting stimulus orientation preference were generated within $\sim$250 μm vicinity of the electrode tip (Katzner et al., 2009). This indicates that LFPs can indeed be interpreted as the average activity of a truly local population of neurons.

As indicated repeatedly in the text, spatial sampling of LFPs in non-laminated structures such as the basal ganglia may well be different from that in cortical regions. However, as we will point out again below, there are good reasons to assume that also in these cases LFPs can often be taken to mostly reflect localized activities because of their distinct relationships to multi- and single-unit activities, timing or amplitude differences between recording sites or differential coupling to input sources or output targets (e.g., van der Meer et al., 2010). We are thus confident that our LFP measurements also mostly represent average electrical signals of local neuronal populations.

4.2 LFP power characteristics

Power spectra of both cortical and striatal monopolar LFPs exhibited strikingly similar characteristics. They were marked by strong increases in power between rest and running as well as prominent low- and high-frequency peaks that shifted between behavioral

states. Striatal low as well as cortical and striatal high power peak frequencies even scaled significantly in a linear fashion with running speed.

The peaks in cortical and striatal LFP power spectra indicate the presence of true oscillatory processes of band-limited frequency in the underlying signals (Wang, 2010). Remarkably, both low- and high-frequency peaks were of comparable extents, spanning approximately one octave of spectral bandwidth each. Their center frequencies were located in the so-called *theta* (θ, ~4–9 Hz) and *gamma* (γ, ~30–100 Hz) frequency bands, respectively. Neuronal activities in these spectral regions have been shown to be associated with a variety of behavioral aspects, ranging from learning and memory formation to spatial navigation and also locomotion in case of the former, and from elementary sensory processing mechanisms to diverse cognitive functions such as attention in case of the latter (e.g., Bland and Oddie, 2001; Engel et al., 2001; Buzsáki, 2002; Fries, 2009).

Power characteristics in cortex and striatum were partly similar and partly different from those reported in previous studies in the same species and comparable overall conditions. In particular, prominent peaks of oscillatory power have been observed in striatal LFPs in theta and *alpha* (α, ~9–13 Hz) frequency ranges during rest and movement episodes in rats (Berke et al., 2004; Dejean et al., 2007). In another study, theta power was differentially modulated at various stages of a spatial navigation task, indicating an involvement in more complex behaviors (DeCoteau et al., 2007b). In contrast to some reports (Berke et al., 2004; Dejean et al., 2007), localized low-frequency oscillatory activities did not exhibit the shape of high-voltage spindles in our case as verified through visual inspection of raw and LFP-data band-pass filtered in the theta range.

Previous experiments have not consistently found distinct relationships between the strength and peak frequencies of striatal oscillatory theta power and movement parameters such as running speed and acceleration (DeCoteau et al., 2007b). In contrast, theta oscillations in the hippocampus have explicitly been linked to sensorimotor processes in addition to their well-documented functions in memory formation, learning, and spatial navigation (Bland and Oddie, 2001; Kahana et al., 2001; Buzsáki, 2002). Accordingly, LFP recordings from hippocampal areas in rodents have repeatedly been shown to exhibit marked theta power during rest and running episodes. On top, hippocampal theta power has been reported to scale with running speed in terms of magnitude and sometimes even peak-frequency (Vanderwolf, 1969; McFarland et al., 1975; Teitelbaum et al., 1975; Bragin et al., 1995; Rivas et al., 1996; Buzsáki et al., 2003; Wyble et al., 2004; Chen et al., 2011), which is in striking agreement with our results. However, more recent investigations have questioned a direct relationship between theta oscillations and locomotor behavior, arguing that various sensory and cognitive factors involved in many of those task may better account for the observed effects (Montgomery et al., 2009).

It has been argued that a large part of theta activities recorded in both cortical and subcortical structures may not only be influenced by but also directly originate from hippocampal sources, thus essentially reflecting volume conduction effects (Sirota et al., 2008). We cannot unequivocally resolve the true anatomical source of theta activities we recorded in cortical and striatal structures. However, the same authors (Sirota et al., 2008) and also others (Kahana et al., 2001) have noted that this does not preclude local generation of theta oscillations in regions distant from the hippocampus as revealed for example in intracranial recordings from human subjects (Kahana et al., 1999) or in rodent somatosensory areas (Sirota et al., 2008). Indeed, we have observed prominent peaks of theta power not only in monopolar but also bipolar LFPs, in agreement with other studies (DeCoteau et al., 2007b; Sharott et al., 2009). Furthermore, locking of unit activities in various structures including motor cortex and striatum to oscillations in the theta range has repeatedly been shown (Berke et al., 2004; Dejean et al., 2007) and our spike-field coherence spectra do also exhibit peaks in the same frequency band. We are therefore confident that the prominent theta oscillations reported here at least partially reflect truly localized neuronal population activities. Alternatively, they may also be driven to a substantial degree by brainstem generators that have been argued to be the major source of oscillatory activities in the theta frequency range as found in cortical and subcortical structures during sensorimotor behavior (e.g., MacKay, 1997; Bland and Oddie, 2001; see also Section 4.7 below).

Gamma oscillations also are a prominent feature of striatal LFPs in the rat. Under anesthesia and during quiet rest, they have been found to peak between 50–55 Hz, as in the present case (Berke et al., 2004; Berke, 2009; Sharott et al., 2009). In contrast, gamma power during active behavior has mostly been described to peak at frequencies and to be modulated by tasks demands different from those of our study. Thus, van der Meer and Redish (2009) showed ventral striatal gamma power at around 50 Hz to be increased following reward delivery and before movement initiation, whereas gamma power around 80 Hz ramped up and peaked before reward delivery in a spatial decision task. Similarly, Berke (2009) found ventral striatal gamma oscillations of similar frequencies also to be modulated by reward receipt. The latter study also demonstrated a shift of gamma power peaks from below 60 to around 80 Hz after administration of psychomotor stimulant drugs. Kalenscher et al. (2010) reported gamma power characteristics in ventral striatal LFPs in a spatial decision task similar to those of van der Meer and Redish (2009) and Berke (2009). Their investigation of movement-related effects revealed no distinct relationship between neither velocity nor acceleration on striatal gamma power.

In contrast, Masimore et al. (2005) found striatal LFP gamma power peaks between 48-58 Hz in awake rats to occur in brief bursts of about 150 ms length around movement

onset. Furthermore, this so-called *γ-50* power increased markedly with increasing movement speed of the animals. Oscillatory gamma power has also been shown to peak above 50 Hz in LFP recordings in another basal ganglia structure, the subthalamic nucleus (see Figure 1.1, page 2), both in Parkinson's disease patients and in healthy rats during rest (Brown et al., 2002). This spectral signature exhibited distinct increases in magnitude during movement as compared to quiet resting states. Resting gamma peaks at around 60 Hz have also been observed in the entopeduncular nucleus, the rodent equivalent of the external palladium of primates, in rats (Dejean et al., 2011).

In summary, available evidence suggests that gamma oscillations are a prominent feature of population activities in the basal ganglia and that they are functionally relevant as indicated by their task-dependent modulation. While the true origin of gamma oscillations recorded at striatal sites has also been questioned (Berke, 2005), precise locking of striatal unit activities to LFPs suggests at least a partial local origin and again points to their relevance for striatal network function (see Section 4.7 for an in-depth discussion of this topic). Our results underscore and extend these findings in that they demonstrate a scaling of cortical and striatal gamma power magnitudes and peak frequencies with motor demand. This indicates that these activities are indeed of direct behavioral relevance rather than volume conducted from distant sites or merely an epiphenomenal consequence of population dynamics.

Oscillations in sensorimotor cortical regions have so far been described to be most prominent in alpha and *beta* (β, ∼13–30 Hz) frequency bands. As such, they have been related to preparatory and organizing aspects of movement, sustained motor activities such as contractions or even sensorimotor feedback and attentional mechanisms rather than movement *per se* like proper locomotion (Murthy and Fetz, 1992; Sanes and Donoghue, 1993; Murthy and Fetz, 1996a,b; MacKay, 1997; Salenius and Hari, 2003; Baker, 2007). Indeed, both theta and alpha rhythms are also a prominent feature in rat somatosensory and motor cortical regions associated with whisking behavior, indicating a role in the interplay between motor activity and sensory feedback during natural movements and orienting behavior (Nicolelis et al., 1995; MacKay, 1997; Buzsáki, 2002).

However, we note that sensorimotor behavior has also been found to be accompanied by patterns of faster synchronous oscillations in the (low) gamma band (mostly between 30 and 60 Hz) as recorded within or above motor and somatosensory cortical sites (Bouyer et al., 1981; Pfurtscheller et al., 1993; MacKay, 1997; Donoghue et al., 1998; Brown, 2000; Mima et al., 2000; Baker, 2007; Omlor et al., 2007). As in the case of beta frequency activities, low gamma field potential oscillations often exhibit distinct relationships to electromyographic (EMG) signals recorded from peripheral muscles during periods of sustained and ongoing movement (MacKay, 1997; Brown, 2000; Mima et al., 2000; Baker,

2007; Omlor et al., 2007). Further, firing of single- and multi-units in sensorimotor cortical areas has been shown to be entrained by and to exhibit oscillatory and synchronized patterns in clear relation to beta and gamma field potential oscillations (Murthy and Fetz, 1996a,b; Donoghue et al., 1998; Fetz et al., 2000). Again, close examination of the behavioral correlates of these activities raised doubts about their direct involvement in the encoding of sensorimotor variables. Instead, these findings have fueled speculations about a more global role of synchronous oscillations in gating or routing of information flow in cortical and subcortical sensorimotor neuronal networks (Brown and Marsden, 1998; Brown, 2000; Fetz et al., 2000), an idea that we will return to below (Section 4.7).

It is interesting that Niell and Stryker very recently have found both theta and gamma oscillatory LFP power in visual cortex of mice to decrease and increase, respectively, between rest and locomotion on a spherical treadmill (Niell and Stryker, 2010). Theta peaks in their recordings were virtually identical to ours, while gamma resting peaks were centered above 60 Hz. Both low- and high-frequency peaks shifted upwards between behavioral states. This suggests that locomotion as a state of increased behavioral activity is characterized by a generally stronger drive of not just sensorimotor but also other cortical areas exerted by ascending brainstem projections and possibly partly mediated by thalamocortical loops (Steriade et al., 1991; Munk et al., 1996; Steriade et al., 1996, 2001). As we discuss below (Section 4.7), activation of widespread cortical but also subcortical areas like the striatum may be accompanied by strong increases of low- and high-frequency activities facilitating both sensory and motor processing alike. This is in partial contrast to the results of Niell and Stryker (2010) but agrees well with our finding of a spectrum-wide increase of power between resting and running states which nevertheless shows a clear separation between effects in low and high frequency bands, indicating distinct underlying network mechanisms (Steriade et al., 1996; Siegel and Konig, 2003).

4.3 LFP phase-coupling characteristics

Coherence and phase-locking analyses of cortical and striatal monopolar LFPs revealed prominent low- and high-frequency coupling patterns within and between structures. Center frequencies of low- and high-frequency coupling were the same as in power spectra, thus located in theta and gamma bands, respectively. Phase-coupling increased between rest and running in a frequency-specific manner, and both low- and high-frequency peaks shifted markedly between behavioral states. On top, theta and gamma LFP peak frequencies exhibited highly significant linear scaling with increasing motor demand. Results of imaginary coherence and phase angle analyses indicated a near-zero phase synchronization of LFP signals within structures but a temporally delayed coupling of cortex and

striatum in low and high frequency ranges. Furthermore, LFP phase-coupling patterns showed a strong, frequency-specific intra- vs. cross-hemispheric bias.

As indicated above (Section 4.2), prominent patterns of localized low- and high-frequency LFP oscillations have been described in regions along the cortico-striatal axis. In particular, theta and gamma oscillations have been shown to be highly synchronous across wide regions of the striatum (Berke et al., 2004; Masimore et al., 2005; DeCoteau et al., 2007b; Dejean et al., 2007). Also, theta and gamma oscillations are strongly synchronized between cortical ECoG or LFP and striatal LFP signals as determined by visual inspection or coherency analyses (Dejean et al., 2007; Berke, 2009; Sharott et al., 2009; Syed et al., 2011). Theta coherence peaks reported in these studies are mostly similar to ours or slightly lower or higher. In contrast, gamma coherence peaks are only partially the same. For instance, Berke (2009) reported on gamma LFP coherence peaks centered slightly above 50 Hz but also around 80 Hz, and differential coherence patterns between striatal LFPs and ECoGs recorded from different cortical regions. In general, coherence between striatal LFPs has been found to be rather high in both low and high spectral regions (Berke et al., 2004; DeCoteau et al., 2007b; Berke, 2009). This has been argued by some to indicate volume conduction effects (Berke, 2005) but may also well be a sign of a strong and physiological coordination of population activities in this anatomically largely homogenous, non-laminated structure.

The reason for the partial discrepancy between our results of coherency and also power analyses and those of previous studies is unknown. For one thing, they may be due to differences in animal strains, since we employed Brown Norway rats which are hardly ever used in neurophysiological experiments. For another thing, differences in primary electrode targets may also have played a role, since some of the above studies explicitly recorded from ventral striatum (Berke, 2009; van der Meer and Redish, 2009) whereas we aimed at recording from dorsolateral striatal regions. Most importantly, however, results may be different mainly because of fundamental differences between behavioral paradigms. Ours was designed to the most possible extend as a purely sensorimotor task whereas other studies involved more cognitive elements such as spatial navigation and decision-making, reward-related behaviors, and processing of auditory or visual stimuli. Still, in all of these conditions animals were required to move between resting episodes, and it is therefore surprising to see our results to differ so much in some regards from those of other investigations. Even more so, van der Meer and Redish (2009) explicitly noted that both low and high gamma effects in their study could not straightforwardly be explained by effects of running speed of the animals. Similarly, Berke et al. (2004) found strong general increases in theta, beta, and gamma band coherence between striatal electrodes when comparing resting with movement episodes, but no shifts of peak

frequencies. However, many studies do not explicitly account for possible movement-related effects on changes in power and coherence. That being said, our experiment was certainly exceptional in that it required animals to exert rhythmic, continuous running at moderate to high speeds, which is a clearly different behavioral demand than exploration of and shuffling through a maze. This may well explain the peculiar findings of this study and also offer an explanation for the scaling of power and phase-coupling peak frequencies with running speed which we discuss in more detail below (Section 4.7).

We found phase-coupling between cortico-cortical, cortico-striatal, and striato-striatal electrode pairs to exhibit strikingly similar structure, in analogy to LFP power spectra. Phase-locking values were smaller in every case compared to corresponding coherence values although spectra exhibited exactly the same qualitative characteristics. This is a strong indication for a true physiological coupling of low- and high-frequency rhythms within and between structures that goes beyond a mere correlation of amplitude fluctuations. The results of imaginary coherence and phase angle analyses further support the finding of a frequency-specific coupling between cortical and striatal regions. This is because the corresponding spectra and histograms exhibit non-zero values and distinct shape including phase-lags between pairs from different but not the same regions as can be expected when considering the underlying anatomy and associated circuit dynamics.

Most strikingly, imaginary coherence and phase angle analyses indicate a substantial temporal lead of cortical over striatal structures in the theta range, but a reverse relationship within the gamma range. While this is another strong argument against the notion of a purely artificial, volume conducted origin of cortical and striatal LFPs, it also indicates different temporal dynamics between and potentially distinct roles of population activities subserving low- and high-frequency oscillations. The strong influence that cortical regions exert on the striatum is easy to reconcile with the underlying anatomy given the one-way makeup of cortico-striatal projections. Still, although coherency analysis measures provide only correlative instead of causal information about the interaction between brain structures, the partially closed anatomical loops of cortico-basal ganglia circuitry could also subserve feeding of subcortical rhythms back into the frontal cortex. Indeed, learning-related changes of task-specific striatal unit activities have been shown to precede similar changes in cortex (Pasupathy and Miller, 2005), and subsets of striatal units often increase their discharge rates prior to movement onset which is generally thought to depend on motor cortical activities (e.g., Crutcher and DeLong, 1984b; Hikosaka et al., 1989a; Alexander and Crutcher, 1990b; Crutcher and Alexander, 1990; Georgopoulos, 1994). The results of the present study are, however, the first to indicate comparable temporal dynamics between oscillatory cortico-striatal population activities.

Our data are among the first to describe the frequency-specific synchronization of population activities recorded directly from within both cortex and striatum in the awake rat during rest and sensorimotor behavior. The nearly zero-phase coupling between within-structure electrode pairs is in good agreement with previous studies showing this to be a typical feature of cortical and striatal LFP recordings (e.g., Frien et al., 1994; Murthy and Fetz, 1996a,b; Roelfsema et al., 1997; Courtemanche et al., 2003; DeCoteau et al., 2007b; Wang, 2010). Modeling work has provided important insight into mechanisms potentially subserving zero-phase coupling between distant cortical sites, whether they are based solely on cortico-cortical or, alternatively, cortico-thalamocortical interactions (Traub et al., 1996; Vicente et al., 2008; Gollo et al., 2010; Wang, 2010). Whatever the underlying mechanism, zero-phase or near-zero phase coupling between different brain areas is an essential ingredient in currently popular theories regarding the large-scale organization of neuronal networks underlying organized behavior (Fries, 2005; see also Fell and Axmacher (2011) for a brief discussion of the peculiarities of zero-phase synchronization). Our results lend further support to these notions in that they indicate similar coupling dynamics to subserve the interaction of cortical and basal ganglia structures. At this point, we note that what appears as zero or near-zero phase synchronization may also reflect interactions temporally delayed by one or more full oscillatory cycles, particularly with regard to gamma band activities and associated short conduction delays.

To the best of our knowledge, the present study is the first to directly investigate differences between coupling patterns of cortical and striatal regions across hemispheres. We found markedly stronger coherence and phase-locking between ipsi- as compared to contralateral LFP pairs. This effect was the same for within- and between structure pairings, which in the case of cortico-striatal electrode pairs nicely reflects the stronger ipsilateral anatomical projection (Section 1.2.2). In addition, these data are another strong argument against a purely volume conducted origin of LFPs, since in that case one would not expect comparable cross-hemispheric biases in coupling.

Although significant across almost the entire spectrum in each case, cross-hemispheric LFP coupling differences exhibited distinct, frequency-specific patterns. Phase-coupling in the gamma band showed a much greater hemispheric bias than phase-coupling in the theta range, and non-significant phase-locking and coherence values were exclusively confined to low spectral regions. This agrees very well with common notions regarding low- and high-frequency oscillations to preferentially reflect, respectively, global and local scales of neuronal processing (Donner and Siegel, 2011; but see Section 4.7 below).

Last but not least, we also quantified the discrepancy between cross-hemispheric coherence and phase-locking differences. Cross-hemispheric biases were significantly larger for phase-locking values or zero at exactly the center frequencies of low- and high-frequency

peaks in power and phase-coupling spectra. These data further underscore that the synchronization of theta and gamma oscillations within and between structures does indeed reflect frequency-specific phase-coupling rather than mere amplitude correlations.

4.4 LFP cross-frequency interactions

Only a few studies have as yet investigated the relationship between different frequency components of population activities in structures along the cortico-basal ganglia loop and the cortico-striatal axis in particular. Phase-amplitude coupling analyses of monopolar LFPs indicated substantial modulations of the amplitudes of high-frequency oscillations by the phase of low-frequency rhythms. The magnitude of cross-frequency interactions increased markedly between rest and running. Similarly, LFP power correlation analyses revealed strong co-fluctuations between low and high spectral components. However, band-limited correlations between theta and gamma rhythms decreased significantly between behavioral states. Low and high peak frequencies at phase-amplitude coupling and power correlation maxima deviated from those of power and phase-coupling spectra.

4.4.1 LFP phase-amplitude coupling

Phase-amplitude coupling analyses are increasingly applied to study the interactions between low- and high-frequency components of neuronal population activities (Jensen and Colgin, 2007; Le Van Quyen and Bragin, 2007; Tort et al., 2010; Fell and Axmacher, 2011). For example, Canolty et al. (2006) showed the amplitude of gamma oscillations in recordings from the human neocortex to be strongly modulated by the phase and also the amplitude of concomitant theta oscillations. Axmacher et al. (2010) investigated phase-amplitude coupling in the human hippocampus and found working memory associated processes to be favored by theta phase modulation of beta and gamma amplitudes. Theta-gamma coupling was also reported to increase during item-context association learning in the hippocampus of rats (Tort et al., 2009). In contrast, Cohen et al. (2009) demonstrated a reward-related phase-amplitude modulation between alpha and gamma oscillations in the human nucleus accumbens, the most anterior part of the ventral striatum.

Of particular relevance for our study, Chen et al. (2011) found the amplitudes of low and high hippocampal gamma oscillations to increase with running speed. Interestingly, the phase-dependence of the different gamma components was restricted to distinct theta phases that dissociated with increasing running speed (see also Section 4.7 below). Overall, theta phase and gamma amplitude frequencies around coupling maxima were strikingly similar to power and phase-coupling peak frequencies in our study.

Another recent paper demonstrated theta-gamma cross-frequency coupling patterns within and between hippocampal and interconnected striatal regions in the rat (Tort et al., 2008). Striatal and hippocampal LFP gamma power was strongly modulated by low to high (3–8 Hz) theta phase, and the peak-frequency of that modulation shifted to higher values across subsequent events of a spatial navigation (t-maze) task. Furthermore, strong patterns of phase-amplitude coupling were found between hippocampal and striatal low- and high-frequency oscillations, demonstrating the reciprocal cross-frequency interaction of population activities between the two areas.

The outcomes of the study of Tort et al. (2008) are very important for the interpretation of our results for two reasons. First, gamma amplitudes peaked at the falling flanks and troughs of theta phases, as we have found in our data. Second and most importantly, the data of Tort et al. (2008) demonstrate a similar discrepancy between low and high power and coherence peak frequencies and the frequency pairs of maximum phase-amplitude coupling. More specifically, theta–gamma phase-amplitude coupling peak frequencies during t-maze running were centered around 7 and broadly between 80–120 Hz instead of around to above 8 and below to around 60 Hz. The authors interpreted this finding as possibly being due to the diverse sources of input reaching the striatum other than those from the hippocampus, such as neocortical, thalamic, or pallidal projections. Thus, the most striking result of phase-amplitude coupling analyses in our study agrees well with the findings of another recently published investigation.

In summary, the present study is the first to demonstrate the modulation of high-frequency amplitudes by the phase of low-frequency oscillations in structures along the neocortical-striatal axis. This indicates that fluctuations of population activities in different frequency bands are not independent but exhibit distinct relationships within and between those structures. The potential functional relevance of such cross-frequency interactions is further underscored by the finding of a marked increase of the strength and more distinct shape of the pattern of phase-amplitude coupling between rest and running. We will return to this issue below (Section 4.7). At this point, it may be argued that some of the effects described above are mainly due to the increase of oscillatory amplitudes in both structures between behavioral states and thus be essentially the consequence of an increase in signal-to-noise ratio. As the results of cross-frequency power correlations discussed in the next section (4.4.2) demonstrate, this is not likely to be the case.

4.4.2 LFP power correlations

Functional coupling of brain structures can also occur in terms of a correlation of amplitude or power fluctuations of local signals which is different from phase-coupling proper

as assessed by coherency analysis (Bruns et al., 2000). Furthermore, in addition to phase–amplitude coupling, interactions between different frequency components may also take the form of amplitude–amplitude or power–power modulations. We investigated the correlations of signal amplitudes at the same and across different frequency components.

To give a few examples of similar analyses from the basal ganglia literature, Sharott et al. (2009) examined power correlations between ECoGs and striatal LFPs in anesthetized rats. They found strong negative correlations between low (35–55 Hz) and high (60–80 Hz) gamma frequency oscillations but positive correlations between various low frequency components in *delta* (δ, ∼1–4 Hz) and theta ranges. In contrast, Dejean et al. (2011) investigated LFPs recorded from the globus pallidus in awake rats during quiet rest. Power spectra exhibited prominent peaks at around 14 and, in particular, close to 60 Hz, which is in very good agreement with our cortical and striatal resting gamma peaks. Cross-frequency correlation analyses showed low- and high-frequency oscillations to be strongly anticorrelated. Interestingly, both oscillatory components were also nested in different phases of slow delta frequency oscillations. In addition, these cross-frequency interactions were differentially modulated by D1 and D2 dopamine receptor antagonists.

Our results for the first time show an extended spectral band of significant positive correlation between low- and high-frequency monopolar LFP power components in the resting rat within and between cortical and striatal structures. Low- and high-frequency peaks were centered on 8 and broadly stretched between 64 and 128 Hz, which is in glaring contrast to the corresponding resting power and phase-coupling peaks. Most strikingly, power correlations between low- and high-frequency components decreased significantly during running. However, power correlations increased strongly between various combinations of lower frequency components.

We do treat the latter changes with some caution since the maxima of their distributions and corresponding center frequencies may largely represent harmonic pairs. However, we still note the interesting property that power correlations increase most strongly along those bands which are not marked by prominent peaks of oscillatory power and phase-coupling during running. On the one hand, these changes may well and mainly be the consequence of the broad-band and spectrum-wide increase of power between rest and running non-specifically reflecting global activation of the brain or associated rate changes. On the other hand, they strongly suggest that it is indeed frequency-specific dynamics that are crucial for the interplay of localized population activities along the cortico-striatal axis during active behavior. This is also because correlations between the same frequency components of local power estimates exhibited very similar qualitative characteristics but were generally smaller than corresponding phase-coupling estimates. In light of the highly significant scaling of low- and high-frequency phase-locking peaks

with motor demand, this indicates that true phase-coupling instead of mere amplitude correlations possibly driven by a different source support interactions within and between cortical and striatal circuits. This conclusion is also warranted by the results of phase-locking–power correlation interaction measures discussed in the next section (4.5).

4.5 LFP coupling interrelations

Same-frequency monopolar LFP power correlation and phase-coupling spectra were qualitatively very similar. However, phase-locking was consistently stronger than power correlation both within and between structures. Interrelation of both interaction measures revealed frequency-specific dynamics that changed between behavioral states. Most strikingly, temporally precise intercorrelation of phase-locking and power fluctuations decreased in a significant manner exclusively at low and high running peak frequencies.

To our knowledge, this study provides the first investigation of the relationships between phase-locking and concomitant amplitude correlation strengths of the same underlying signals recorded in structures along the cortico-striatal axis. Interestingly, phase-locking–power correlation ratios were consistently greater than 1 but at the same time they were smallest in low and high spectral regions exactly at the resting and running peak frequencies of either measure. This nicely illustrates that indeed, local ensembles of cells oscillating in synchrony are the functional-anatomical substrate for the coupling of neuronal populations within and between different brain structures. At the same time, it strongly suggests that synchronous oscillations of local neuronal assemblies on the one hand and the coupling of different ensembles on the other may have partly similar but also partly distinct underlying mechanisms and functional consequences.

Furthermore, increases in phase-amplitude coupling and decreases in power correlations between low- and high-frequency components and behavioral states indicate that a better temporal coordination of different rhythmic activities between areas may be accompanied by a concomitant decrease in coupling of their amplitudes possibly reflecting the reduced drive of a common external source. Such a common drive may impose idling rhythms of comparably low frequency, potentially in the delta (Dejean et al., 2011) or even suprasecond range (Walters and Bergstrom, 2010), onto widespread brain regions including cortico-basal ganglia structures during quiet rest that are similar to those observed during sleep or anesthesia (Steriade, 2000) and that collectively entrain oscillations of higher frequency. Accordingly, phase-locking–power correlation interrelations were strongest during rest in a broad band within the gamma range while they were weakest during running at exactly the theta peak-frequency of 8 Hz and strongly reduced within that gamma frequency band centered on 64 Hz.

Thus, we speculate that during active behavior requiring temporally accurate flow of neuronal information cellular activities become better and more specifically coordinated by phase-locking mechanisms. At the same time, they are less susceptible to global idling rhythms as reflected in strong cross-frequency amplitude correlation patterns during rest. Together with the finding that phase-locking values were consistently stronger than corresponding same-frequency power correlation values this indicates that phase-locking of population activities within and between cortex and striatum may be more important for functional coupling of neuronal assemblies along that axis than amplitude correlations.

4.6 Multi-unit activities

As explained above (Section 4.1.5), we interpret the results of MUA analyses with caution. Within those boundaries, firing rates robustly increased between behavioral conditions. Also, MUA power and MUA coherences increased strongly between rest and running across the entire spectrum in both structures. Interestingly, the faint bumps of running MUA power around 8 Hz which are better visible in percentage than in raw spectra (cf. Figures 3.3.2.1 and 3.3.2.2 on pages 72 and 73, respectively) as well as similar MUA coherence peaks exhibited roughly the same frequencies as average running firing rates.

Partly for reasons of unit data quality, we did not make any further attempts to differentiate between possible rate vs. true oscillatory effects underlying the generation of MUA power and coherence peaks. However, note that monopolar LFP-MUA coherence spectra also display small but localized peaks at exactly 8 Hz during running (cf. Figure 3.13, page 80). Even more strikingly, coherence was significant between cortical spikes and striatal fields but not cortical fields and striatal spikes. Under the assumption that LFPs and spikes primarily represent input and output components of population signals, respectively (Section 4.1.9), this further supports the notion that the coupling of population oscillations found in this study may indeed reflect the frequency-specific functional interaction of sensorimotor cortical and subcortical structures during rhythmic whole-body movement along the strictly unidirectional cortico-striatal anatomical axis.

The latter notion is further supported by LFP-MUA coherence difference results showing that the most prominent change between behavioral states is a sharp, significant peak of coherence increase centered slightly above 8 Hz. In contrast, the fairly broad-band changes in higher frequency ranges are more likely to reflect rate changes. The absence of localized high-frequency LFP-MUA coherence peaks and changes thereof may be due to either signal quality issues or have physiological reasons. In particular, it may first simply reflect the fact that the great majority of striatal cells consists of projection neurons which thus dominate the MUA signal. Second and in relation to this, locking of

projection and interneurons to theta oscillations has indeed been shown to be strong in the striatum, whereas locking to gamma oscillations is probably largely confined to interneurons. Third, if the theta rhythm is indeed the overall driving and coordinating force of striatal output dynamics, this may well explain the preferential entrainment of unit activities to oscillations of lower frequency (Section 4.7).

In any case, the absence of prominent peaks in power and coherence spectra of spike signals does not by itself proof the lack of a relationship between synchronized population oscillations as measured by LFPs and concomitant unit activities. Much to the contrary, prominent oscillatory field activities are perfectly compatible with stochastic spike patterns emitted by individual neurons (Wang, 2010). Indeed, it may be a distinguishing feature of striatal macro- and microcircuits and their role as integral parts of the cortico-striatal axis that they exhibit tight functional connections with their input areas as established by synchronous population oscillations in different frequency bands but at the same time are able to produce fine-grained output spike patterns, thus serving as contextually adaptive, dynamic spatio-temporal filters (Section 4.7).

4.7 Functional implications

There is as yet not unifying theory on the functional role of oscillatory synchronization of neuronal activities along cortico-basal ganglia loops and the cortico-striatal axis in particular (Boraud et al., 2005; Walters and Bergstrom, 2010). Also, no comprehensive models have been developed that are able to account in detail for the respective activity patterns observed in experimental data. Much to the contrary, there has even been considerable debate and doubt about the physiological role of oscillations and synchrony in cortico-basal ganglia structures partly because pairs of single cells in the different nuclei have only rarely been found to exhibit both properties in the healthy as compared to the diseased state (e.g., Nini et al., 1995; Raz et al., 1996; Goldberg et al., 2004).

Indeed, there is a growing body of literature on the adverse effects of a pathological increase of synchronized oscillations, mostly in the beta-frequency band, in human basal ganglia nuclei during movement disorders such as Parkinson's disease (Brown, 2003; Eusebio and Brown, 2007; Hammond et al., 2007). Although many issues remain, it has been proposed that beta-frequency band oscillations may be particularly associated with brady- or akinesia, i.e., pronounced slowing to almost complete cessation of spontaneous movement (Brown, 2007). Recordings in animal models of PD have confirmed that lesioning of the nigro-striatal dopaminergic projection is accompanied by an increase of low-frequency oscillations and enhanced synchronization of single cell activities as well as prominent patterns of beta band oscillations in LFPs recorded in the subthalamic

nucleus and the globus pallidus of parkinsonian rodents and non-human primates (e.g., Bergman et al., 1994; Nini et al., 1995; Raz et al., 1996; Boraud et al., 2002; Goldberg et al., 2004; Mallet et al., 2008; Cruz et al., 2009; Avila et al., 2010).

As mentioned above (Section 4.2), oscillatory synchronization in the alpha- to beta-frequency band has also been associated with motor processing in the healthy state. However, such activities have first and foremost been assigned a role in sustaining resting or holding motor states rather than movement *per se* (Murthy and Fetz, 1992; Sanes and Donoghue, 1993; Salenius and Hari, 2003; Baker, 2007). Accordingly, it has been proposed that exaggerated low-frequency oscillations in the basal ganglia and associated cortical regions may be disruptive of their classically presumed roles in movement initiation, execution, and adaptation (Brown, 2003, 2007).

However, apart from prominent beta-frequency rhythms, (low) gamma oscillations have been recorded in motor cortical and subcortical structures during active task engagement (Murthy and Fetz, 1992; Sanes and Donoghue, 1993; Murthy and Fetz, 1996a,b; MacKay, 1997; Brown and Marsden, 1998; Donoghue et al., 1998; Brown, 2000). It has further been shown that in Parkinson's disease patients under dopaminergic medication or during movement episodes, high-frequency oscillatory activities in the gamma range as measured in the STN become more prominent whereas the power of low-frequency oscillations is reduced (Brown et al., 2001). Similarly, a study in mice found that acute dopamine depletion led to an enhancement of delta and beta but a reduction of theta and gamma-frequency population activities along the cortico-striatal axis (Costa et al., 2006).

Based on such findings, it has been proposed that in sensorimotor areas including cortico-basal ganglia loops, frequency-specific oscillatory population activities may have roles similar to those in other brain systems. Most generally speaking, they are thought to subserve the temporal coupling of distributed cells and to support the gating of activities between groups of neurons located in the same or in distant areas that contribute to the processing of behavioral variables (Engel et al., 2001; Salinas and Sejnowski, 2001; Varela et al., 2001; Fries, 2005; Akam and Kullmann, 2010). Notably, as in the case of sensorimotor cortical areas (Murthy and Fetz, 1992; Sanes and Donoghue, 1993; Murthy and Fetz, 1996a,b; Donoghue et al., 1998), the presumed coupling or gating role of synchronous oscillations along cortico-basal ganglia loops has been formulated by some authors not specifically with regard to motor processes, but rather more broadly conceived as a temporally and spatially organized, predictable engagement of distributed neuronal elements according to a broad range of behavioral demands (e.g., Brown and Marsden, 1998). In case of the striatum, this idea has received general experimental support by the above cited studies demonstrating prominent patterns of synchronized oscillations in various frequency bands in awake behaving animals under a wide variety of task conditions (e.g.,

Berke et al., 2004; Masimore et al., 2005; DeCoteau et al., 2007a; Dejean et al., 2007; Berke, 2009; van der Meer and Redish, 2009; Kalenscher et al., 2010). Specifiying the coupling or gating role of synchronized population oscillations for the cortico-striatal axis as a whole, in a first approximation one could argue that the accurate timing of the massive input from mostly cortical structures reaching the striatum would provide the coordinated, contextually specific (Section 1.1.3), strongly driving pattern of activities needed to excite striatal neurons across extended regions of the structure above firing threshold, thus enabling them to further influence their output targets. Is such a scenario physiologically realistic, and what is the experimental evidence for it?

As we have pointed out in previous sections, the functional relevance of synchronized oscillations for neuronal interactions along the cortico-striatal axis is suggested by, amongst other things, the findings of a number of groups demonstrating locking of single neuron firing to striatal and cortical population activities as measured by LFP or ECoG signals. Notably, entrainment of single striatal cells to field potential activities has also been shown to be specific with regard to either neuron types or oscillation frequency, or both. For example, Berke et al. (2004) found entrainment of both putative medium-spiny projection (pMSN) and putative fast-spiking interneurons (pFSI) to high-voltage spindles (HVS) at theta-frequency. Entrainment of MSNs to striatal HVS was also observed by Dejean et al. (2007) in rats during quiet rest. Similarly, DeCoteau et al. (2007a) reported on locking of MSNs to striatal non-HVS theta rhythms, and van der Meer and Redish (2009) showed FSIs to be coherent with ventral striatal LFPs in the theta-frequency range. Importantly, Kalenscher et al. (2010) observed entrainment of both MSNs and FSIs to ventral striatal gamma oscillations during reward-related behavioral epochs, although the percentage of significantly phase-locked MSNs was very low (∼3.3%) in comparison to FSIs (∼92%). Even more strikingly, van der Meer and Redish (2009) and Berke (2009) found a differential locking of subtypes of FSIs to either low or high gamma rhythms, which led them to speculate that the activities of different kinds of interneurons may subserve striatal gamma oscillations in distinct frequency subbands.

In an exhaustive recent effort, Sharott and coworkers (Sharott et al., 2009) demonstrated locking of both putative MSNs and three types of striatal interneurons to low (2–9 Hz) ECoG oscillations in halothane-anesthetized rats. In contrast, entrainment to high-frequency (23–55 Hz) activities was specific to putative FSIs. When looking for signs of immediate interactions on the level of single neurons, they found stronger cross-correlations between pMSNs and pFSIs than between pMSNs and other interneuron types. Moreover, oscillatory cross-correlations between neurons markedly depended on cell types, with only pFSIs exhibiting such characteristics in both low and high frequency ranges. Importantly, these patterns were strongly related to similar oscillatory autocor-

relations of cortical ECoGs, indicating frequency-specific coupling of input (cortex) and output (striatum) structures on macroscopic and microscopic levels.

Another recent study which is very important to our discussion (Schulz et al., 2011) investigated the spectral characteristics of intracellularly recorded subthreshold membrane potential oscillations as well as the spike output of different types of striatal neurons in urethane-anesthetized rats during both up- and down-states (Section 1.3.3). Interestingly, high-frequency voltage content was much larger in membrane potentials of FSIs, whereas power in lower (theta) spectral regions was larger in MSNs. Even more importantly, fast membrane potential fluctuations preceded spike output of FSIs during up-states, and cortical stimulation was most effective at driving MSN output when delivered at frequencies below 20 but not at 100 Hz, in marked contrast to FSIs.

The outcomes of all these studies indicate that frequency-specific oscillatory population activities and their synchronization within and between structures along the cortico-striatal axis are functionally relevant. In particular, they demonstrate that although evidence for oscillatory firing of individual striatal neurons, especially MSNs, and oscillatory cross-correlation patterns between pairs of projection neurons is lacking, this does not preclude the importance of oscillatory synchronization of *population activities* as reflected in LFPs on both the single cell and the network level. More specifically, as the results of studies investigating the up- and down-state dynamics of cortico-striatal and striatal neurons (Section 1.3.3) suggest, spike output of striatal projection neurons may well be under the control of frequency-specific membrane potential oscillations but at the same time retain their fine-grained coding capacities (Stern et al., 1998). Thus, it is crucial for the discussion of the role of synchronized population oscillations to differentiate between the driving forces of membrane potential dynamics that sculpt the firing patterns of individual or groups of cells and spike output *per se*. In this regard, the findings of the study of Schulz et al. (2011) for example strongly suggest that synchronized population oscillations of both low and high frequency may indeed differentially drive neuronal activities in the striatum, maybe even in a cell-type specific manner.

Importantly, under physiological conditions, population oscillations in different frequency bands are most probably dependent on a balance of excitatory and inhibitory neuronal activities (Wang, 2010) as has been repeatedly shown *in vivo* and *in vitro* and as has been predicted by and been reproduced in modeling studies (e.g., Steriade et al., 1993a; Shu et al., 2003; Traub et al., 2004; Hasenstaub et al., 2005; Buzsáki, 2006; Bartos et al., 2007; Atallah and Scanziani, 2009; Haider and McCormick, 2009; Kopell et al., 2010). The highly recurrent architecture of cortical microcircuits composed of excitatory and inhibitory neurons readily endows them with the cellular machinery needed for the generation of rhythmic activities (Haider and McCormick, 2009; Wang, 2010). The

anatomical makeup of the striatum is markedly different from that of its input structures. For the following reasons, we think that it may still be in a position to support signal processing and transmission as subserved by synchronized population oscillations.

Apart from the massive input to MSNs, cortico-striatal projection neurons also directly target striatal FSIs (Bennett and Bolam, 1994). Interestingly, inputs to FSIs arising from primary motor and somatosensory cortical areas overlap in their striatal target zones in the rat (Ramanathan et al., 2002). Also, FSIs are more quickly and easily activated by cortical inputs than MSNs (Mallet et al., 2005; Bolam et al., 2006). Finally, they are well capable of accurately and specifically controlling the output of projection neurons by means of powerful feedforward inhibition (Koos and Tepper, 1999; Tepper and Bolam, 2004; Mallet et al., 2005; Gittis et al., 2011). Thus, the functional-anatomical properties of striatal microcircuits (cf. Figure 1.2, page 7) and of the cortico-striatal axis indeed appear to exhibit the basic prerequisites for sustaining oscillatory neuronal synchronization. To be more precise, we argue that the roughly concomitant but also slightly delayed excitation of striatal projection and fast-spiking interneurons by the cortico-striatal inputs they both receive provide the aforementioned balance of excitatory and inhibitory cellular dynamics underlying the generation of synchronized population oscillations in different frequency bands.

Currently available models of cortico-striatal network dynamics are not comparable in terms of anatomical and physiological details to those of, e.g., hippocampal circuitry regarding the generation and maintenance of neuronal population oscillations (Traub et al., 2004; Bartos et al., 2007; Wang, 2010). However, it is well possible that as in hippocampal and neocortical networks (Soltesz and Deschênes, 1993; Pike et al., 2000; Cardin et al., 2009), different neuron types may be involved to a different degree in sustaining low- and high-frequency oscillatory dynamics in the striatum. In particular, fast-spiking interneurons appear to be of primary importance for sustaining striatal gamma oscillations, a notion which is substantially supported by the above cited studies showing a preferential locking of FSIs to high-frequency LFP activities. In contrast, projection neurons may primarily be driven by inputs of lower frequency. Nevertheless striatal output dynamics may still crucially rely on the well-timed inhibition of MSNs by FSIs as supported by high-frequency oscillations. Indeed, the finding of a locking of the latter cell type also to low and of the former to high-frequency population oscillations indicates that although they presumably drive different cell types in a differential and even preferential manner, the interplay of both slow and fast rhythms may be what is crucial for shaping striatal network activities. As is further discussed below, these suppositions may provide a clue to the roughly bimodal distribution of cortico-striatal power and phase-coupling values

we found in our data. They may also help to explain the strikingly similar scaling of frequency-specific activities in low and high spectral regions with behavioral demand.

Interactions between cortical and striatal groups of neurons in a functionally specific and temporally accurate manner is possibly even more difficult to achieve than between cortical assemblies because of the intricate makeup of cortico-striatal projections and the need for a really substantial, well-timed excitatory input to drive striatal neurons above firing threshold (Section 1.2.2). Based on the results of the present and of previous studies, we thus argue here that the rapid grouping of neuronal activities within cortex and striatum by means of synchronous population oscillations as reflected in low- and high-frequency power peaks as well as their functional coupling as reflected in prominent phase-locking peaks at the same frequencies may provide the physiological basis for the coordinated and predictable interaction of both structures (Fries, 2005; Buzsáki, 2006). Having established the general empirical grounds for a possibly important role of synchronized population oscillations along the cortico-striatal axis, how can the data of the present study be reconciled with current theories regarding low- and high-frequency oscillatory activities in the brain and in cortico-basal ganglia systems in particular?

We will limit the scope of the final part of this section to the idea that low (theta) and high (gamma) frequency-specific oscillations subserve the functional coupling of groups of neurons on both small and large scales, albeit to different temporal and spatial degrees (Kopell et al., 2000; von Stein and Sarnthein, 2000; Fries, 2009). In addition, we will also argue that the present results support the notion of an intimate link between low- and high-frequency oscillatory activities in cortical and subcortical brain structures (Lisman, 2005; Wang, 2010). For obvious reasons, we will often refer to synchronized oscillatory activities in the context of sensorimotor behavior. However, the principles exposed below most probably also pertain to other behavioral aspects and associated brain dynamics.

Theta oscillations have repeatedly been linked to sensorimotor behavior (Vanderwolf, 1971; Bland, 1986; Kahana et al., 2001; Bland and Oddie, 2001; Buzsáki, 2002). The data of the present study are in excellent agreement with the results of previous investigations that showed a modulation of hippocampal theta activities with voluntary movement (Vanderwolf, 1971; Bland and Oddie, 2001). This includes our demonstration of a significant scaling of theta oscillation amplitudes and peak frequencies with motor parameters, in the present case the animals' running speed. As Bland and Oddie (2001) have pointed out, theta oscillations may be particularly suited to temporally coordinate neuronal activities across large regions of the brain. They based their argumentation on the fact that the origin of the theta-rhythmic drive of forebrain regions, including the hippocampus, can be traced back to ascending, multisynaptic brainstem projections originating in the pontine reticular formation and the pedunculopontine nucleus that reach

medial temporal lobe regions via the posterior hypothalamus and the supramammilary nucleus and via projections from the medial septum which are the external drivers of theta oscillations in the hippocampus (Bland and Oddie, 2001). Importantly, these ascending projections are not limited to areas in the medial temporal lobe, but also provide links to structures that are closely related to striatal regions, such as the intralaminar thalamus (Groenewegen and Berendse, 1994). Moreover, there are various other anatomical roots that provide an interface between limbic and sensorimotor brain regions such as the basal ganglia, like the connections between hippocampus and nucleus accumbens or striatal projections originating in the entorhinal cortex (Mogenson et al., 1980; Hallworth and Bland, 2004), and the former have indeed recently been shown to be coupled by synchronized activities *in vivo* (Goto and O'Donnell, 2001b). Thus, Bland and Oddie (2001) emphasize that the widespread projections of brainstem and limbic areas are well positioned to sculpt sensorimotor activities in cortical and subcortical regions.

There is currently no established theory on the generation of theta oscillations in brain regions other than the hippocampus (Wang, 2010). It is thus unclear to what extent the theta activities we found in sensorimotor cortical and striatal regions are generated locally or are imposed by external sources, or even volume conducted from distant areas (Section 4.2). In agreement with the above theories, we propose that they are driven to a substantial degree by ascending, widespread brainstem projections reaching cortical and striatal regions via multisynaptic pathways and that they shape local processing as well as functional coupling of these areas through the *resonance* properties of neuronal networks in both structures. This idea is supported by the prominence of theta power peaks in monopolar and bipolar cortical and striatal LFPs and their strong phase-coupling which exhibits only very small cross-hemispheric biases. Furthermore, the significant scaling of theta power and phase-coupling peak frequencies with behavioral demand is in good agreement with the notion that theta-frequency characteristics are modulated by the intensity of the sensorimotor engagement of a subject (Bland and Oddie, 2001).

To what degree sensorimotor-related theta rhythms have a direct link to brainstem central motor pattern generating mechanisms (Marder and Calabrese, 1996) is not known. However, voluntary movement is a complex behavior based on a continuous interplay between inputs from sensory modalities, outputs of motor structures, and even cognitive domains such as those subserving attention and arousal (Bland and Oddie, 2001). In fact, there is maybe no clear-cut anatomical or functional line distinctly separating sensory or cognitive from motor processes and associated neurophysiological underpinnings during complex behaviors involving forebrain areas (Fuster, 2008). Accordingly, various authors (Vanderwolf, 1971; Bland and Oddie, 2001; Kahana et al., 2001; Buzsáki, 2002) have underscored the notion that theta rhythms may be fundamental to the spatially and

temporally accurate integration of sensory and motor signals during behavior, including cognition. More specifically, theta oscillations have been proposed to subserve processes of rhythmic sensorimotor sampling or updating during active behavior by supporting the temporal grouping and coordination of neural activities across extended regions and between various functional brain systems (Bland and Oddie, 2001; Uchida and Mainen, 2003; Kay, 2005). These theories are partly based on the observation that theta rhythms are differentially modulated by sensory and motor variables alike, and that they exhibit scaling with various aspects of behavioral demand, like running speed of the animal (Vanderwolf, 1971; Bland and Oddie, 2001).

The prominent power as well as phase-coupling signatures found in the present study in conjunction with multi-unit firing rates in that frequency range underscore the potential relevance of theta oscillations for functional coupling of structures during rhythmic, movement-related activation of sensorimotor cortical and striatal areas. It is indeed intriguing that under conditions of continuous running at constant speed like in the present task, strong synchronized oscillations in the theta-frequency range are a prominent feature of neuronal activities along an anatomical axis that has classically been involved in the modulation of such behaviors. On the one hand, this may be taken as an indication of the presumed integrative role of cortico-basal ganglia loops in the generation of organized behavior to be subserved by theta oscillatory activities. On the other hand, theta oscillations along the cortico-striatal axis may also support coupling of neuronal activities on smaller spatial and temporal scales by providing an overall, clock-like background of periodic excitation and inhibition for the orchestration of fast functional interactions in discrete epochs as subserved by synchronized gamma oscillations (see below).

A very recent review on the functional role of gamma oscillations in the ventral striatum primarily focused on their putative role in reward-related processes (van der Meer et al., 2010). It was mainly based on the findings of a number of rodent studies indicating a substantial modulation of gamma LFP power and gamma-entrained cortical and striatal spiking activities at different stages of spatial decision tasks (Berke, 2009; van der Meer and Redish, 2009; Kalenscher et al., 2010). In their discussion, van der Meer et al. (2010) point out that gamma-frequency oscillations in the ventral striatum may either be primarily input-driven or to a substantial degree generated within the striatum itself, or a mixture of the two. The very same may probably hold true for more dorsal parts of the striatum which receive equally strong projections from mostly cortical areas and are structurally very similar to their ventral counterparts.

However, as in the case of theta oscillations, there are as yet no comprehensive models and theories on the generation and functional importance of gamma oscillations within the striatum and along the cortico-striatal axis. Until recently, gamma oscillations have

mostly been associated with local processes such as the temporal grouping of neurons into coherent ensembles or their functional coupling within circumscribed areas (Singer and Gray, 1995; Chrobak and Buzsáki, 1998; Csicsvari et al., 1999, 2003). There is now increasing evidence that they may also subserve the large-scale interaction of activities between more or less distant areas (Siegel et al., 2008; Colgin et al., 2009; Gregoriou et al., 2009; Hipp et al., 2011). Although the mechanisms underlying the large-scale synchronization of local gamma rhythms are also not known, they have been proposed to be particularly well-suited for mediating fast interactions between neurons located in different cortical areas (Fries, 2005, 2009). The same may be true for interactions between cortical and subcortical structures such as the striatum, and we think that the data of the present study do indeed support this view.

At this point, it is very important to note that gamma oscillations even more than low-frequency rhythms are transient phenomena that typically only last for a limited number of cycles (a few tenths to hundredths of milliseconds) at the respective recording sites and are also variable in frequency (Gray et al., 1992; Murthy and Fetz, 1992; Bragin et al., 1995; Donoghue et al., 1998; Harris et al., 2003; Masimore et al., 2005; Colgin et al., 2009; Wang, 2010). When examining the time-resolved power spectra of our LFP recordings, we also noted a continuous waxing and waning of epochs of gamma oscillations and variable center frequencies of oscillatory bursts (Figure 2.16, page 58). We did not further analyze the temporal structure of power and phase-coupling estimates because of the lack of distinct task events in our behavioral paradigm. For the interpretation of our results it is however probably crucial that the functional coupling of cortical and striatal regions may indeed be fundamentally characterized by a rapid switch between interacting ensembles along this anatomical axis depending on the context-specific[2] engagement of groups of distributed neurons in both areas on short timescales (Figure 1.3, page 10).

At present, we do not know wether, if at all, synchronized oscillations of low (e.g., theta) or high (e.g., gamma) frequency play the leading role in the interaction of cortical and striatal areas. With regard to its temporal scale, it has been noted that the functional coupling of neuronal activities may be supported by synchronous oscillations in different frequency bands (Fries, 2005; Wang, 2010). Furthermore, is has also been suggested that *interactions* between synchronous oscillations of different frequency may be essential for the spatio-temporal coordination of neuronal activities, their grouping into meaningful sequences, and their large-scale coupling between distant sites (Fries, 2005; Lisman, 2005; Jensen and Colgin, 2007; Wang, 2010). We indeed found striking

[2] We use the term 'context' here to refer not only to the behavioral circumstances as a whole but more specifically to the physiological demands proper that change on a moment-to-moment, i.e., fractions of a second basis, such as those underlying the recruitment of specific groups of muscles during movement.

similarities between the patterns of oscillatory synchronization in low and high frequency bands as well as their modulation with behavioral demand. This thus suggests that theta and gamma activities are not completely independent processes in the interaction of cortical and striatal structures. Much to the contrary, as the results of phase-amplitude coupling analyses show, they appear to be well coordinated, and the characteristics of their relationship also substantially modulated by behavioral demand.

As Lisman (2005) and Lisman and Buzsáki (2008) have explained in more detail, the coordination of theta and gamma rhythmic synchronization of neuronal activities may be fundamental to signal encoding and routing within and between different parts of the brain. This proposition was originally based on theoretical considerations regarding the coalescence of multiple gamma cycles within one theta cycle, with the latter thought to provide a temporal reference frame for the ordered sequencing of firing patterns as grouped by fast gamma oscillations (Lisman and Idiart, 1995; Lisman, 2005). It is indeed well-documented that both types of population oscillations often co-occur and are coupled under awake behaving conditions in hippocampal, neocortical, and also other areas (Buzsáki et al., 1983; Bragin et al., 1995; Lisman and Idiart, 1995; Chrobak and Buzsáki, 1998; Buzsáki et al., 2003; Csicsvari et al., 2003; Canolty et al., 2006; Tort et al., 2008). For obvious reasons, we do not further discuss here the possible role of theta-gamma coupling and phase-coding in memory processes or spatial navigation. We do, however, stress the idea that slow theta oscillations may facilitate large-scale neuronal interactions along the cortico-striatal axis by providing a master-clock like signal subserving the discretization of brief signal encoding and transmission epochs as supported by fast gamma rhythms (Buzsáki, 2002; Harris et al., 2003; Lisman, 2005; Lisman and Buzsáki, 2008).

These considerations may indeed help to explain the strikingly parallel temporal evolution of theta and gamma power and phase-coupling characteristics with behavioral demand. Furthermore, they also indicate how both slow and fast rhythms may play differential but synergistic roles for neuronal interactions along the cortico-striatal axis. As we have outlined above, different striatal neuron types appear to be preferentially locked to slow and fast rhythms, no matter the degree to which they are imposed by external sources or internally generated. Interestingly, FSIs seem to be better capable of sustaining both slow and fast oscillations, in contrast to MSNs which may exhibit a strong preference for the former. Thus, it may be that theta oscillations dominate the temporal structuring of striatal output and at the same time sustain the ordered integration of external information provided by (cortical, thalamic, and other) spiking inputs as coordinated rhythmically by brief bursts of gamma oscillations.

The above proposition is well compatible with the notion of the striatum to serve as a context-specific, spatio-temporal filter and integrator of input activities (Section 1.2.3). It

is also compatible with the idea that large-scale coupling of distant brain structures may be supported by slow and fast synchronized oscillations because interactions on both time scales may physiologically matter. In light of the idea that theta oscillations may figure as a global rhythm that fundamentally supports integrative brain functions underlying sensorimotor behavior, it is indeed striking that in a highly structured sensorimotor task such as the one in the present study they are so prominent and apparently well-coordinated with transient gamma oscillations thought to subserve neuronal assembly formation and interactions on fast timescales (Harris et al., 2003; Fries, 2005; Buzsáki, 2006; Colgin et al., 2009). However, it is important to note that we have no means of testing, with the present data set, the possibility that theta-gamma interactions may also reflect a coding scheme in which the actual *order* and, thereby, the respective *phase*[3] of subsequent gamma bursts within a given theta cycle by itself has informational value by signifying the order of gamma-encoded behavioral variables (i.e., the "informational units" or "items" according to Lisman, 2005). Similarly, a modeling study (Fukai, 1999) proposed that nesting of theta and gamma oscillations along the cortico-striatal axis may support sequence generation processes underlying movement by means of a short-term memory buffer mechanism akin to the one proposed by Lisman and Idiart (1995). All these ideas remain to be tested in future experiments (Section 4.8).

If the transient, frequency-specific oscillatory synchronization of neuronal activities does indeed subserve the functional coupling of cells in that it groups and aligns the time points of their spike firing according to the cycle length of the population oscillation, one might expect that narrowing the temporal windows of increased mutual excitability by increasing the oscillation frequency may render information transmission between cells by means of spike firing more precise (Fries et al., 2007). In turn, such a process might also be adaptive according to behavioral demands, in that a stronger drive of the system brings about faster transmission of neuronal signals which entails an increase of coupling frequencies. The results of the present study provide strong support for these ideas in that they are, to the very best of our knowledge, the first to demonstrate a systematic, linear scaling of the peak *frequencies* but not the *magnitudes* of synchronous oscillations and their coupling in theta- and gamma-frequency bands with increasing motor demand. Thus, our data strongly suggest that what may eventually matter for interactions between groups of neurons are the frequencies rather than the amplitudes of oscillatory patterns and the absolute strengths of their synchronization.

[3] In contrast to its well-established role regarding hippocampal theta oscillations (O'Keefe and Recce, 1993; Skaggs et al., 1996; Buzsáki, 2002; Lubenov and Siapas, 2009), the issue of phase-dependent coding in the gamma range is a matter of ongoing debate (Harris et al., 2003; Lisman, 2005; Fries et al., 2007; Lisman and Buzsáki, 2008; Montemurro et al., 2008; Cardin et al., 2009; Wang, 2010).

The latter notion is also supported by the results of phase-coupling–power correlation interrelation analyses that show a frequency-specific temporal dissociation of the fluctuations of both measures. It is indeed striking that the temporal coordination of neuronal activities along the cortico-striatal axis is improved and retains its specificity particularly in terms of the *phase* relationships between signals and different frequency components (phase-locking and phase-amplitude coupling, respectively) but is reduced with regard to the amplitude correlations between theta and gamma rhythms. As we have discussed above, these findings may possibly reflect the reduced influence of globally imposed idling rhythms of low frequency (< 4 Hz) that we unfortunately have no means of reliably testing with the current data set due to the filter settings used for recording and data analysis (Sections 2.4 and 2.6.2.1, respectively). Alternatively or in addition, they indicate the intriguing possibility of a more specific drive and phase-coupling of temporally and spatially or numerically more restricted groups of neurons engaged during running as compared to rest in structures along the cortico-striatal axis (Section 4.8).

To summarize, based on the results of the present study we suggest that the functional interaction of cortical and striatal ensembles may indeed be supported by the rapid, transient, and frequency-specific temporal coupling of groups of neurons oscillating in synchrony at theta and gamma frequencies in both structures. While synchronous theta oscillations may provide an overall coupling signal coordinating interactions along the cortico-striatal axis, gamma oscillations may subserve the rapid transmission of neuronal information encoded on a very short timescale. This is because first, we found striking similarities of theta and gamma power and phase-coupling characteristics within and between cortical and striatal areas. Second, coupling of population activities occurred around zero-phase within and with slight phase-delays between areas, consistent with anatomical and physiological network properties and in agreement with popular theories of neuronal communication (Fries, 2005; cf. Figure 1.4, page 17). In addition, cross-hemispheric biases of phase-coupling measures indicate a more global role of theta but a more locally restricted role of gamma oscillations in the interaction between cortex and striatum. Third, fluctuations of theta and gamma oscillations were temporally closely related, as suggested by prominent phase-amplitude coupling patterns. Fourth, low and high peak frequencies of power and phase-coupling estimates exhibited a similar linear scaling with motor demand, indicating a direct behavioral relevance of the frequencies of synchronized population oscillations and underscoring the importance of a temporal coordination of slow and fast rhythms. Fifth, we found evidence for a more specific modulation of frequency as compared to amplitude characteristics in intra- and inter-areal coupling, further supporting the notion of an explicit frequency-dependence of neuronal interactions in the brain as supported by synchronous population oscillations.

4.8 Future directions

Are synchronized oscillations really important for sculpting striatal network function, and do they support neuronal interactions along the cortico-striatal axis? The results of this study and their discussion indicate a number of fundamental issues to be investigated and clarified in future experiments. We only explicitly name here a couple of them, but this list is by no means to be taken exhaustive. Also, we point out the essential need to integrate the outcomes of experiments involving the below means into better models of cortico-basal ganglia function of both microscopic and macroscopic scales to help coherently and consistently explain empirical findings and stimulate future research in this field (Humphries et al., 2006; Leblois et al., 2006; Bogacz and Gurney, 2007).

First, as the studies reviewed in Section 1.3.3 have shown, cellular dynamics during up- and down-states indicate that cortico-striatal and striatal neurons are indeed capable of following synchronized input patterns. However, intracellular recordings under more specific stimulation conditions including sinusoidal inputs (Pike et al., 2000; Wang, 2010), have to be performed both *in vitro* and *in vivo* to investigate the driving forces of membrane potential fluctuations and thus the impact of synchronized population oscillations on the spike output patterns of these neurons (Azouz and Gray, 2000, 2003). Ideally, these experiments would be complemented by intracellular recordings *in vivo* which, although technically highly challenging, could provide verification of the results even under awake behaving conditions (Lee et al., 2006, 2009).

Second, population oscillations as measured by LFPs have to be more closely and specifically linked to spiking patterns of individual as well as particular types and groups of neurons (Klausberger et al., 2003) during behavior to clarify the cellular and network substrates of both signal *encoding* and *routing* mechanisms along the cortico-striatal axis. Recordings from clearly identified neuronal subtypes, in particular in light of the ever-growing number of different kinds of striatal interneurons that are being discovered (Tepper, 2010), are only one step in that direction. The greater endeavor should also involve attempts to causally manipulate single neuron and population activities, either through electrical and pharmacological or, even better, optogenetic manipulations (Boyden et al., 2005). This technique may allow to investigate, with high temporal precision and cellular specificity, the contributions of different neuron types to behaviorally relevant computations in structures along cortico-basal ganglia loops (Kravitz et al., 2010), their involvement in oscillatory dynamics on a population level, and the role of synchronized oscillations in large-scale network interactions between areas (Cardin et al., 2009).

Third, we need to extend even further the spatial and temporal scale and the specificity of our monitoring of neuronal and behavioral variables to better understand their

intricate relationships. This demands massively parallel recordings and manipulations on various temporal and spatial scales, including, in case of cortico-basal ganglia interactions, simultaneous measurements and perturbations of signals along the full loop of this brain system (Figure 1.1, page 2). This would for example allow to investigate whether neuronal interactions along the cortico-striatal axis as supported by population oscillations do shape striatal output patterns in a way which is indeed relevant for downstream structures. In addition, targeting of brainstem areas to better track the origins of global rhythms such as theta oscillations may help to embed cortio-striatal interactions into a wider scope of brain dynamics during natural behaviors. Similarly, important input structures to the striatum such as the thalamus (Haber and McFarland, 2001) have to be included in investigations of cortico-basal ganglia network functions, not mentioning the effects of diverse neurotransmitter systems such as dopaminergic inputs which are crucial in shaping cortico-striatal activities (Surmeier et al., 2007).

Fourth, the details of cortico-striatal projections, their striatal target zones, and the synaptic interactions between the different types of input and output neurons have to be more clearly elucidated in the context of functional interactions between the two areas (Bolam et al., 2006). This would allow for an improved targeting of corresponding subregions in both structures and hence a greater specificity of recordings. Further, it would improve our understanding of striatal network physiology, in particular with regard to the question of whether or not synchronized population oscillations are indeed a viable mechanism for cortico-striatal interactions. That would also help to better define the notion of *assemblies* of functionally coupled cells (Harris, 2005) on the level of both cortico-striatal and striatal neurons whose activity and interactions have been proposed to be coordinated by synchronous oscillations.

To finally make but one still vague, grand experimental suggestion, it would be intriguing to combine optogenetic manipulations of cortico-striatal projection neuron activities with parallel recordings from a substantial number of anatomically identified striatal target cells, including principal and interneurons, under well defined behavioral conditions. This would allow for a much more specific investigation of the mechanisms underlying the interactions of input and output structures along the cortico-striatal axis, granting crucial insights into the role of synchronized population oscillations in signal encoding and routing at the possibly most important stage of the cortico-basal ganglia loop. Monitoring of the second most important striatal input as well as its output areas by parallel recordings from thalamic and pallidal or nigral regions would provide indispensable information on the generation of cortico-striatal synchronized population oscillations and their impact on downstream structures. This would substantially facilitate interpretations of their origin as well as their physiological role in cortico-basal ganglia-thalamocortical systems.

References

Abeles M (1982a) Role of the cortical neuron: integrator or coincidence detector? *Isr J Med Sci* 18:83–92.

Abeles M (1982b) *Local cortical circuits: an electrophysiological study*, Vol. 6 Springer-Verlag, Berlin.

Adrian ED (1942) Olfactory reactions in the brain of the hedgehog. *J Physiol* 100:459–73.

Akam T, Kullmann DM (2010) Oscillations and filtering networks support flexible routing of information. *Neuron* 67:308–20.

Albin RL, Young AB, Penney JB (1989) The functional anatomy of basal ganglia disorders. *Trends Neurosci* 12:366–75.

Alexander GE, Crutcher MD (1990a) Functional architecture of basal ganglia circuits: neural substrates of parallel processing. *Trends Neurosci* 13:266–71.

Alexander GE, Crutcher MD (1990b) Preparation for movement: neural representations of intended direction in three motor areas of the monkey. *J Neurophysiol* 64:133–50.

Alexander GE, Crutcher MD, DeLong MR (1990) Basal ganglia-thalamocortical circuits: parallel substrates for motor, oculomotor, "prefrontal" and "limbic" functions. *Prog Brain Res* 85:119–46.

Alexander GE, DeLong MR, Strick PL (1986) Parallel organization of functionally segregated circuits linking basal ganglia and cortex. *Annu Rev Neurosci* 9:357–81.

Alonso JM, Usrey WM, Reid RC (1996) Precisely correlated firing in cells of the lateral geniculate nucleus. *Nature* 383:815–9.

Andrews R (1965) Treadmill for small laboratory animals. *J Appl Physiol* 20:572–4.

Antzoulatos EG, Miller EK (2011) Differences between neural activity in prefrontal cortex and striatum during learning of novel abstract categories. *Neuron* 71:243–9.

Apicella P, Ljungberg T, Scarnati E, Schultz W (1991) Responses to reward in monkey dorsal and ventral striatum. *Exp Brain Res* 85:491–500.

Araque A, Carmignoto G, Haydon PG (2001) Dynamic signaling between astrocytes and neurons. *Annu Rev Physiol* 63:795–813.

Atallah BV, Scanziani M (2009) Instantaneous modulation of gamma oscillation frequency by balancing excitation with inhibition. *Neuron* 62:566–77.

Averbeck BB, Latham PE, Pouget A (2006) Neural correlations, population coding and computation. *Nat Rev Neurosci* 7:358–66.

Avila I, Parr-Brownlie LC, Brazhnik E, Castañeda E, Bergstrom DA, Walters JR (2010) Beta frequency synchronization in basal ganglia output during rest and walk in a hemiparkinsonian rat. *Exp Neurol* 221:307–19.

Axmacher N, Henseler MM, Jensen O, Weinreich I, Elger CE, Fell J (2010) Cross-frequency coupling supports multi-item working memory in the human hippocampus. *Proc Natl Acad Sci U S A* 107:3228–33.

Azouz R, Gray CM (2000) Dynamic spike threshold reveals a mechanism for synaptic coincidence detection in cortical neurons in vivo. *Proc Natl Acad Sci U S A* 97:8110–5.

Azouz R, Gray CM (2003) Adaptive coincidence detection and dynamic gain control in visual cortical neurons in vivo. *Neuron* 37:513–23.

Baker SN (2007) Oscillatory interactions between sensorimotor cortex and the periphery. *Curr Opin Neurobiol* 17:649–55.

Bar-Gad I, Bergman H (2001) Stepping out of the box: information processing in the neural networks of the basal ganglia. *Curr Opin Neurobiol* 11:689–95.

Bar-Gad I, Morris G, Bergman H (2003) Information processing, dimensionality reduction and reinforcement learning in the basal ganglia. *Prog Neurobiol* 71:439–73.

Bartos M, Vida I, Jonas P (2007) Synaptic mechanisms of synchronized gamma oscillations in inhibitory interneuron networks. *Nat Rev Neurosci* 8:45–56.

Bennett BD, Bolam JP (1994) Synaptic input and output of parvalbumin-immunoreactive neurons in the neostriatum of the rat. *Neuroscience* 62:707–19.

Bergman H, Feingold A, Nini A, Raz A, Slovin H, Abeles M, Vaadia E (1998) Physiological aspects of information processing in the basal ganglia of normal and parkinsonian primates. *Trends Neurosci* 21:32–8.

Bergman H, Wichmann T, Karmon B, DeLong MR (1994) The primate subthalamic nucleus. II. Neuronal activity in the MPTP model of parkinsonism. *J Neurophysiol* 72:507–20.

Berke JD (2009) Fast oscillations in cortical-striatal networks switch frequency following rewarding events and stimulant drugs. *Eur J Neurosci* 30:848–59.

Berke JD, Okatan M, Skurski J, Eichenbaum HB (2004) Oscillatory entrainment of striatal neurons in freely moving rats. *Neuron* 43:883–96.

Berke J (2005) Participation of striatal neurons in large-scale oscillatory networks In Bolam JP, Ingham CA, Magill PJ, Bures J, Kopin I, McEwen B, Pribram K, Rosenblatt J, Weiskranz L, editors, *The Basal Ganglia VIII*, Vol. 56 of *Advances in Behavioral Biology*, pp. 25–35. Springer US.

Bevan MD, Magill PJ, Terman D, Bolam JP, Wilson CJ (2002) Move to the rhythm: oscillations in the subthalamic nucleus-external globus pallidus network. *Trends Neurosci* 25:525–31.

Bhatia KP, Marsden CD (1994) The behavioural and motor consequences of focal lesions of the basal ganglia in man. *Brain* 117:859–76.

Bland BH (1986) The physiology and pharmacology of hippocampal formation theta rhythms. *Prog Neurobiol* 26:1–54.

Bland BH, Oddie SD (2001) Theta band oscillation and synchrony in the hippocampal formation and associated structures: the case for its role in sensorimotor integration. *Behav Brain Res* 127:119–36.

Bogacz R, Gurney K (2007) The basal ganglia and cortex implement optimal decision making between alternative actions. *Neural Comput* 19:442–77.

Bolam JP, Bergman H, Graybiel AM, Kimura M, Plenz D, Seung HS, Surmeier DJ, J.R.Wickens (2006) Microcircuits, molecules, and motivated behavior: Microcircuits in the striatum In Grillner S, Graybiel AM, editors, *Microcircuits: the interface between neurons and global brain function*, Vol. 93 of *Dahlem Workshop Report*, chapter 9, pp. 165–190. The MIT Press in cooperation with Dahlem University Press, Cambridge, MA.

Bolam JP, Hanley JJ, Booth PA, Bevan MD (2000) Synaptic organisation of the basal ganglia. *J Anat* 196:527–42.

Boraud T, Bezard E, Bioulac B, Gross CE (2002) From single extracellular unit recording in experimental and human parkinsonism to the development of a functional concept of the role played by the basal ganglia in motor control. *Prog Neurobiol* 66:265–83.

Boraud T, Brown P, Goldberg JA, Graybiel AM, Magill PJ (2005) Oscillations in the basal ganglia: The good, the bad, and the unexpected In Bolam JP, Ingham CA, Magill PJ, editors, *The Basal Ganglia VIII*, Vol. 56 of *Advances in Behavioral Biology*, pp. 1–24. Springer US 10.1007/0-387-28066-9-1.

Bouyer JJ, Montaron MF, Rougeul A (1981) Fast fronto-parietal rhythms during combined focused attentive behaviour and immobility in cat: cortical and thalamic localizations. *Electroencephalogr Clin Neurophysiol* 51:244–52.

Boyden ES, Zhang F, Bamberg E, Nagel G, Deisseroth K (2005) Millisecond-timescale, genetically targeted optical control of neural activity. *Nat Neurosci* 8:1263–8.

Bragin A, Jandó G, Nádasdy Z, Hetke J, Wise K, Buzsáki G (1995) Gamma (40-100 Hz) oscillation in the hippocampus of the behaving rat. *J Neurosci* 15:47–60.

Bressler SL, Coppola R, Nakamura R (1993) Episodic multiregional cortical coherence at multiple frequencies during visual task performance. *Nature* 366:153–6.

Brown LL (1992) Somatotopic organization in rat striatum: evidence for a combinational map. *Proc Natl Acad Sci U S A* 89:7403–7.

Brown LL, Schneider JS, Lidsky TI (1997) Sensory and cognitive functions of the basal ganglia. *Curr Opin Neurobiol* 7:157–63.

Brown LL, Sharp FR (1995) Metabolic mapping of rat striatum: somatotopic organization of sensorimotor activity. *Brain Res* 686:207–22.

Brown LL, Smith DM, Goldbloom LM (1998) Organizing principles of cortical integration in the rat neostriatum: corticostriate map of the body surface is an ordered lattice of curved laminae and radial points. *J Comp Neurol* 392:468–88.

Brown MB, Forsythe AB (1974) Robust tests for the equality of variances. *Journal of the American Statistical Association* 69:364–367.

Brown P (2000) Cortical drives to human muscle: the piper and related rhythms. *Prog Neurobiol* 60:97–108.

Brown P (2003) Oscillatory nature of human basal ganglia activity: relationship to the pathophysiology of parkinson's disease. *Mov Disord* 18:357–63.

Brown P (2007) Abnormal oscillatory synchronisation in the motor system leads to impaired movement. *Curr Opin Neurobiol* 17:656–64.

Brown P, Marsden CD (1998) What do the basal ganglia do? *Lancet* 351:1801–4.

Brown P, Oliviero A, Mazzone P, Insola A, Tonali P, Di Lazzaro V (2001) Dopamine dependency of oscillations between subthalamic nucleus and pallidum in Parkinson's disease. *J Neurosci* 21:1033–8.

Brown P, Kupsch A, Magill PJ, Sharott A, Harnack D, Meissner W (2002) Oscillatory local field potentials recorded from the subthalamic nucleus of the alert rat. *Exp Neurol* 177:581–5.

Bruno RM, Sakmann B (2006) Cortex is driven by weak but synchronously active thalamocortical synapses. *Science* 312:1622–7.

Bruns A, Eckhorn R, Jokeit H, Ebner A (2000) Amplitude envelope correlation detects coupling among incoherent brain signals. *Neuroreport* 11:1509–14.

Buhusi CV, Meck WH (2005) What makes us tick? Functional and neural mechanisms of interval timing. *Nat Rev Neurosci* 6:755–65.

Burgess ML, Davis JM, Borg TK, Buggy J (1991) Intracranial self-stimulation motivates treadmill running in rats. *J Appl Physiol* 71:1593–7.

Buschman TJ, Miller EK (2007) Top-down versus bottom-up control of attention in the prefrontal and posterior parietal cortices. *Science* 315:1860–2.

Buzsáki G (2006) *Rhythms of the brain* Oxford University Press, Oxford.

Buzsáki G, Bickford RG, Ryan LJ, Young S, Prohaska O, Mandel RJ, Gage FH (1989) Multisite recording of brain field potentials and unit activity in freely moving rats. *J*

Neurosci Methods 28:209–17.

Buzsáki G, Buhl DL, Harris KD, Csicsvari J, Czéh B, Morozov A (2003) Hippocampal network patterns of activity in the mouse. *Neuroscience* 116:201–11.

Buzsáki G, Draguhn A (2004) Neuronal oscillations in cortical networks. *Science* 304:1926–9.

Buzsáki G, Leung LW, Vanderwolf CH (1983) Cellular bases of hippocampal eeg in the behaving rat. *Brain Res* 287:139–71.

Buzsáki G (2002) Theta oscillations in the hippocampus. *Neuron* 33:325–40.

Buzsáki G (2004) Large-scale recording of neuronal ensembles. *Nat Neurosci* 7:446–51.

Canolty RT, Edwards E, Dalal SS, Soltani M, Nagarajan SS, Kirsch HE, Berger MS, Barbaro NM, Knight RT (2006) High gamma power is phase-locked to theta oscillations in human neocortex. *Science* 313:1626–8.

Cardin JA, Carlén M, Meletis K, Knoblich U, Zhang F, Deisseroth K, Tsai LH, Moore CI (2009) Driving fast-spiking cells induces gamma rhythm and controls sensory responses. *Nature* 459:663–7.

Carelli RM, West MO (1991) Representation of the body by single neurons in the dorsolateral striatum of the awake, unrestrained rat. *J Comp Neurol* 309:231–49.

Carman JB, Cowan WM, Powell TP (1963) The organization of cortico-striate connections in the rabbit. *Brain* 86:525–62.

Carman JB, Cowen WM, Powell TP, Webster KE (1965) A bilateral cortico-striate projection. *J Neurol Neurosurg Psychiatry* 28:71–7.

Chalk M, Herrero JL, Gieselmann MA, Delicato LS, Gotthardt S, Thiele A (2010) Attention reduces stimulus-driven gamma frequency oscillations and spike field coherence in V1. *Neuron* 66:114–25.

Chang JY, Shi LH, Luo F, Woodward DJ (2003) High frequency stimulation of the subthalamic nucleus improves treadmill locomotion in unilateral 6-hydroxydopamine lesioned rats. *Brain Res* 983:174–84.

Chang JY, Shi LH, Luo F, Woodward DJ (2006) Neural responses in multiple basal ganglia regions following unilateral dopamine depletion in behaving rats performing a treadmill locomotion task. *Exp Brain Res* 172:193–207.

Chapin JK, Loeb GE, Woodward DJ (1980) A simple technique for determination of footfall patterns of animals during treadmill locomotion. *J Neurosci Methods* 2:97–102.

Chapin JK, Woodward DJ (1982a) Somatic sensory transmission to the cortex during movement: gating of single cell responses to touch. *Exp Neurol* 78:654–69.

Chapin JK, Woodward DJ (1982b) Somatic sensory transmission to the cortex during movement: phasic modulation over the locomotor step cycle. *Exp Neurol* 78:670–84.

Chen Z, Resnik E, McFarland JM, Sakmann B, Mehta MR (2011) Speed controls the amplitude and timing of the hippocampal gamma rhythm. *PLoS One* 6:e21408.

Chevalier G, Deniau JM (1990) Disinhibition as a basic process in the expression of striatal functions. *Trends Neurosci* 13:277–80.

Chrobak JJ, Buzsáki G (1998) Gamma oscillations in the entorhinal cortex of the freely behaving rat. *J Neurosci* 18:388–98.

Cohen MR, Kohn A (2011) Measuring and interpreting neuronal correlations. *Nat Neurosci* 14:811–9.

Cohen MX, Axmacher N, Lenartz D, Elger CE, Sturm V, Schlaepfer TE (2009) Good vibrations: cross-frequency coupling in the human nucleus accumbens during reward processing. *J Cogn Neurosci* 21:875–89.

Colgin LL, Denninger T, Fyhn M, Hafting T, Bonnevie T, Jensen O, Moser MB, Moser EI (2009) Frequency of gamma oscillations routes flow of information in the hippocampus. *Nature* 462:353–7.

Costa RM, Lin SC, Sotnikova TD, Cyr M, Gainetdinov RR, Caron MG, Nicolelis MAL (2006) Rapid alterations in corticostriatal ensemble coordination during acute dopamine-dependent motor dysfunction. *Neuron* 52:359–69.

Courtemanche R, Fujii N, Graybiel AM (2003) Synchronous, focally modulated beta-band oscillations characterize local field potential activity in the striatum of awake behaving monkeys. *J Neurosci* 23:11741–52.

Crutcher MD, Alexander GE (1990) Movement-related neuronal activity selectively coding either direction or muscle pattern in three motor areas of the monkey. *J Neurophysiol* 64:151–63.

Crutcher MD, DeLong MR (1984a) Single cell studies of the primate putamen. i. functional organization. *Exp Brain Res* 53:233–43.

Crutcher MD, DeLong MR (1984b) Single cell studies of the primate putamen. ii. relations to direction of movement and pattern of muscular activity. *Exp Brain Res* 53:244–58.

Cruz AV, Mallet N, Magill PJ, Brown P, Averbeck BB (2009) Effects of dopamine depletion on network entropy in the external globus pallidus. *J Neurophysiol* 102:1092–102.

Csicsvari J, Hirase H, Czurkó A, Mamiya A, Buzsáki G (1999) Oscillatory coupling of hippocampal pyramidal cells and interneurons in the behaving rat. *J Neurosci* 19:274–87.

Csicsvari J, Jamieson B, Wise KD, Buzsáki G (2003) Mechanisms of gamma oscillations in the hippocampus of the behaving rat. *Neuron* 37:311–22.

DeCoteau WE, Thorn C, Gibson DJ, Courtemanche R, Mitra P, Kubota Y, Graybiel AM (2007a) Learning-related coordination of striatal and hippocampal theta rhythms during acquisition of a procedural maze task. *Proc Natl Acad Sci U S A* 104:5644–9.

DeCoteau WE, Thorn C, Gibson DJ, Courtemanche R, Mitra P, Kubota Y, Graybiel AM (2007b) Oscillations of local field potentials in the rat dorsal striatum during spontaneous and instructed behaviors. *J Neurophysiol* 97:3800–5.

Dejean C, Gross CE, Bioulac B, Boraud T (2007) Synchronous high-voltage spindles in the cortex-basal ganglia network of awake and unrestrained rats. *Eur J Neurosci* 25:772–84.

Dejean C, Arbuthnott G, Wickens JR, Le Moine C, Boraud T, Hyland BI (2011) Power fluctuations in beta and gamma frequencies in rat globus pallidus: association with specific phases of slow oscillations and differential modulation by dopamine D1 and D2 receptors. *J Neurosci* 31:6098–107.

DeLong MR (1971) Activity of pallidal neurons during movement. *J Neurophysiol* 34:414–27.

DeLong MR (1972) Activity of basal ganglia neurons during movement. *Brain Res* 40:127–35.

DeLong MR (1990) Primate models of movement disorders of basal ganglia origin. *Trends Neurosci* 13:281–5.

Delong MR, Georgopoulos AP, Crutcher MD, Mitchell SJ, Richardson RT, Alexander GE (1984) Functional organization of the basal ganglia: contributions of single-cell recording studies. *Ciba Found Symp* 107:64–82.

DeLong MR, Wichmann T (2007) Circuits and circuit disorders of the basal ganglia. *Arch Neurol* 64:20–4.

Diesmann M, Gewaltig MO, Aertsen A (1999) Stable propagation of synchronous spiking in cortical neural networks. *Nature* 402:529–33.

Donner TH, Siegel M, Fries P, Engel AK (2009) Buildup of choice-predictive activity in human motor cortex during perceptual decision making. *Curr Biol* 19:1581–5.

Donner TH, Siegel M (2011) A framework for local cortical oscillation patterns. *Trends Cogn Sci* 15:191–9.

Donner TH, Siegel M, Oostenveld R, Fries P, Bauer M, Engel AK (2007) Population activity in the human dorsal pathway predicts the accuracy of visual motion detection. *J Neurophysiol* 98:345–59.

Donoghue JP, Sanes JN, Hatsopoulos NG, Gaál G (1998) Neural discharge and local field potential oscillations in primate motor cortex during voluntary movements. *J Neurophysiol* 79:159–73.

Donoghue JP, Wise SP (1982) The motor cortex of the rat: cytoarchitecture and microstimulation mapping. *J Comp Neurol* 212:76–88.

Eckhorn R, Bauer R, Jordan W, Brosch M, Kruse W, Munk M, Reitboeck HJ (1988) Coherent oscillations: a mechanism of feature linking in the visual cortex? Multiple

electrode and correlation analyses in the cat. *Biol Cybern* 60:121–30.

Ehringer H, Hornykiewicz O (1960) [Distribution of noradrenaline and dopamine (3-hydroxytyramine) in the human brain and their behavior in diseases of the extrapyramidal system]. *Klin Wochenschr* 38:1236–9.

Ellender TJ, Huerta-Ocampo I, Deisseroth K, Capogna M, Bolam JP (2011) Differential modulation of excitatory and inhibitory striatal synaptic transmission by histamine. *J Neurosci* 31:15340–51.

Engel AK, Fries P, Singer W (2001) Dynamic predictions: oscillations and synchrony in top-down processing. *Nat Rev Neurosci* 2:704–16.

Engel AK, König P, Singer W (1991) Direct physiological evidence for scene segmentation by temporal coding. *Proc Natl Acad Sci U S A* 88:9136–40.

Engel AK, Kreiter AK, König P, Singer W (1991) Synchronization of oscillatory neuronal responses between striate and extrastriate visual cortical areas of the cat. *Proc Natl Acad Sci U S A* 88:6048–52.

Engel AK, König P, Gray CM, Singer W (1990) Stimulus-dependent neuronal oscillations in cat visual cortex: Inter-columnar interaction as determined by cross-correlation analysis. *Eur J Neurosci* 2:588–606.

Ernst M (2004) Permutation methods: A basis for exact inference. *Statistical Science* 19:676–685.

Eusebio A, Brown P (2007) Oscillatory activity in the basal ganglia. *Parkinsonism Relat Disord* 13 Suppl 3:S434–6.

Farmer SF (1998) Rhythmicity, synchronization and binding in human and primate motor systems. *J Physiol* 509:3–14.

Fell J, Axmacher N (2011) The role of phase synchronization in memory processes. *Nat Rev Neurosci* 12:105–18.

Fetz EE, Chen D, Murthy VN, Matsumura M (2000) Synaptic interactions mediating synchrony and oscillations in primate sensorimotor cortex. *J Physiol Paris* 94:323–31.

Flaherty AW, Graybiel AM (1991) Corticostriatal transformations in the primate somatosensory system. Projections from physiologically mapped body-part representations. *J Neurophysiol* 66:1249–63.

Flaherty AW, Graybiel AM (1993) Two input systems for body representations in the primate striatal matrix: experimental evidence in the squirrel monkey. *J Neurosci* 13:1120–37.

Flaherty AW, Graybiel AM (1995) Motor and somatosensory corticostriatal projection magnifications in the squirrel monkey. *J Neurophysiol* 74:2638–48.

Freeman W (1975) *Mass action in the nervous system* Academic Press, New York.

Frien A, Eckhorn R, Bauer R, Woelbern T, Kehr H (1994) Stimulus-specific fast oscillations at zero phase between visual areas V1 and V2 of awake monkey. *Neuroreport* 5:2273–7.

Fries P (2009) Neuronal gamma-band synchronization as a fundamental process in cortical computation. *Annu Rev Neurosci* 32:209–24.

Fries P, Nikolic D, Singer W (2007) The gamma cycle. *Trends Neurosci* 30:309–16.

Fries P, Reynolds JH, Rorie AE, Desimone R (2001) Modulation of oscillatory neuronal synchronization by selective visual attention. *Science* 291:1560–3.

Fries P (2005) A mechanism for cognitive dynamics: neuronal communication through neuronal coherence. *Trends Cogn Sci* 9:474–80.

Fukai T (1999) Sequence generation in arbitrary temporal patterns from theta-nested gamma oscillations: a model of the basal ganglia-thalamo-cortical loops. *Neural Netw* 12:975–987.

Fuster J (2008) *The Prefrontal Cortex* Academic Press, 4th edition.

Gatev P, Darbin O, Wichmann T (2006) Oscillations in the basal ganglia under normal conditions and in movement disorders. *Mov Disord* 21:1566–77.

Georgopoulos AP (1994) New concepts in generation of movement. *Neuron* 13:257–68.

Gerfen CR (1992) The neostriatal mosaic: multiple levels of compartmental organization in the basal ganglia. *Annu Rev Neurosci* 15:285–320.

Gerfen CR, Engber TM, Mahan LC, Susel Z, Chase TN, Monsma J FJ, Sibley DR (1990) D1 and D2 dopamine receptor-regulated gene expression of striatonigral and striatopallidal neurons. *Science* 250:1429–32.

Gerfen CR (2004) Basal ganglia In Paxinos G, editor, *The Rat Nervous System*, pp. 455–508. Academic Press, Burlington, 3rd edition.

Gerfen CR, Bolam JP (2010) The neuroanatomical organization of the basal ganglia In Steiner H, Tseng KY, editors, *Handbook of Basal Ganglia Structure and Function*, Vol. 20 of *Handbook of Behavioral Neuroscience*, pp. 3–28. Elsevier.

Gerstner W, Kreiter AK, Markram H, Herz AV (1997) Neural codes: firing rates and beyond. *Proc Natl Acad Sci U S A* 94:12740–1.

Gervasoni D, Lin SC, Ribeiro S, Soares ES, Pantoja J, Nicolelis MAL (2004) Global forebrain dynamics predict rat behavioral states and their transitions. *J Neurosci* 24:11137–47.

Gioanni Y, Lamarche M (1985) A reappraisal of rat motor cortex organization by intracortical microstimulation. *Brain Res* 344:49–61.

Gittis AH, Leventhal DK, Fensterheim BA, Pettibone JR, Berke JD, Kreitzer AC (2011) Selective inhibition of striatal fast-spiking interneurons causes dyskinesias. *J Neurosci* 31:15727–31.

Goldberg JA, Rokni U, Boraud T, Vaadia E, Bergman H (2004) Spike synchronization in the cortex/basal-ganglia networks of parkinsonian primates reflects global dynamics of the local field potentials. *J Neurosci* 24:6003–10.

Gollo LL, Mirasso C, Villa AEP (2010) Dynamic control for synchronization of separated cortical areas through thalamic relay. *Neuroimage* 52:947–55.

Goto Y, O'Donnell P (2001a) Network synchrony in the nucleus accumbens in vivo. *J Neurosci* 21:4498–504.

Goto Y, O'Donnell P (2001b) Synchronous activity in the hippocampus and nucleus accumbens in vivo. *J Neurosci* 21:RC131.

Graffin G, Olson S (2010) *Anarchy evolution: faith, science, and bad religion in a world without God* ItBooks, New York, 1st edition.

Gray CM (1999) The temporal correlation hypothesis of visual feature integration: still alive and well. *Neuron* 24:31–47.

Gray CM, Engel AK, König P, Singer W (1992) Synchronization of oscillatory neuronal responses in cat striate cortex: temporal properties. *Vis Neurosci* 8:337–47.

Gray CM, Konig P, Engel AK, Singer W (1989) Oscillatory responses in cat visual cortex exhibit inter-columnar synchronization which reflects global stimulus properties. *Nature* 338:334–7.

Gray CM, Singer W (1989) Stimulus-specific neuronal oscillations in orientation columns of cat visual cortex. *Proc Natl Acad Sci U S A* 86:1698–702.

Graybiel AM (2005) The basal ganglia: learning new tricks and loving it. *Curr Opin Neurobiol* 15:638–44.

Graybiel AM, Aosaki T, Flaherty AW, Kimura M (1994) The basal ganglia and adaptive motor control. *Science* 265:1826–31.

Gregoriou GG, Gotts SJ, Zhou H, Desimone R (2009) High-frequency, long-range coupling between prefrontal and visual cortex during attention. *Science* 324:1207–10.

Groenewegen HJ, Berendse HW (1994) The specificity of the 'nonspecific' midline and intralaminar thalamic nuclei. *Trends Neurosci* 17:52–7.

Gurney K, Prescott TJ, Redgrave P (2001a) A computational model of action selection in the basal ganglia. i. a new functional anatomy. *Biol Cybern* 84:401–10.

Gurney K, Prescott TJ, Redgrave P (2001b) A computational model of action selection in the basal ganglia. ii. analysis and simulation of behaviour. *Biol Cybern* 84:411–23.

Haber S, McFarland NR (2001) The place of the thalamus in frontal cortical-basal ganglia circuits. *Neuroscientist* 7:315–24.

Haber S, Lynd-Balta E, Spooren W (1994) Integrative aspects of basal ganglia circuitry In Percheron G, McKenzie JS, Férger J, editors, *The Basal ganglia IV: new ideas and data on structure and function*, Advances in behavioral biology, pp. xiii, 616 p. Plenum

Press, New York.

Haber SN, Calzavara R (2009) The cortico-basal ganglia integrative network: the role of the thalamus. *Brain Res Bull* 78:69–74.

Haider B, McCormick DA (2009) Rapid neocortical dynamics: cellular and network mechanisms. *Neuron* 62:171–89.

Hall RD, Lindholm EP (1974) Organization of motor and somatosensory neocortex in the albino rat. *Brain Research* 66:23–38.

Hallworth NE, Bland BH (2004) Basal ganglia–hippocampal interactions support the role of the hippocampal formation in sensorimotor integration. *Exp Neurol* 188:430–43.

Hammond C, Bergman H, Brown P (2007) Pathological synchronization in parkinson's disease: networks, models and treatments. *Trends Neurosci* 30:357–64.

Harris KD (2005) Neural signatures of cell assembly organization. *Nat Rev Neurosci* 6:399–407.

Harris KD, Csicsvari J, Hirase H, Dragoi G, Buzsáki G (2003) Organization of cell assemblies in the hippocampus. *Nature* 424:552–6.

Hasenstaub A, Shu Y, Haider B, Kraushaar U, Duque A, McCormick DA (2005) Inhibitory postsynaptic potentials carry synchronized frequency information in active cortical networks. *Neuron* 47:423–35.

Heimer L (2003) A new anatomical framework for neuropsychiatric disorders and drug abuse. *Am J Psychiatry* 160:1726–39.

Hikosaka O, Sakamoto M, Usui S (1989a) Functional properties of monkey caudate neurons. i. activities related to saccadic eye movements. *J Neurophysiol* 61:780–98.

Hikosaka O, Sakamoto M, Usui S (1989b) Functional properties of monkey caudate neurons. ii. visual and auditory responses. *J Neurophysiol* 61:799–813.

Hikosaka O, Sakamoto M, Usui S (1989c) Functional properties of monkey caudate neurons. iii. activities related to expectation of target and reward. *J Neurophysiol* 61:814–32.

Hikosaka O, Takikawa Y, Kawagoe R (2000) Role of the basal ganglia in the control of purposive saccadic eye movements. *Physiol Rev* 80:953–78.

Hipp JF, Engel AK, Siegel M (2011) Oscillatory synchronization in large-scale cortical networks predicts perception. *Neuron* 69:387–96.

Hoover JE, Strick PL (1993) Multiple output channels in the basal ganglia. *Science* 259:819–21.

Houk JC, Wise SP (1995) Distributed modular architectures linking basal ganglia, cerebellum, and cerebral cortex: their role in planning and controlling action. *Cereb Cortex* 5:95–110.

Humphries MD, Stewart RD, Gurney KN (2006) A physiologically plausible model of action selection and oscillatory activity in the basal ganglia. *J Neurosci* 26:12921–42.

Jensen O, Colgin LL (2007) Cross-frequency coupling between neuronal oscillations. *Trends Cogn Sci* 11:267–9.

Joel D, Weiner I (1994) The organization of the basal ganglia-thalamocortical circuits: open interconnected rather than closed segregated. *Neuroscience* 63:363–79.

Joel D, Weiner I (2000) The connections of the dopaminergic system with the striatum in rats and primates: an analysis with respect to the functional and compartmental organization of the striatum. *Neuroscience* 96:451–74.

Jog MS, Connolly CI, Kubota Y, Iyengar DR, Garrido L, Harlan R, Graybiel AM (2002) Tetrode technology: advances in implantable hardware, neuroimaging, and data analysis techniques. *J Neurosci Methods* 117:141–52.

Jones EG, Coulter JD, Burton H, Porter R (1977) Cells of origin and terminal distribution of corticostriatal fibers arising in the sensory-motor cortex of monkeys. *J Comp Neurol* 173:53–80.

Jones EG, Wise SP (1977) Size, laminar and columnar distribution of efferent cells in the sensory-motor cortex of monkeys. *J Comp Neurol* 175:391–438.

Jones EG (2007) *The Thalamus* Cambridge University Press, Cambridge, 2nd edition.

Jones EG (2009) Synchrony in the interconnected circuitry of the thalamus and cerebral cortex. *Ann N Y Acad Sci* 1157:10–23.

Jutras MJ, Buffalo EA (2010) Synchronous neural activity and memory formation. *Curr Opin Neurobiol* 20:150–5.

Kahana MJ, Seelig D, Madsen JR (2001) Theta returns. *Curr Opin Neurobiol* 11:739–44.

Kahana MJ, Sekuler R, Caplan JB, Kirschen M, Madsen JR (1999) Human theta oscillations exhibit task dependence during virtual maze navigation. *Nature* 399:781–4.

Kalenscher T, Lansink CS, Lankelma JV, Pennartz CMA (2010) Reward-associated gamma oscillations in ventral striatum are regionally differentiated and modulate local firing activity. *J Neurophysiol* 103:1658–72.

Kasanetz F, Riquelme LA, Della-Maggiore V, O'Donnell P, Murer MG (2008) Functional integration across a gradient of corticostriatal channels controls UP state transitions in the dorsal striatum. *Proc Natl Acad Sci U S A* 105:8124–9.

Kasanetz F, Riquelme LA, Murer MG (2002) Disruption of the two-state membrane potential of striatal neurones during cortical desynchronisation in anaesthetised rats. *J Physiol* 543:577–89.

Kasanetz F, Riquelme LA, O'Donnell P, Murer MG (2006) Turning off cortical ensembles stops striatal up states and elicits phase perturbations in cortical and striatal slow oscillations in rat in vivo. *J Physiol* 577:97–113.

Katzner S, Nauhaus I, Benucci A, Bonin V, Ringach DL, Carandini M (2009) Local origin of field potentials in visual cortex. *Neuron* 61:35–41.

Kay LM (2005) Theta oscillations and sensorimotor performance. *Proc Natl Acad Sci U S A* 102:3863–8.

Kayser C, Logothetis NK (2009) Directed interactions between auditory and superior temporal cortices and their role in sensory integration. *Front Integr Neurosci* 3:7.

Kemp JM, Powell TP (1970) The cortico-striate projection in the monkey. *Brain* 93:525–46.

Kimeldorf D (1961) The measurement of performance in small laboratory animals. In Spector H, Brozek J, Peterson MS, editors, *Performance capacity*, pp. 99–112. National Research Council, Washington, D.C.

Kincaid AE, Zheng T, Wilson CJ (1998) Connectivity and convergence of single corticostriatal axons. *J Neurosci* 18:4722–31.

Klausberger T, Magill PJ, Márton LF, Roberts JDB, Cobden PM, Buzsáki G, Somogyi P (2003) Brain-state- and cell-type-specific firing of hippocampal interneurons in vivo. *Nature* 421:844–8.

König P, Engel AK, Singer W (1996) Integrator or coincidence detector? The role of the cortical neuron revisited. *Trends Neurosci* 19:130–7.

Koos T, Tepper JM (1999) Inhibitory control of neostriatal projection neurons by gabaergic interneurons. *Nat Neurosci* 2:467–72.

Kopell N, Ermentrout GB, Whittington MA, Traub RD (2000) Gamma rhythms and beta rhythms have different synchronization properties. *Proc Natl Acad Sci U S A* 97:1867–72.

Kopell N, Kramer MA, Malerba P, Whittington MA (2010) Are different rhythms good for different functions? *Front Hum Neurosci* 4:187.

Kornhuber HH (1971) Motor functions of cerebellum and basal ganglia: the cerebellocortical saccadic (ballistic) clock, the cerebellonuclear hold regulator, and the basal ganglia ramp (voluntary speed smooth movement) generator. *Kybernetik* 8:157–62.

Kralik JD, Dimitrov DF, Krupa DJ, Katz DB, Cohen D, Nicolelis MA (2001) Techniques for long-term multisite neuronal ensemble recordings in behaving animals. *Methods* 25:121–50.

Kravitz AV, Freeze BS, Parker PRL, Kay K, Thwin MT, Deisseroth K, Kreitzer AC (2010) Regulation of parkinsonian motor behaviours by optogenetic control of basal ganglia circuitry. *Nature* 466:622–6.

Kreiter AK, Singer W (1996) Stimulus-dependent synchronization of neuronal responses in the visual cortex of the awake macaque monkey. *J Neurosci* 16:2381–96.

Kreitzer AC (2009) Physiology and pharmacology of striatal neurons. *Annu Rev Neurosci* 32:127–47.

Kreitzer AC, Malenka RC (2008) Striatal plasticity and basal ganglia circuit function. *Neuron* 60:543–54.

Kumar A, Rotter S, Aertsen A (2010) Spiking activity propagation in neuronal networks: reconciling different perspectives on neural coding. *Nat Rev Neurosci* 11:615–27.

Künzle H (1975) Bilateral projections from precentral motor cortex to the putamen and other parts of the basal ganglia. An autoradiographic study in Macaca fascicularis. *Brain Res* 88:195–209.

Lachaux JP, Rodriguez E, Martinerie J, Varela FJ (1999) Measuring phase synchrony in brain signals. *Hum Brain Mapp* 8:194–208.

Lalo E, Thobois S, Sharott A, Polo G, Mertens P, Pogosyan A, Brown P (2008) Patterns of bidirectional communication between cortex and basal ganglia during movement in patients with parkinson disease. *J Neurosci* 28:3008–16.

Lamme VA, Spekreijse H (1998) Neuronal synchrony does not represent texture segregation. *Nature* 396:362–6.

Le Van Quyen M, Foucher J, Lachaux J, Rodriguez E, Lutz A, Martinerie J, Varela FJ (2001) Comparison of hilbert transform and wavelet methods for the analysis of neuronal synchrony. *J Neurosci Methods* 111:83–98.

Le Van Quyen M, Bragin A (2007) Analysis of dynamic brain oscillations: methodological advances. *Trends Neurosci* 30:365–73.

Leblois A, Boraud T, Meissner W, Bergman H, Hansel D (2006) Competition between feedback loops underlies normal and pathological dynamics in the basal ganglia. *J Neurosci* 26:3567–83.

Lee AK, Epsztein J, Brecht M (2009) Head-anchored whole-cell recordings in freely moving rats. *Nat Protoc* 4:385–92.

Lee AK, Manns ID, Sakmann B, Brecht M (2006) Whole-cell recordings in freely moving rats. *Neuron* 51:399–407.

Lee D (2002) Analysis of phase-locked oscillations in multi-channel single-unit spike activity with wavelet cross-spectrum. *J Neurosci Methods* 115:67–75.

Levy R, Friedman HR, Davachi L, Goldman-Rakic PS (1997) Differential activation of the caudate nucleus in primates performing spatial and nonspatial working memory tasks. *J Neurosci* 17:3870–82.

Levy R, Ashby P, Hutchison WD, Lang AE, Lozano AM, Dostrovsky JO (2002) Dependence of subthalamic nucleus oscillations on movement and dopamine in Parkinson's disease. *Brain* 125:1196–209.

Li X, Yao X, Fox J, Jefferys JG (2007) Interaction dynamics of neuronal oscillations analysed using wavelet transforms. *J Neurosci Methods* 160:178–85.

Lim TS, Loh WY (1996) A comparison of tests of equality of variances. *Computational Statistics & Data Analysis* 22:287–301.

Lisman JE, Idiart MA (1995) Storage of 7 +/- 2 short-term memories in oscillatory subcycles. *Science* 267:1512–5.

Lisman J (2005) The theta/gamma discrete phase code occuring during the hippocampal phase precession may be a more general brain coding scheme. *Hippocampus* 15:913–22.

Lisman J, Buzsáki G (2008) A neural coding scheme formed by the combined function of gamma and theta oscillations. *Schizophr Bull* 34:974–80.

Llinás RR (1988) The intrinsic electrophysiological properties of mammalian neurons: insights into central nervous system function. *Science* 242:1654–64.

Logothetis NK, Pauls J, Augath M, Trinath T, Oeltermann A (2001) Neurophysiological investigation of the basis of the fMRI signal. *Nature* 412:150–7.

Lubenov EV, Siapas AG (2009) Hippocampal theta oscillations are travelling waves. *Nature* 459:534–9.

MacKay W (1997) Synchronized neuronal oscillations and their role in motor processes. *Trends in Cognitive Sciences* 1:176–183.

Magill PJ, Bolam JP, Bevan MD (2000) Relationship of activity in the subthalamic nucleus-globus pallidus network to cortical electroencephalogram. *J Neurosci* 20:820–33.

Magill PJ, Bolam JP, Bevan MD (2001) Dopamine regulates the impact of the cerebral cortex on the subthalamic nucleus-globus pallidus network. *Neuroscience* 106:313–30.

Magill PJ, Pogosyan A, Sharott A, Csicsvari J, Bolam JP, Brown P (2006) Changes in functional connectivity within the rat striatopallidal axis during global brain activation in vivo. *J Neurosci* 26:6318–29.

Magill PJ, Sharott A, Bolam JP, Brown P (2004a) Brain state-dependency of coherent oscillatory activity in the cerebral cortex and basal ganglia of the rat. *J Neurophysiol* 92:2122–36.

Magill PJ, Sharott A, Bevan MD, Brown P, Bolam JP (2004b) Synchronous unit activity and local field potentials evoked in the subthalamic nucleus by cortical stimulation. *J Neurophysiol* 92:700–14.

Magill PJ, Sharott A, Bolam JP, Brown P (2006) Delayed synchronization of activity in cortex and subthalamic nucleus following cortical stimulation in the rat. *J Physiol* 574:929–46.

Mahon S, Deniau JM, Charpier S (2001) Relationship between EEG potentials and intracellular activity of striatal and cortico-striatal neurons: an in vivo study under

different anesthetics. *Cereb Cortex* 11:360–73.

Mahon S, Vautrelle N, Pezard L, Slaght SJ, Deniau JM, Chouvet G, Charpier S (2006) Distinct patterns of striatal medium spiny neuron activity during the natural sleep-wake cycle. *J Neurosci* 26:12587–95.

Mallet N, Le Moine C, Charpier S, Gonon F (2005) Feedforward inhibition of projection neurons by fast-spiking GABA interneurons in the rat striatum in vivo. *J Neurosci* 25:3857–69.

Mallet N, Pogosyan A, Marton LF, Bolam JP, Brown P, Magill PJ (2008) Parkinsonian beta oscillations in the external globus pallidus and their relationship with subthalamic nucleus activity. *J Neurosci* 28:14245–58.

Marder E, Calabrese RL (1996) Principles of rhythmic motor pattern generation. *Physiol Rev* 76:687–717.

Maris E, Oostenveld R (2007) Nonparametric statistical testing of EEG- and MEG-data. *J Neurosci Methods* 164:177–90.

Maris E, Schoffelen JM, Fries P (2007) Nonparametric statistical testing of coherence differences. *J Neurosci Methods* 163:161–75.

Markram H, Lübke J, Frotscher M, Sakmann B (1997) Regulation of synaptic efficacy by coincidence of postsynaptic APs and EPSPs. *Science* 275:213–5.

Marsden CD (1984a) Function of the basal ganglia as revealed by cognitive and motor disorders in parkinson's disease. *Can J Neurol Sci* 11:129–35.

Marsden CD (1984b) Which motor disorder in parkinson's disease indicates the true motor function of the basal ganglia? *Ciba Found Symp* 107:225–41.

Masimore B, Kakalios J, Redish AD (2004) Measuring fundamental frequencies in local field potentials. *J Neurosci Methods* 138:97–105.

Masimore B, Schmitzer-Torbert NC, Kakalios J, Redish AD (2005) Transient striatal gamma local field potentials signal movement initiation in rats. *Neuroreport* 16:2021–4.

McFarland WL, Teitelbaum H, Hedges EK (1975) Relationship between hippocampal theta activity and running speed in the rat. *J Comp Physiol Psychol* 88:324–8.

McGeorge AJ, Faull RL (1987) The organization and collateralization of corticostriate neurones in the motor and sensory cortex of the rat brain. *Brain Res* 423:318–24.

McGeorge AJ, Faull RL (1989) The organization of the projection from the cerebral cortex to the striatum in the rat. *Neuroscience* 29:503–37.

McMahon D (2007) *Signals and systems demystified* Demystified series. McGraw-Hill, New York.

McNab F, Klingberg T (2008) Prefrontal cortex and basal ganglia control access to working memory. *Nat Neurosci* 11:103–7.

Middleton FA, Strick PL (1994) Anatomical evidence for cerebellar and basal ganglia involvement in higher cognitive function. *Science* 266:458–61.

Middleton FA, Strick PL (1996) The temporal lobe is a target of output from the basal ganglia. *Proc Natl Acad Sci U S A* 93:8683–7.

Middleton FA, Strick PL (2000) Basal ganglia output and cognition: evidence from anatomical, behavioral, and clinical studies. *Brain Cogn* 42:183–200.

Miller KJ, Sorensen LB, Ojemann JG, den Nijs M (2009) Power-law scaling in the brain surface electric potential. *PLoS Comput Biol* 5:e1000609.

Mima T, Steger J, Schulman AE, Gerloff C, Hallett M (2000) Electroencephalographic measurement of motor cortex control of muscle activity in humans. *Clin Neurophysiol* 111:326–37.

Mink JW (1996) The basal ganglia: focused selection and inhibition of competing motor programs. *Prog Neurobiol* 50:381–425.

Mitzdorf U (1985) Current source-density method and application in cat cerebral cortex: investigation of evoked potentials and EEG phenomena. *Physiol Rev* 65:37–100.

Mogenson GJ, Jones DL, Yim CY (1980) From motivation to action: functional interface between the limbic system and the motor system. *Prog Neurobiol* 14:69–97.

Montemurro MA, Rasch MJ, Murayama Y, Logothetis NK, Panzeri S (2008) Phase-of-firing coding of natural visual stimuli in primary visual cortex. *Curr Biol* 18:375–80.

Montgomery SM, Betancur MI, Buzsáki G (2009) Behavior-dependent coordination of multiple theta dipoles in the hippocampus. *J Neurosci* 29:1381–94.

Moran A, Bar-Gad I (2010) Revealing neuronal functional organization through the relation between multi-scale oscillatory extracellular signals. *J Neurosci Methods* 186:116–29.

Moran A, Bergman H, Israel Z, Bar-Gad I (2008) Subthalamic nucleus functional organization revealed by parkinsonian neuronal oscillations and synchrony. *Brain* 131:3395–409.

Morlet J, Arens G, Fourgeau E, Giard D (1982a) Wave propagation and sampling theory—Part I: Complex signal and scattering in multilayered media. *Geophysics* 47:203–221.

Morlet J, Arens G, Fourgeau E, Giard D (1982b) Wave propagation and sampling theory—Part II: Sampling theory and complex waves. *Geophysics* 47:222–236.

Motulsky H (1995) *Intuitive biostatistics* Oxford University Press, New York.

Munk MH, Roelfsema PR, Konig P, Engel AK, Singer W (1996) Role of reticular activation in the modulation of intracortical synchronization. *Science* 272:271–4.

Murer MG, Tseng KY, Kasanetz F, Belluscio M, Riquelme LA (2002) Brain oscillations, medium spiny neurons, and dopamine. *Cell Mol Neurobiol* 22:611–32.

Murthy VN, Fetz EE (1992) Coherent 25- to 35-hz oscillations in the sensorimotor cortex of awake behaving monkeys. *Proc Natl Acad Sci U S A* 89:5670–4.

Murthy VN, Fetz EE (1996a) Oscillatory activity in sensorimotor cortex of awake monkeys: synchronization of local field potentials and relation to behavior. *J Neurophysiol* 76:3949–67.

Murthy VN, Fetz EE (1996b) Synchronization of neurons during local field potential oscillations in sensorimotor cortex of awake monkeys. *J Neurophysiol* 76:3968–82.

Nakao M, Murakami H, Tanaka H (1982) Improved treadmill to avoid foot and tail injuries of small animals. *Experientia* 38:140–1.

Nambu A (2011) Somatotopic organization of the primate basal ganglia. *Front Neuroanat* 5:26.

Nauta WJ, Mehler WR (1966) Projections of the lentiform nucleus in the monkey. *Brain Res* 1:3–42.

Nicolelis MA, Baccala LA, Lin RC, Chapin JK (1995) Sensorimotor encoding by synchronous neural ensemble activity at multiple levels of the somatosensory system. *Science* 268:1353–8.

Niell CM, Stryker MP (2010) Modulation of visual responses by behavioral state in mouse visual cortex. *Neuron* 65:472–9.

Nini A, Feingold A, Slovin H, Bergman H (1995) Neurons in the globus pallidus do not show correlated activity in the normal monkey, but phase-locked oscillations appear in the MPTP model of parkinsonism. *J Neurophysiol* 74:1800–5.

Nisenbaum ES, Wilson CJ (1995) Potassium currents responsible for inward and outward rectification in rat neostriatal spiny projection neurons. *J Neurosci* 15:4449–63.

Nolte G, Bai O, Wheaton L, Mari Z, Vorbach S, Hallett M (2004) Identifying true brain interaction from EEG data using the imaginary part of coherency. *Clin Neurophysiol* 115:2292–307.

O'Keefe J, Recce ML (1993) Phase relationship between hippocampal place units and the EEG theta rhythm. *Hippocampus* 3:317–30.

Omlor W, Patino L, Hepp-Reymond MC, Kristeva R (2007) Gamma-range corticomuscular coherence during dynamic force output. *Neuroimage* 34:1191–8.

Oorschot DE (1996) Total number of neurons in the neostriatal, pallidal, subthalamic, and substantia nigral nuclei of the rat basal ganglia: a stereological study using the cavalieri and optical disector methods. *J Comp Neurol* 366:580–99.

Oorschot DE (2010) Cell types in the different nuclei of the basal ganglia In Steiner H, Tseng KY, editors, *Handbook of Basal Ganglia Structure and Function*, Vol. 20 of *Handbook of Behavioral Neuroscience*, pp. 63–74. Elsevier.

Oostenveld R, Fries P, Maris E, Schoffelen JM (2011) FieldTrip: Open source software for advanced analysis of MEG, EEG, and invasive electrophysiological data. *Comput Intell Neurosci* 2011:156869.

Packard MG, Knowlton BJ (2002) Learning and memory functions of the basal ganglia. *Annu Rev Neurosci* 25:563–93.

Panzeri S, Brunel N, Logothetis NK, Kayser C (2010) Sensory neural codes using multiplexed temporal scales. *Trends Neurosci* 33:111–20.

Parent A (1990) Extrinsic connections of the basal ganglia. *Trends Neurosci* 13:254–8.

Parent A, Bouchard C, Smith Y (1984) The striatopallidal and striatonigral projections: two distinct fiber systems in primate. *Brain Res* 303:385–90.

Parent A, Hazrati LN (1993) Anatomical aspects of information processing in primate basal ganglia. *Trends Neurosci* 16:111–6.

Parent A, Hazrati LN (1995) Functional anatomy of the basal ganglia. i. the cortico-basal ganglia-thalamo-cortical loop. *Brain Res Brain Res Rev* 20:91–127.

Pasupathy A, Miller EK (2005) Different time courses of learning-related activity in the prefrontal cortex and striatum. *Nature* 433:873–6.

Paxinos G, Watson C (2005) *The rat brain in stereotaxic coordinates* Elsevier Academic Press, Amsterdam, 5th edition.

Penttonen M, Buzsáki G (2003) Natural logarithmic relationship between brain oscillators. *Thalamus & Related Systems* 2:145–152.

Pesaran B, Nelson MJ, Andersen RA (2008) Free choice activates a decision circuit between frontal and parietal cortex. *Nature* 453:406–9.

Pesaran B, Pezaris JS, Sahani M, Mitra PP, Andersen RA (2002) Temporal structure in neuronal activity during working memory in macaque parietal cortex. *Nat Neurosci* 5:805–11.

Pfurtscheller G, Neuper C, Kalcher J (1993) 40-Hz oscillations during motor behavior in man. *Neurosci Lett* 164:179–82.

Phillips JG, Bradshaw JL, Iansek R, Chiu E (1993) Motor functions of the basal ganglia. *Psychol Res* 55:175–81.

Pike FG, Goddard RS, Suckling JM, Ganter P, Kasthuri N, Paulsen O (2000) Distinct frequency preferences of different types of rat hippocampal neurones in response to oscillatory input currents. *J Physiol* 529:205–13.

Plenz D, Aertsen A (1996) Neural dynamics in cortex-striatum co-cultures–ii. spatiotemporal characteristics of neuronal activity. *Neuroscience* 70:893–924.

Plenz D, Kitai ST (1998) Up and down states in striatal medium spiny neurons simultaneously recorded with spontaneous activity in fast-spiking interneurons studied in cortex-striatum-substantia nigra organotypic cultures. *J Neurosci* 18:266–83.

Plenz D, Kital ST (1999) A basal ganglia pacemaker formed by the subthalamic nucleus and external globus pallidus. *Nature* 400:677–82.

Popescu AT, Popa D, Paré D (2009) Coherent gamma oscillations couple the amygdala and striatum during learning. *Nat Neurosci* 12:801–7.

Quiroga RQ, Nadasdy Z, Ben-Shaul Y (2004) Unsupervised spike detection and sorting with wavelets and superparamagnetic clustering. *Neural Comput* 16:1661–87.

Rakic P (2009) Evolution of the neocortex: a perspective from developmental biology. *Nat Rev Neurosci* 10:724–35.

Ramanathan S, Hanley JJ, Deniau JM, Bolam JP (2002) Synaptic convergence of motor and somatosensory cortical afferents onto GABAergic interneurons in the rat striatum. *J Neurosci* 22:8158–69.

Ray S, Maunsell JHR (2010) Differences in gamma frequencies across visual cortex restrict their possible use in computation. *Neuron* 67:885–96.

Raz A, Feingold A, Zelanskaya V, Vaadia E, Bergman H (1996) Neuronal synchronization of tonically active neurons in the striatum of normal and parkinsonian primates. *J Neurophysiol* 76:2083–8.

Raz A, Frechter-Mazar V, Feingold A, Abeles M, Vaadia E, Bergman H (2001) Activity of pallidal and striatal tonically active neurons is correlated in mptp-treated monkeys but not in normal monkeys. *J Neurosci* 21:RC128.

Redgrave P, Prescott TJ, Gurney K (1999) The basal ganglia: a vertebrate solution to the selection problem? *Neuroscience* 89:1009–23.

Reiner A, Medina L, Veenman CL (1998) Structural and functional evolution of the basal ganglia in vertebrates. *Brain Res Brain Res Rev* 28:235–85.

Reiner A (2010a) The conservative evolution of the vertebrate basal ganglia In Steiner H, Tseng KY, editors, *Handbook of Basal Ganglia Structure and Function*, Vol. 20 of *Handbook of Behavioral Neuroscience*, pp. 29–62. Elsevier.

Reiner A (2010b) Organization of corticostriatal projection neuron types In Steiner H, Tseng KY, editors, *Handbook of Basal Ganglia Structure and Function*, Vol. 20 of *Handbook of Behavioral Neuroscience*, pp. 323–339. Elsevier.

Reiner A, Hart NM, Lei W, Deng Y (2010) Corticostriatal projection neurons - dichotomous types and dichotomous functions. *Front Neuroanat* 4:142.

Reiner A, Jiao Y, Del Mar N, Laverghetta AV, Lei WL (2003) Differential morphology of pyramidal tract-type and intratelencephalically projecting-type corticostriatal neurons and their intrastriatal terminals in rats. *J Comp Neurol* 457:420–40.

Reynolds JN, Hyland BI, Wickens JR (2001) A cellular mechanism of reward-related learning. *Nature* 413:67–70.

Riehle A, Grun S, Diesmann M, Aertsen A (1997) Spike synchronization and rate modulation differentially involved in motor cortical function. *Science* 278:1950–3.

Rivas J, Gaztelu JM, García-Austt E (1996) Changes in hippocampal cell discharge patterns and theta rhythm spectral properties as a function of walking velocity in the guinea pig. *Exp Brain Res* 108:113–8.

Robbins TW, Everitt BJ (2002) Limbic-striatal memory systems and drug addiction. *Neurobiol Learn Mem* 78:625–36.

Roelfsema PR, Engel AK, Konig P, Singer W (1997) Visuomotor integration is associated with zero time-lag synchronization among cortical areas. *Nature* 385:157–61.

Romo R, Scarnati E, Schultz W (1992) Role of primate basal ganglia and frontal cortex in the internal generation of movements. II. Movement-related activity in the anterior striatum. *Exp Brain Res* 91:385–95.

Salenius S, Hari R (2003) Synchronous cortical oscillatory activity during motor action. *Curr Opin Neurobiol* 13:678–84.

Salinas E, Sejnowski TJ (2000) Impact of correlated synaptic input on output firing rate and variability in simple neuronal models. *J Neurosci* 20:6193–209.

Salinas E, Sejnowski TJ (2001) Correlated neuronal activity and the flow of neural information. *Nat Rev Neurosci* 2:539–50.

Sanes JN, Donoghue JP (1993) Oscillations in local field potentials of the primate motor cortex during voluntary movement. *Proc Natl Acad Sci U S A* 90:4470–4.

Schoffelen JM, Oostenveld R, Fries P (2005) Neuronal coherence as a mechanism of effective corticospinal interaction. *Science* 308:111–3.

Schultz W, Tremblay L, Hollerman JR (2000) Reward processing in primate orbitofrontal cortex and basal ganglia. *Cereb Cortex* 10:272–84.

Schultz W (2006) Behavioral theories and the neurophysiology of reward. *Annu Rev Psychol* 57:87–115.

Schultz W, Tremblay L, Hollerman JR (2003) Changes in behavior-related neuronal activity in the striatum during learning. *Trends Neurosci* 26:321–8.

Schulz JM, Pitcher TL, Savanthrapadian S, Wickens JR, Oswald MJ, Reynolds JNJ (2011) Enhanced high-frequency membrane potential fluctuations control spike output in striatal fast-spiking interneurones in vivo. *J Physiol* 589:4365–81.

Selemon LD, Goldman-Rakic PS (1985) Longitudinal topography and interdigitation of corticostriatal projections in the rhesus monkey. *J Neurosci* 5:776–94.

Shadlen MN, Movshon JA (1999) Synchrony unbound: a critical evaluation of the temporal binding hypothesis. *Neuron* 24:67–77, 111–25.

Sharott A (2005) The Role of Oscillatory Population Activity in Cortico-Basal Ganglia Circuits Ph.D. diss., University College London, Sobell Department of Motor Neuro-

science and Movement Disorders, Institute of Neurology, University College London, Queen Square, London WC1N 3BG, England.

Sharott A, Grosse P, Kuhn AA, Salih F, Engel AK, Kupsch A, Schneider GH, Krauss JK, Brown P (2008) Is the synchronization between pallidal and muscle activity in primary dystonia due to peripheral afferance or a motor drive? *Brain* 131:473–84.

Sharott A, Magill PJ, Bolam JP, Brown P (2005) Directional analysis of coherent oscillatory field potentials in the cerebral cortex and basal ganglia of the rat. *J Physiol* 562:951–63.

Sharott A, Moll CK, Engler G, Denker M, Grun S, Engel AK (2009) Different subtypes of striatal neurons are selectively modulated by cortical oscillations. *J Neurosci* 29:4571–85.

Sherman SM (2007) The thalamus is more than just a relay. *Curr Opin Neurobiol* 17:417–22.

Shi LH, Luo F, Woodward DJ, Chang JY (2004) Neural responses in multiple basal ganglia regions during spontaneous and treadmill locomotion tasks in rats. *Exp Brain Res* 157:303–14.

Shi LH, Luo F, Woodward DJ, Chang JY (2006) Basal ganglia neural responses during behaviorally effective deep brain stimulation of the subthalamic nucleus in rats performing a treadmill locomotion test. *Synapse* 59:445–57.

Shu Y, Hasenstaub A, McCormick DA (2003) Turning on and off recurrent balanced cortical activity. *Nature* 423:288–93.

Siegel M, Donner TH, Oostenveld R, Fries P, Engel AK (2008) Neuronal synchronization along the dorsal visual pathway reflects the focus of spatial attention. *Neuron* 60:709–719.

Siegel M, Konig P (2003) A functional gamma-band defined by stimulus-dependent synchronization in area 18 of awake behaving cats. *J Neurosci* 23:4251–60.

Siegel M, Warden MR, Miller EK (2009) Phase-dependent neuronal coding of objects in short-term memory. *Proc Natl Acad Sci U S A* 106:21341–6.

Singer W (1993) Synchronization of cortical activity and its putative role in information processing and learning. *Annu Rev Physiol* 55:349–74.

Singer W (1999) Neuronal synchrony: a versatile code for the definition of relations? *Neuron* 24:49–65, 111–25.

Singer W, Gray CM (1995) Visual feature integration and the temporal correlation hypothesis. *Annu Rev Neurosci* 18:555–86.

Sirota A, Montgomery S, Fujisawa S, Isomura Y, Zugaro M, Buzsaki G (2008) Entrainment of neocortical neurons and gamma oscillations by the hippocampal theta rhythm. *Neuron* 60:683–97.

Skaggs WE, McNaughton BL, Wilson MA, Barnes CA (1996) Theta phase precession in hippocampal neuronal populations and the compression of temporal sequences. *Hippocampus* 6:149–72.

Smith AD, Bolam JP (1990) The neural network of the basal ganglia as revealed by the study of synaptic connections of identified neurones. *Trends Neurosci* 13:259–65.

Smith SW (1997) *The scientist and engineer's guide to digital signal processing* California Technical Pub., San Diego, California, 1st edition.

Smith Y, Bevan MD, Shink E, Bolam JP (1998) Microcircuitry of the direct and indirect pathways of the basal ganglia. *Neuroscience* 86:353–87.

Soltesz I, Deschênes M (1993) Low- and high-frequency membrane potential oscillations during theta activity in CA1 and CA3 pyramidal neurons of the rat hippocampus under ketamine-xylazine anesthesia. *J Neurophysiol* 70:97–116.

Stephenson-Jones M, Samuelsson E, Ericsson J, Robertson B, Grillner S (2011) Evolutionary conservation of the basal ganglia as a common vertebrate mechanism for action selection. *Curr Biol* 21:1081–91.

Steriade M (2000) Corticothalamic resonance, states of vigilance and mentation. *Neuroscience* 101:243–76.

Steriade M, Contreras D, Amzica F, Timofeev I (1996) Synchronization of fast (30-40 Hz) spontaneous oscillations in intrathalamic and thalamocortical networks. *J Neurosci* 16:2788–808.

Steriade M, Dossi RC, Paré D, Oakson G (1991) Fast oscillations (20-40 Hz) in thalamocortical systems and their potentiation by mesopontine cholinergic nuclei in the cat. *Proc Natl Acad Sci U S A* 88:4396–400.

Steriade M, Llinás RR (1988) The functional states of the thalamus and the associated neuronal interplay. *Physiol Rev* 68:649–742.

Steriade M, McCormick DA, Sejnowski TJ (1993a) Thalamocortical oscillations in the sleeping and aroused brain. *Science* 262:679–85.

Steriade M, Nuñez A, Amzica F (1993b) A novel slow ($<$ 1 Hz) oscillation of neocortical neurons in vivo: depolarizing and hyperpolarizing components. *J Neurosci* 13:3252–65.

Steriade M, Timofeev I, Grenier F (2001) Natural waking and sleep states: a view from inside neocortical neurons. *J Neurophysiol* 85:1969–85.

Sterling MJ (2005) *Trigonometry for dummies* Wiley, Hoboken, N.J.

Stern EA, Jaeger D, Wilson CJ (1998) Membrane potential synchrony of simultaneously recorded striatal spiny neurons in vivo. *Nature* 394:475–8.

Stern EA, Kincaid AE, Wilson CJ (1997) Spontaneous subthreshold membrane potential fluctuations and action potential variability of rat corticostriatal and striatal neurons in vivo. *J Neurophysiol* 77:1697–715.

Surmeier DJ, Ding J, Day M, Wang Z, Shen W (2007) D1 and D2 dopamine-receptor modulation of striatal glutamatergic signaling in striatal medium spiny neurons. *Trends Neurosci* 30:228–35.

Syed ECJ, Sharott A, Moll CKE, Engel AK, Kral A (2011) Effect of sensory stimulation in rat barrel cortex, dorsolateral striatum and on corticostriatal functional connectivity. *Eur J Neurosci* 33:461–70.

Tallon-Baudry C, Bertrand O (1999) Oscillatory gamma activity in humans and its role in object representation. *Trends Cogn Sci* 3:151–162.

Teitelbaum H, Lee JF, Johannessen JN (1975) Behaviorally evoked hippocampal theta waves: a cholinergic response. *Science* 188:1114–6.

Tepper JM, Bolam JP (2004) Functional diversity and specificity of neostriatal interneurons. *Curr Opin Neurobiol* 14:685–92.

Tepper JM (2010) GABAergic interneurons of the striatum In Steiner H, Tseng KY, editors, *Handbook of Basal Ganglia Structure and Function*, Vol. 20 of *Handbook of Behavioral Neuroscience*, pp. 151–166. Elsevier.

Thiele A, Stoner G (2003) Neuronal synchrony does not correlate with motion coherence in cortical area MT. *Nature* 421:366–70.

Tort AB, Kramer MA, Thorn C, Gibson DJ, Kubota Y, Graybiel AM, Kopell NJ (2008) Dynamic cross-frequency couplings of local field potential oscillations in rat striatum and hippocampus during performance of a t-maze task. *Proc Natl Acad Sci U S A* 105:20517–22.

Tort ABL, Komorowski R, Eichenbaum H, Kopell N (2010) Measuring phase-amplitude coupling between neuronal oscillations of different frequencies. *J Neurophysiol* 104:1195–210.

Tort ABL, Komorowski RW, Manns JR, Kopell NJ, Eichenbaum H (2009) Theta-gamma coupling increases during the learning of item-context associations. *Proc Natl Acad Sci U S A* 106:20942–7.

Traub RD, Whittington MA, Stanford IM, Jefferys JG (1996) A mechanism for generation of long-range synchronous fast oscillations in the cortex. *Nature* 383:621–4.

Traub RD, Bibbig A, LeBeau FEN, Buhl EH, Whittington MA (2004) Cellular mechanisms of neuronal population oscillations in the hippocampus in vitro. *Annu Rev Neurosci* 27:247–78.

Turner RS, Desmurget M (2010) Basal ganglia contributions to motor control: a vigorous tutor. *Curr Opin Neurobiol* 20:704–16.

Uchida N, Mainen ZF (2003) Speed and accuracy of olfactory discrimination in the rat. *Nat Neurosci* 6:1224–9.

Usrey WM, Reid RC (1999) Synchronous activity in the visual system. *Annu Rev Physiol* 61:435–56.

Vaadia E, Haalman I, Abeles M, Bergman H, Prut Y, Slovin H, Aertsen A (1995) Dynamics of neuronal interactions in monkey cortex in relation to behavioural events. *Nature* 373:515–8.

van der Meer MAA, Johnson A, Schmitzer-Torbert NC, Redish AD (2010) Triple dissociation of information processing in dorsal striatum, ventral striatum, and hippocampus on a learned spatial decision task. *Neuron* 67:25–32.

van der Meer MAA, Redish AD (2009) Low and high gamma oscillations in rat ventral striatum have distinct relationships to behavior, reward, and spiking activity on a learned spatial decision task. *Front Integr Neurosci* 3:9.

van der Meer MAA, Kalenscher T, Lansink CS, Pennartz CMA, Berke JD, Redish AD (2010) Integrating early results on ventral striatal gamma oscillations in the rat. *Front Neurosci* 4:28.

van Drongelen W (2007) *Signal processing for neuroscientists: introduction to the analysis of physiological signals* Elsevier/Academic Press, Amsterdam.

Vanderwolf CH (1969) Hippocampal electrical activity and voluntary movement in the rat. *Electroencephalogr Clin Neurophysiol* 26:407–18.

Vanderwolf CH (1971) Limbic-diencephalic mechanisms of voluntary movement. *Psychol Rev* 78:83–113.

Varela F, Lachaux JP, Rodriguez E, Martinerie J (2001) The brainweb: phase synchronization and large-scale integration. *Nat Rev Neurosci* 2:229–39.

Vicente R, Gollo LL, Mirasso CR, Fischer I, Pipa G (2008) Dynamical relaying can yield zero time lag neuronal synchrony despite long conduction delays. *Proc Natl Acad Sci U S A* 105:17157–62.

von der Malsburg C, Schneider W (1986) A neural cocktail-party processor. *Biol Cybern* 54:29–40.

von Nicolai C (2011) Treadmill running capacities of Brown Norway rats. Equivalence thesis, Department of Biology, Faculty of Mathematics, Informatics and Natural Sciences, University of Hamburg, Hamburg, Germany.

von Stein A, Sarnthein J (2000) Different frequencies for different scales of cortical integration: from local gamma to long range alpha/theta synchronization. *Int J Psychophysiol* 38:301–13.

Walker JS (2008) *A primer on wavelets and their scientific applications* Chapman & Hall/CRC, Boca Raton, 2nd, updated and fully revised edition.

Walters JR, Bergstrom DA (2010) Synchronous activity in basal ganglia circuits In Steiner H, Tseng KY, editors, *Handbook of Basal Ganglia Structure and Function*,

Vol. 20 of *Handbook of Behavioral Neuroscience*, pp. 429–443. Elsevier.

Wang Q, Webber RM, Stanley GB (2010) Thalamic synchrony and the adaptive gating of information flow to cortex. *Nat Neurosci* 13:1534–41.

Wang XJ (2010) Neurophysiological and computational principles of cortical rhythms in cognition. *Physiol Rev* 90:1195–268.

Webster KE (1961) Cortico-striate interrelations in the albino rat. *J Anat* 95:532–44.

Webster KE (1965) The cortico-striatal projection in the cat. *J Anat* 99:329–37.

Welsh JP, Lang EJ, Suglhara I, Llinas R (1995) Dynamic organization of motor control within the olivocerebellar system. *Nature* 374:453–7.

West MO, Carelli RM, Pomerantz M, Cohen SM, Gardner JP, Chapin JK, Woodward DJ (1990) A region in the dorsolateral striatum of the rat exhibiting single-unit correlations with specific locomotor limb movements. *J Neurophysiol* 64:1233–46.

Wickens JR, Arbuthnott GW (2010) Gating of cortical input to the striatum In Steiner H, Tseng KY, editors, *Handbook of Basal Ganglia Structure and Function*, Vol. 20 of *Handbook of Behavioral Neuroscience*, pp. 341–351. Elsevier.

Wilson CJ, Kawaguchi Y (1996) The origins of two-state spontaneous membrane potential fluctuations of neostriatal spiny neurons. *J Neurosci* 16:2397–410.

Wise SP, Murray EA, Gerfen CR (1996) The frontal cortex-basal ganglia system in primates. *Crit Rev Neurobiol* 10:317–56.

Womelsdorf T, Schoffelen JM, Oostenveld R, Singer W, Desimone R, Engel AK, Fries P (2007) Modulation of neuronal interactions through neuronal synchronization. *Science* 316:1609–12.

Womelsdorf T, Fries P, Mitra PP, Desimone R (2006) Gamma-band synchronization in visual cortex predicts speed of change detection. *Nature* 439:733–6.

Wyble BP, Hyman JM, Rossi CA, Hasselmo ME (2004) Analysis of theta power in hippocampal EEG during bar pressing and running behavior in rats during distinct behavioral contexts. *Hippocampus* 14:662–74.

Yeterian EH, Van Hoesen GW (1978) Cortico-striate projections in the rhesus monkey: the organization of certain cortico-caudate connections. *Brain Res* 139:43–63.

Yin HH, Knowlton BJ (2006) The role of the basal ganglia in habit formation. *Nat Rev Neurosci* 7:464–76.

Zheng T, Wilson CJ (2002) Corticostriatal combinatorics: the implications of corticostriatal axonal arborizations. *J Neurophysiol* 87:1007–17.

Appendices

Zusammenfassung

Das aus kortikalen Arealen, Basalganglien und thalamokortikalen Verbindungen bestehende zentralnervöse System ist ein wesentlicher Bestandteil des Vorderhirns von Vertebraten und entscheidend an der Erzeugung, Anpassung und Auswahl koordinierter Muster motorischen und nicht-motorischen Verhaltens beteiligt. Es wird angenommen, dass synchrone, oszillatorische neuronale Gruppenaktivitäten von grundsätzlicher Bedeutung für die Kodierung und Übertragung von Signalen entlang der kortiko-striatalen Achse, der Eingangsebene der Basalganglien, sein könnten. Diese Auffassung bedarf der grundsätzlichen experimentellen Untermauerung.

Wanderratten (*Rattus norvegicus*) wurden darauf trainiert, sich in einem Laufbandversuch bei unterschiedlichen Geschwindigkeiten zu bewegen. Wir implantierten Mikroelektroden in sensomotorische kortikale und striatale Areale beider Hemisphären und leiteten Feldpotential- sowie Multizellaktivitäten (LFP und MUA) unter Ruhe und Bewegungsbedingungen ab. Wir führten Leistungs-, Phasenkopplungs- sowie Zwischenfrequenz-Interaktionsanalysen durch, um die spektralen Eigenschaften neuronaler Signale sowie ihre Wechselwirkung innerhalb und zwischen den beiden Strukturen zu charakterisieren. Die Modulation von Leistungsspektren und Phasenkopplungsmerkmalen wurde in Abhängigkeit von der motorischen Beanspruchung im Detail untersucht.

Die Daten zeigen markante Spitzenwerte oszillatorischer Amplituden und eine Synchronisation kortikaler und striataler LFPs in niedrigen (theta) und hohen (gamma) Frequenzbereichen unter Ruhe und Bewegung. Multizellaktivitiäten zeigten nur schwache Anzeichen niedrigfrequenter oszillatorischer Synchronisation, wohingegen die Kohärenz von LFPs und MUA im theta-Frequenzbereich statistisch signifikant war. Die Spitzenfrequenzen von LFP-Amplituden und -Kohärenzen stiegen zwischen den Verhaltensbedingungen an und zeigten einen linearen Zusammenhang mit der motorischen Beanspruchung. Zusätzlich beobachteten wir eine verhaltensmodulierte Koppelung von theta-Phasen und gamma-Amplituden und eine Abnahme der Amplitudenkorrelationen zwischen LFP-Frequenzkomponenten im Vergleich von Ruhe- und Laufbedingungen. Die Analyse von Wechselwirkungen zwischen Phasenkopplung und Amplitudenkorrelation ergab eine Abnahme ihrer zeitlichen Kofluktuation spezifisch an den Punkten niedriger und hoher Spitzenfrequenzwerte unter Bewegung.

Diese Resultate unterstreichen die Wichtigkeit frequenzspezifischer Synchronisation oszillatorischer Gruppenaktivitätsmuster für neuronale Wechselwirkungen entlang der kortiko-striatalen Achse. Koordinierte rhythmische Aktivitäten im theta- und gamma-Frequenzbereich könnten der funktionellen Kopplung beider Strukturen auf kurzen und langen Zeitskalen entsprechend akuter Verhaltensanforderungen förderlich sein. Ähnliche Aktivitätsmuster könnten der Signalkodierung und -übertragung auf anderen Ebenen der Basalganglienschleife zugrunde liegen.

Publications

Some parts of this study have previously been published in abstract form:

von Nicolai C, Engler, G, Moll CKE, Sharott A, Engel, AK (2007) Different levels of motor activity are reflected in changes of oscillatory neuronal patterns along the cortico-striatal axis of awake rats. *9th Triennial Meeting of the International Basal Ganglia Society (IBAGS).* Eegmond an Zee, The Netherlands, September 6–9, 2007.

von Nicolai C, Engler G, Moll CKE, Sharott A, Engel AK (2008) Changes in oscillatory neuronal patterns along the cortico-striatal axis accompany the switch from rest to running in the awake behaving rat. *38th Annual Meeting of the Society for Neuroscience (SfN).* Washington DC, USA, November 15–19, 2008.

Other parts have been taken and adapted from an equivalence thesis of the author:

von Nicolai C (2011) Treadmill running capacities of Brown Norway rats. *Equivalence thesis*, Department of Biology, Faculty of Mathematics, Informatics and Natural Sciences, University of Hamburg, Hamburg, Germany.

Erratum

The published version of this dissertation largely corresponds to the one submitted for examination. Apart from orthographic corrections, the following changes have been made:

(1) The Doctoral Committee's approval has been added behind the title page.
(2) The year of the citation in the front matter has been removed.
(3) The term 'coherence' has been changed to 'coherency' in the short title of Figure 2.14 (page iv).
(4) The term 'intercorrelation' has been changed to 'interrelation' in the short title of Figure 3.28 (page v).
(5) The terms 'in particular' on page 18, line 21, and 'below' on page 89, line 18, have been removed for overall formatting reasons.
(6) The address term 'Main St.' has been removed on page 30, line 4.
(7) The term 'rates of' has been changed to 'rates from' on page 44, line 1.
(8) The figure reference on page 77, line 9, has been corrected.
(9) The term 'Wilcoxon' has been added on page 85, line 13.
(10) The number 3.31 has been added to the listing of figures on page 100, line 7.
(11) The term 'hyperdrive' has been changed to 'microdrive' on page 106, lines 18 and 23, and page 107, line 2.
(12) The word 'as' has been added on page 107, line 25.
(13) The temporal order of citations has been corrected on page 114, line 12, and page 117, line 9.
(14) The term 'coherency' has been changed to 'coherence' on page 118, lines 10 and 11, respectively.
(15) The Curriculum Vitae has been removed for reasons of data privacy protection.
(16) Units of power results have been corrected and axis labels changed to V^2/Hz in case of non-normalized and normalized raw power. More precisely, changes have been made to axis labels in Figures 2.9 (panel a), 2.10, 2.13 (panels a, b), 2.14 (panel a), 2.16 (panel a), 2.17, 3.3 (panels a, c), 3.5 (panel a), 3.29 (panel a), 3.30 (panel a). Also, the footnote on page 68 has been modified accordingly.
(17) Arbitrary units have been added to the y-axis label in panel b of Figure 3.6.

Acknowledgment

I'm more or less indebted to many, but most of all to the following people:

Prof. Dr. med. Andreas K. Engel, my thesis advisor, for his long lasting support of and the opportunity to realize this demanding, highly instructive project.

Dr. rer. nat. Gerhard Engler, my laboratory manager, for his outstanding technical assistance, never-ending trust, and permanent, soothing presence.

Benjamin M. Grieb, for being the best friend and most supportive colleague that long, shared working days and nights and rare times off could have brought about.

Christian Moll, my very first research tutor, for all his theoretical and practical input and for dragging me into the subcortical terrains of the brain in the first place.

Dr. Andrew Sharott, for analytical assistance as well as highly inspiring research times and idle hours in offices and downtown bars.

Dr. med. Markus Siegel, for his personal as much as for his technical and professional mentoring and friendship, the programming *spirit* and for his patience in the end.

Everyone at the Department of Biology who supported the finalization of this project.

Dr. med. Dorothea von Nicolai and Prof. Dr. rer. nat. Hubertus von Nicolai, my loving parents, for their endless support, generosity, and liberality over 30 Years Live; and C. von Nicolai ($n = 5$), simply the best brothers and sisters around. Cya all in hell!

Friederice Pirschel, Conradin von Nicolai, Andrew Sharott, Catharina von Nicolai for proofreading of the manuscript.

This is for one who understands.

Statutory Declaration of Authorship

This little volume summarizes part of the work the author carried out as a research team member of the *Basal Ganglia Physiology* group at the Department of Neurophysiology and Pathophysiology, University Medical Center Hamburg-Eppendorf, Hamburg, Germany, between the years 2004–2011.

I hereby declare, on oath, that I have written the present dissertation by my own and have not used any other than the acknowledged resources and aids.

Tübingen, 22.05.2012

Constantin von Nicolai